UNIVERSITÀ DEGLI STUDI DI MODENA E REGGIO EMILIA

PhD Course in
"Physics and Nanosciences"

# Supramolecular self-assembly and characterization of synthetic two-dimensional materials

PhD Candidate: VASILIKI BENEKOU

Supervisor: Dr. VINCENZO PALERMO (CNR-ISOF)

Co-supervisors: Dr. ANDREA CANDINI (CNR-ISOF), Prof. ANDREA ALESSANDRINI (UNIMORE)

Coordinator of the PhD Course: Prof. MARCO AFFRONTE

XXXVI Edition
February 2024

Σα βγεις στον πηγαιμό για την Ιθάκη,
να εύχεσαι να΄ναι μακρύς ο δρόμος,
γεμάτος περιπέτειες, γεμάτος γνώσεις.

[…]

As you set out for Ithaka
hope your road is a long one,
full of adventure, full of discovery.
[…]

Constantine P. Cavafy, *Ithaca*, 1911

# Abstract

The field of two-dimensional materials (2DMs) has seen a surge in interest, driven by the groundbreaking emergence of graphene as a pioneer material in this domain. The unique chemical and physical characteristics of 2DMs have opened up new opportunities for applications in electronics, energy storage, and conversion technologies to meet modern societal demands. While graphene continues to be at the forefront of research, a wide range of other 2D materials, including metal chalcogenides, boron nitride, MXenes, and two-dimensional polymers, are now being explored.

The urgent need to close the knowledge gap between two-dimensional materials' scientific discovery and practical applications is the motivation behind this doctoral dissertation. The primary goal is to comprehensively understand the intrinsic properties of newly synthesized 2D materials and improve synthesis procedures to facilitate the smooth integration of these materials into tangible products. Additionally, the project addresses the creation of novel two-dimensional materials, focusing on the intricate process of organic molecules self-assembling on surfaces and exploring their subtle interactions with existing 2D materials.

The project's three-year goal was to develop various processing methods for efficiently self-assemble of specific building blocks into carefully planned 2D structures. Multiscale characterization techniques, including Atomic Force Microscopy (AFM), Kelvin Probe Force Microscopy (KPFM) and Conductive AFM were employed for structural analysis and electrical characterization with nanometer size resolution and X-ray photoelectron spectroscopy for the chemical composition characterization.

More specifically, the electrical properties and interactions between diverse 2D materials on various substrates are thoroughly investigated in this thesis. Using Kelvin probe force microscopy, changes in the work function of synthetic two-dimensional materials were monitored with respect to their thickness, polymer formation time, crystallinity, and substrate for 2D polymers and coordination polymer thin films, and with respect to the type of functionalization for other two-dimensional materials like MXenes. Additionally, the vertical

conductivity of 2D polymers and coordination polymer thin films was evaluated by employing conductive AFM. Conductivity was monitored with respect to the 2D polymers' crystallinity, formation time, and film thickness.

Another important goal of this thesis was the realization of a platform for controlled self-assembly of molecules on different substrates. The Temperature-enhanced solvent vapor annealing (TESVA) technique is the basis of the platform's function offering the ability to self-assemble different molecules on any type of substrate (silicon and gold were used in this work), with control over experimental parameters such as temperature and height of the sample on the solvent reservoir. These factors are key parameters to achieve a controlled self-assembly. Utilizing TESVA, we successfully synthesized porphyrin crystals with distinct morphological features that are significantly larger and more homogeneous than the ones obtained with spontaneous self-assembly.

In summary, we were able to effectively synthesize and self-assemble a variety of 2D materials on various substrates during the course of this thesis. These materials were then thoroughly studied utilizing a vast number of characterization techniques with an emphasis on their electrical properties. Our goal is that this work will serve as a roadmap for improved characterization and further research on two-dimensional materials.

# Sommario
# (abstract in Italian)

Il campo dei materiali bidimensionali (2DM) ha suscitato negli ultimi anni un interesse enorme e sempre crescente, grazie all'emergere del grafene, il materiale pioniere in questo settore. Le caratteristiche chimiche e fisiche uniche dei materiali bidimensionali offrono opportunità per nuove applicazioni in elettronica, immagazzinamento e conversione dell'energia per soddisfare le esigenze della società moderna. Sebbene il grafene rimanga il materiale più studiato, si sta ora esplorando un'ampia gamma di ulteriori materiali 2D, come i calcogenuri metallici, il nitruro di boro, gli MXenes e i polimeri bidimensionali.

L'urgente necessità di colmare il divario di conoscenze tra la scoperta scientifica dei materiali bidimensionali e le applicazioni pratiche è la motivazione alla base di questa tesi di dottorato. L'obiettivo principale è comprendere le proprietà intrinseche dei materiali 2D di nuova sintesi e migliorare le procedure di sintesi per facilitare l'integrazione di questi materiali in prodotti tangibili. Inoltre, il progetto affronta la creazione di nuovi materiali bidimensionali, concentrandosi sull'intricato processo di autoassemblaggio delle molecole organiche sulle superfici ed esplorando le loro sottili interazioni con i materiali 2D esistenti.

L'obiettivo triennale del progetto era quello di sviluppare vari metodi di lavorazione per l'autoassemblaggio efficiente di specifici blocchi di costruzione in strutture 2D accuratamente pianificate. Sono state impiegate tecniche di caratterizzazione multiscala, tra cui la microscopia a forza atomica (AFM), la microscopia a sonda Kelvin Probe (KPFM) e l'AFM conduttivo per l'analisi strutturale e la caratterizzazione elettrica con risoluzione nanometrica e la spettroscopia di fotoelettroni a raggi X per la caratterizzazione della composizione chimica.

In particolare, in questa tesi vengono studiate a fondo le proprietà elettriche e le interazioni tra diversi materiali 2D. Utilizzando la microscopia di Kelvin Probe, sono stati monitorati i cambiamenti nella funzione di lavoro dei materiali bidimensionali sintetici in relazione allo spessore, al tempo di formazione del polimero, alla cristallinità e al substrato per i polimeri 2D e i film sottili di polimeri di coordinazione, e in relazione al tipo di funzionalizzazione per altri materiali bidimensionali come gli MXenes. Inoltre, la conducibilità verticale dei due tipi di

polimeri è stata valutata utilizzando l'AFM conduttivo. La conduttività è stata monitorata in relazione alla cristallinità, al tempo di formazione e allo spessore del film.

Un altro importante obiettivo di questa tesi è stata la realizzazione di una piattaforma per l'autoassemblaggio controllato di molecole su diversi substrati. La tecnica TESVA (Temperature-enhanced solvent vapor annealing) è alla base del funzionamento della piattaforma e offre la possibilità di autoassemblare diverse molecole su qualsiasi tipo di substrato con il controllo di temperatura e l'altezza del campione sul serbatoio di solvente. Questi fattori sono parametri chiave per ottenere un autoassemblaggio controllato. Utilizzando TESVA, abbiamo sintetizzato con successo cristalli di porfirina, significativamente più grandi e più omogenei di quelli ottenuti con l'autoassemblaggio spontaneo.

Riassumendo, nel corso di questa tesi siamo stati in grado di sintetizzare e autoassemblare efficacemente una varietà di materiali 2D su vari substrati. Questi materiali sono stati poi studiati a fondo utilizzando diverse tecniche di caratterizzazione avanzata, con particolare attenzione alle loro proprietà elettriche. Il nostro obiettivo è che questo lavoro serva da roadmap per guidare le future ricerche sui materiali bidimensionali e migliorare la loro caratterizzazione.

# TABLE OF CONTENTS

# INTRODUCTION AND AIM OF THE THESIS

**The present chapter provides an introduction, the aim and motivation of the current doctoral thesis, along with a short description for each of the following chapters.**

Graphene, as a pioneer, has sparked widespread interest in the fascinating world of two-dimensional materials (2DMs) [1], [2], [3]. The chemical and physical characteristics of this novel class of materials have impressed the entire research community. They also hold promise for future emerging technologies that will address a wide range of societal needs, including energy conversion and storage and faster and more efficient electronics. While graphene research remains at the forefront of this area of interest, also other 2D materials are garnering more and more attention, especially in recent years. Many atomically thin materials have been produced or isolated: these include, among others, metal chalcogenides and boron nitride. More recently, novel 2D materials have also emerged as promising candidates: MXenes and 2D polymers [3]. However, much more research is needed to make it easier to synthesize these materials, and their unique properties must be understood and investigated before they can be used in real-world applications. Despite the fact that this new class of materials is continually expanding, research is currently concentrated on comprehending both their synthesis method and their basic properties, with the aid of numerous characterization techniques.

Aside from the scientific curiosity surrounding 2D materials due to their distinct mechanical and electrical characteristics, there is still a gap that needs to be filled between basic science and application-making. In order to do that, we must gain firsthand experience with commercially available products, comprehend their shortcomings, and attempt to overcome their limitations by adding new two-dimensional materials to those that already exist.

In this rapidly expanding research area focusing on 2DMs, this doctoral thesis is inserted in the framework of a European Marie Curie ITN project, called ULTIMATE (https://ultimate.u-strasbg.fr/index.php). It is coordinated by prof. Samorì at the university of Strasbourg and featuring some of the most recognized European groups working in the field of basic and applied research on 2D materials.

The focus of the project is on how to generate novel atomically precise 2D materials with defined structure and composition, and how to best exploit their unique and tunable properties for electronics and energy applications. In this context, this doctoral thesis aims to employ advanced characterization techniques to investigate, understand and possibly improve the self-assembly and processing of organic molecules from solution onto surfaces (such as solvent vapor annealing, crystal growth, and self-assembly from solution) to create new types of two-dimensional materials and to investigate their interactions with other two-dimensional materials currently in use[4]. More precisely, we will introduce the reader into various processing and post-processing methods that enable the chosen building blocks to self-assemble into ordered 2D architectures. The main characterization techniques that we used include structural characterization with Atomic Force Microscopy (AFM), electrical characterization via Kelvin Probe Force Microscopy (KPFM) [5]and Conductive AFM (C-AFM), and other structural and chemical characteristics via X-ray photoelectron spectroscopy. Such wide range of multiscale techniques have been utilized to study the structure as well as the physical and chemical properties of the various 2D materials.

When 2D materials are newly synthesized, AFM may provide information on their thickness and surface morphology under ambient conditions as well as under various post-treatment parameters (such as changes in height or surface morphology over time, under illumination, after temperature changes etc.). We applied KPFM in order to gain new understanding of the electrical properties [6] of various 2D materials, to investigate possible changes in their electrical characteristics, to identify any charge transport properties and interactions between various 2D materials on various substrates. We employed also C-AFM in order to get insight on their electrical conductivity features.

As previously stated, there are still physical and chemical phenomena that need to be studied in this developing class of 2DMs, even though the scientific interest in them has increased over the past few years. The fact that most of these newly developed 2DMs have not undergone sufficient research to the point where they could be used in applications makes this doctoral thesis particularly significant for what concerns its novelty. Thus, this is the primary focus of the present thesis.

We focused on both novel and well-established methods in order to produce the materials under study (developed in our laboratory or coming from partners inside the ULTIMATE project) along with a number of high-end characterization techniques in order to realize the anticipated properties of these materials and study in detail their fundamental characteristics.

Chapter 1 introduces the basic principles of all the characterization methods used to investigate the properties of the materials under study throughout this Thesis. This chapter provides the reader with all information about the characterization techniques that were utilized from a scientific perspective as well as the associated equipment. The morphological and chemical features of the materials under study have been studied Atomic Force Microscopy (AFM) and X-ray photoemission spectroscopy (XPS) respectively. An emphasis was given on utilizing conductive AFM and the Kelvin probe technique to determine the electrical properties of these materials [5].

Chapter 2 covers the chemical, electrical and thermal properties of thin coordination polymer films produced by a novel and versatile synthesis method. More specifically various coordination polymer thin films have been prepared using a shear-coating technique [7], [8]. A detailed characterization of the films that distinguishes their chemical and physical properties is centred on two important electronic properties: work function and conductivity. Indeed, these traits may be affected by the main metal element of the coordination polymer, thickness of the produced film, and formation time of the polymer. Furthermore, the thermal stability of these entities is examined regarding both their morphological and electronic characteristics.

Chapter 3 presents the electrical properties of 2D polyaniline synthesized by a novel technique. To achieve high-performance organic electronics, it seems promising to construct conducting polymer thin films with morphological homogeneity and long-range molecular ordering. A lot of attention has been focused on polyaniline (PANI) because of its interesting electrical conductivity and appealing chemistry [9]. However, because aniline oligomers have intricated intermolecular interactions, synthesizing large-area PANI thin films and controlling their thickness and crystallinity continue to be difficult tasks. In this chapter, a large area 2D PANI has been synthesized by a novel and versatile technique. A study of the electrical characteristics of this promising two-dimensional Polyaniline film is the main focus of the chapter.

Chapter 4 focuses on the morphological and electrical properties of various 2DMs at the level of individual layers, nominally Mxenes [10], isolated sheets of $In_2Se_3$, functionalised $MoS_2$ and isolated soot molecules. In this chapter, MXenes, in their pristine form as well as chemically functionalized with different organic molecules, isolated sheets of $In_2Se_3$, electrochemically

functionalised $MoS_2$ films and soot molecules are studied with atomic force microscope to understand their morphology and with Kelvin probe force microscopy (KPFM) as well as with conductive AFM in order to investigate their electrical properties [11], [12], [13]. In all cases, functionalisation causes changes in the work function of the materials under study, providing an exciting opportunity for tuning their electrical properties. Chapter 4 also includes an atomic resolution AFM and STM study of soot molecules, which provides important information about the origin of these molecules that are so important to health and the environment.

Last, Chapter 5 discusses the realisation of a universal platform for the assembly and manipulation of molecules at the nanoscale. More specifically, we developed an experimental setup to perform temperature enhanced solvent vapor annealing for the growth and manipulation of various molecules when deposited on a substrate. The self-assembly and/or growth is performed in a home-made chamber specifically engineered to control the temperature difference between the solvent used and the surface of the substrate where our initial system has been deposited[14]. By changing the temperature difference, substrate, or solvent we can realise novel nano-structures, which cannot be obtained by conventional deposition methods. The newly organised networks are then characterised by SPM techniques.

# REFERENCES


[1] F. H. L. Koppens, T. Mueller, Ph. Avouris, A. C. Ferrari, M. S. Vitiello, and M. Polini, "Photodetectors based on graphene, other two-dimensional materials and hybrid systems," *Nat Nanotechnol*, vol. 9, no. 10, pp. 780–793, Oct. 2014, doi: 10.1038/nnano.2014.215.

[2] K. S. Novoselov, V. I. Fal'ko, L. Colombo, P. R. Gellert, M. G. Schwab, and K. Kim, "A roadmap for graphene," *Nature*, vol. 490, no. 7419, pp. 192–200, Oct. 2012, doi: 10.1038/nature11458.

[3] S. Yang, P. Zhang, A. S. Nia, and X. Feng, "Emerging 2D Materials Produced via Electrochemistry," *Advanced Materials*, vol. 32, no. 10, Mar. 2020, doi: 10.1002/adma.201907857.

[4] G. De Luca *et al.*, "Solvent vapour annealing of organic thin films: Controlling the self-assembly of functional systems across multiple length scales," *J Mater Chem*, vol. 20, no. 13, pp. 2493–2498, 2010, doi: 10.1039/b921612j.

[5] V. Palermo, M. Palma, and P. Samori, "Electronic characterization of organic thin films by Kelvin probe force microscopy," *Advanced Materials*, vol. 18, no. 2. pp. 145–164, Jan. 19, 2006. doi: 10.1002/adma.200501394.

[6] A. Liscio *et al.*, "Charge transport in graphene–polythiophene blends as studied by Kelvin Probe Force Microscopy and transistor characterization," *J Mater Chem*, vol. 21, no. 9, p. 2924, 2011, doi: 10.1039/c0jm02940h.

[7] S. R. Batten, "Coordination polymers," 2001.

[8] K. Haase, J. Zessin, K. Zoumboulis, M. Müller, M. Hambsch, and S. C. B. Mannsfeld, "Solution Shearing of a High-Capacitance Polymer Dielectric for Low-Voltage Organic Transistors," *Adv Electron Mater*, vol. 5, no. 6, Jun. 2019, doi: 10.1002/aelm.201900067.

[9] A. G. Macdiarmid, J. C. Chiang, A. F. Richter, and A. J. Epstein, "POLYANILINE: A NEW CONCEPT IN CONDUCTING POLYMERS," 1987.

[10] Y. Gogotsi and B. Anasori, "The Rise of MXenes," *ACS Nano*, vol. 13, no. 8. American Chemical Society, pp. 8491–8494, Aug. 27, 2019. doi: 10.1021/acsnano.9b06394.

[11] A. Agresti *et al.*, "Titanium-carbide MXenes for work function and interface engineering in perovskite solar cells," *Nat Mater*, vol. 18, no. 11, pp. 1228–1234, Nov. 2019, doi: 10.1038/s41563-019-0478-1.

[12] O. Samy, S. Zeng, M. D. Birowosuto, and A. El Moutaouakil, "A Review on MoS2 Properties, Synthesis, Sensing Applications and Challenges," *Crystals (Basel)*, vol. 11, no. 4, p. 355, Mar. 2021, doi: 10.3390/cryst11040355.

[13] L. A. Lieske *et al.*, "Portraits of Soot Molecules Reveal Pathways to Large Aromatics, Five-/Seven-Membered Rings, and Inception through π-Radical Localization," *ACS Nano*, vol. 17, no. 14, pp. 13563–13574, Jul. 2023, doi: 10.1021/acsnano.3c02194.

[14] E. Treossi, A. Liscio, X. Feng, V. Palermo, K. Müllen, and P. Samorì, "Temperature-enhanced solvent vapor annealing of a C3 symmetric hexa-peri-hexabenzocoronene: Controlling the self-assembly from nano- to macroscale," *Small*, vol. 5, no. 1, pp. 112–119, Jan. 2009, doi: 10.1002/smll.200801002.

# CHAPTER 1

# Characterization techniques

**The present chapter discusses the characterization methods used to investigate the properties of the materials under study throughout this thesis.**

The overall objective of the current doctoral thesis is to characterize the morphological, chemical, and electrical properties of various two-dimensional materials. To this end, we employed a multi-tool and multi-scale approach. This chapter discusses the characterization techniques that have been utilized from a scientific perspective as well as the associated equipment. The morphological and chemical features of the materials under study have been studied by Atomic Force Microscopy (AFM) and X-ray photoemission spectroscopy (XPS) respectively. In addition, the electrical properties of these materials have been addressed using conductive AFM and Kelvin Probe Force microscopy (KPFM).

## 1.1 Morphological characterization

### *1.1.1 Atomic Force Microscopy (AFM)*

Atomic force microscopy (AFM) is a popular characterization technique that offers information on the material's topography at the nanoscale and even below. An AFM image is created by measuring the forces experienced by a solid, pointy tip as it scans the sample surface. Nowadays, modern AFMs offer the possibility to analyse multiple properties of the material under study, such as morphological, mechanical, electrical, magnetic, electro-chemical, etc., by combining different signals, depending on how the tip interacts with the sample. AFM images typically have a vertical range of hundreds of nanometres with sub-nanometre height resolution and a horizontal range of several tens of micrometres up to 100 µm with the best (physical) lateral resolution of only a few nm. Newer atomic resolution AFMs, on the other hand, are capable of much higher quality—less than 7 Å in lateral resolution and 1 Å in vertical resolution have already been reported in literature [1], [2], [3].

Importantly, any substance, regardless of how hard or soft, conducting or insulating, may in principle be imaged.

An essential component of the method is the assessment of interatomic forces, which differentiate between repulsive forces associated with short-range order (roughly $10^{-1}$ nm) and attractive forces linked to long-range order (between $10^{0} \div 10^{1}$ nm). Van der Waals forces that are attractive originate from several sources, including dipole-dipole, dipole-induced, and induced dipole-induced interactions. Repulsive forces, on the other hand, originate from the Pauli exclusion principle, which states that electrons with the same quantum number cannot occupy the same spatial region[4]. The Lennard-Jones potential[5] can be used to model the interaction between an atom or molecule on the sample surface and the apex atom or molecule of an ultra-sharp tip:

$$\mathrm{V}(z) = -\frac{A}{z^6} + \frac{B}{z^{12}} \qquad (1.1)$$

Where A and B are empirical parameters, and z is the distance between the two atoms/molecules. The potential is negligible for large z. The attractive region of $V$ begins to decrease at a certain distance and reaches a minimum at $z_0$, which is the two-particle system's equilibrium distance. As z is reduced further, $V$ increases and atoms repel one another.

An Atomic Force Microscopy (AFM) instrument typically consists of a flexible cantilever with a tip attached to one end that is free to move and the other one that is fixed. (see Figure 1-1a). The measurement range of the instrument is $10^{-12}$ N to $10^{-6}$ N, depending on the stiffness of the cantilever. The sample is placed on a platform that is below the tip. All three spatial directions (x, y, and z) can be moved by using a piezoelectric device: either by moving the tip relative to the sample, or by moving the sample stage relative to the tip. The relative motion occurs along a line, which forms the fast-scanning direction. By repeating this process along multiple lines that are parallel to the first line, a two-dimensional image of the surface is formed. The cantilever, which can be roughly modelled as a driven harmonic oscillator, experiences a deflection ($\Delta z = z_0 - z$) at each point due to the interatomic force between the tip and the sample. Typically, a laser beam is used to measure the cantilever's deflection: a screen or photodetector records the intensity of the light that scatters as the laser beam hits at the upper portion of the cantilever; light will hit the screen at a different point if the cantilever moves from its free force position ($z_0$). In this way, the surface image of the sample is formed since the photodetector's signal will correspond to its morphology (or the other

physical properties that are measured). Very often, it is convenient to equip the system with a feedback loop: in such cases, a predetermined setpoint value is compared with the photodetector signal and a counter signal is applied to the tip-sample system in order to restore the setpoint value in the event of any deviations. Then, a calibrated image is produced using this counter signal.

The traditional method of measuring consists in making tip-sample contact at each measurement point by keeping the tip as close to the sampled structure as feasible. In this case, "contact" suggests that tip-sample interactions take place in the repulsive portion of the potential curve[4] (eq. 1.1).

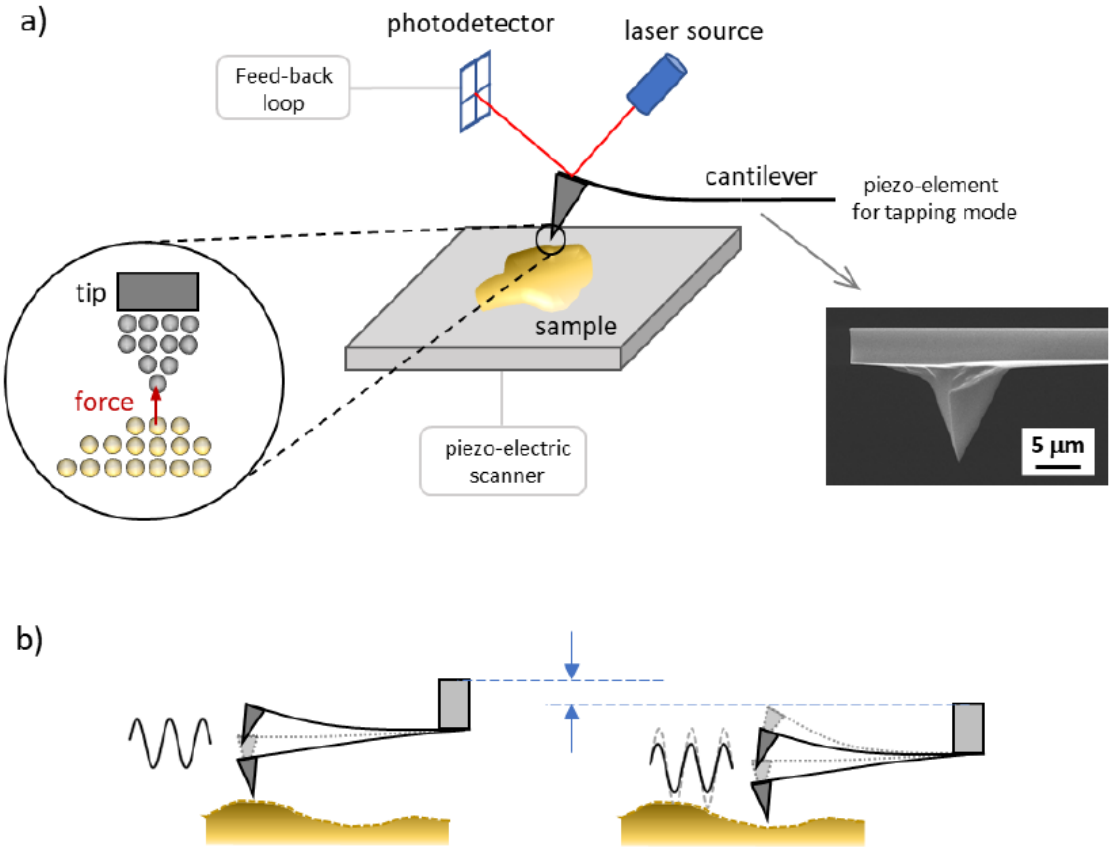


*Figure 1-1. (a) An illustration of a standard AFM setup. The interaction that takes place between a sharp tip and the sample structure is what drives the imaging mechanism. An electronic micrograph (SEM) of the tip utilized for topographic imaging is in the right corner.*

*(b) An illustration of the "tapping" imaging mode: to maintain amplitude constant, the potential applied to the cantilever is changed to respond to variations in topography that alters the sample-tip interaction*[4].

Intermittent contact is a more sophisticated but frequently used type of AFM operating modes. Among these, "tapping mode," which uses amplitude modulation as shown in Fig. 1-1b, is the most popular choice among AFM users. In intermittent contact, as opposed to contact mode, oscillation in the cantilever is created while scanning. An additional piezoelectric device attached to the cantilever induces this oscillation. The selected oscillation frequency usually accounts for shifts associated with tip-sample engagement and is marginally lower than the cantilever's natural resonant oscillation frequency, determined by the dimensions and form of the probe assembly—consisting of the cantilever and tip—. Changes in the oscillation frequency and amplitude are a result of the interactions between the tip and the sample. Through a feedback loop, the measured amplitude at each imaging point is compared to a predefined set point value. In order to track surface topography and adjust the amplitude if there is a change, a correction voltage is applied to the additional piezoelectric device. The selection of the amplitude set point considers sample surface properties, tip wear, and imaging objectives. This set-point represents the allowable amplitude variation prior to the feedback mechanism being triggered and is associated with the free (i.e., away from the sample) oscillation amplitude[4]. A lower set-point therefore suggests a stronger tip-sample interaction force. The shortened interaction time with the sample causes the tip to experience alternating repulsive and attractive forces in intermittent contact. Compared to an approach where the tip is in constant contact with the sample, this slows down the wear of the tip, minimizes contributions due to lateral force, reduces the risk of damaging of the sample, and lowers the risk of dragging particles of dirt potentially present on the sample. Taking into account the sample structure, these considerations are especially important when studying two-dimensional materials deposited on a substrate with weak adhesion. In contrast to contact mode, the cantilever responds to significant topographic changes more slowly, so a slower scanning rate might be necessary[4].

AFM images are prone to several artifacts, some of which can be digitally corrected by post-processing the image to improve data clarity[4]. Specifically, "scanner bow," "edge z-overshoot," and "scanner creep" are artifacts caused by piezoelectric scanners. The "scanner bow" phenomenon is noted when scanning across relatively large dimensions (several tens of micrometers) in tube piezoelectric devices attached at one end of the microscope structure. Along the fast-scanning axis, this effect manifests as a curvature or "bow" in the z-direction. AFM images' edge overshoots can be attributed to z-axis hysteresis in the piezoelectric ceramic material. The name refers to the inaccurate tracing of step profiles, where the edges have z-values that are either higher or lower. When the piezo material's response deviates from the applied voltage precisely, creeps are created, which cause distortions in the image that resemble sample drift. Reapplying the voltage or waiting for the piezo response to

stabilize are potential fixes, which would essentially mean starting the scanning from the beginning. Inaccurate distance measurements may arise from non-linearity in piezo movements. If available, though, accurate calibration of the scanner sensors may alleviate this problem. Other common artifacts are related to the tip conditions; the tip may be too big (blunt tip) to follow object features accurately, or it may be damaged or contaminated during scanning. As a result, the picture might show undersized cavities, repeating patterns, and oddly shaped objects. One example of probe damage is the formation of double (or multiple) tips at the tip apex, which appear in the image as double (or multiple) copies that are slightly shifted from one another. Sadly, there is no way to digitally fix tip-related artifacts. Although there are certain tip-cleaning techniques available, changing the probe is frequently the easiest solution. When artifacts show up in the image as regular oscillations, they usually are related to noise phenomena. These can be caused by malfunctioning electronics in the microscope or mechanical vibrations in the surrounding environment, such as vibrations from connected lab instruments, buildings, or acoustic disturbances. High-frequency oscillations or asymmetrically enlarged shapes can be caused by improper scanning rates and feedback parameters[4]. By subtracting averaged and line-by-line polynomials from the raw image, one can correct artifacts caused by the piezoelectric scanner's z-height while also eliminating nano-objects from the process (i.e., flattening procedure). Histogram analysis is used to monitor the flattening process, as shown in Figure 1-2 [6]. Fc represents a discrete 1D function whose domain is defined by the obtained signal's minimum and maximum values (z value). The measured SPM image is represented by a (x,y) plane, where Fc denotes the relative frequency of the collected data. When statistical noise occurs and data points randomly scatter around a mean value, Fc can be described by a Gaussian function (G).

For our research, we used an NT-MDT *Ntegra-I* and a Brucker *Multimode 8* (Figure 1-3) commercial AFM [7]. Both instruments employ a laser/photodetector measuring system and include a tube scanner underneath the sample stage. In addition, to minimize the effects of outside vibrations in the lab, they are installed on independent vibration isolation systems, a mechanically damped stage, and a gas-damped bench. We chose to operate them in intermittent contact mode in order to obtain comprehensive data concerning the morphology of polymeric films and two-dimensional material flakes. A rectangular Si cantilever with quite a high force constant *k* (RTESPA-300, Brucker, *k*=40N/m, ω=300kHz) was typically used. For image processing, we utilized the SPIP software, specifically version 6 from Image Metrology. To collect data for statistical analysis on flakes of several two-dimensional materials, the "particle analysis" tool was utilized. Last, the images were filtered to remove unwanted objects by applying filters to quantities like area, mean z, and geometric shape. More details about image processing are provided in the chapters related to the results.

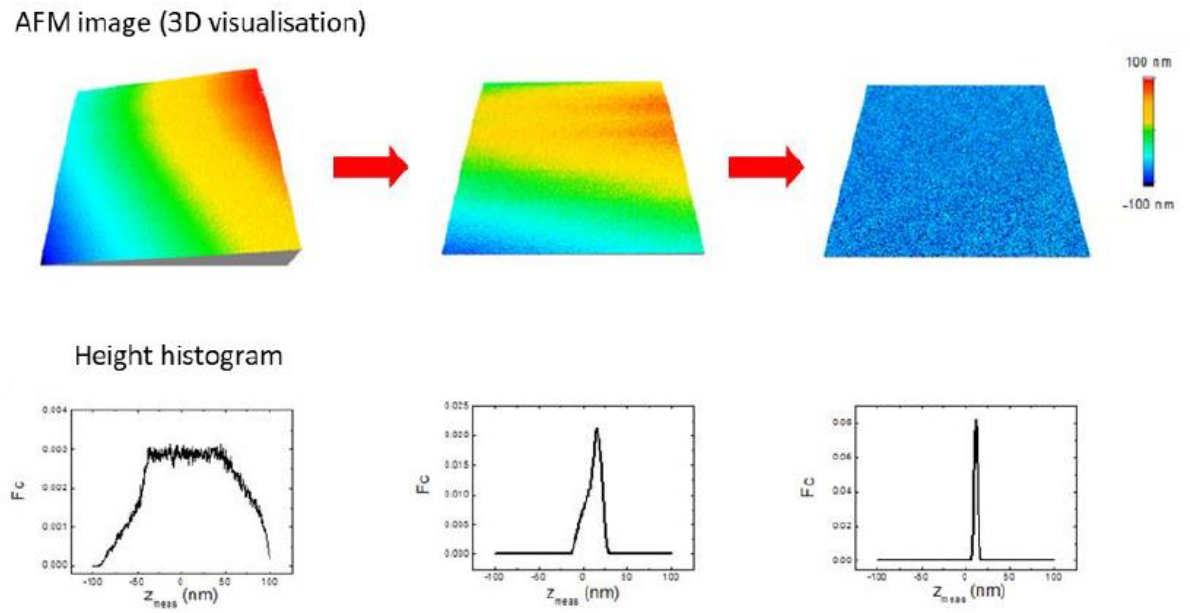


*Figure 1-2. An overview of the AFM image flattening process. From left to right, three AFM images are shown with a matching height histogram below, arranged in order of increasing data processing. After subtracting artefacts due to non-linear scanner movement, fitted as polynomials, the real, flat substrate is represented by the right image, whereas the raw data is shown on the left. Below each image, a histogram shows the height distribution inside the image. Picture taken from reference*[6].

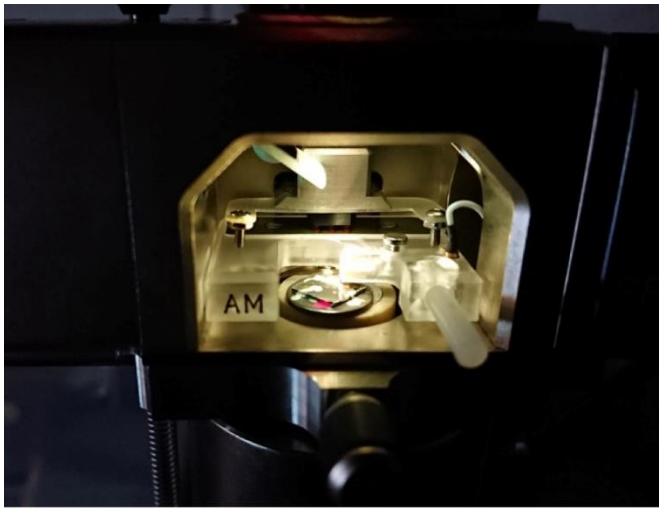


*Figure 1-3. Bruker Multimode 8, AFM head, located at CNR-ISOF* [7].

### *1.1.2 Optical Microscopy*

Optical microscopy (OM) is a quick and accurate method for examining a sample's morphology in the millimetric to several micrometric range. It uses visible light as the illuminating source. A system of physical lenses that focus and gather either reflected or transmitted light from the sample to produce an enlarged view is the foundation of the OM operating principle. The magnified sample image can be seen through eyepieces in standard laboratory equipment, appear on the retina of a human, or be digitally captured and stored with a digital camera[4].

Here, we employed a Nikon *Eclipse 80i* optical microscope in reflection mode to quickly characterize the morphology of our materials under study prior to any characterization with AFM. A digital colour camera (Nikon Coolpix 5400), a bright light source, and a set of appropriate objective lenses (4x, 10x, 20x, and 40x) are included with the microscope[4].

## 1.2 Chemical characterization

### *1.2.1 X-ray Photoelectron Spectroscopy (XPS)*

The term "photoemission spectroscopy," also known as "photoelectron spectroscopy," describes the process of measuring the energy of electrons released by solids, gases, or liquids via the photoelectric effect. This measurement enables the determination of the electron binding energies within a substance. XPS offers a quantitative assessment of the atomic composition and chemical state of the atoms. It is sensible only to the first few nanometers of the sample because of the limited escape depth of the photoemitted electrons from solids[8]. The technique is based on the photoelectric effect, initially observed by Hertz[9] and subsequently explained theoretically by Einstein in 1905 as the consequence of electromagnetic radiation's wave-particle duality[10]; it was for this theory that he was awarded the Nobel Prize in 1921. When a material is subjected to electromagnetic radiation with a sufficiently high energy $h\nu$, it releases electrons with kinetic energy $E_{\mathrm{K}}$. The process's energy balance is expressed by:

$$h\nu = E_B + E_K + w \qquad (1.2)$$

where $w$ is the energy difference between the vacuum and the Fermi level, and $E_B$ is the binding energy of the electron prior to emission (Figure 1-4b). Different levels of electrons that are associated with various atomic states and/or levels (chemical environment, oxidation state etc…) in the material may be excited by the fixed radiation $h\nu$ and result in their emission, or ionization. Different kinetic energies $E_{\mathrm{K}}$ result from this. The photoemitted spectrum is the plot obtained from a PE measurement, which involves counting the number of electrons that are photoemitted as a function of their kinetic energy. Additionally, it is typical for $E_B$ to be presented on the abscissa-axis in literature rather than $E_{\mathrm{K}}$.

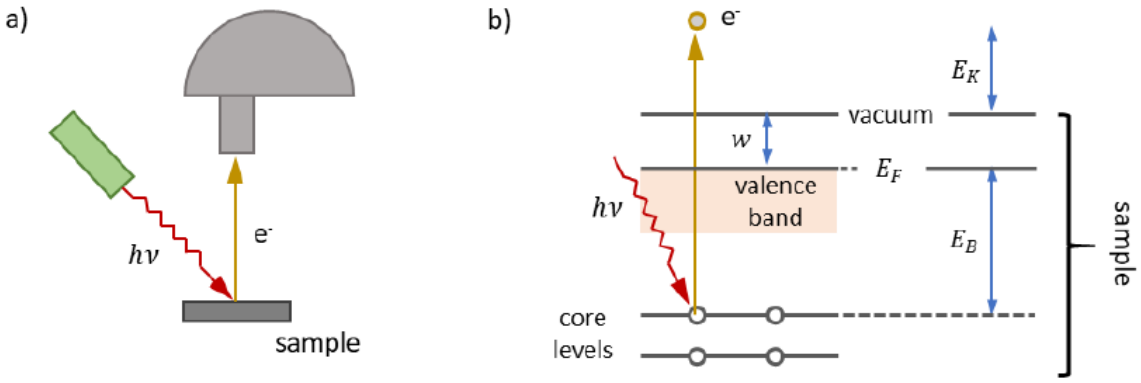


*Figure 1-4. (a) Basic concept of photoelectron spectroscopy: incident light with energy $h\nu$ occurs the sample surface, causing an electron $e^-$ to be emitted. This electron is then detected, and its kinetic energy is measured. (b) Energy diagram that illustrates the same electron photoemission process. Atoms with a continuum band of valence energy levels and deep energy core levels comprise the sample* [4].

A complementary technique, Ultraviolet photoelectron spectroscopy (UPS), enables the investigation of valence band structures and density of states for ultraviolet radiation ($\hbar\nu$ ~$10 \div 10^2$ eV).

Conversely, XPS measures core states (0.4 keV < $h\nu$ <3 keV). XPS is also called with the acronym ESCA (Electron Spectroscopy for Chemical Analysis) in the materials science community.

Electrons that are not primarily involved in chemical bonding are found in the states known as atomic core states. The XPS spectrum of the material under investigation displays peaks that correspond to such ejected electrons. One can determine the composition of the

material because the $E_B$ of an electron in a particular atomic shell varies depending on the element. The only two exceptions are helium and hydrogen, for which lab-scale instrumentation cannot enable the emission due to low photoionization cross-section[11],[12]. Unlike x-ray radiation, which can penetrate deep into a solid, excited electrons experience inelastic scatterings with other bound electrons and energy loss over short distances. When they originate farther away from the surface, their probabilities of escaping the substance decrease exponentially with the distance from the surface. This explains why the surface sensitivity of XPS is so high—only photoelectrons originating from the first few nanometers are able to escape from the material.

An ultra-high vacuum (UHV) chamber, an X-ray source, and an electron analyser make up a basic XPS apparatus[4]. The CNR-ISOF instrument features an XR50 source and a Phoibos 100 analyzer, both of which were manufactured by SPECS (Figure 1.5). Its chamber is divided into three stages: a UHV preparation chamber, a UHV analysis chamber, and a high-vacuum load lock chamber[7]. A separate pumping system is provided for each sub-chamber. In order to collect photoelectrons and maintain the lowest possible pressure in the analysis area, a multi-stage system is required. Following all wall desorption processes (*i.e.,* bake-out), the base pressure in the analysis chamber can be as low as $5 \cdot 10^{-10}$ mbar[4], [7].

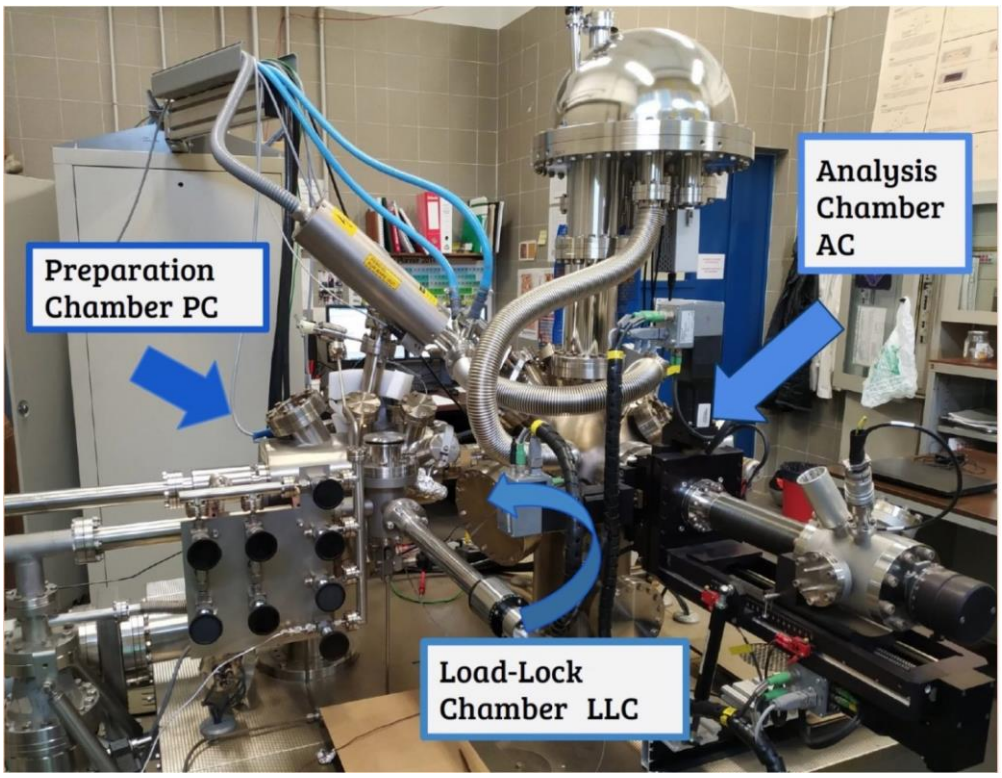


*Figure 1-5. XPS Instrumentation located at ISOF/CNR* [7].

The preparation chamber has a special sample holder with a resistive heater for sample thermal treatments, as well as an ion gun for sample sputtering connected to an argon gas line.

A magnesium anode, whose strongest x-ray emission is located in the Kα characteristic line, is mounted on the x-ray source. Kα denotes the radiative atomic transition 2p→1s after electron impact creates a 1s (or K) excitation. The equivalent electromagnetic energy $h\nu$ is 1253.6 eV. Since our instrument's radiation is not monochromatic, the energy of the x-ray beam is dispersed around the transition's central value. The counter-effect of this is a slight decrease in resolution. The source is continuously water-cooled and runs at 125W of power. Water with low conductivity is used to avert harmful electrostatic discharge while also preventing excessive corrosion of the source walls.

The analyser is comprised of a series of lenses, a multichannel detector (Chevron microchannel plate type) that counts the electrons, and a hemispherical electrostatic analyser (HSA) that efficiently separates photoelectrons at different energy levels ($E_K$). The lens system sets the sampled area (spatial resolution) and the accepting solid angle, adjusting the electron energy to a fixed level in addition to projecting the sample plane onto the HSA entrance. One important factor affecting energy resolution is the analyser's constant energy mode, in which the pass energy, or $E_P$, stays constant. While lower $E_P$ increases energy resolution, signal intensity decreases. The intrinsic width of photoemission lines resulting from particular atomic level lifetimes, flaws in electron kinetic energy analysis, and broadening due to the x-ray source used are additional factors that contribute to signal broadening and decreased resolution[4]. For $E_P$ = 10eV in this instrument, a 0.9 eV spectral resolving power was estimated, which is necessary for obtaining high-resolution data. Resolving power is an important factor, but it's not the only one when it comes to derive quantitative data from an X-ray photoelectron spectroscopy (XPS) measurement. Equally important is the signal-to-noise (S/N) ratio. S/N helps to clearly identify the presence of a particular chemical element by measuring the peak intensity relative to the noise away from the peak. S/N can be improved by increasing the acceptability time for each energy value on the analyser or averaging multiple measurements over the same energy range[4], although these methods lengthen the measurement times.

For the photoelectron to be detected during a real measurement, its energy needs to exceed the analyser's work function ($w_A$). However, the problem is that $w_A$ is usually unknown. To avoid this problem, standard procedure calls for calibrating the device through the analysis of pure or standard samples using pre-established X-ray photoelectron spectroscopy (XPS) spectra. The cancellation of $w_A$ is then made possible by comparing the spectrum of the

sample under investigation with the standard one. In this instance, we used the Ag $3d_{5/2}$ signal ($E_B$= 368.3eV) or the Au $4f_{7/2}$ signal ($E_B$ = 84.0eV) that were extracted from calibration samples immediately after $Ar^+$ sputtering.

When analysing an XPS spectrum, the line-shape and background must be correctly attributed to an atomic signal or peak. Both intrinsic features of the photoemission process and experimental parameters in the detection system, such as energy resolution and angular acceptance, affect the observed peak's shape. the intrinsic atomic photoemission line-shape is Lorentzian, while the contribution of the detection system is typically described by a Gaussian curve thus the peak observed by XPS is a combination of a Lorentzian and a Gaussian curve. To guarantee a finite area integral during peak analysis, a more flexible line shape—typically a modified Lorentzian—is commonly employed[13].

## 1.3 Electrical characterization

### *1.3.1 Kelvin Probe Force Microscopy (KPFM)*

The Kelvin probe technique was first established in 1898 by William Thomson, also known as Lord Kelvin, to explain the production of built-in contact potential variations in metals, which had previously been noted by Alessandro Volta at the start of the 19th century[14]. First, the idea of work function—one of the fundamental physical properties of a solid that is connected to its electrical structure—must be introduced to better comprehend the Kelvin probe technique. The work function can be defined as the potential that an electron at the Fermi level needs to overcome in order to be extracted to the vacuum with zero kinetic energy. Since this definition strictly applies only to metals, in semiconductors and insulators the work function can be defined as the energy difference between the most loosely bound electrons in the solid and an electron at rest in the vacuum immediately outside the solid (i.e., at the level of zero kinetic energy). Thus, the work function is an important parameter describing the electronic structure of a solid[15].

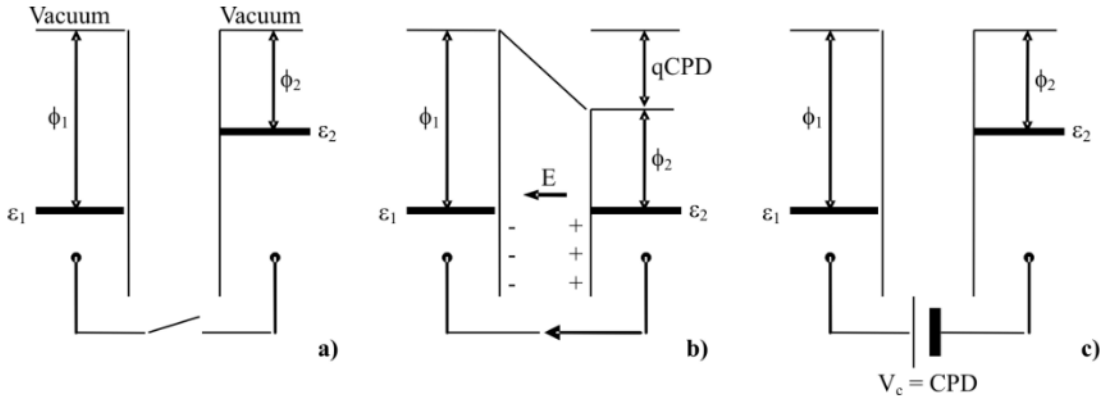


*Figure 1-6. Schematic diagram of the physical process used for the Kelvin Probe technique*. a) *Two different kinds of materials 1 and 2, whose respective work functions ($\varphi_1$ and $\varphi_2$) represent the energy difference between the vacuum level and their Fermi level ε. b) An electrical contact between the two materials causes electrons to flow from 2 to 1 until the Fermi levels line up, creating a contact potential $V_b$. An electric field (E, where q is the electron charge and CPD is the contact potential difference) is created by the charges in the two materials.* c) *An external potential $V_c$ equal to the contact potential is applied to eliminate the electric field*[16].

When two distinct material capacitor plates are electrically connected (as shown in Fig. 1-6a), electrons will flow from the lower-work function material ($\varphi_2$ in Figure 1-6) to the higher-work function material ($\varphi_1$ in Fig. 1-6) [14]. A contact potential difference (CPD) will be created between the two materials as a result of this motion, which also causes charges of opposite sign to develop on the capacitor plates, causing an electric field in the capacitor. An external potential, denoted by $V_c$, can be used to cancel out this field, which corresponds to the difference between the two work functions (Fig. 1-6c). At equilibrium the field in the capacitor becomes zero and the work function of the material under study ($\varphi_2$) can be found as follows: $\varphi_2 = \varphi_1 - qV_c$, where q is the elementary charge. This is possible if the work function of the reference plate ($\varphi_1$) is known[16].

In order to test this theory, Lord Kelvin measured the charge transfer that occurs when two large, flat, polished discs of copper and zinc came into electrical contact. He carried out this experiment using a gold-leaf electroscope.

Zisman made improvements to the technique in 1932 by utilizing a vibrating reference surface. The mechanical oscillation in this vibrating capacitor arrangement causes variations in the system capacitance and, consequently, in the reference plate voltage at frequency ω[17]. A tiny alternating current that is produced by this change in capacitance is easily detectable.

The current *i(t)* is actually determined by the periodic vibration of the distance between the two plates at $\omega$, and is expressed as[18]:

$$i(t)=V_c\omega\Delta C\cos(\omega t), \quad (1.3)$$

where $V_c$ is the contact potential difference and $\Delta C$ is the change in capacitance. An additional voltage is applied between the two plates for the purpose of measuring the CPD until the gap between them becomes field-free and the current *i(t)* drops to zero.

Wickramasinghe et al. created Kelvin probe force microscopy a few years after scanning atomic force microscopy was first used. The reference capacitor plate in this arrangement is a very flexible cantilever that is connected to a sharp, conductive AFM tip[18]. Because the tip-sample interaction is highly localized, it is possible to measure work function with high spatial and electrical resolution by detecting possible differences between the tip and sample through the measurement of the cantilever's deflection resulting from electrostatic interactions.

In the Kelvin probe force microscopy (KPFM) setup used by Wickramasinghe [18], a conductive tip is scanned across a sample surface in non-contact mode[19], [20], tracing its topography. The fundamental idea is similar to the Kelvin method, except forces are measured rather than currents. During the scanning process, an oscillating potential ($V_{ac}$) at frequency $\omega$ is applied to the tip. The tip interacts electrostatically with the surface, attracting and repelling at the same frequency as $V_{ac}$. As such, the cantilever exhibits an oscillation mode at frequency $\omega$. The scanning force microscopy (SFM) photodiode detects this oscillation by sending a signal through a lock-in amplifier, which isolates the oscillation mode at $\omega$. At frequency $\omega$, the amplitude of the oscillation is proportional to the surface-potential difference between the tip and the surface[16]. However, because of the tip's shape and the complex dynamics of the system, it is difficult to quantify accurately this interaction. An alternative method is to use electrostatic force microscopy (EFM) to obtain qualitative two-dimensional (2D) maps of the surface potential[16].

An additional feedback loop is added in order to measure the sample's work function precisely. In order to reduce the electrostatic interaction between the cantilever tip and the surface, this loop applies a specific direct current (DC) offset potential voltage ($V_{dc}$) to the tip (Fig. 1-7).

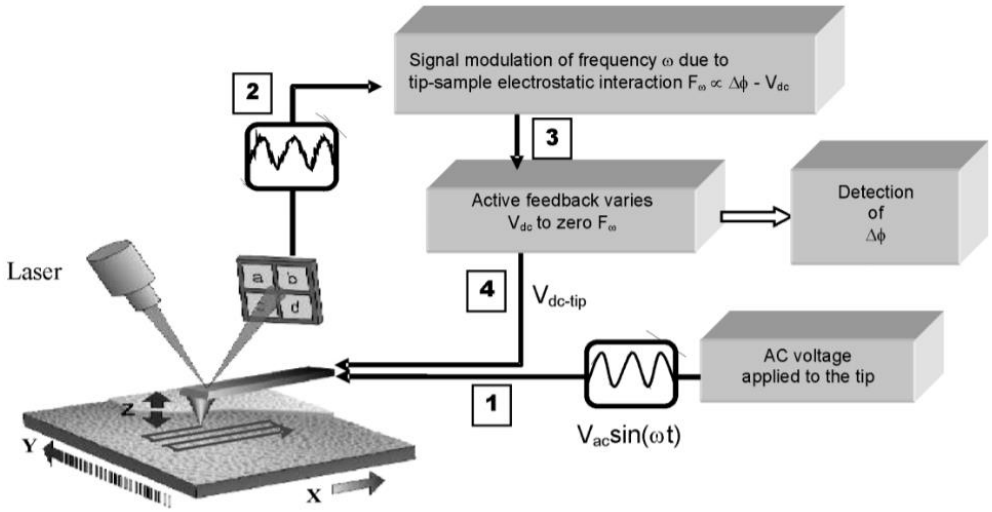


*Figure 1-7. KPFM apparatus. 1) An alternating voltage $V_{ac}$ with a frequency ω is applied to the tip. 2) At a frequency ω, the cantilever mechanically oscillates due to the electrostatic tip-sample interaction. 3) A lock-in amplifier isolates the cantilever oscillation at ω and sends the signal to a feedback circuit. 4) By applying a $V_{dc}$ voltage to the tip, the feedback seeks to reduce $F_\omega$, which is proportional to the tip–sample interaction. In certain instances, an alternative configuration is utilized in which the external potential bias is applied directly to the sample. Figure taken by ref.* [16].

Subsequently, a DC voltage bias signal and an alternating current (AC) are applied between the tip and the sample. The voltage between the tip and the sample in this instance can be expressed as follows:

$$\Delta V = \Delta\varphi - V_{dc} + V_{ac}\sin(\omega t) \quad (1.4),$$

where $V_{ac}$ and $\omega$ represent the applied AC voltage signal's amplitude and frequency, respectively, and $\Delta\varphi$ is the contact potential—that is, the difference in the tip-to-sample work function.

Assuming a parallel-plate-capacitor geometry, equation 2 can be used to derive an expression for the electrostatic force $F$ between the tip and the sample (other geometries can also be considered, although they require more complicated models). The formula for expressing the energy $U$ in a parallel plate capacitor is:

$$U = 1/2C\Delta V^2 \quad (1.5),$$

where *C* represents the local capacitance between the sample and the tip.
The force can then be defined as the energy's rate of change with the tip-sample separation distance, or z

$$F = -\frac{\vartheta U}{\vartheta z} = -\frac{1}{2}\frac{\vartheta C}{\vartheta z}\Delta V^2 = F_{dc} + F_{\omega} + F_{2\omega} \quad (1.6)$$

with components at DC

$$F_{dc} = -\frac{1}{2}\frac{\vartheta c}{\vartheta z}\left[(\Delta\varphi - V_{dc})^2 + \frac{V_{ac}^2}{2}\right] \quad (1.7)$$

and at frequencies $\omega$ and $2\omega$

$$F_{\omega} = -\frac{\vartheta c}{\vartheta z}[(\Delta\varphi - V_{dc})V_{ac}\sin(\omega t)] \quad (1.8)$$

$$F_{2\omega} = \frac{1}{4}\frac{\vartheta c}{\vartheta z}[(V_{ac})^2\cos(\omega t)] \quad (1.9)$$

These three distinct force signals—$F_{dc}$, $F_{\omega}$, and $F_{2\omega}$—can be isolated and analysed independently to provide information on the electrical characteristics of the sample.

$V_{dc}$ is equal to the difference in the work function ($\Delta\varphi$) between the tip and the sample surface when the x-component of the electrostatic force interaction becomes zero ($V_{dc} = \Delta\varphi$). As a result, by tracking the voltage Vdc applied by the feedback signal, a 2D quantitative map of $\Delta\varphi$ can be created. The work function of the sample is then determined if the work function of the tip is known. By using surfaces with known work functions to calibrate the setup, it is simple to determine the tip's frequency ($\varphi$). To determine the local work function on the sample surface, Kelvin Probe Force Microscopy (KPFM) essentially uses the first harmonic component ($F\omega$) of the electrostatic force interaction.

As an alternative, measurements can be made using the frequency-modulation method (FM-KPFM), which uses the force gradient as a dataset rather than the force, which is discussed in the following section. Furthermore, through the capacitance gradient (∂C/∂z), the 2x component of the force at the tip can provide information about the local dielectric

properties. Thus, this signal can be utilized to learn more about surface heterogeneities or defects.

There are two popular KPFM modes. In one, topographical signals and the Kelvin probe are detected at two distinct tip oscillation frequencies simultaneously. In the other, a first scan records the topographic signal, and a second scan, carried out at a larger tip-surface distance, records the Kelvin probe signal in what is referred to as the "lift mode."

### Interpreting the signal in KPFM measurements

The process of interpreting images acquired via Kelvin Probe Force Microscopy (KPFM) is complex and requires the utilization of theoretical models[16]. The KPFM setup can be conceptualized as a sample surface consisting of *n* ideally conducting electrodes with constant potential $V_i$ and a potential $V_t$ tip. This allows for the establishment of a correlation between the measured quantities and the effective surface potential distribution. The measured KPFM potential doesn't exactly match the surface potential at a given location, as Stemmer and colleagues have shown. Rather, it symbolizes a weighted mean of all the surface local potentials below the tip apex. The derivatives of probe-surface capacitances in z serve as the weighting factors for this average[16].

The following formula can be used to express this weighted average:

$$V_{dc} = \frac{\sum_{i=1}^{n}(C'itVi)}{\sum_{i=1}^{n}(C'it)} \qquad (1.10)$$

where $V_i$ denotes the local surface potential at point I on the surface, $V_{dc}$ is the voltage applied to the tip during the initial KPFM scan, and $C_{it}'$ is the derivative of the capacitance versus distance between the tip and the point I on the surface.

It is important to note that the mutual capacitances between the tip and surface $C_{it}$, rather than the mutual capacitances between various surface elements, are the only factors influencing the first harmonic component of the tip force, or $F_\omega$.

The surface is perceived as an array of capacitor plates with lateral dimensions $\Delta x$, $\Delta y$. The $V_{dc}$ that KPFM measures in relation to the location of the capacitors ($x_i$, $y_i$) can be expressed as:

$$V_{\mathrm{dc}}(x_i, y_i) = \int_{-\infty}^{+\infty} \int_{-\infty}^{+\infty} h(x - x_i, y - y_i) V(x, y) dx dy \tag{1.11}$$

$$h(x - x_i, y - y_i) = \lim_{\Delta x, \Delta y \to 0} \left[ \frac{C'(x_i - x_t, y_i - y_t)}{C'_{\mathrm{tot}} \Delta x, \Delta y} \right] \tag{1.12}$$

where $C'_{tot}$ is the derivative of the total capacitance between surface and tip,

$$C'_{\mathrm{tot}} \equiv \sum_{j=-\infty}^{j=+\infty} \sum_{i=-\infty}^{i=+\infty} C'(x_i - x_t, y_j - y_t) \tag{1.13}$$

and where the tip location is defined by $x_t$ and $y_t$. The KPFM potential maps that are measured, or $V_{dc}(x,y)$, can be understood as effectively 2D convolutions of the surface-potential distribution $V(x,y)$ with the corresponding transfer function $h(x,y)$, which is determined by the tip geometry. This can be seen in Equation 9.

Due to the long-range nature of electrostatic interactions, the surface's interactions with the AFM tip apex, the tip's bulk, and even the cantilever that supports the tip can also contribute to the KPFM signal. At a cantilever–sample distance of about 15 µm, the cantilever's influence on this interaction becomes significant. Numerical simulations on microscopic dots and sharp steps were performed to evaluate the impact of system geometry on KPFM resolution. The results of electrostatic calculations and experiments (refer to Fig. 1-8) showed that the cantilever's effect becomes insignificant at tip–sample distances less than 100 nm and becomes predominant for distances greater than 1000 nm. Figure 1-8b, for instance, illustrates how the tip-sample distance affects the measurement error of sample bias ($V_{peak}$ or $V_{valley}$) for two intentionally created metallic patterns[21]. Furthermore, it was discovered that tips with a high aspect ratio, a cantilever as small as feasible, and a relatively large tip apex (up to 100 nm) can yield the best resolution[21], [22].

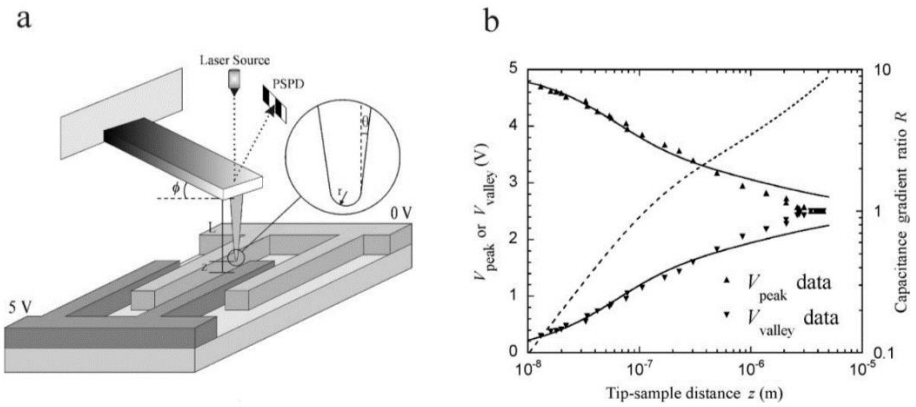


*Figure 1-8. a) Schematic diagram of the test structure and scanning probe used in* [21] *to examine how the tip-sample distance z affects the measured potential. The test structure is made up of two macroscopic metal pads that were biased to 0 and 5 V, from which alternating electrodes emerge. Both the electrodes' width and the distance between them is 1.7 µm. The truncated conical part's tip, which is magnified in the inset, is modelled as a hemisphere. PSPD: photosensitive position detector. b) The theoretically calculated variations (represented by two dark lines, one upper for $V_{peak}$ and one lower for $V_{valley}$) are compared to experimentally observed variations with z of $V_{peak}$ (voltage measured over 5 V biased finger, shown as triangles) and $V_{valley}$ (voltage measured over 0 V biased tip, shown as inverted triangles). A dashed line also represents the computed ratio, R, of the cantilever's capacitance gradient to that of the tip when plotted against z. Figure taken by ref.* [21]

More accurate calculations are challenging because electrostatic forces and tip-sample capacitances depend on the charge distribution and sample polarization, which are both influenced by the potential difference and the tip-sample distance. Furthermore, the tip is not positioned at a constant distance from the surface, even if it follows the surface topography to some extent. This is due to the oscillation of the tip above the surface caused by the piezoactuator in non-contact mode. As a result, there is a continuous variation in the tip-sample distance between 10 and 600 nm[23]. During the oscillation, the electrostatic interaction varies and reaches its maximum at the tip's lower end. When using wide oscillations and tips with large masses, the effect of oscillation on the electrostatic force can be significant[23].

To reduce the effect of long-range interactions in Kelvin Probe Force Microscopy (KPFM) measurements, a number of strategies have been employed. While the conventional KPFM setup uses amplitude modulation (AM) to detect the electrostatic force ($F$), an experimental approach to reducing long-range electrostatic contributions involves measuring the force gradient along the $z$-axis: $\nabla = \partial F/\partial z$.

Unlike the tip's apex-sample interaction, which permits their separation, the forces resulting from the sample's interaction with the cantilever and the tip cone show gradual variations in proximity to the sample. This distinction is only valid when the tip's oscillation amplitude is small in relation to the range where the potential shows a lot of variation[24].

The frequency shift[25] or phase shift[24][26], [27]of the tip oscillation at x can be used to calculate the force gradient. The responding techniques are known as FM-KPFM and EFM-phase, respectively.

The tip oscillates during the lift scan in these measurements, as detailed above in Section 1.2.1: The resonant frequency of the tip and the phase shift caused by the electrostatic force gradient F/z are measured. The resonant phase shift and frequency shift for small force gradients are[26]:

$$\Delta\omega = \frac{\omega_0}{2k}\frac{\partial F}{\partial z} \tag{1.14}$$

and

$$\Delta\phi = \arcsin\left(\frac{Q}{k}\frac{\partial F}{\partial z}\right) \tag{1.15}$$

where $Q$ is the cantilever's quality factor, $k$ is the spring constant, and $\omega_0$ is the resonant frequency. For a parallel plate capacitor:

$$\frac{\partial F}{\partial z} = -\frac{1}{2}\frac{\partial^2 C}{\partial z^2}(\Delta V)^2 \tag{1.16}$$

Equations 12, 13, and 14 can be combined to directly relate the frequency and phase shift to the potential difference ($\Delta V$)

$$\Delta\omega = -\frac{\omega_0}{4k}\frac{\partial^2 C}{\partial z^2}(\Delta V)^2 \tag{1.17}$$

$$\Delta\phi = -\arcsin\left(\frac{Q}{2k}\frac{\partial^2 C}{\partial z^2}(\Delta V)^2\right) \quad (1.18)$$

This indicates that the resolution of the method is determined by the lateral variations of the gradient $\partial^2 C/\partial z^2$, and that the phase and frequency shift are squared functions of the potential difference $\Delta V$ between the tip and the sample. Because $\partial^2 C/\partial z^2$ is positive, the phase shift is always negative[26].

Additionally, a straightforward analytical model explaining tip–surface interactions has been reported [22], [28]. When studying relatively simple structures (spherical Au- or CdSe-based nanoparticles), modelling the tip as a hemisphere and a truncated cone can yield an extremely accurate estimation of the $\partial C/\partial z$ components of the electrostatic interaction. KPFM can even determine the amount of charge in a structure, down to the level of a single electron, by using simple and regular structures like well-defined silicon dots[22], [28].

A thorough theoretical and experimental analysis of the accuracy and resolution provided by the frequency-modulation method and the amplitude-sensitive method was published[29]. By contrasting the two methods, Zerweck and colleagues were able to demonstrate that, in the majority of cases, the frequency-modulation method is better because it offers a significantly higher lateral resolution, produces quantitative surface potential values on areas larger than the tip radius, and is not appreciably impacted by changes in the tip-sample distance during topographic imaging[29].

Even when recording a single image, an inversion in the image contrast may occur when the Kelvin probe and the topography measurements are carried out concurrently without the need for a second scan (i.e., lift mode). This means that certain areas may appear to have a lower potential in comparison to the background. This is because the $V_{dc}$ KPFM signal includes non-electrostatic forces[30]. To effectively distinguish the electrostatic force signal from the non-electrostatic forces signal, the FM-mode KPFM's AC bias amplitude needs to be fairly large[30].

An alternative method for carrying out KPFM measurements is to apply the bias voltage $V(t)=|V_{dc}|+V_{ac}\sin(\omega t)$ directly to the sample while maintaining the tip at ground potential. Nonetheless, it is necessary to consider the impact that the AC sample voltage may have on the recorded contract potential. Bias-induced band bending at the semi-conductor surface can account for this dependency[31].

### *1.3.2 Conductive AFM*

Conductive atomic force microscopy (C-AFM) has evolved continuously since its invention in 1993 by Murrel et al. [32], and it is now one of the most powerful tools for studying the electrical properties of materials and devices at the nanoscale[33], [34]. In essence, the conductive AFM (C-AFM), also known as C-AFM, conductive probe AFM (CP-AFM), conductive scanning probe microscope (C-SPM), or conductive scanning force microscope (C-SFM), is an AFM that records the currents flowing at the tip/sample nanojunction simultaneously to the topography. The three main differences between a standard AFM and a C-AFM are as follows: (i) the probe tip needs to be conductive; (ii) a voltage source is required to apply a potential difference between the tip and the sample holder; and (iii) a preamplifier is used to convert the (analogical) current signal into (digital) voltages that the computer can read. The structure of a standard AFM is shown in Figure 1-1. AFM controllers already contain the voltage source, so no additional hardware is needed; additionally, AFM manufacturers sell preamplifiers at competitive prices. Finally, obtaining C-AFM probes is simple and accessible from any manufacturer[33]. The most common conductive tape or paste used in C-AFM experiments to fix the sample to the sample holder is silver paint [35]. Another practical tool for shielding the sample from outside electrical interference is a Faraday cage[36]. With this configuration, an electrical field is produced when a potential difference is applied between the tip and the sample, and a net current flow from the tip to the sample or vice versa. As a result, it is possible to monitor the samples' local electrical characteristics at a very high nanometric resolution. The currents collected by the C-AFM follow Eq. (1.19), where $A_{eff}$ is the effective emission area through which electrons can flow, J is the current density, and I is the total current flowing through the tip/sample nanojunction (henceforth referred to as the effective area)[36]:

$$I = J \cdot A_{eff} \qquad (1.19)$$

J is primarily determined by the voltage applied between the tip and sample systems, as well as by their conductivity. Intrinsic inhomogeneities in the samples, such as doping, local defects, and thickness fluctuations, have a significant impact on J's value[36].

The term $A_{eff}$ defines the technique's lateral resolution, which can vary from tenths of square nanometers to thousands of square micrometers based on a variety of experimental factors, such as the sample's conductivity, the tip's geometry, the force of contact between the tip and the sample, the stiffness of the tip and the sample, and even the relative humidity of the environment in which the experiment is conducted.

In C-AFM measurements, the most frequent error is assuming that the physical contact area ($A_c$) and the effective emission area ($A_{eff}$) are equal. This assumption is strictly incorrect because the applied electrical field can propagate laterally in a variety of tip/sample systems (refer to Figure 1-9). For instance, because of the metallic electrode's high lateral electrical conductivity, when the C-AFM tip is placed on it, $A_{eff}$ equals the electrode's total covered area [37], [38]. The effective area $A_{eff}$ can be defined as the total of all the minuscule spatial locations on the sample surface that are electrically connected to the C-AFM tip (the potential difference is negligible). Consequently, $A_{eff}$ is a virtual entity that, over the course of which the current density is taken to be constant, combines all electrically significant effects within the tip/sample contact system into a single value. The current densities passing through the tip/sample system are incredibly high due to $A_{eff}$*'s* small dimensions. The electrical noise of a C-AFM, which is (in the best cases) hundreds of femtoamperes, defines the smallest currents that the device can detect. A current density of 1 A/cm$^2$ is obtained by passing a 1 pA current through a typical $A_{eff}$ of 100 nm$^2$. The majority of C-AFM probe tips can degrade dramatically at such high current densities, which lowers measurement accuracy and raises research expenses. The high lateral frictions in the tip/sample system during the scans exacerbate this issue even more [39], [40].

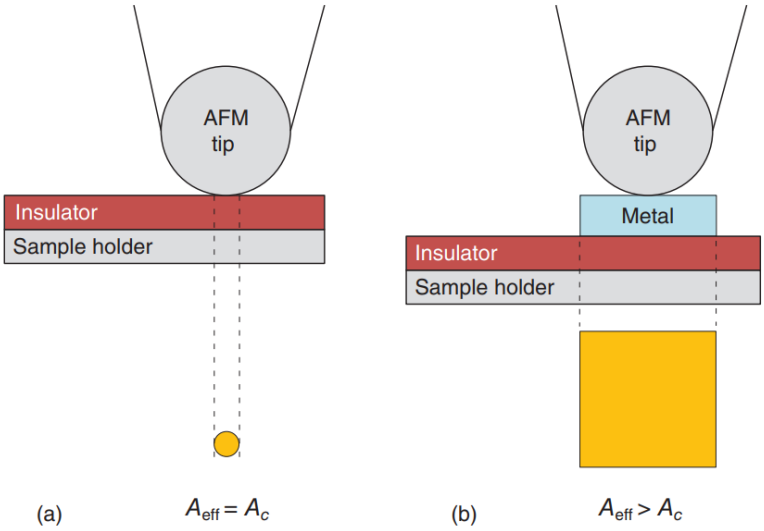


*Figure 1-9. Diagram illustrating the effective emission area ($A_{eff}$) in a C-AFM when the tip is positioned on (a) a flat metallic electrode deposited on an insulating sample, and (b) a flat insulating sample. Picture taken from ref.* [36]

Standard silicon nanoprobes coated with thin metallic films, such as Pt, Au, Ru, Ti, and/or Cr, were the first conductive nanoprobe types used in C-AFM experiments and are still commonly

used today (Figure 1-10). In order to preserve the tip sharpness and guarantee a high lateral resolution during the measurements, the coating should be both thick enough to withstand high current densities and frictions and thin enough not to noticeably increase the radius of the tip apex. Because of the melting of metallic varnish and tip mass loss during the scans, as previously pointed out, the lifetime of conductive tips for C-AFM experiments is significantly shorter than in any other AFM mode. In order to address this issue, new C-AFM silicon tips with full conductive tips[41], [42], [43] and hard materials coated on them (such as graphene[39] [40],[44] [45], [46], [47]and phosphorous-doped diamond[48]) have emerged (see Figure 1-10). When choosing the kind of tip to use in a C-AFM analysis, other sample-related characteristics like conductivity, stickiness, stiffness, and rugosity are crucial considerations.

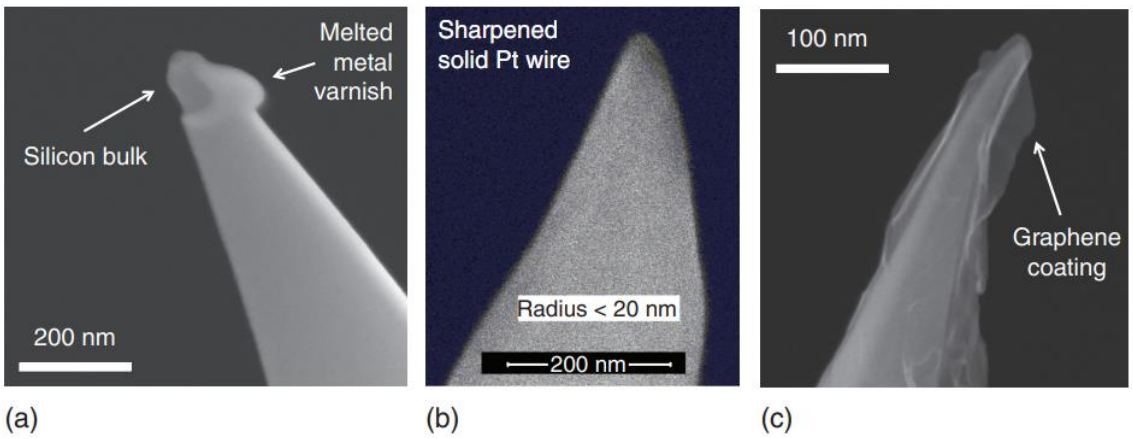


*Fig 1-10. (a) scanning electron microscopy (SEM) images of a metal-varnished silicon nanoprobe, (b) a solid Pt wire that has been sharpened and is suitable for C-AFMs, and (c) a metal-varnished silicon nanoprobe covered in a single-layer graphene sheet. In order to highlight the silicon's core bulk, the tip in (a) is purposefully shown with the metallic varnish worn off. Picture taken from ref.* [36]

Analogous current signals via the tip/sample nanojunction are routed to the preamplifier (Figure 1-11 a, b), which converts them into digital voltages that are readable by the computer's data acquisition (DAQ) card (Figure1-11). Many manufacturers include the preamplifier in the "C-AFM application module," a detachable part that can be attached to the AFM and is typically placed very near the tip to reduce electrical noise. AFMs can also carry out various other functions, like scanning capacitance microscopy (SCM) and scanning spreading resistance microscopy (SSRM), thanks to a variety of additional modules (see Figure 1-11c). In the majority of C-AFM experiments, the voltages readable by the DAQ card typically

range between -3 and +3 V, while the currents measured can typically range from a few picoamperes to hundreds of microamperes[49].

In nearly all C-AFM experiments, the currents that flow through the tip/sample as a result of applying a voltage between the tip and the sample holder. Only a small percentage of the works published with C-AFM—that is, experiments where the current is generated by other methods, like photoelectric[50] or piezoelectric[51] effects—did not involve for the application of a bias. The majority of C-AFMs allow the user to choose the bias's value and polarity, which should be applied to the tip while maintaining the sample holder's ground state, or vice versa. As a result, currents typically flow through the sample vertically[52]. However, lateral currents can also be measured by using a wire bonder or silver paint to connect the sample's surface to the sample holder[53]. As previously mentioned, the voltages that can be applied to C-AFM electronics typically range from -10 to +10 V. The currents that can be observed span three or four orders of magnitude, never going below 1 pA or above 10 µA. Ramped voltage stresses (RVS) can be used in addition to constant voltage stresses (CVS) applied during a scan to gather current versus voltage (I–V) curves. The RVS involves keeping the tip stationary at a single location. Even though this setup is more than sufficient for a lot of experiments, some studies might need to make use of advanced electronic capabilities. Examples of these include the use of current limitations, the application of constant current stresses (CCS), the measurement of current versus time curves (I–t), or just applying or measuring higher voltages or currents. Many AFMs have an input/output that is directly connected to the tip, the sample holder, or even both. This makes it possible to apply and collect electrical signals using an external sourcemeter or an semiconductor parameter analyser (SPA).

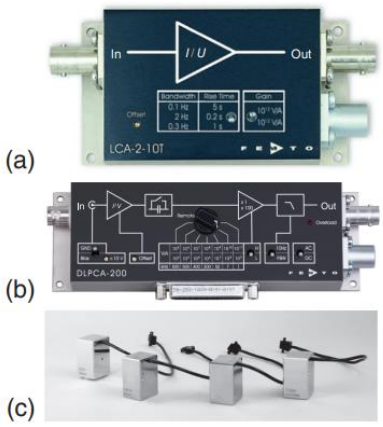


*Figure 1.11. (a, b) Pictures of two C-AFM preamplifiers—the first having a fixed gain and the second having a variable gain. (c) Images of various Bruker AFM application modules, such as the C-AFM module (which has a preamplifier). Picture taken from ref.* [36]

In recent years, a wide range of experiments have been conducted with this setup. With atomic resolution, the C-AFM can be used to both monitor and alter the properties of materials [54], [55], [56], [57], [58].

# REFERENCES


[1] G. R. Heath *et al.*, "Localization atomic force microscopy," *Nature*, vol. 594, no. 7863, pp. 385–390, Jun. 2021, doi: 10.1038/s41586-021-03551-x.

[2] B. W. Hoogenboom, "Stretching the resolution limit of atomic force microscopy," *Nat Struct Mol Biol*, vol. 28, no. 8, pp. 629–630, Aug. 2021, doi: 10.1038/s41594-021-00638-x.

[3] S. Scheuring, D. Müller, H. Stahlberg, H.-A. Engel, and A. Engel, "Sampling the conformational space of membrane protein surfaces with the AFM," *European Biophysics Journal*, vol. 31, no. 3, pp. 172–178, Jun. 2002, doi: 10.1007/s00249-001-0197-8.

[4] "PhD_thesis_BOSCHI_Alex".

[5] J. E. Lennard-Jones, "No. 240 COHESION," 1931.

[6] A. Liscio, "Scanning probe microscopy beyond imaging: A general tool for quantitative analysis," *ChemPhysChem*, vol. 14, no. 6, pp. 1283–1292, Apr. 2013, doi: 10.1002/cphc.201200880.

[7] "https://www.isof.cnr.it/institute/facilities-and-instrumentation/".

[8] C. J. Powell, "The quest for universal curves to describe the surface sensitivity of electron spectroscopies," *J Electron Spectros Relat Phenomena*, vol. 47, no. C, pp. 197–214, Jan. 1988, doi: 10.1016/0368-2048(88)85012-6.

[9] H. Hertz, "Ueber einen Einfluss des ultravioletten Lichtes auf die electrische Entladung," *Ann Phys*, vol. 267, no. 8, pp. 983–1000, Jan. 1887, doi: 10.1002/andp.18872670827.

[10] A. Einstein, "Über einen die Erzeugung und Verwandlung des Lichtes betreffenden heuristischen Gesichtspunkt," *Ann Phys*, vol. 322, no. 6, pp. 132–148, 1905, doi: 10.1002/andp.19053220607.

[11] J. H. Scofield, "HARTREE-SLATER SUBSHELL PHOTOIONIZATION CROSS-SECTIONS AT 1254 AND 1487 eV."

[12] J. Q. Zhong, M. Wang, W. H. Hoffmann, M. A. Van Spronsen, D. Lu, and J. A. Boscoboinik, "Synchrotron-based ambient pressure X-ray photoelectron spectroscopy of hydrogen and helium," *Appl Phys Lett*, vol. 112, no. 9, Feb. 2018, doi: 10.1063/1.5022479.

[13] "CasaXPS Processing Software NO WARRANTY," 2009.

[14] Lord Kelvin, " V. Contact electricity of metals ," *The London, Edinburgh, and Dublin Philosophical Magazine and Journal of Science*, vol. 46, no. 278, pp. 82–120, Jul. 1898, doi: 10.1080/14786449808621172.

[15] S. R. Bare and G. A. Somorjai, "Surface Chemistry," in *Encyclopedia of Physical Science and Technology*, Third., R. A. Meyers, Ed., Elsevier, 2003, pp. 373–421. doi: 10.1016/B0-12-227410-5/00757-2.

[16] V. Palermo, M. Palma, and P. Samori, “Electronic characterization of organic thin films by Kelvin probe force microscopy,” *Advanced Materials*, vol. 18, no. 2. pp. 145–164, Jan. 19, 2006. doi: 10.1002/adma.200501394.

[17] W. A. Zisman, “A new method of measuring contact potential differences in metals,” *Review of Scientific Instruments*, vol. 3, no. 7, pp. 367–370, 1932, doi: 10.1063/1.1748947.

[18] M. Nonnenmacher, M. P. O’Boyle, and H. K. Wickramasinghe, “Kelvin probe force microscopy,” *Appl Phys Lett*, vol. 58, no. 25, pp. 2921–2923, 1991, doi: 10.1063/1.105227.

[19] C. Bustamante and D. Keller, “Scanning Force Microscopy in Biology,” *Phys Today*, vol. 48, no. 12, pp. 32–38, 1995, doi: 10.1063/1.881478.

[20] H. Takano, J. R. Kenseth, S. S. Wong, J. C. O’Brien, and M. D. Porter, “Chemical and Biochemical Analysis Using Scanning Force Microscopy,” *Chem Rev*, vol. 99, no. 10, pp. 2845–2890, 1999, doi: 10.1021/cr9801317.

[21] G. Koley, M. G. Spencer, and H. R. Bhangale, “Cantilever effects on the measurement of electrostatic potentials by scanning Kelvin probe microscopy,” *Appl Phys Lett*, vol. 79, no. 4, pp. 545–547, Jul. 2001, doi: 10.1063/1.1384004.

[22] O. Cherniavskaya, L. Chen, V. Weng, L. Yuditsky, and L. E. Brus, “Quantitative noncontact electrostatic force imaging of nanocrystal polarizability,” *Journal of Physical Chemistry B*, vol. 107, no. 7, pp. 1525–1531, Feb. 2003, doi: 10.1021/jp0265438.

[23] T. Takahashi and S. Ono, “Tip-to-sample distance dependence of an electrostatic force in KFM measurements,” in *Ultramicroscopy*, Aug. 2004, pp. 287–292. doi: 10.1016/j.ultramic.2004.01.017.

[24] “A_Gil_2003_Nanotechnology_14_332 (1)”.

[25] J. Colchero, A. Gil, and A. M. Baró, “Resolution enhancement and improved data interpretation in electrostatic force microscopy,” *Phys Rev B Condens Matter Mater Phys*, vol. 64, no. 24, 2001, doi: 10.1103/PhysRevB.64.245403.

[26] C. H. Lei, A. Das, M. Elliott, and J. E. Macdonald, “Quantitative electrostatic force microscopy-phase measurements,” *Nanotechnology*, vol. 15, no. 5, pp. 627–634, May 2004, doi: 10.1088/0957-4484/15/5/038.

[27] T. Takahashi and T. Kawamukai, “Phase detection of electrostatic force by AFM with a conductive tip.”

[28] O. Cherniavskaya, L. Chen, V. Weng, L. Yuditsky, and L. E. Brus, “Quantitative noncontact electrostatic force imaging of nanocrystal polarizability,” *Journal of Physical Chemistry B*, vol. 107, no. 7, pp. 1525–1531, Feb. 2003, doi: 10.1021/jp0265438.

[29] U. Zerweck, C. Loppacher, T. Otto, S. Grafström, and L. M. Eng, “Accuracy and resolution limits of Kelvin probe force microscopy,” *Phys Rev B Condens Matter Mater Phys*, vol. 71, no. 12, Mar. 2005, doi: 10.1103/PhysRevB.71.125424.

[30] K. Okamoto, Y. Sugawara, and S. Morita, “The Imaging Mechanism of Atomic-scale Kelvin Probe Force Microscopy and its Application to Atomic-Scale Force Mapping,” *Japanese Journal of Applied Physics, Part 1: Regular Papers and Short Notes and Review Papers*, vol. 42, no. 11, pp. 7163–7168, 2003, doi: 10.1143/jjap.42.7163.

[31] C. Sommerhalter, T. Glatzel, T. Matthes, A. Jager-Waldau, and Mc. Lux-Steiner, “Kelvin probe force microscopy in ultra high vacuum using amplitude modulation detection of the electrostatic forces,” 2000. [Online]. Available: www.elsevier.nlrlocaterapsusc

[32] M. P. Murrell *et al.*, “Spatially resolved electrical measurements of SiO2 gate oxides using atomic force microscopy,” *Appl Phys Lett*, vol. 62, no. 7, pp. 786–788, 1993, doi: 10.1063/1.108579.

[33] “NanoWorld Nanoworld atomic force microscope probes catalogue, http:// www.nanoworld.com/afm-probes-catalog (accessed 4 February 2016).”.

[34] R. R. L. De, D. A. C. Albuquerque, T. G. S. Cruz, F. M. Yamaji, and F. L. Leite, “Measurement of the Nanoscale Roughness by Atomic Force Microscopy: Basic Principles and Applications,” in *Atomic Force Microscopy - Imaging, Measuring and Manipulating Surfaces at the Atomic Scale*, InTech, 2012, pp. 147–174. doi: 10.5772/37583.

[35] “SPI supplies http://www.2spi.com/category/silver-paints-pastes (accessed 4 February 2016).”.

[36] C. Pan, Y. Shi, F. Hui, E. Grustan-Gutierrez, and M. Lanza, “History and Status of the CAFM,” 2017.

[37] M. Rommel *et al.*, “ Influence of parasitic capacitances on conductive AFM I-V measurements and approaches for its reduction ,” *Journal of Vacuum Science & Technology B, Nanotechnology and Microelectronics: Materials, Processing, Measurement, and Phenomena*, vol. 31, no. 1, Jan. 2013, doi: 10.1116/1.4768679.

[38] V. Yanev, T. Erlbacher, M. Rommel, A. J. Bauer, and L. Frey, “Comparative study between conventional macroscopic IV techniques and advanced AFM based methods for electrical characterization of dielectrics at the nanoscale,” *Microelectron Eng*, vol. 86, no. 7–9, pp. 1911–1914, Jul. 2009, doi: 10.1016/j.mee.2009.03.094.

[39] M. Lanza *et al.*, “Graphene-coated atomic force microscope tips for reliable nanoscale electrical characterization,” *Advanced Materials*, vol. 25, no. 10, pp. 1440–1444, Mar. 2013, doi: 10.1002/adma.201204380.

[40] F. Hui *et al.*, “Moving graphene devices from lab to market: Advanced graphene-coated nanoprobes,” *Nanoscale*, vol. 8, no. 16, pp. 8466–8473, Apr. 2016, doi: 10.1039/c5nr06235g.

[41] E. Bussmann and C. C. Williams, “Sub-10 nm lateral spatial resolution in scanning capacitance microscopy achieved with solid platinum probes,” *Review of Scientific Instruments*, vol. 75, no. 2, pp. 422–425, Feb. 2004, doi: 10.1063/1.1641161.

[42] “Rocky Mountain Nanotechnology http://rmnano.com/ (accessed 4 February 2016).”.

[43] T. Hantschel *et al.*, “Conductive diamond tips with sub-nanometer electrical resolution for characterization of nanoelectronics device structures,” *Physica Status Solidi (A) Applications and Materials Science*, vol. 206, no. 9, pp. 2077–2081, Sep. 2009, doi: 10.1002/pssa.200982212.

[44] Y. Wen, J. Chen, Y. Guo, B. Wu, G. Yu, and Y. Liu, “Multilayer graphene-coated atomic force microscopy tips for molecular junctions,” *Advanced Materials*, vol. 24, no. 26, pp. 3482–3485, Jul. 2012, doi: 10.1002/adma.201200579.

[45] C. Martin-Olmos, H. I. Rasool, B. H. Weiller, and J. K. Gimzewski, “Graphene MEMS: AFM probe performance improvement,” *ACS Nano*, vol. 7, no. 5, pp. 4164–4170, May 2013, doi: 10.1021/nn400557b.

[46] W. Shim, K. A. Brown, X. Zhou, B. Rasin, X. Liao, and C. A. Mirkin, “Multifunctional cantilever-free scanning probe arrays coated with multilayer graphene,” *Proc Natl Acad Sci U S A*, vol. 109, no. 45, pp. 18312–18317, Nov. 2012, doi: 10.1073/pnas.1216183109.

[47] M. Lanza *et al.*, “Nanogap based graphene coated AFM tips with high spatial resolution, conductivity and durability,” *Nanoscale*, vol. 5, no. 22, pp. 10816–10823, Nov. 2013, doi: 10.1039/c3nr03720g.

[48] “Diamond coated AFM tips, Nanoworld product catalogue, http://www.nanoworld.com/diamond-coated-afm-tips (accessed 13 February 2017).”.

[49] “Instriuments http://www.ni.com/data-acquisition/ (accessed 4 February 2016).”.

[50] Y. Ji *et al.*, “Characterization of the photocurrents generated by the laser of atomic force microscopes,” *Review of Scientific Instruments*, vol. 87, no. 8, Aug. 2016, doi: 10.1063/1.4960597.

[51] Z. L. Wang and J. Song, “Piezoelectric Nanogenerators Based on Zinc Oxide Nanowire Arrays.” [Online]. Available: https://www.science.org

[52] W. Frammelsberger, G. Benstetter, J. Kiely, and R. Stamp, “C-AFM-based thickness determination of thin and ultra-thin SiO 2 films by use of different conductive-coated probe tips,” *Appl Surf Sci*, vol. 253, no. 7, pp. 3615–3626, Jan. 2007, doi: 10.1016/j.apsusc.2006.07.070.

[53] M. Ahmad, S. A. Han, D. H. Tien, J. Jung, and Y. Seo, “Local conductance measurement of graphene layer using conductive atomic force microscopy,” in *Journal of Applied Physics*, Sep. 2011. doi: 10.1063/1.3626058.

[54] L. Britnell *et al.*, “Electron Tunneling through Ultrathin Boron Nitride Crystalline Barriers,” *Nano Lett*, vol. 12, no. 3, pp. 1707–1710, Mar. 2012, doi: 10.1021/nl3002205.

[55] P. K. Sahoo, G. Mangamma, A. Rajesh, M. Kamruddin, and S. Dash, “Polarization induced conductive AFM on cobalt doped ZnO nanostructures,” 2017, p. 050170. doi: 10.1063/1.4980403.

[56] B. Kiss-Pataki, J. Tiusanen, G. Dobrik, Z. Vértesy, and Z. E. Horváth, “Visualization of the conductive paths in injection moulded MWNT/polycarbonate nanocomposites by conductive AFM,” *Compos Sci Technol*, vol. 90, pp. 102–109, Jan. 2014, doi: 10.1016/j.compscitech.2013.10.016.

[57] R. Khoury *et al.*, “Observation of photovoltaic effect within locally doped silicon nanojunctions using conductive probe AFM,” *Nano Energy*, vol. 76, p. 105072, Oct. 2020, doi: 10.1016/j.nanoen.2020.105072.

[58] B. Zhang, P. Kutalek, P. Knotek, L. Hromadko, J. M. Macak, and T. Wagner, “Investigation of the resistive switching in AgxAsS2 layer by conductive AFM,” *Appl Surf Sci*, vol. 382, pp. 336–340, Sep. 2016, doi: 10.1016/j.apsusc.2016.04.152.

# CHAPTER 2

## Metal-organic coordination polymer multilayers produced by sequential in situ self-assembly

**Chemical, electrical, and thermal characterization.**

Recent significant advancements in supramolecular chemistry allowed the creation of a wide range of architectures; in particular, specific interaction of metal ions with organic molecules can drive the self-assembly of solid frameworks in the form of thin layers. In this chapter we describe the characterization of coordination polymer thin films prepared using a novel and versatile technique. In particular, we studied some electronic properties of such materials, i.e. their work function and their conductivity, important for their possible future application in electronics.

*Part of this work, specifically the synthesis and some of the material characterizations, was carried out during my secondment period at the University of Dresden, working with Prof. Xinliang Feng's group as part of the Marie-Curie ITN project ULTIMATE. The materials under study were prepared in a laboratory at the University of Dresden, while the majority of the film characterization was done in our ISOF/CNR laboratory and our group in Bologna.*

### 2.1 Introduction

Significant progress has been made recently in the field of molecular inorganic-organic hybrid compounds. A phase of rapid development has been observed in the synthesis and characterization of large networks in one, two, and three dimensions (1D, 2D, and 3D). In particular, attention has been drawn to coordination compounds with almost infinite periodic structures were organic building blocks act as ligands and metal ions as nodes to form the network[1]. These compounds are typically termed Coordination polymers (CP) [1]. More specifically, a coordination polymer is made up of metal ions or clusters connected with

organic ligands in order to form an infinite array. Coordination bonds define this infinite net. Consequently, a structure connected by coordination bonds in one direction and supramolecular interactions (like hydrogen bonding and π-π stacking) in two additional directions is referred to as a one-dimensional (1D) coordination polymer; a structure connected by coordination bonds in two directions and supramolecular interactions (like hydrogen bonding and π-π stacking) in a third direction is referred to as a two-dimensional (2D) coordination polymer; and a structure connected by coordination bonds in three directions is clearly a three-dimensional (3D) coordination polymer [2].

Coordination polymers are typically assembled into highly ordered three-dimensional structures by metal ions (or metal clusters) and bridging organic ligands, occasionally with additional supramolecular interactions. Topologic nets can be used to describe such regular 3D structures. A polymeric metal-organic net can be reduced topologically to a set of nodes with a specific symmetry (triangular, tetrahedral, octahedral, etc.) and linkers that join the nodes to form an infinite 1D-3D periodic net. In addition to helping to comprehend the net structure, topological description can be applied to the creation of novel coordination polymers. Reticular chemistry is the name given to the net-based methodology [3]. In general, organic ligands act as the linkers and metal ions or clusters as the nodes. Higher multitopic (tri-topic, for example) organic ligands may also occasionally be thought of as the nodes, particularly when the metal ions act as multiple (two or three, for example) connectors in the network. In theory, a specific net can be assembled by using the right nodes and linkers [2].

Thus far, an extensive number of nets have been documented. As seen in Figure 2-1, these include the ladder, zigzag or helical, square, or rectangular, honeycomb and brick-wall structures for 2D nets, diamondoid, and cubic for 3D nets, and railway chains for 1D nets. Of course, the literature has also documented a great deal of more intricate and intriguing nets [4].

In comparison to hydrogen bonds and other weak supramolecular interactions, coordination bonds are typically stronger and possess a more pronounced directional character. These metal-ligand coordination bonds are a particular kind of non-covalent interaction that occurs between a metal ion (also referred to as coordination center) and the organic molecules that surround it (referred to as the ligand) [5]. While its nature (covalent to ionic) and strength are heavily dependent on the chemical nature of both the central metal ions and the ligands, the coordination bond is typically categorized as being of intermediate strength between purely covalent (strong) and supramolecular (weak) bonds. Coordination bonds are highly adjustable given the wide range of metallic cations (originating from the s, p, d, or f blocks) and complexing groups (either anionic: carboxylate, phosphonate, azolate, phenolate, etc.) that

are available [5]. Thus, a key factor in the formation of coordination polymeric nets is the coordination preference of metal ions (or clusters) and the structures of organic bridging ligands. As a result, it should be possible to predict coordination polymer structures more easily, compared to a molecular crystal's.

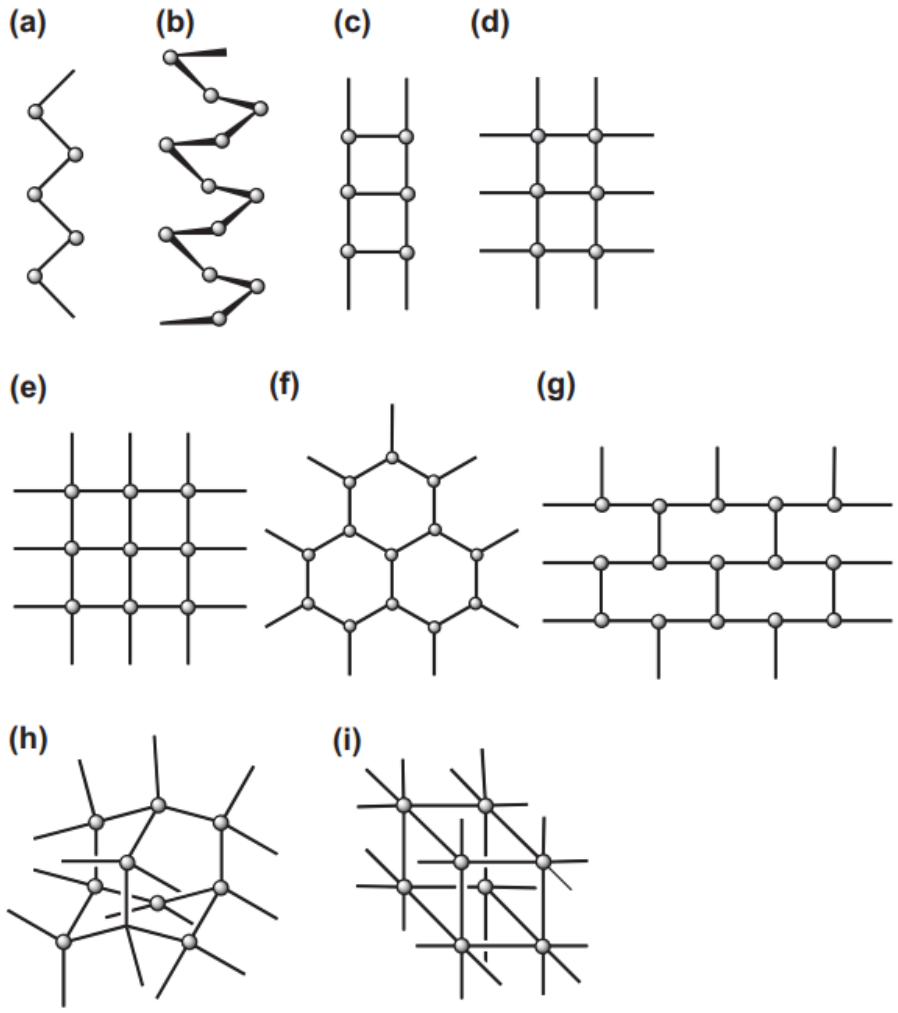


*Figure 2-1. Examples of simple coordination polymer nets. (a) A zigzag chain, (b) a helical chain, (c) a ladder chain, (d) a railway chain, (e) a square net, (f) a honeycomb net, (g) a brick-wall net, (h) diamondoid net, and (i) a cubic net. Picture taken from ref.* [2]

However, both the structures of organic ligands and the coordination geometry of metal ions are typically diverse, if not variable. The arrangements of various metal ions (or clusters) and organic bridging ligands can form nearly infinite coordination net structures. Furthermore,

coordination bonds are typically more flexible than typical covalent bonding because they have a weaker interaction. There could be additional weaker interactions between molecules due to supramolecular forces (van der Waals, π-π stacking etc.). Therefore, a self-assembly system made up of metal ions, organic ligands, counter anions, and solvent molecules naturally possesses structural uncertainty.

The formation of coordination nets can be influenced by a wide range of reaction parameters, including pH, solvent, reaction/crystallization temperature, template/additive, and counter ions [6]. A complex self-assembly system's result would therefore be hard to predict using only molecular design (the selection of metal ions, metal clusters, and ligand structure). Actually, different coordination polymers can be produced by different reaction conditions for a given set of metal and ligand at a given molar ratio. Different components and solvents, along with additional species like additives and templates, are used in a system to produce a specific coordination polymer. Before nucleation or crystallization, the components may combine into a small intermediate species (Fig. 2-2) under the guidance of coordination bonding and possibly in conjunction with other supramolecular interactions. By combining these intermediate species, one or more types of large molecular assemblies can be formed, which can result in the formation of crystal seeds and crystals with the same or different superstructures. Supramolecular isomerism, which is commonly seen for coordination polymers, is one example of the structural diversity [6], [7]. Different products may be favored kinetically or thermodynamically. The energy barrier for a thermodynamically favored product is typically larger than that of a kinetically favored product when different products can be generated from a reaction system (Fig. 2-3).

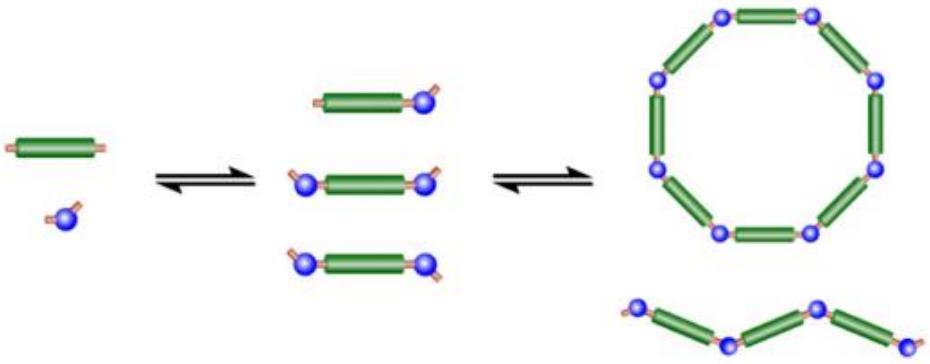

*Figure 2-2. An illustration of two potential products that di-topic organic ligands and metal ions may assemble. Picture taken from ref.* [2]

Because thermal energy is directly correlated with reaction temperature, a higher reaction temperature will yield the thermodynamically favored isomer linked to a high activation energy, whereas a lower temperature will favor the kinetic product. As a result, the formation of products can be changed by adjusting the reaction temperature and/or other reaction parameters. For the kinetically favored product, high concentration and low temperature are typically preferred, whereas for the thermodynamically favored product, low concentration and high temperature are preferred. In practice, additional reaction parameters like pH, template/additive, solvent, and counter ions can also have a big effect on the kinetic process and cause different products to form.

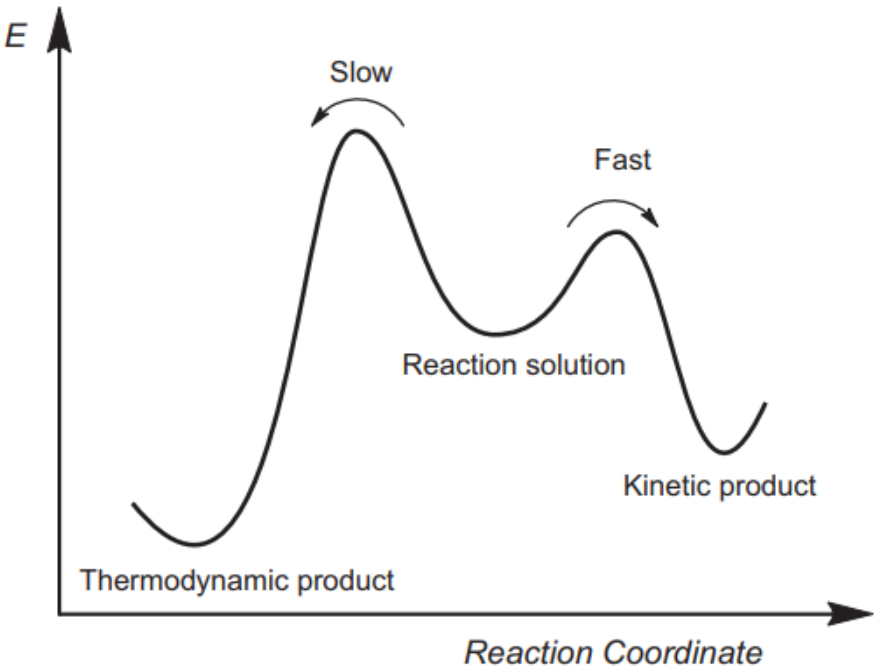


*Figure 2-3. Products crystallization via both thermodynamic and kinetic processes. Picture taken from ref.* [6]

Many strategies have been developed to use molecular building blocks to synthesize tailored target structures. Designing these molecular building blocks to control the formation of desired chemical, physical, and architectural properties in the resulting solid-state materials is critical to success.

Chemists, physicists, and materials scientists have shown a keen interest in CP, given their high surface area. This special characteristic results from the interconnection of organic ligands and metal ions, which forms a three-dimensional structure with distinct channels and cavities. Coordination polymers have attracted commercial interest as promising options for gas separation and storage applications because of their porosity, which enables the adsorption and storage of gases like carbon dioxide and hydrogen. Additionally, one noteworthy feature of coordination polymers that results from the selection of metal ions and organic ligands is the tunability of their properties. Researchers can control the coordination polymer's size, shape, and functionality by altering the constituents, resulting in a large library of materials with customized properties. This tunability opens up new possibilities for sensing, drug delivery, catalysis, and electrochemical devices.

Historically, the two most well-known subclasses of microporous inorganic solids were aluminosilicates and aluminophosphates. Among them, a particular interest has always been paid to zeolites, having the general formula $M^{n+}{}_{x/n}[(AlO_2)_x(SiO_2)_y]^{x-}\cdot wH_2O$ (where M=metal), that are 3D crystalline, hydrated alkaline, or alkaline-earth aluminosilicates. Their structure, built from corner-sharing $TO_4$ tetrahedra (T=Al, Si), creates networked tunnels or cages that can take M ions and water molecules. In order to develop porosity, water molecules are removed, usually without affecting the framework. Initially, the cavities—which are identified by the number of surrounding polyhedra—were used as molecular sieve applications in catalytic and gas separation processes. In 1862, synthetic zeolites were first discovered; [1]. Zeolites display unique structural features that characterize their adaptability and functionality. Their crystalline structure and the possibility to precisely control the pore size have a significant impact on both their molecular sieving and adsorption capabilities. Ion exchange sites are established by the presence of exchangeable cations, which are propelled by the positive charge of aluminium in the framework. The overall characteristics of the zeolite can be affected by substituting different ions in solution for these cations, which include potassium and sodium. Interestingly, certain zeolites exhibit structural flexibility, enabling modifications in reaction to outside stimuli. Moreover, they are indispensable in a wide range of industrial and scientific applications because of their exceptional adsorption and selectivity properties, which are a result of this special features.

Zeolites are useful in the processes of gas separation, purification, and drying because of their remarkable adsorption capacities for both gases and liquids. They also serve as catalysts in a variety of chemical reactions that are important to the production of petrochemicals, industrial catalysis, and petroleum refining because of their porous nature and ion-exchange capacity. Additionally, they mitigate water hardness by exchanging sodium ions for calcium and magnesium ions, which is a crucial function of zeolites in water-softening systems.

Zeolites are used in processes such as gas and liquid drying because of their precisely defined pore sizes, which transform them into molecular sieves. Moreover, they are employed in environmental applications to improve soil, treat wastewater, and act as radioactive and heavy metal adsorbents. Last, zeolites are promising candidates for drug delivery systems because of their porous structure, which allows for the controlled release of medications. Aluminophosphates, or AlPO4s, are composed of $Al^{3+}$ and $P^{5+}$ tetrahedra connected by oxygen atoms that share a corner. These atoms create a three-dimensional neutral framework with molecular-sized channels and/or pores[8]. Aluminophosphates differ from zeolites due to the special arrangement of phosphorus and aluminum in their framework. Among their many useful characteristics are molecular sieving ability, catalytic activity, and ion-exchange capacity. They are useful in procedures like gas separation and purification because of their porous structure, which enables the selective adsorption of molecules based on size and shape. Like zeolites, aluminophosphates are also used as catalysts in a variety of chemical reactions. Their performance in adsorption and catalysis can be influenced by precisely controlling their composition, which allows for the customization of pore size. Microporous crystalline aluminophosphates were first reported in 1982[9]. Since then, other related crystalline oxides have also been found, including porous chalcogenides, halides, and nitrides, as well as silicoaluminophosphates, metallosilicates, metalloaluminophosphate, and metallophosphates[10], [11].[12], [13], [14], [15].

Another material that is widely employed for its porosity is activated carbons, that, despite possessing a disordered structure, has a high specific surface area and open porosity. A twisted network of imperfect hexagonal carbon layers connected by aliphatic bridging groups constitutes the fundamental structural component. Although it varies, the layers' width is normally 5 nm. Heteroelements and simple functional groups are bound to the edges of the carbon layers and integrated into the network.

The previous classes of porous materials are not as broad as the recently developed porous coordination polymers, since the possibility to directly control their structure and hence their properties directly from the synthesis holds the promise to overcome the limitations of the materials discussed previously. CP frameworks are highly tunable, highly porous, and completely regular. Their synthesis takes place in mild environments, and the so-called bottom-up approach involves selecting a specific combination of organic ligands and metal ions to produce the intended extended network. The structural stability of the building units is preserved all throughout the reactions, allowing them to be used as modules in the assembly of extended structures. Prussian blue compounds, [16], [17], [18], Werner complexes[19], [b-M(4-methylpyridyl)4(NCS)2] (M=NiII or CoII), Hofmann clathrates, and their derivatives have frameworks made of CN linkages between square-planar or tetrahedral

tetracyanometallate (ii) units and octahedral metal (ii) units coordinated by complementary ligands,[16], [20] which are known to be materials that can reversibly absorb small molecules (Figure 2-4). Examples of porous coordination polymer structures with functional micropores have been published since the early 1990s.

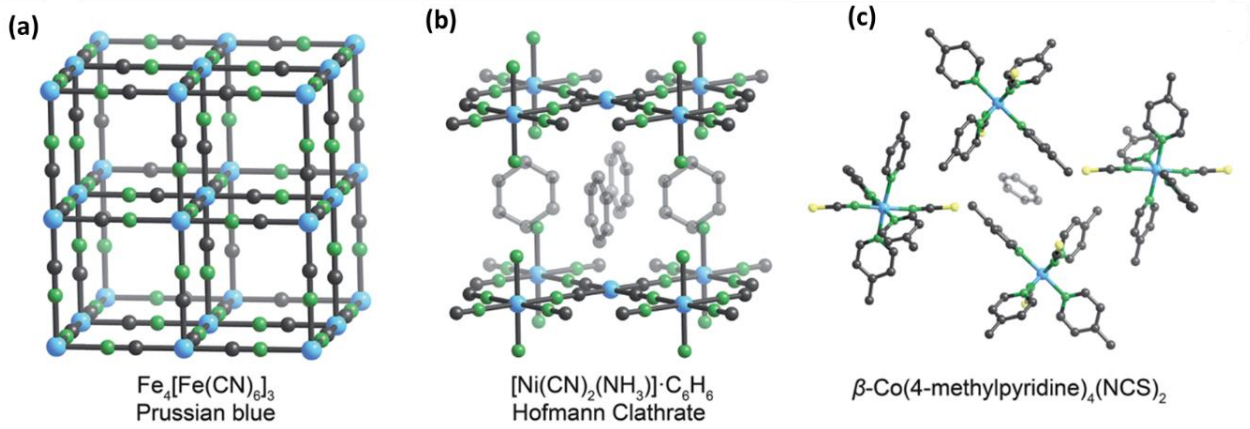


*Figure 2-4. Metal–cyanide frameworks: (a) Prussian blue and (b) Hofmann clathrates with benzene molecules filling the gap between the layers. Atom labelling scheme: metals are blue, N is green, and C is black. For clarity, H atoms are not included. A Werner complex inclusion compound: (c) β-Co(4-methylpyridine)$_4$(NCS)$_2$, NCS=thiocyanate crystal structure, with benzene occupying the gaps between the complexes. Picture taken from ref.* [21]

An anion exchange-capable porous coordination polymer was first described by Robson et al. in 1990[22]. Fujita et al. examined the catalytic characteristics of a 2D [Cd(II)-4,4'-bpy] (bpy = bipyridine) coordination polymer in 1994 [23]. The groups of Yaghi[24] and Moore[25] investigated the adsorption of guest molecules in 1995, and Kondo et al. reported gas adsorption at room temperature in 1997[26].

Recent advances in characterization and synthetic methodologies have led to a massive growth in the field of coordination polymers. Coordination polymers can be created using a variety of techniques, from conventional solution-based methods to more advanced techniques like solvothermal and mechanochemical synthesis. The size, shape, and crystallinity of the coordination polymer thin films can all be precisely controlled with the help of these methods. Understanding the structure, morphology, and characteristics of coordination polymers depends heavily on characterization methods like X-ray diffraction,

scanning electron microscopy, and spectroscopy. These analytical instruments offer important insights into the configuration of the porous network and the connectivity between ligands and metal ions.

In this work we describe CP produced using the shearing method, a type of meniscus-guided coating known for low-cost and high-throughput thin-film fabrication. It is a versatile and easy method for achieving uniformity, superior molecular arrangement, and stacking in the films with the least amount of material waste. We used a planar conjugated ligand, 2,3,6,7,11,12,15,16- octahydroxyphenanthro[9,10:b]triphenylene (OHPTP) with $D_{2h}$-symmetry and four connecting points as monomer. We realized two types of coordination polymer thin films combining this ligand with Cu and Zn ions, yielding with $Cu_2$(OHPTP) and with $Zn_2$(OHPTP). These novel synthesised CP films have exhibited intriguing electronic properties, and the simplicity of their synthesis makes them suitable candidates for several applications and electronic devices.

The production of such CP has been described in [27]. We change the reaction time of the coordination polymer thin film from 5 minutes to 20 minutes and the thickness of the films. We then study the effect of metal ion used, reaction time and fil, thickness on the chemical, electrical and stability properties.

## 2.2 Preparation of CP thin films by shear coating technique

The shear coating is a versatile method that can be used to rapidly produce multilayers and thin films with a range of properties[28], [29], [30][31][32], [33]. The shear coating technique involves an organic semiconductor (PSC) that is confined between a top movable blade and a temperature-controlled substrate (Figure 2-5) [29], [33], [34], [35]. The material is translated across the substrate by rotating the blade at a set speed, resulting in a guided and regulated film deposition. Solution-sheared PSC films have higher crystallinity and molecular packing than spin-coated films, leading to effective charge transport in OFETs [36]. Shear coating parameters, including stage temperature, blade gap, and shear speed, can affect these films' properties [29]. In addition, a variety of well-established techniques exist for regulating the final film morphology. These include pre-processing methods for ink formulation, alignment methods for post-processing, substrate patterning, and modified shear coating geometries methods[34].

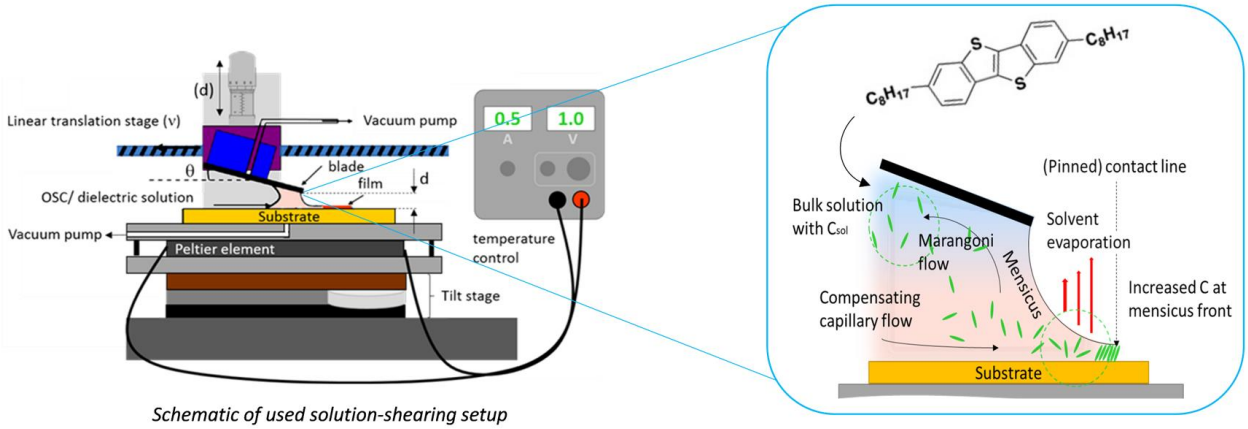


*Figure 2-5. Schematic illustration of the shear coating technique. Picture taken from* [37]

Numerous variables, including the substrate's surface energy, solution concentration and viscosity, shearing speed, and substrate temperature, affect the final morphology of the deposited material[35]. The OHPTP monomer (Figure 2-6) utilized to prepare the CP films under study is synthesized as described in [38]. For preparing the films a blend of the OHPTP monomer dissolved in THF is first solution sheared on Au or Si substrates at 35°C (Figure 2-7). During the shear-coating the gap between the blade and the substrate is fixed at a distance of 250 µm and the speed of the coating process is 6 cm $s^{-1}$. After the monomer is shear-coated onto the substrate, it is dipped into a solution containing the second component of the CP, i.e. the metal ion. Solutions of $Cu(OAc)_2$ or $Zn(NO_3)_2$ (both dissolved in $H_2O$) are used for 1 minute to initiate the formation of the coordination polymer, as shown in Figure 2-7. We prepared four separate samples for each of the two reactants, varying reaction/dipping times, with t=5, 10, 15 or 20 minutes. Furthermore, the shear coating technique can be applied multiple times, using different solutions, on the same substrate; this allows to realize CP multilayers. Figure 2-7 shows the process of each coating and how multiple coatings are produced. For this study, we have realized two samples, one for each of the reactants, repeating the coating for six-time. All the different CP films configurations are presented in the figure 2-8 below. Samples 2-8a and 2-8b have been prepared four times each for a different reaction time keeping the thickness stable, while in samples 2-8c and 2-8d we changed the thickness fixing the reaction time to 1 minute for each coating cycle but repeating the coating 6 times. In Appendix A, A1-A3 the final single and multicoated samples and the

relative thickness of each coating is being illustrated. Thus, it is possible to study how the chemical, structural and electronic properties are changing with respect to the different reaction times and thicknesses.

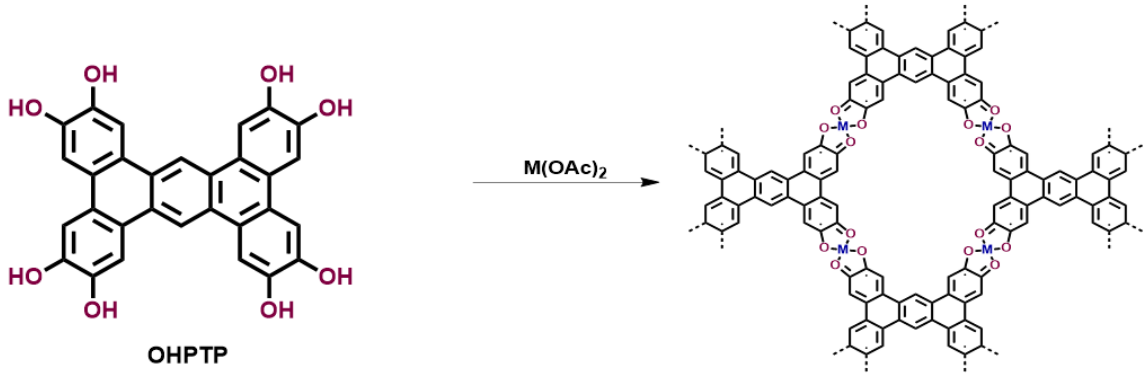


*Figure 2-6. Chemical structure of the OHPTP monomer and the final expected chemical structure after the coordination. M stands for the metal element (Cu, Zn)*[27]

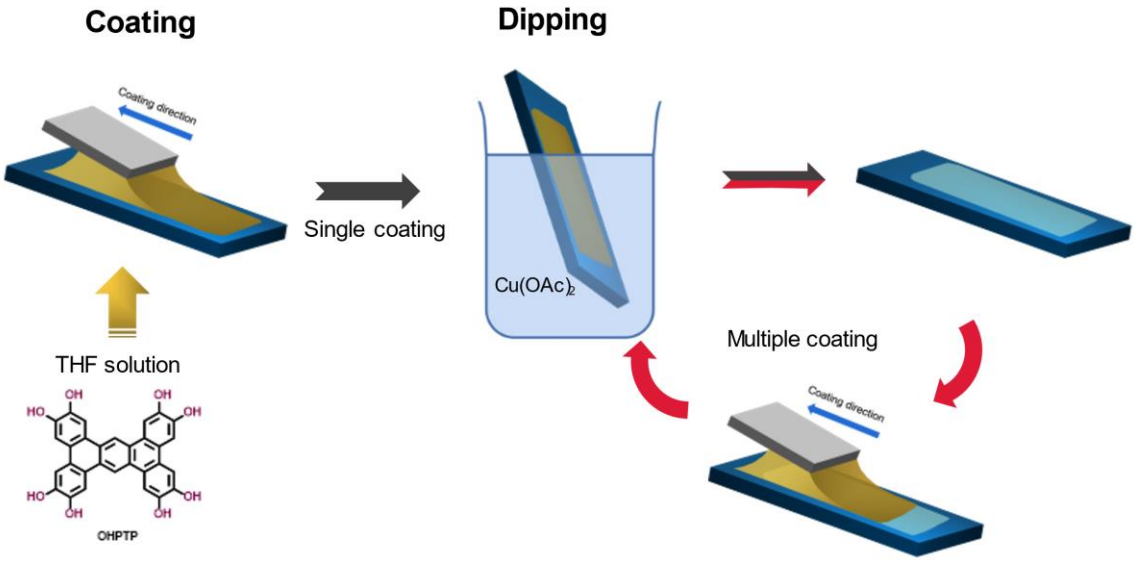


*Figure 2-7. Scheme illustration of shear-coating technique used to prepare the films under study.*[29], [33]

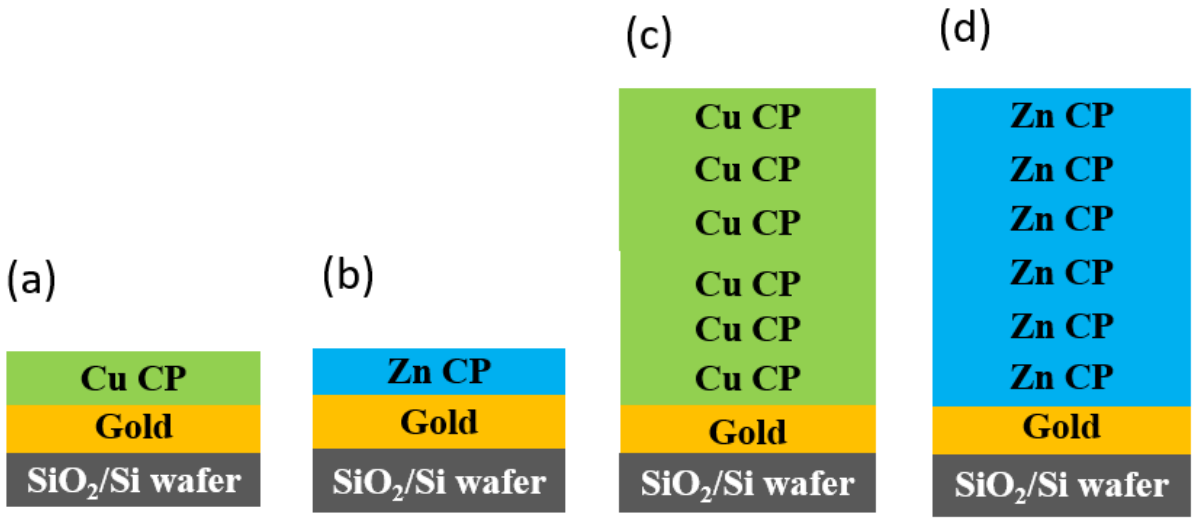


*Figure 2-8. All four types of CP thin film configurations (a) one coating of Cu-CP (b) one coating of Zn-CP (c) Multi-coating of Cu-CP (6 coatings) (f) Multi-coating of Zn-CP (6 coatings).*

## 2.3 Results and discussion

### *2.3.1 Characterization of CP thin films*

All CP samples were characterised by X-ray Photoemission spectroscopy (XPS), Fourier-transform infrared (FT-IR) spectroscopy and UV-Vis spectroscopy. X-ray Photoemission spectroscopy (XPS) was used to confirm the presence of the expected elements in the CP thin films (C, O, Cu and Zn) and the ratio of the present elements as shown in Figure 2-9. In Cu CP samples, high resolution XPS spectra of O 1s shows a broad peak that may be attributed to a combination of C=O-Cu (531 eV), C-O-Cu (533eV) signals and contributions of water presence (Figure A4 and A5). Zn CP samples also exhibit the same contributions to the O 1s signal as Cu CP samples, but with Zn in place of Cu. The C 1s signal of both type of films, showing three main peaks at 283.8 eV, 285.16 eV and 287.54 eV, is attributed to carbonate or carboxyl acid

groups. In the energy range typical of Cu 2p, a peak at 934.96 eV suggests the presence of Cu (II), while the faint signal observed at 932.73 eV and usually attributed to Cu(I) is attributed to photoreduction occurring during the measurements. Finally, the presence of Zn is deduced from the Zn 2p signal at around 1150 eV. We underline that the Cu signal can only be observed in the XPS spectrum of the Cu CP thin film and not in the Zn CP film, and vice versa, confirming that no contamination is present.

The table presented in Figure 2-10 displays the abundance ratio of main element in each of the Cu and Zn CP single coated samples for two distinct reaction times (1 and 20 minutes) extracted from the XPS spectra, reported as atom percentage. Gold signal is also recorded due to the substrate, but it is not present in the table below since it is not the focus of our work. It is shown that the ratio of the metal elements, that act as the linker that bonds the ligand units into the coordination polymer, is changing distinctively. The percent of both Cu and Zn increase almost by 50% after 20 minutes of reaction, while the percent of C and O remain constant in both cases.

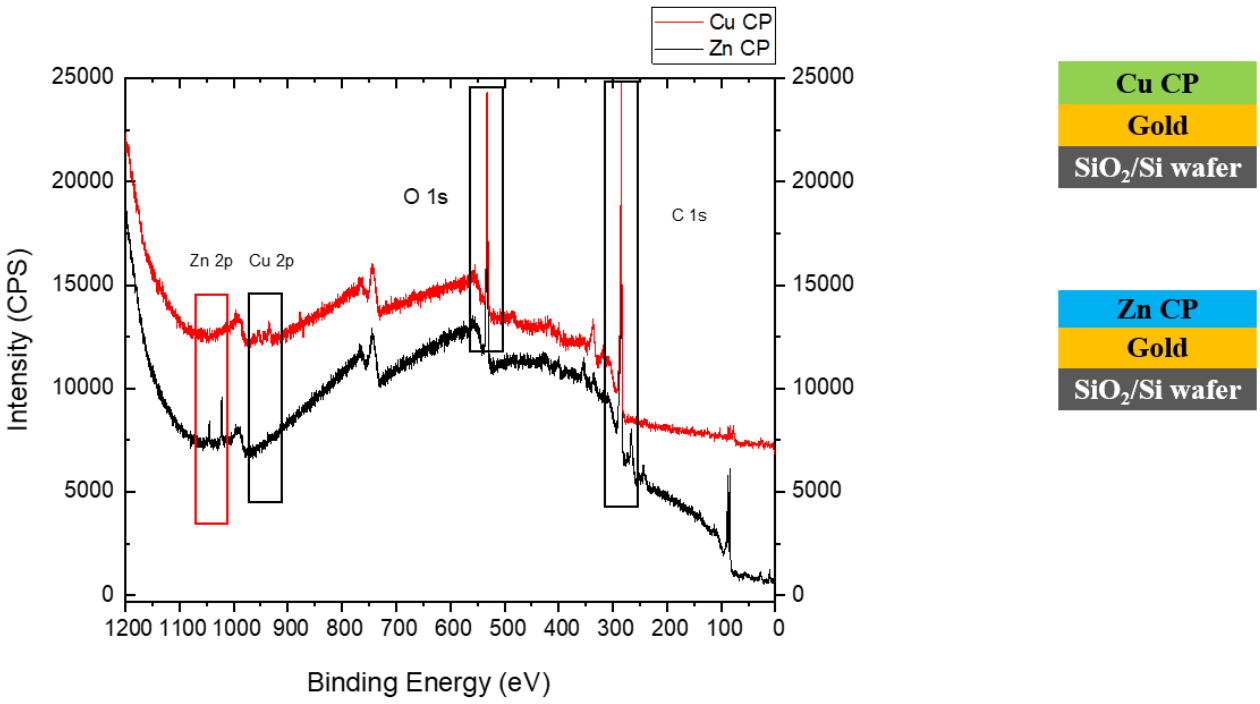


*Figure 2-9. XPS spectra confirming all elements used to synthesize the CP films.*

| (%) | C | O | Zn | Cu |
|---|---|---|---|---|
| Cu CP 1min | 61,5 | 22,8 | 0,0 | **1,6** |
| Cu CP 20mins | 64,9 | 25,8 | 0,0 | **3,1** |
| Zn CP 1min | 46,9 | 18,7 | **0,4** | 0,0 |
| Zn CP 20mins | 50,2 | 18,8 | **0,9** | 0,0 |

*Figure 2-10. Table with the ratios of the main elements for 1 and 20 minutes of reaction time for the Cu and Zn single coated film (formation time of the coordination polymer)*

Successful formation of coordination bonds is additionally indicated by Fourier-transform infrared (FT-IR) spectroscopy (Fig. 2.11a): O-H stretching vibration band of OHPTP at 3000–3500 $cm^{-1}$ decreases after the complexation of the ligand film with $Cu_2$(OHPTP) and $Zn_2$(OHPTP). However, thin films of Cu CP and Zn CP prepared via shear-coating are significantly different structurally from the bulk crystals of the corresponding materials. These bulk crystals have been prepared via solvothermal synthesis by coordination of the OHPTP and copper acetate (in case of $Cu_2$OHPTP crystal) and zinc nitrate (in case of the $Zn_2$OHPTP) in a mixed solvent of water and DMF (7:3) at 85°C for 24 hours, [27] Figure A6 illustrates how the main bands are either missing or shifted. For instance, the crystals show complete coordination of the OH since they lack the characteristic band of the O-H stretching vibration at 3000-35000, but the thin films still exhibit this band. This could be attributed to the fact that some OH are not coordinated, as well as the presence of water. Moreover, UV visible spectroscopy provides additional confirmation of the polymer's formation. In Figure 2-11b a bathochromic shift from 520 to > 600 may be observed which can be assigned to ligand to-metal charge transfer band [27], [39] further confirming the formation of the coordination polymer. Additionally, despite using different measurement conditions, the absorbance bands found in both bulk crystals and thin films UV/vis spectra (A7) are in a good match in respect to the bands found in the UV/vis spectrum of the ligand.

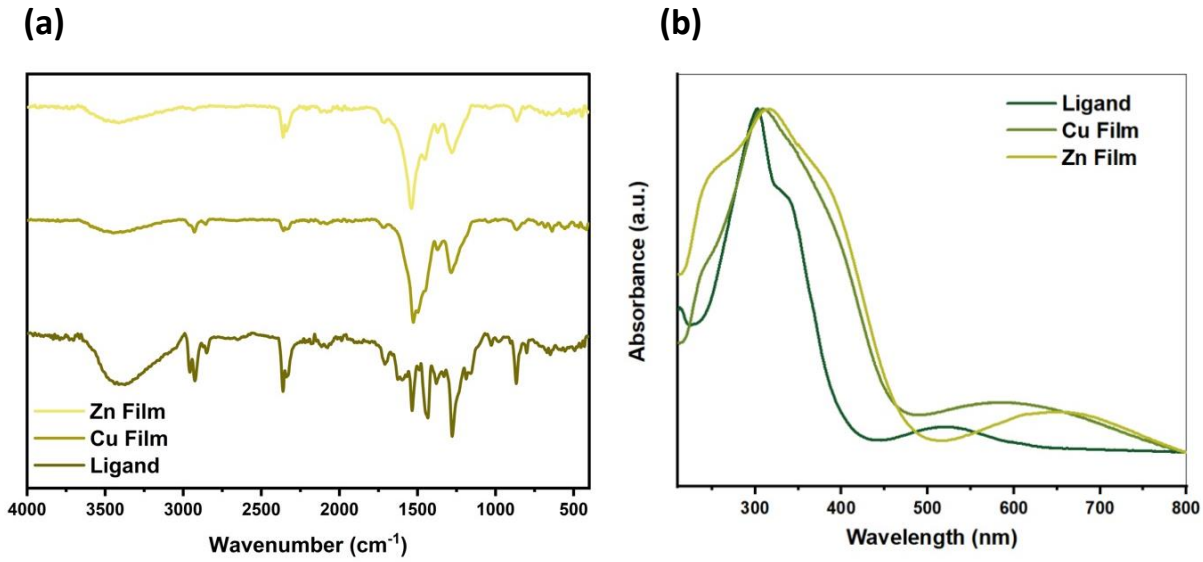


*Figure 2-11. (a) IR spectra and (b) UV/Vis spectra of the ligand, Cu CP Film and Zn CP Film.*

### *2.3.2 Changes in work function among different CPs.*

The different metallic elements binding the monomer units to form the coordination polymer contribute to different electronic properties of the final film. Using Kelvin probe force microscopy we measured the work function values for each film to understand how the metal elements, formation time of the coordination polymer and additional coating in the multi coated films alter these values.

KPFM measures the sample's surface potential (SP), which is equal to the difference between the sample's WF and the tip value (i.e., $WF = WF_{tip} - WF_{sample}$), along with any electric potential (V) applied to the sample[40]. [41], [42] the $V_{cpd}$ value can be extracted from the surface potential maps recorded by KPFM and from the formula $V_{cpd}=WF_{tip}-WF_{sample}$ we can calculate the WF value of the sample under study. Given that KPFM is a highly sensitive characterization technique, to ensure that the value of our tip stays constant, we have used freshly cleaved

HOPG and gold as a reference. More details about KPFM may be found in Chapter 1 in the corresponding section.

Figure 2-12 shows the work function values calculated using the formula given above. The mean surface potential values ($V_{cpd}$) have been extracted from the corresponding KPFM images in the case of the single coated Cu and Zn CP. This calculation of the work function values is repeated for various reaction times of the polymer, as well as the monomer (OHPTP). Surface potential images have been recorded for each sample.

Interestingly, the surface potential images exhibit a uniform colour (surface potential value) indicating that the surface properties are uniform. Consequently, in each case, a mean surface potential value can be extracted. Some examples of these images can be found in Appendix A (Figure A8). The graph of figure 2-12 summarize the systematic changes in the work function of the films due to both the different metallic elements and the reaction time for the formation of the polymer. We find that, the Cu-CP film consistently displays a larger work function than the Zn-CP film. Both films show a decrease in the work function value with increasing reaction time, with the Zn-CP film demonstrating the largest variation with time.

The change in the work function can be justified by the increase of the metal element percent observed by XPS (Figure 2-10). This will likely change as well to the final structure of the film after the reaction. Preliminary DFT calculations suggest that Zn has a preferential tendency to form 3D networks while Cu remains planar (work in progress, not reported here. Because the ratios of the main metal elements increase noticeably after long reaction periods, the final structure may be affected, as each coating consists of several layers. As a result, each layer may not be perfectly aligned with the others resulting in the work function pattern shown in Figure 2-12. In order to better understand our results and determine whether each node is connected to the suggested number of ligands for the proposed chemical structure shown in Figure 2.1, we can also calculate the C/Cu and C/Zn ratios from the table in Figure 2-12. The data indicate that in the case of the Cu CP for 1 minute of reaction, the C/Cu is roughly comparable to the ideal structure of a MOF; consequently, we have the least amount of excess Cu or C elements, giving us the best possible final product out of the four samples. More precisely, 1.27 ligands can be allocated to each Cu atom. The situation varies as we increase the reaction time. A longer reaction time of 20 minutes results in a higher percentage of Cu in the Cu CP, which makes the ideal C/Cu quite different. In that instance, 0.68 of the ligands can be assigned to each Cu atom. As a result, the final composition and structure may differ significantly from the proposed one or even the one with the fastest reaction time. This excess of nodes could cause the layers to assemble more chaotically. These changes are even more pronounced in Zn CP films after both 1 and 20 minutes of reaction time. In the first

case, with the shorter reaction time, the C/Zn ratio demonstrates that each Zn atom may be allocated to 3.53 organic ligands, whereas in the second case, with the 20-minute reaction time, each Zn atom may be assigned to 1.78 ligands, since the Zn percentage increases with longer reaction times. The crystallinity and chemical composition of the films may be impacted by these stoichiometric diversities, which could have an effect on the materials' overall chemical and physical characteristics.

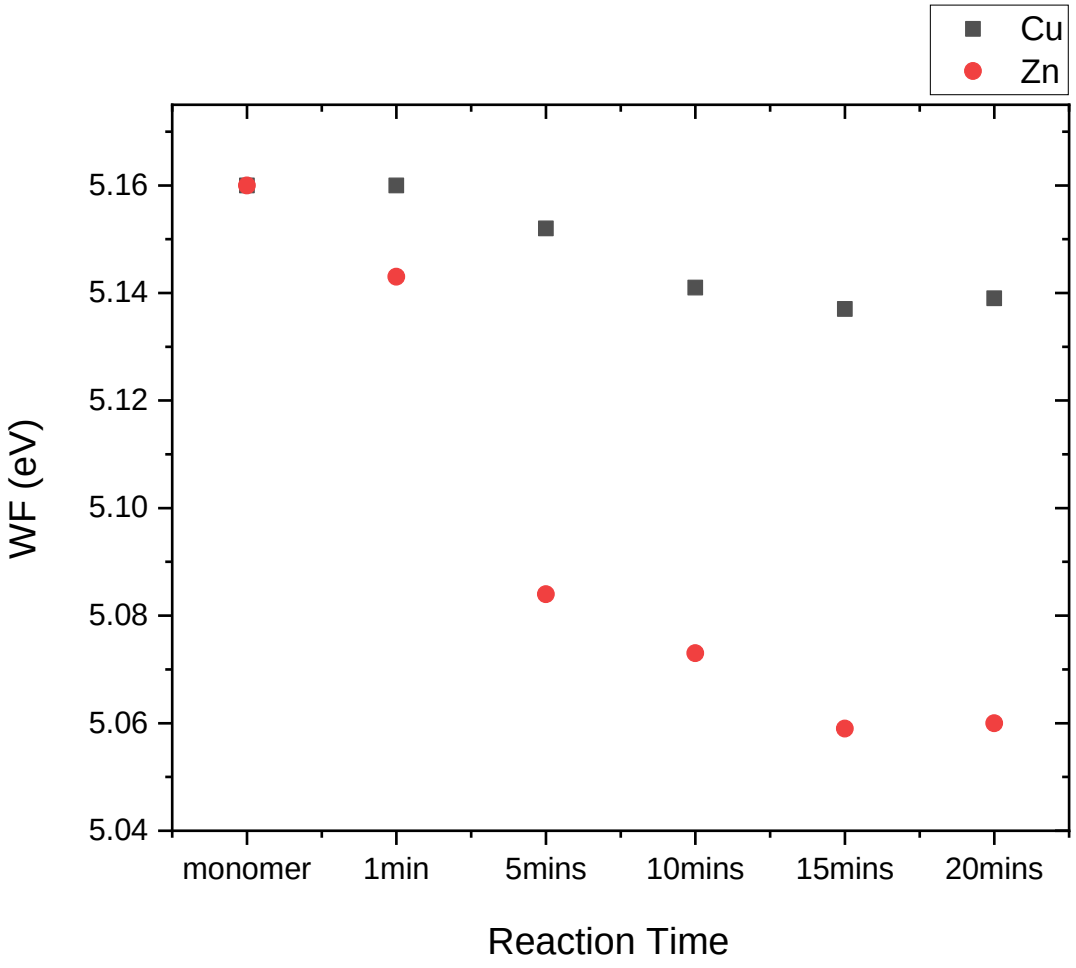


*Figure 2-12. Work function diagram in respect to the reaction time.*

It must be noted that in the case of the multicoated samples, the work function of the Cu CP is again higher than the Zn CP sample. With additional coatings the work function values in both cases relatively decrease as shown in Figure 2-13. Even though the WF values clearly diminish for the first three coatings, a plateau can be observed after the third coating. This can be justified by the fact that each coating is made up of several layers that may or may not be perfectly aligned with one another.

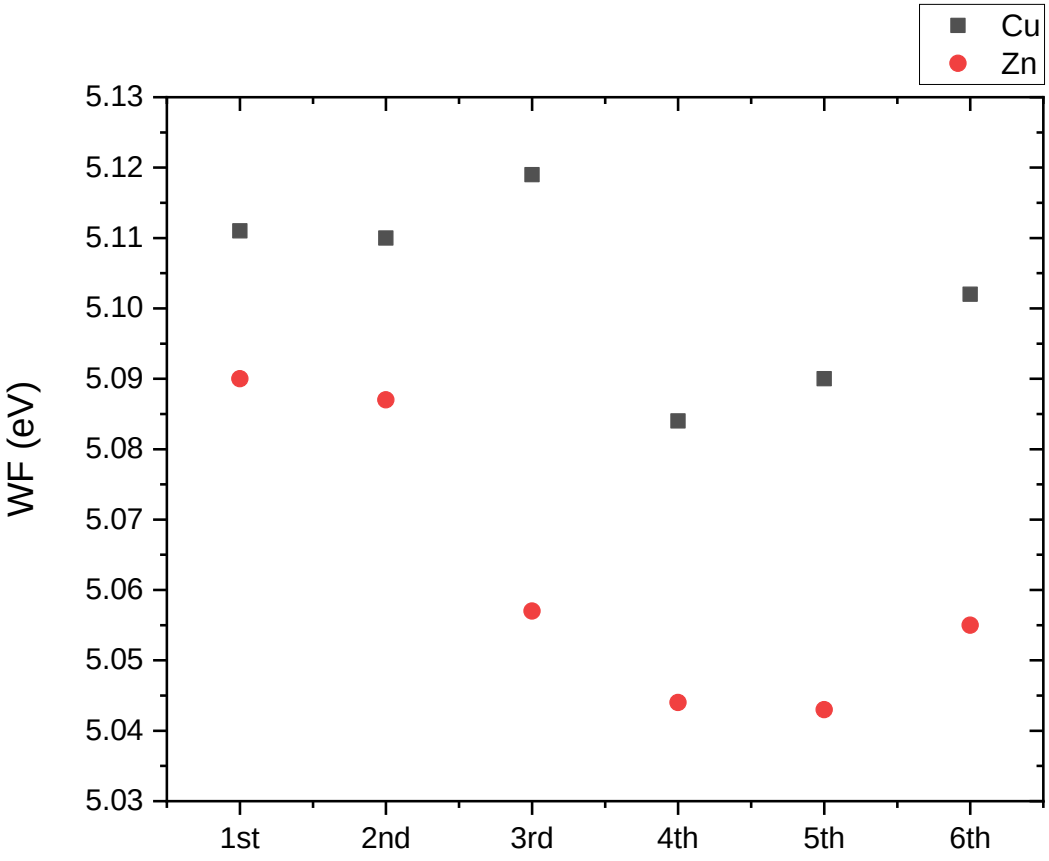


*Figure 2-13. Work function diagram in respect to thickness.*

In conclusion, we have demonstrated the possibility of tuning the work function of several CP films. Tuning can be accomplished by adjusting the reaction time of polymer formation, the metal element, or the thickness.

*2.3.3 Conductivity among the different coordination polymer films*

The conductivity of all CP films was studied via conductive AFM (Figure 2-14). Conductive AFM is a contact technique that can be utilized to study electrical properties of materials and devices in the nanoscale. The technique has been already described in Chapter 1.

Like many polyaromatic molecules, triphenilene (OHPTP) units can conduct electricity by stacking on top of each other, through interactions of their π orbitals (π-π stacking). This of course depends strongly on the orientational order of the molecules in the film, and their ability to form long stacks. The presence of metal ions and the formation of CP could, ideally, foster a more ordered alignment and stacking and thus influence the electrical resistivity.

The resistance of the single coated Cu CP film produced with different reaction times was investigated in Figure 2-14a. The resistance rises as the reaction time increases. First, we can rule out the possibility that these variations are related to varying film thicknesses because the same preparation process (same ligand deposition procedure) was used in all of the cases for the various reaction times. As previously stated, the C/Cu ratio for the one-minute reaction time CP film is close to the expected and rather ordered chemical structure (see previous XPS section). Since there is little possibility of metallic Cu-Cu bonds forming, the organic ligands primarily interact with one another through π-π* interactions, with each layer being slightly stacked on top of the other in an ordered but misaligned manner. Therefore, these π-π* interactions are more prominent when the reaction time is the smallest and the C/Cu ratio is closer to the ideal network of the proposed CP. As the reaction time and Cu ratio increase, these interactions may become less prevalent due to disordered layer assembly. This could be an indicator of the reason why resistance rises as reaction time increases. In case of the multicoated Cu CP sample the resistance graph follows an opposite path as illustrated in the Figure 2-14b.. S We observe that the initial coating on the gold still has a fairly high resistance, which significantly drops (almost one order of magnitude) with subsequent coatings, where the deposition might be better and more uniform than with the first coating deposited on the gold. After the fourth coating, the resistance increases once more as a result of the material's thickness becoming noticeable (Figure 2-14b). This increase in resistance may be attributed to this noticeable change in thickness, which possibly reaches a limit after which the network of the final CP becomes more disordered.

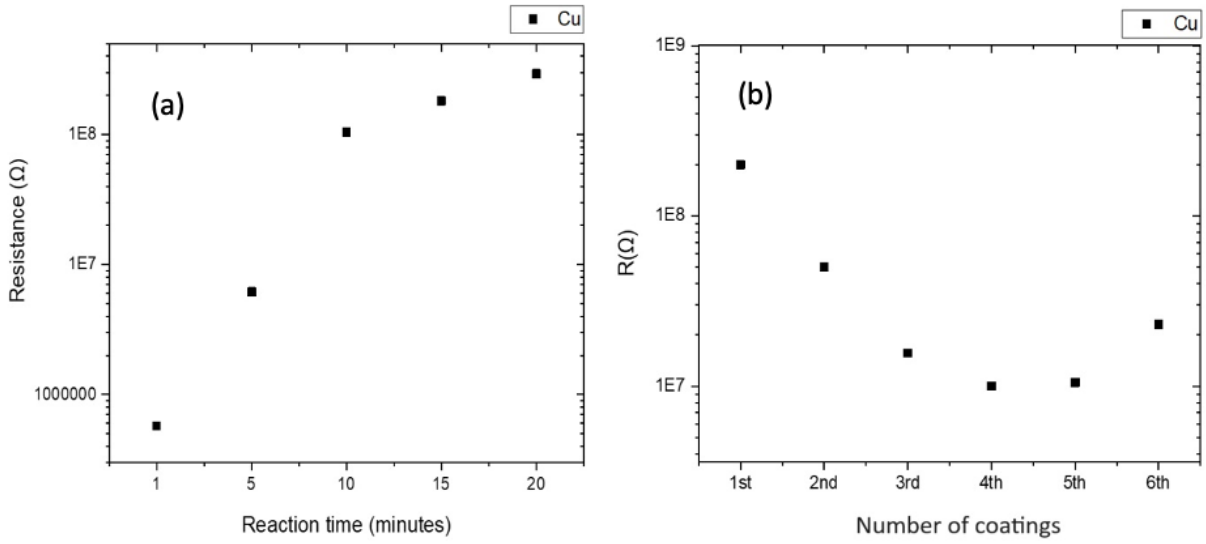


*Figure 2-14. Resistance diagram of Cu CP thin film in respect to (a) reaction time and (b) number of coatings.*

Conversely, Zn CP samples showed consistent behaviour in both single and multicoated samples; that is, no conductivity was detected above the instrument's sensitivity limit. The zero conductivity that is found can be explained by Zn's preferential tendency to form 3D structures, which causes the final structure of the film to be slightly disordered or layer misaligned as the reaction time increases or coatings are added.

### *2.3.4 Thermal stability of the different CP thin films*

Thermal stability studies were performed using a Residual Gas Analyzer (RGA) mounted inside our home built XPS (Chapter 1), ramping up to 300 °C with a heating rate of 2 °C/min. A spectrum of each standard single coated sample (1 minute formation polymer time) was recorded prior and after the heating treatment to compare possible changes in their chemical composition due to the heating.

Firstly, we have studied the single coated Cu CP film by XPS prior to any heating treatment. Figure 2-15a shows the spectra recorded. Cu 2p shows the existence of Cu (II) signal, as expected, and Cu(I) signal own to photoreduction caused by the irradiation. Zn signal is not present, as expected, but it was examined to reassure us that no contamination took place. O1s is present and the carbon spectrum can be attributed to carbonate or carboxyl acid groups. After heating up to 300$^{o}$C we can see that Cu is not present anymore(Fig. 2-15b). This may be further confirmed from the RGA data showing in Figure A9.

Following the same procedure as described above, we recorded XPS before and after heating also for the Zn CP film (Figure 2-16). Cu 2p was examined as a possible contaminant but as anticipated it was not present. Zn 2p was resent, as the main metal element in the CP film. After heating up to 300$^{o}$C. Zn 2p showed the exact same signal as prior to any heating, remaining stable throughout the heating process (Fig. 2-15d).

Consequently, Zn as the metal element seems to be more stable since it remains present before and after heating while the Cu signal disappears after the heating process.

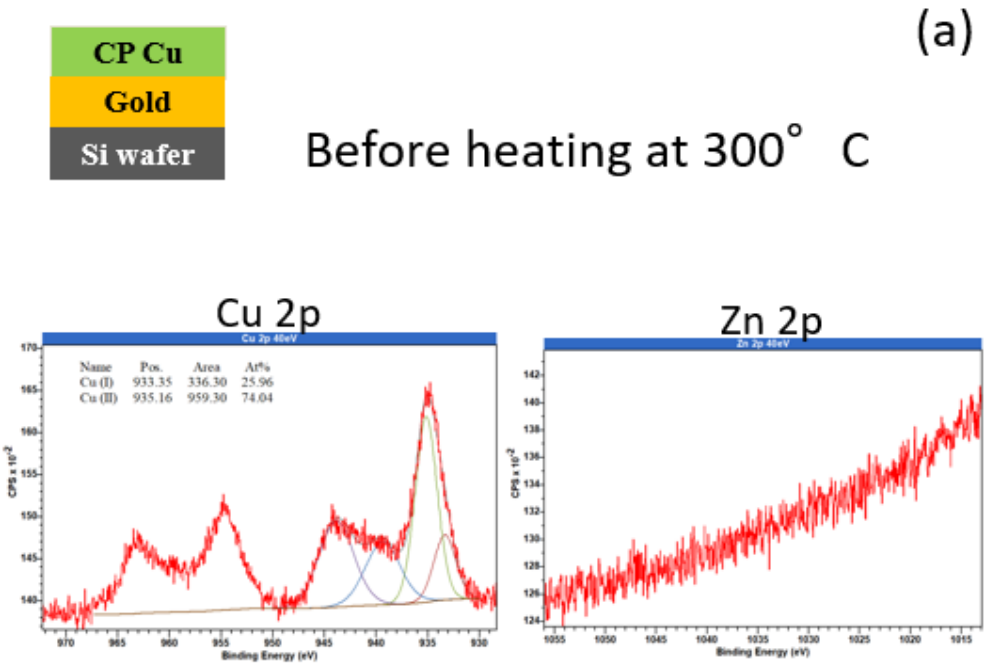

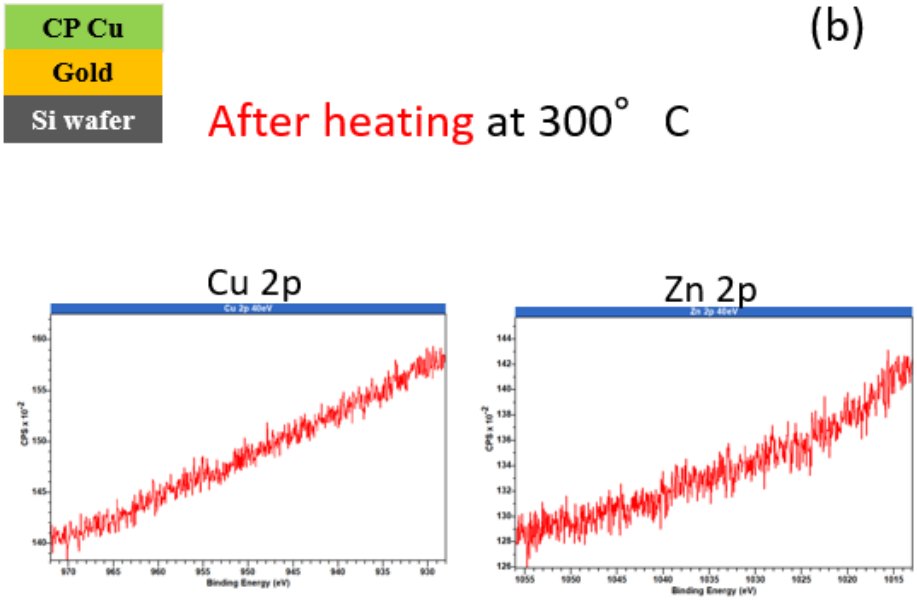


*Figure 2-15. Thermal stability of single coated Cu and Zn thin films for heating up to 300℃ in vacuum. XPS spectra for Cu single coated thin film (a) prior to any heating and (b) after heating at 300 °C.*

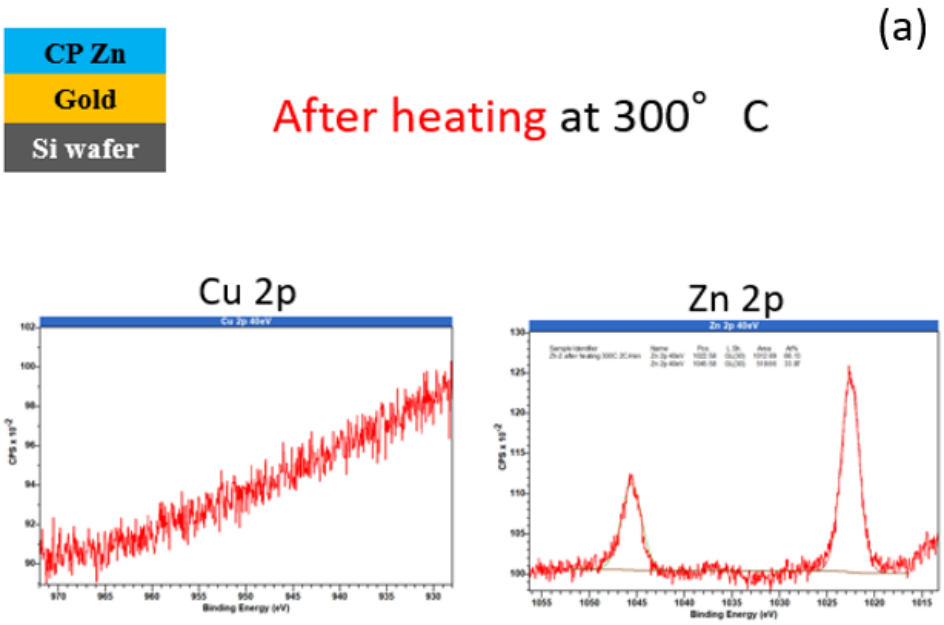

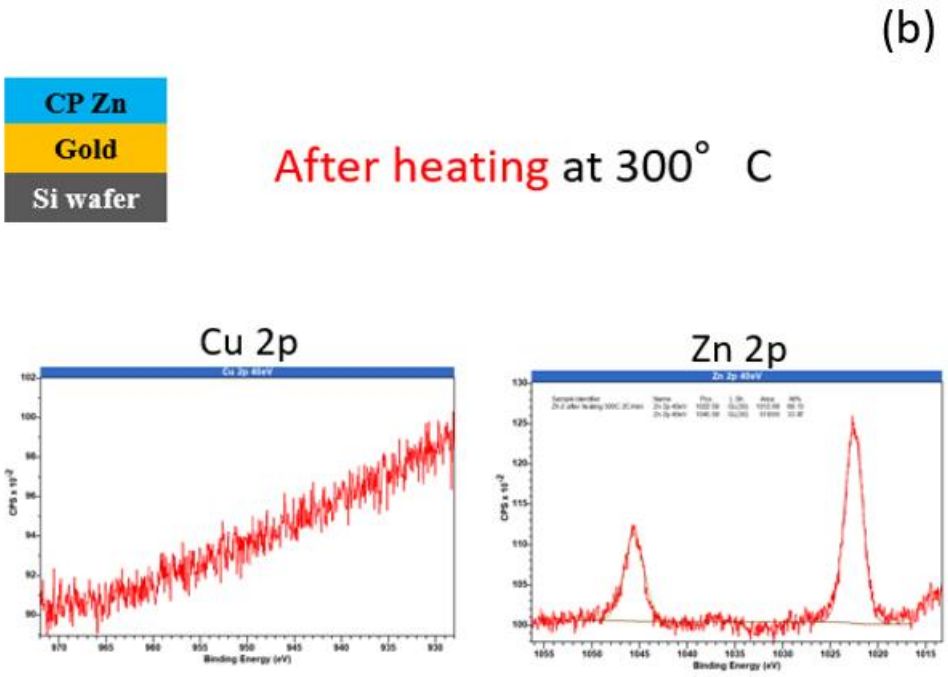


*Figure 2-16. Thermal stability of single coated Cu and Zn thin films for heating up to 300o C in vacuum. XPS spectra for Zn single coated thin film (a) prior to any heating and (b) after heating at 300 ° C.*

Both samples were also investigated via AFM and KPFM to detect any changes in their morphology or electrical properties linked to their thermal properties. Figure 2-17a-d shows the morphology of both films prior and after their heat treatment. Indeed, an increase in the roughness of their surface can be detected. The Cu CP film also exhibits obvious changes in the work function. The absence of the Cu element in the film after the treatment results in a higher work function value. As expected, the Zn CP films retains almost the same work function value since its composition doesn't change with heat treatment. This is another possible way to tune the electronic properties of the films under study.

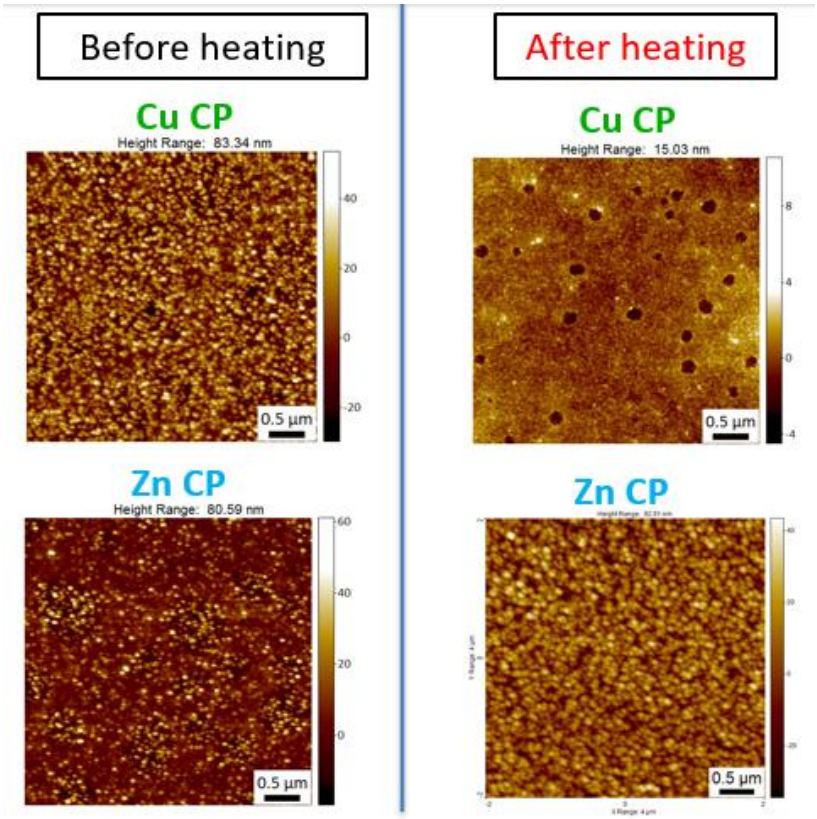


*Figure 2-17. AFM images of the CP films before and after heat treatment.*

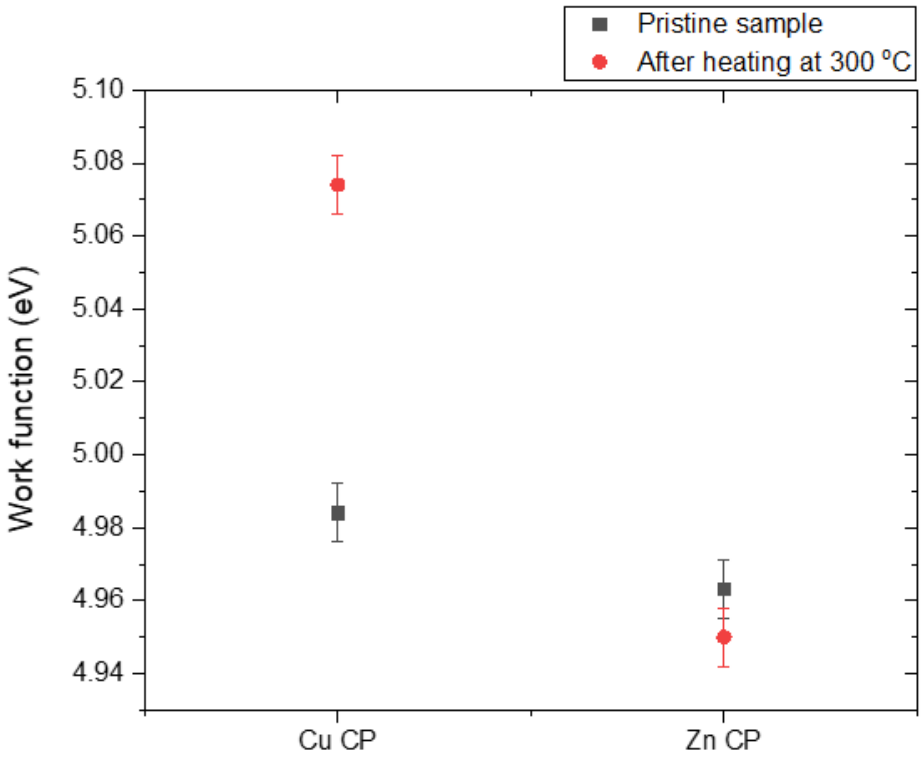


*Figure 2-18. Work function diagram for both CP films before and after heat treatment.*

## 2.4 Conclusions

We have investigated the electrical properties of various coordination polymer films produced via a versatile and innovative technique, i.e. shear coating. We investigated the possibility of tuning their work function based on the metal of the CP under study, the period for polymer formation, and the number of coatings. In every instance, Cu-based CPs demonstrated a higher work function value than Zn-based CPs, and variations in the reaction time and number of coatings also affected the work function. In contrast to Cu-based CPs, Zn-based CPs were found to be non-conductive By adjusting the reaction time or number of coatings, Cu CPs' resistance can also be tuned. Studies on thermal stability have revealed that, in comparison to Cu CPs, Zn CPs can tolerate higher temperatures. The Cu CPs changing after heat treatment can be used as a tool to tune the work function of the film, as it was found to become higher after thermal treatment. Additional coatings, different substrates, and the use of other metal elements can help us explore these CPs further and fully realize their potential in electronics and beyond.

# REFERENCES


[1] S. Kitagawa, R. Kitaura, and S. I. Noro, "Functional porous coordination polymers," *Angewandte Chemie - International Edition*, vol. 43, no. 18. pp. 2334–2375, Apr. 26, 2004. doi: 10.1002/anie.200300610.

[2] X. M. Chen, "Assembly Chemistry of Coordination Polymers," in *Modern Inorganic Synthetic Chemistry*, Elsevier, 2011, pp. 207–225. doi: 10.1016/B978-0-444-53599-3.10010-1.

[3] O. M. Yaghi, M. O'Keeffe, N. W. Ockwig, H. K. Chae, M. Eddaoudi, and J. Kim, "Reticular synthesis and the design of new materials," *Nature*, vol. 423, no. 6941, pp. 705–714, Jun. 2003, doi: 10.1038/nature01650.

[4] *Coordination Polymers*. Cambridge: Royal Society of Chemistry, 2008. doi: 10.1039/9781847558862.

[5] C. H. Li and J. L. Zuo, "Self-Healing Polymers Based on Coordination Bonds," *Advanced Materials*, vol. 32, no. 27. Wiley-VCH Verlag, Jul. 01, 2020. doi: 10.1002/adma.201903762.

[6] J.-P. Zhang, X.-C. Huang, and X.-M. Chen, "Supramolecular isomerism in coordination polymers," *Chem Soc Rev*, vol. 38, no. 8, p. 2385, 2009, doi: 10.1039/b900317g.

[7] B. Moulton and M. J. Zaworotko, "From Molecules to Crystal Engineering: Supramolecular Isomerism and Polymorphism in Network Solids," *Chem Rev*, vol. 101, no. 6, pp. 1629–1658, Jun. 2001, doi: 10.1021/cr9900432.

[8] J. V Smith, "Topochemistry of Zeolites and Related Materials. 1. Topology and Geometry," 1988. [Online]. Available: https://pubs.acs.org/sharingguidelines

[9] J. L. Spafford *et al.*, "Aluminophosphate Molecular Sieves: A New Class of Microporous Crystalline Inorganic Solids," American Chemical Society, 1982. [Online]. Available: https://pubs.acs.org/sharingguidelines

[10] B. M. Weckhuysen, R. R. Rao, J. A. Martens, and R. A. Schoonheydt, "Transition metal ions in microporous crystalline aluminophosphates: Isomorphous substitution," *European Journal of Inorganic Chemistry*, no. 4. Wiley-VCH Verlag, pp. 565–577, 1999. doi: 10.1002/(SICI)1099-0682(199904)1999:4<565::AID-EJIC565>3.0.CO;2-Y.

[11] A. K. Cheetham, G. Férey, and T. Loiseau, "Open-framework inorganic materials," *Angewandte Chemie - International Edition*, vol. 38, no. 22. Wiley-VCH Verlag, pp. 3268–3292, Nov. 15, 1999. doi: 10.1002/(sici)1521-3773(19991115)38:22<3268::aid-anie3268>3.0.co;2-u.

[12] S. Inagaki, S. Guan, T. Ohsuna, and O. Terasaki, "An ordered mesoporous organosilica hybrid material with a crystal-like wall structure," *Nature*, vol. 416, no. 6878, pp. 304–307, Mar. 2002, doi: 10.1038/416304a.

[13] C. T. Kresge, M. E. Leonowicz, W. J. Roth, J. C. Vartuli, and J. S. Beck, “Ordered mesoporous molecular sieves synthesized by a liquid-crystal template mechanism,” *Nature*, vol. 359, no. 6397, pp. 710–712, Oct. 1992, doi: 10.1038/359710a0.

[14] A. Corma, “From Microporous to Mesoporous Molecular Sieve Materials and Their Use in Catalysis,” 1997. [Online]. Available: https://pubs.acs.org/sharingguidelines

[15] J. Y. Ying, C. P. Mehnert, and M. S. Wong, “Synthesis and applications of supramolecular-templated mesoporous materials,” *Angewandte Chemie - International Edition*, vol. 38, no. 1–2. Wiley-VCH Verlag, pp. 56–77, Jan. 15, 1999. doi: 10.1002/(sici)1521-3773(19990115)38:1/2<56::aid-anie56>3.0.co;2-e.

[16] K. R. Dunbar and R. A. Heintz, “Chemistry of Transition Metal Cyanide Compounds: Modern Perspectives,” 1996, pp. 283–391. doi: 10.1002/9780470166468.ch4.

[17] H. J. Buser, D. Schwarzenbach, W. Petter, and A. Ludi, “The crystal structure of Prussian Blue: Fe4[Fe(CN)6]3.xH2O,” *Inorg Chem*, vol. 16, no. 11, pp. 2704–2710, Nov. 1977, doi: 10.1021/ic50177a008.

[18] R. E. Wilde, S. N. Ghosh, and B. J. Marshall, “Prussian blues,” *Inorg Chem*, vol. 9, no. 11, pp. 2512–2516, Nov. 1970, doi: 10.1021/ic50093a027.

[19] R. M. Barrer, “Molecular Sieves,” *Berichte der Bunsengesellschaft für physikalische Chemie*, vol. 69, no. 9–10, pp. 786–802, Dec. 1965, doi: 10.1002/bbpc.19650690908.

[20] S. Nishikiori and T. Iwamoto, “The crystal structures of ?,?-diaminoalkanecadmium(II) tetracyanonickelate(II)-aromatic molecule inclusion compounds. I. 1,4-diaminobutanecadmium(II) tetracyanonickelate(II)-2,5-xylidine (1/1): Cd(NH2(CH2)4NH2)Ni(CN)4. (CH3)2C6H3NH2,” *Journal of Inclusion Phenomena*, vol. 2, no. 1–2, pp. 341–349, 1984, doi: 10.1007/BF00663274.

[21] B. Rungtaweevoranit, C. S. Diercks, M. J. Kalmutzki, and O. M. Yaghi, “Spiers Memorial Lecture:: Progress and prospects of reticular chemistry,” *Faraday Discussions*, vol. 201. Royal Society of Chemistry, pp. 9–45, 2017. doi: 10.1039/c7fd00160f.

[22] B. F. Hoskins and R. Robson, “Design and construction of a new class of scaffolding-like materials comprising infinite polymeric frameworks of 3D-linked molecular rods. A reappraisal of the zinc cyanide and cadmium cyanide structures and the synthesis and structure of the diamond-related frameworks [N(CH3)4][CuIZnII(CN)4] and CuI[4,4’,4’’,4’’’-tetracyanotetraphenylmethane]BF4.xC6H5NO2,” *J Am Chem Soc*, vol. 112, no. 4, pp. 1546–1554, Feb. 1990, doi: 10.1021/ja00160a038.

[23] M. Fujita, Y. J. Kwon, S. Washizu, and K. Ogura, “Preparation, Clathration Ability, and Catalysis of a Two-Dimensional Square Network Material Composed of Cadmium(II) and 4,4’-Bipyridine,” *J Am Chem Soc*, vol. 116, no. 3, pp. 1151–1152, Feb. 1994, doi: 10.1021/ja00082a055.

[24] O. M. Yaghi, G. Li, and H. Li, “Selective binding and removal of guests in a microporous metal–organic framework,” *Nature*, vol. 378, no. 6558, pp. 703–706, Dec. 1995, doi: 10.1038/378703a0.

[25] D. Venkataraman, G. B. Gardner, S. Lee, and J. S. Moore, “Zeolite-like Behavior of a Coordination Network,” *J Am Chem Soc*, vol. 117, no. 46, pp. 11600–11601, Nov. 1995, doi: 10.1021/ja00151a034.

[26] M. Kondo, T. Yoshitomi, K. Seki, H. Matsuzaka, and S. Kitagawa, “Dreidimensionale Gerüststrukturen mit kanalförmigen Hohlräumen für kleine Moleküle: {[$M_2$ (4,4′-bpy) $_3$ ($NO_3$ ) $_4$ ]· *x* $H_2O$} $_n$ (M = Co, Ni, Zn),” *Angewandte Chemie*, vol. 109, no. 16, pp. 1844–1846, Aug. 1997, doi: 10.1002/ange.19971091633.

[27] L. Sporrer *et al.*, “Near IR Bandgap Semiconducting 2D Conjugated Metal-Organic Framework with Rhombic Lattice and High Mobility,” *Angewandte Chemie - International Edition*, vol. 62, no. 25, Jun. 2023, doi: 10.1002/anie.202300186.

[28] I. Hoeger, O. J. Rojas, K. Efimenko, O. D. Velev, and S. S. Kelley, “Ultrathin film coatings of aligned cellulose nanocrystals from a convective-shear assembly system and their surface mechanical properties,” *Soft Matter*, vol. 7, no. 5, pp. 1957–1967, Mar. 2011, doi: 10.1039/c0sm01113d.

[29] C. Teixeira Da Rocha *et al.*, “Mitigating Meniscus Instabilities in Solution-Sheared Polymer Films for Organic Field-Effect Transistors,” *ACS Appl Mater Interfaces*, vol. 11, no. 33, pp. 30079–30088, Aug. 2019, doi: 10.1021/acsami.9b07832.

[30] Y. Diao *et al.*, “Understanding Polymorphism in Organic Semiconductor Thin Films through Nanoconfinement,” *J Am Chem Soc*, vol. 136, no. 49, pp. 17046–17057, Dec. 2014, doi: 10.1021/ja507179d.

[31] J. C. Lee, J. O. Kim, H. J. Lee, B. Shin, and S. Park, “Meniscus-Guided Control of Supersaturation for the Crystallization of High Quality Metal Organic Framework Thin Films,” *Chemistry of Materials*, vol. 31, no. 18, pp. 7377–7385, Sep. 2019, doi: 10.1021/acs.chemmater.9b01996.

[32] O. R. Juárez-Rivera, R. A. Mauricio-Sánchez, K. Järrendahl, H. Arwin, and A. Mendoza-Galván, “Shear-coated linear birefringent and chiral cellulose nanocrystal films prepared from non-sonicated suspensions with different storage time,” *Nanomaterials*, vol. 11, no. 9, Sep. 2021, doi: 10.3390/nano11092239.

[33] K. Haase, J. Zessin, K. Zoumboulis, M. Müller, M. Hambsch, and S. C. B. Mannsfeld, “Solution Shearing of a High-Capacitance Polymer Dielectric for Low-Voltage Organic Transistors,” *Adv Electron Mater*, vol. 5, no. 6, Jun. 2019, doi: 10.1002/aelm.201900067.

[34] K. Ditte *et al.*, “Charge carrier mobility improvement in diketopyrrolopyrrole block-copolymers by shear coating,” *Polymers (Basel)*, vol. 13, no. 9, May 2021, doi: 10.3390/polym13091435.

[35] P. Dacha *et al.*, “Tailoring the Morphology of a Diketopyrrolopyrrole-based Polymer as Films or Wires for High-Performance OFETs using Solution Shearing,” *Small Methods*, Nov. 2023, doi: 10.1002/smtd.202300842.

[36] D. Khim *et al.*, “Uniaxial Alignment of Conjugated Polymer Films for High-Performance Organic Field-Effect Transistors,” *Advanced Materials*, vol. 30, no. 20, May 2018, doi: 10.1002/adma.201705463.

[37] https://cfaed.tu-dresden.de/od-research, (Accessed 13 October 2023)

[38] L. Sporrer *et al.*, “Near IR Bandgap Semiconducting 2D Conjugated Metal-Organic Framework with Rhombic Lattice and High Mobility,” *Angewandte Chemie - International Edition*, vol. 62, no. 25, Jun. 2023, doi: 10.1002/anie.202300186.

[39] X. Song *et al.*, “2D Semiconducting Metal–Organic Framework Thin Films for Organic Spin Valves,” *Angewandte Chemie*, vol. 132, no. 3, pp. 1134–1139, Jan. 2020, doi: 10.1002/ange.201911543.

[40] S. Kalinin and A. Gruverman, Eds., *Scanning Probe Microscopy*. New York, NY: Springer New York, 2007. doi: 10.1007/978-0-387-28668-6.

# CHAPTER 3

# Morphological and electrical characterization of 2-dimensional polyaniline films self-assembled on water

**The present chapter discusses the electrical properties of 2D Polyaniline synthesized by a novel technique.**

In the following chapter, we describe the production and characterization of a large area two-dimensional polyaniline film (2D PANI) synthesized by a novel, versatile and easy to implement technique. In particular, we investigated the morphological and electrical characteristics of this two-dimensional material.

*The work presented in the current chapter was a collaboration between our group and Prof. Xinliang Feng's group as part of the Marie-Curie ITN project ULTIMATE. The materials under study were prepared in a laboratory at the University of Dresden, while the morphological and electrical majority film characterization was carried out in our ISOF/CNR laboratory and our group in Bologna.*

## 3.1 Introduction

The discovery of linear conducting polymers composed of organic monomers[1] has sparked interest in their prospective applications, including chemical (bio)sensors, optical displays [2], solar cells [3], organic light-emitting diodes [4], transistors [5], and supercapacitors [6]. The performance of devices is known to be negatively impacted by structural disorder, which prevents effective charge transport in conducting polymer films [7], [8]. Aligning the linear conducting polymer chains into quasi-two-dimensional (q2D) crystalline films is one viable method for achieving long-range and efficient charge transport [9], [10]. The q2D film, which is made up of intricately ordered supramolecular assemblies of molecules/polymers with completely expanded-coil configuration via interchain interactions [11], [12], [13], may offer numerous routes for interchain charge transport[9] and override any imperfections in individual polymer chains [14].

Polyaniline (PANI), the most studied member of the grand family of conductive polymers, possesses exceptional electrical, magnetic, and optical properties [15], [16], [17]. A significant amount of work has gone into creating PANI thin films. These methods include (i) top-down solution processing of PANI chains using spin coating [18], drop casting [19], and Langmuir-Blodgett technology [20], and (ii) bottom-up synthesis from monomers using air (or liquid)-liquid interfacial method [21], chemical vapor deposition [22], and self-assembled monolayer (SAM) templating [17]. However, because of the poor processability of PANIs and the intricate intermolecular interactions of aniline/oligomers, these strategies only produced partially crystalline nanofiber-, rod-, and sphere-shaped PANIs or inhomogeneous and amorphous (i.e., randomly compact-coil conformation) PANI films [19], [21]. As a result, when HCl is used as a dopant, the conductivity of the resulting PANI thin films is usually less than 1 S $cm^{-1}$ [17], [19], [21]. But compared to the undoped PANI, this reported value is still higher [23]. Furthermore, the reported PANI films' molecular structure remains unresolved.

Prior to the discovery of conducting polymers (conjugate polymers), that can have electrical and optical properties that are comparable to those of inorganic semiconductors [24]polymers were thought to be electrical insulators. It now established that the conjugated carbon chain possesses alternating single and double bonds, with the highly delocalized, polarized, and electron-dense π bonds determining its electrical and optical behaviour. Polyacetylene (PA), polyaniline (PANI), polypyrrole (PPy), polythiophene (PTH), poly(para-phenylene) (PPP), poly(phenylenevinylene) (PPV), and polyfuran (PF) are examples of typical conducting polymers (Figure 3-1). Conducting polyacetylene was studied as a result of the discovery of (SN)x sulfur nitride metal, an inorganic substance that demonstrated increased electrical conductivity when doped with bromine. This material was discovered by Alan J. Heeger and Alan G. MacDiarmid. The conductivity of polyacetylene doped with bromine is a million times higher than that of pure polyacetylene, and this research was recognized with a Nobel Prize in 2000 [1]. The number of monomer units that make up conventional polymers range from thousands to millions. A conjugated polymer chain has fewer monomer units but is still stiff and soluble in solvents. The presence of alternating single and double bonds gives it its mechanical property. Conducting polymers are primarily soluble and processable due to their attached side chains, and they possess mechanical, electrical, and optical properties due to the attached dopant ions [25]. Both partially amorphous and crystalline polymers conduct electricity. In conducting polymers, there are localized and delocalized states. The delocalization of π bonds is highly dependent on disorder, and this delocalization is crucial for the production of charge carriers such as polarons, bipolarons, solitons, and so on, which are in charge of converting an insulator into a metal [26]. In their pure state, conjugate polymers' conductivity functions as an insulator against semiconductors, and it rises with dopant

concentration. When undoped, they exhibit the mechanical properties of typical polymers combined with the electrical and optical behavior of semiconductors, behaving like an anisotropic, quasi-one-dimensional electronic structure with a moderate bandgap of 2-3 eV. Conjugated polymers change from a nonlinear excitation state to a metallic state when they are doped or photoexcited, causing the π bond to self-localize and undergo nonlinear excitation as polarons, solitons, bipolarons, etc [24].

.

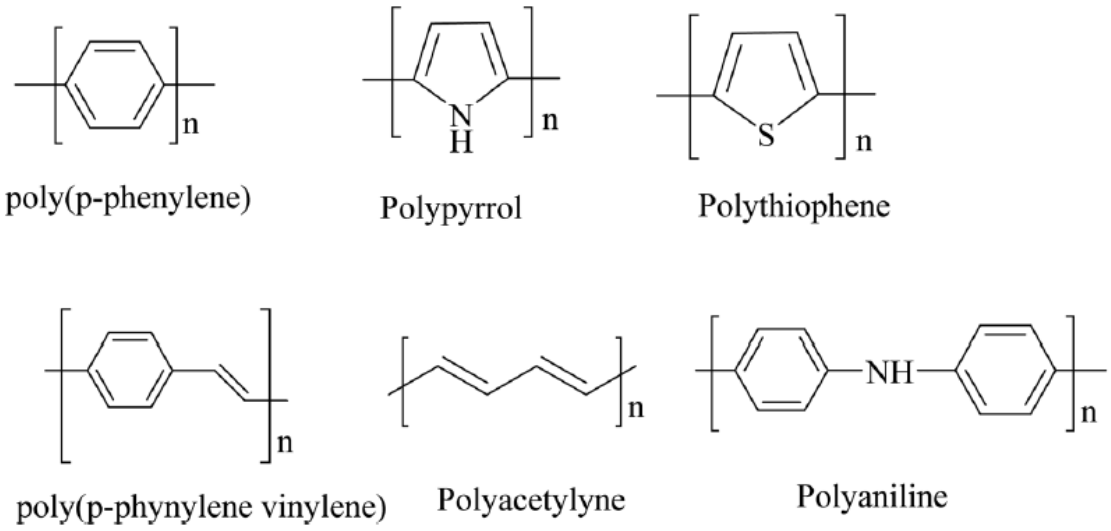


*Figure 3-1. Schematic illustration of various conducting polymers' structures. Figure taken from ref.* [24]

Polyaniline has several advantages over other conducting polymers, including ease of synthesis, low cost, great potential for molecular structure modification, and a unique proton doping mechanism. Specifically, both the oxidation and protonation states regulate its chemical and physical characteristics. Because of these unique characteristics, PANI is one of the best conducting polymers with a great potential for future technological applications[27], [28]. The aniline monomer, when dissolved in an acid-aqueous solution such as 1.0 M HCl, can be chemically oxidized by ammonium peroxy-disulfate (APS) to form a green powder with conductivity as high as 3 S $cm^{1}$. MacDiarmid and his colleagues demonstrated that this material was the emeraldine salt (ES) form of polyaniline (PANI)[29] in 1985 and won the Noble Prize for Chemistry in 2000,[30]. They proposed a molecular structure of polyaniline (PANI) as formed by alternating reduced and oxidized repeated unit chain with three states:

"leucoemeraldine" base form (LEB), "pernigraniline" form (PEN), and "emeraldine base form" (EB)[31], [32]. Based on analysis of its $^{13}C$ NMR spectra, PANI's general molecular formula and the molecular structure of its different forms were later confirmed[33]. PANI was also the first example of a conducting polymer doped with a proton, which causes the polymer to transition from the insulating EB form to the conducting ES form[31]. It is evident from Figure 3-2 that the proton doping dose does not alter the number of electrons linked to the polymer backbone and instead causes the formation of a delocalized poly-semiquinone radical cation[31], [34]. As a result, proton doping is distinct from redox doping, which includes partially adding (reduction) or removing (oxidation) electrons from the polymer backbone. It is important to consider this point when working with PANI and its nanostructures. Powders or films of PANI- are typically produced via a combination of mechanochemical, chemical, and electrochemical polymerization processes[28], [35]. Besides the aforementioned structural attributes and unique proton doping mechanism, PANI offers several benefits such as low cost, facile synthesis, elevated yield, and modifiable physical properties (such as optical, electrical, and magnetic properties) and their associated effects (such as Schottky and thermo-chromic effect and photo-emission effect)[35].

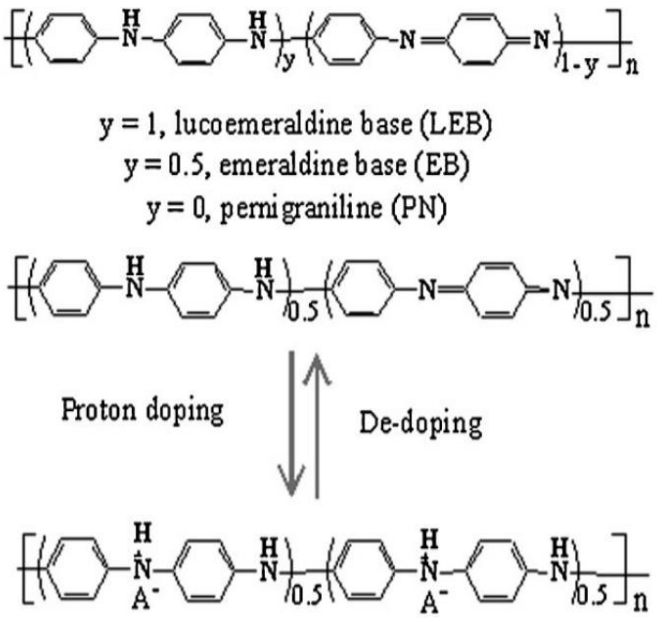


*Figure 3-2. Molecular structure of the different oxidation states of PANI and the reversible doping/dedoping process that converts the insulating EB form into the conducting ES form. Figure taken from ref.* [35]

In addition to its low cost, good conductivity, and large storage capacity, Polyaniline (PANI) has garnered a lot of interest for use as supercapacitor electrodes[36], [37], [38] It may possess better conduction and electrical properties than simple linear, non-aromatic polymers, because of the aniline benzene ring , providing an electron cloud of $\pi$ electrons above and below the molecule[39]. Additionally, PANI can be an ideal material of high-performance supercapacitors [40], combining the advantages of organic conductors with those of conventional polymer materials [30]–[32]. It has a high theoretical specific capacitance of about 2,000 F $g^{-1}$[41]. Nanostructured PANI shows increased surface-active sites as compared to bulk materials, that will greatly improve their capacitive and rate-capability qualities[42], [43], [44].

## 3.2 Novel techniques to self-assemble 2D polymeric structures

Electrically conducting polymer thin films possessing long-range molecular order and morphological homogeneity are essential for the development of high-performance organic electronics. Due to its versatile chemistry and relatively high electrical conductivity, polyaniline (PANI) is a very promising candidate among conductive polymers. The synthesis of large-area ordered PANI films is a difficult task, though, as the films' thickness and crystallinity rely on the intricate, hard-to-control interactions between the aniline oligomers in bulk. Producing 2-dimensional PANI films with large lateral size and nanometric thickness would therefore be beneficial [45].

To date, the ability to prepare 2DMs with the appropriate composition, size, thickness, crystal phase, defect, and surface property has been crucial for both the investigation of possible applications and the ongoing study of their chemical and physical properties [45]. A number of synthetic protocols for the synthesis of 2DMs have been developed, based on "top-down" and "bottom-up" approaches. The mechanical exfoliation method from corresponding bulk layered materials [46] and the chemical exfoliation of bulk layered crystals in solution with assistance from mechanical sonication [47], [48], [49] shear force [50] ion interaction,[51], [52] and exchange, [53], [54], and electrochemical methods [53], [55] are examples of the "top-down" strategies. However, mechanical exfoliation is essentially unscalable. At the same time, chemical exfoliation, although providing a potentially useful tool for producing large-

scale single-layer or few-layer 2DMs under ambient conditions, faces several limitations including low yield, low structural integrity, and poor stability of the product materials. Additionally, the sheet thickness and lateral size distribution are still widely distributed. However, these constraints can be overcome by "bottom-up" strategies like wet-chemistry synthesis and chemical vapor deposition (CVD) [45], [56], [57]. Notably, the interface has been useful in controlling the orientation of the molecules or precursors and has been a major component of most "bottom-up" synthesis techniques. In general, experiments have been conducted on the reactions that occur at the interfaces between air−water (or gas−liquid), liquid−liquid, liquid−solid, and gas−solid (or vacuum-solid). These interfaces have been found to provide an exceptional degree of control over the morphology and structure of both organic (organometallic) and inorganic (2DMs) such as 2DPs, 2DSPs, 2D MOFs, and 2D COFs. As an example, the CVD technique that depends on substrates (metal or carbon) produces an interface between the precursor vapor and the substrate for the adsorption, nucleation, arrangement, and polymerization of corresponding precursors or intermediates (e.g., carbon radicals produced from CH4 for the synthesis of graphene). In this way, the solid substrate offers a restricted two-dimensional geometry for precursor growth or polymerization. Interfacial synthesis has allowed for the controlled synthesis of single-layer or multilayer 2DMs with adjustable lateral size and thickness thus far in the last ten years [45].

The synthesis of crystalline q2D PANI films with long-range order is still a significant challenge, despite recent advancements in synthetic methodologies, such as templating by solid crystals [58], graphene [59], and surfactant bilayers [60], as well as pyrolysis of single crystal solids [61]. Among the most recent results published in the literature, it seems particularly promising the synthesis of two-dimensional PANI films by using a rather novel method known as surfactant-monolayer-assisted interfacial science (SMAIS) [17].

Some of the advantages of SMAIS include that it enables the production of films with a tunable thickness ranging from few to several tens of nanometers and large-scale size without theoretical limitation, by combining a surfactant monolayer (a soft crystalline template) and air-water interface (a confined reaction environment). Approximately 2.3 μm-sized crystalline grains can be found in the resulting q2D PANI films. PANI chains are arranged in a perfect expanded-coil conformation within each grain along the film's lateral direction. With an intrinsic lateral conductivity of $8.7 \times 10^{-3}$ S cm$^{-1}$ and a vertical conductivity of $5.0 \times 10^{-5}$ S cm$^{-1}$, the q2D PANI exhibits anisotropic charge transport characteristics [17].

## 3.3 Preparation of two-dimensional Polyaniline (2D PANI)

The q2D PANI film was produced by our collaborators at the University of Dresden by oxidative polymerization of aniline monomers at the air-water interface with the aid of a surfactant monolayer. Figure 3-3 provides a schematic illustration of the synthesis process. Surfactant monolayer (e.g., sodium oleyl sulfate) was first applied to the water's surface in a glass well (50 mL) with a diameter of Ø = 6 cm, then followed by the incorporation of aniline monomers (11.5 µL in 1 mL water) in the water subphase. Following that, a petri dish was placed over the glass well, and it was left for about 24 hours to allow the aniline monomers to diffuse and adsorb beneath the surfactant monolayer [62]. Subsequently, the subphase was treated to sequential additions of 1 M HCl (1 mL) and ammonium persulfate (APS, 10 mg in 1 mL water), which initiated the oxidative polymerization of aniline at 1 °C (Fig. 3.3 b, c). Low concentrations of monomer and oxidant (APS) were used to slow down the polymerization process, which may have been advantageous for the creation of ultra-thin PANI films with high crystallinity. On the water's surface, a consistent and uninterrupted q2D PANI film developed after about 48 hours of polymerization.

By employing the aforementioned synthetic approach, the formation of crystalline q2D PANI films is largely dependent on the air-water interface and surfactant monolayer: They serve as a confined environment (between the surfactant monolayer and the water surface) for the formation of thin films; (ii) they enable the simultaneous self-assembly and polymerization of aniline monomers into ordered polymer chains under the anionic head groups of the surfactant monolayer through hydrogen bonding and electrostatic interactions; (iii) free oligomers and polymers (in solution) that are unable to interact with the surfactant monolayer would precipitate and so do not take part in the film formation process.

A solid substrate was positioned underneath the floating film in order to transfer the q2D PANI film, and the water subphase was gradually removed until the film settled onto the substrate surface.

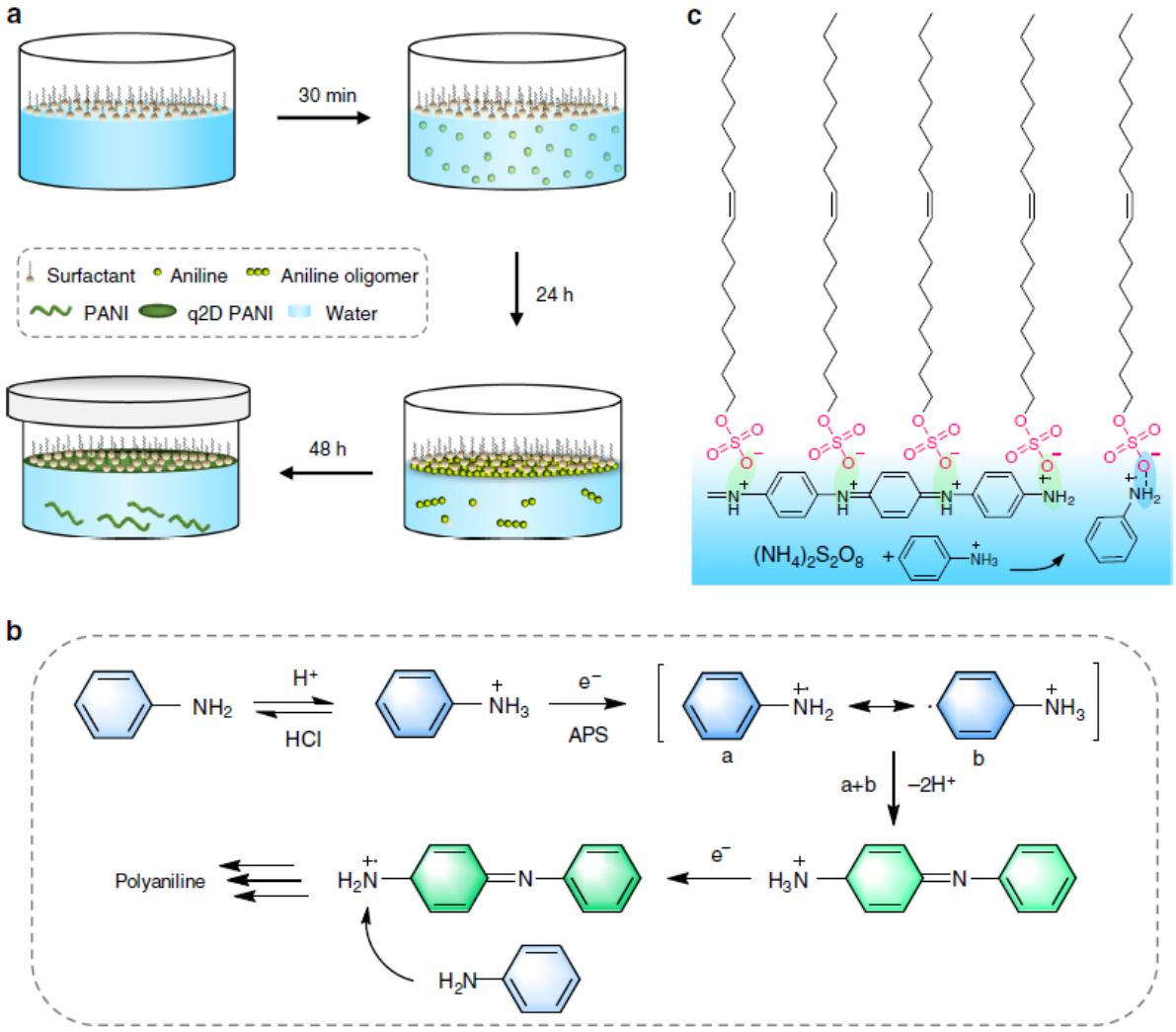


*Figure 3-3. Synthesis of q2D PANI and the reaction mechanism. (a) Schematic representation of the q2D PANI synthetic process: The process involves creating a surfactant monolayer on the water's surface, adding aniline to the water subphase and letting it stand for 24 hours to allow the monomers to diffuse into the subphase and interface, adding HCl and APS to the water subphase, and then oxidatively polymerizing the mixture for 48 hours. (b) Aniline's oxidative polymerization mechanism. (c) Illustration showing the electrostatic interaction (green ellipse) and hydrogen bonding (blue ellipse) between the sodium oleyl sulfate sulfonate group and protonated aniline/oligomer cations. Image taken from ref.* [17]

## 3.4 Results and discussion

The SMAIS method was employed to prepare 2D PANI samples [38]-[42] on two different substrates, Au and bare Si (Figure 3-4 c, d). Figure 3.2a shows a simplified model of the molecular structure and arrangement of the 2D PANI obtained in this way, while Figure 3.2b shows an optical microscope image of the 2D PANI, with a morphology more complex than the uniform layer model proposed in previous works [17], [63]. Two different regions are identifiable in the microscope image. The 2D PANI primarily forms a thinner layer, which is indicated by a lighter colour. In addition, thicker round-shaped "islands", corresponding to the darker colour areas, form on top of the thinner layer. The two distinct areas are more clearly visible using AFM (Figure 3-5). AFM reveals a significant height difference of about 100 nm between the thicker (islands) and the thinner areas of the 2D PANI. A histogram of the height of the different objects can be seen in Figure A10. The islands exhibit a lower roughness compared to the thinner layer beneath them, however we observe inside the islands the presence of small surface cracks.

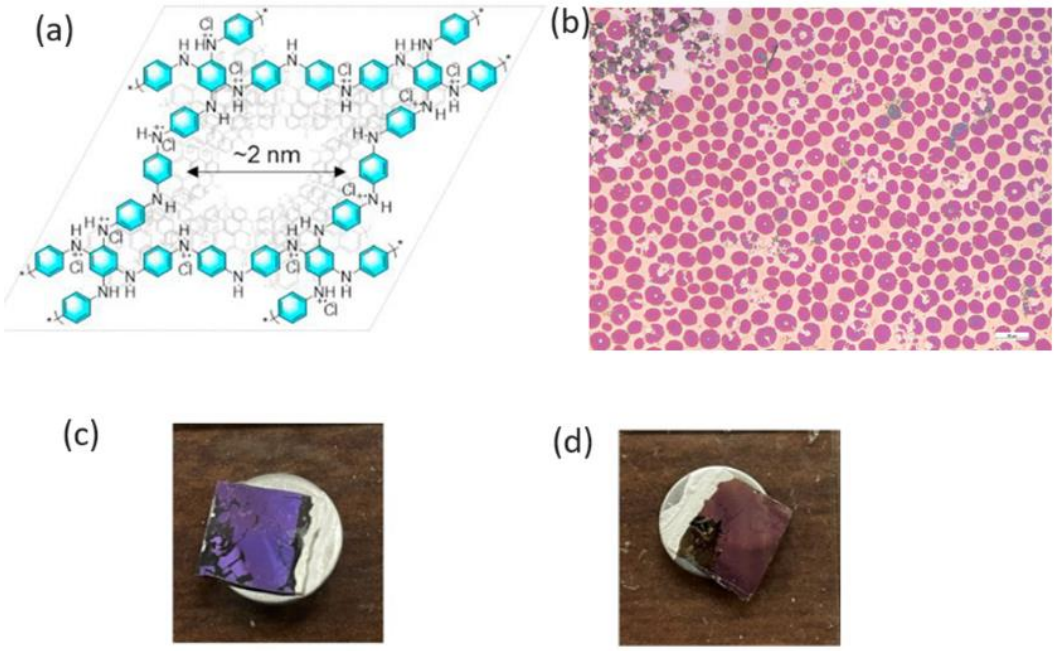


*Figure 3-4. (a) Chemical structure of 2D PANI, (b) Optical microscope image of 2D PANI sample prepared with SMAIS method. 2D PANI deposited (c) on Si substrate and (d) on Au substrate, both samples are prepared on a metallic disk for electrical measurements.*

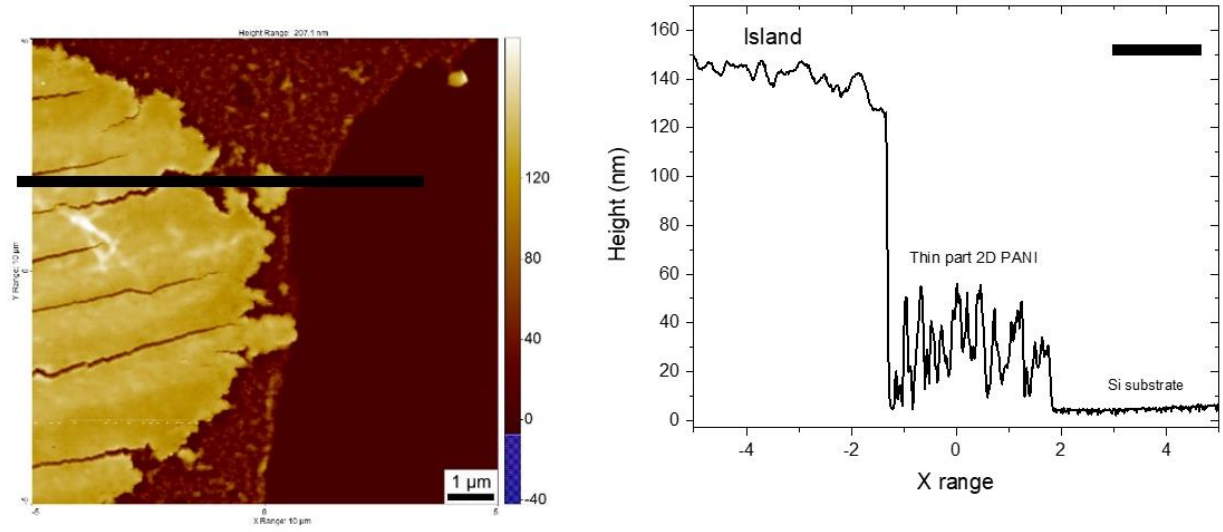


*Figure 3-5. (a)AFM image of 2D PANI, (b) Corresponding height profile across the black line shown in the AFM image.*

We additionally characterized our samples with Raman spectroscopy to further realise their structural characteristics. By comparing the Raman spectra of the two 2D PANI regions (Figure 3-6) we observe that both match the PANI Raman spectra that have been reported in the literature [64], confirming the successful formation of PANI. More specifically, we can distinguish the characteristic vidrations of C-C stretching of the paradistributed benzenoid ring, C = N stretching of the quinoid ring, C = N stretching of the quinoid ring, C–N •+ stretching in polaron form (cationic amine units of the benzenoid ring), C–N + stretching in bipolaron form (cationic imine units of the quinoid ring), C-N stretching assigned by the bands at 1620 $cm^{-1}$, 1513 $cm^{-1}$, 1485 $cm^{-1}$, 1338 $cm^{-1}$, 1312 $cm^{-1}$, and 1255 $cm^{-1}$, respectivily. Moreover the bands found at 1189 $cm^{-1}$, 1162 $cm^{-1}$, 878 $cm^{-1}$, and 832 $cm^{-1}$ can be assigned to vibrations because of C-H bending of the benzenoid ring, C-H bending of the quinoid ring, benzenoid ring deformation, and C–H bending of the quinoid ring and quinoid ring deformation [65]. However, we can observe that the peaks of the distinctive vibrations in case of the islands of PANI are more defined and sharp in respect to the thin part (a trait of crystalline materials). This may be considered an indication that the islands formed exhibit eventually a more crystalline structure in respect to the thinner part of PANI.

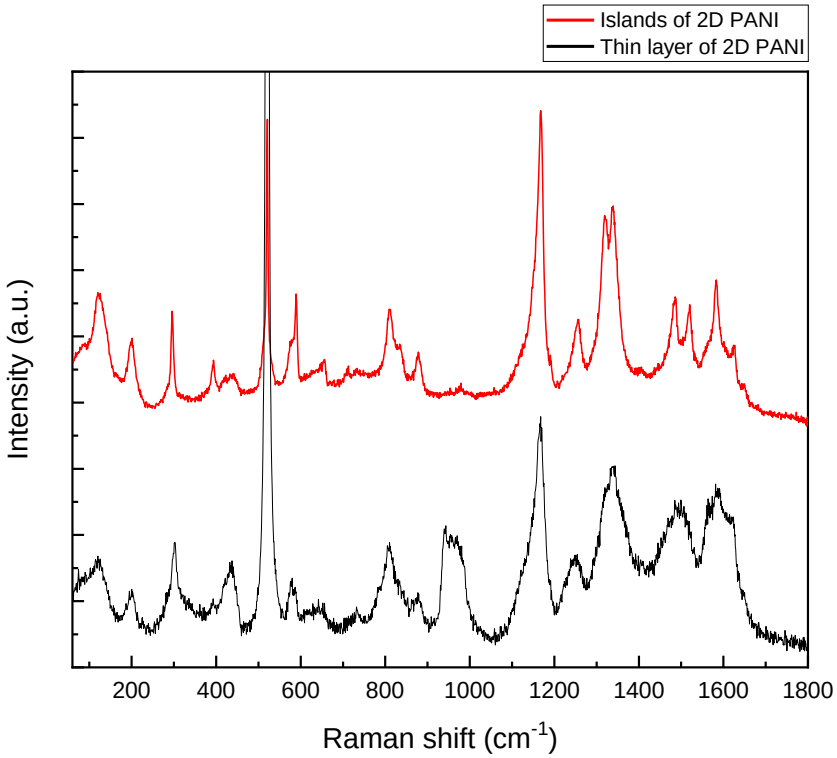


*Figure 3-6. Raman spectra of the two distinct regions of 2D PANI.*

### *3.4.1 Measurement of the Work function of 2D PANI films at the microscale.*

2D PANI is a suitable candidate for a wide range of electronic applications. We now focus on the determination of the material work function, employing Kelvin probe force microscopy (KPFM), a non-contact technique that enables nanoscale electrical measurements. Chapter 1 of the current PhD thesis provides a detailed explanation of the technique and methods of application.

Figures 3-7 and 3-8, as well as A11 and A12 show KPFM images of 2D PANI deposited on Au and Si substrates. As already mentioned, we identified two different PANI areas: a thin film-like area with a thickness of 30-40nm and thicker islands-like structures formed on top of the thinner layer, with a height of approximatively 130nm.

Figures 3-7 and 3-8 demonstrate that, on both substrates tested (Si and Au substrate) the thin layer of the 2D PANI clearly displays a lower surface potential SP than the islands.

We can use the measured SP values to calculate the work function of the material, using the formula: $SP=\phi_{tip}-\phi_{sample}$, where SP is the measured surface potential voltage that is the contact potential difference between the tip and the sample and $\phi_{tip}$ $\phi_{sample}$ are the tip and sample work function, respectively. The SP values are extracted from the corresponding histogram of the surface potential map shown in Figure 3-7b and 3-8b. This method gives a more precise value for the SP, as it is averaged over different positions in the sample.

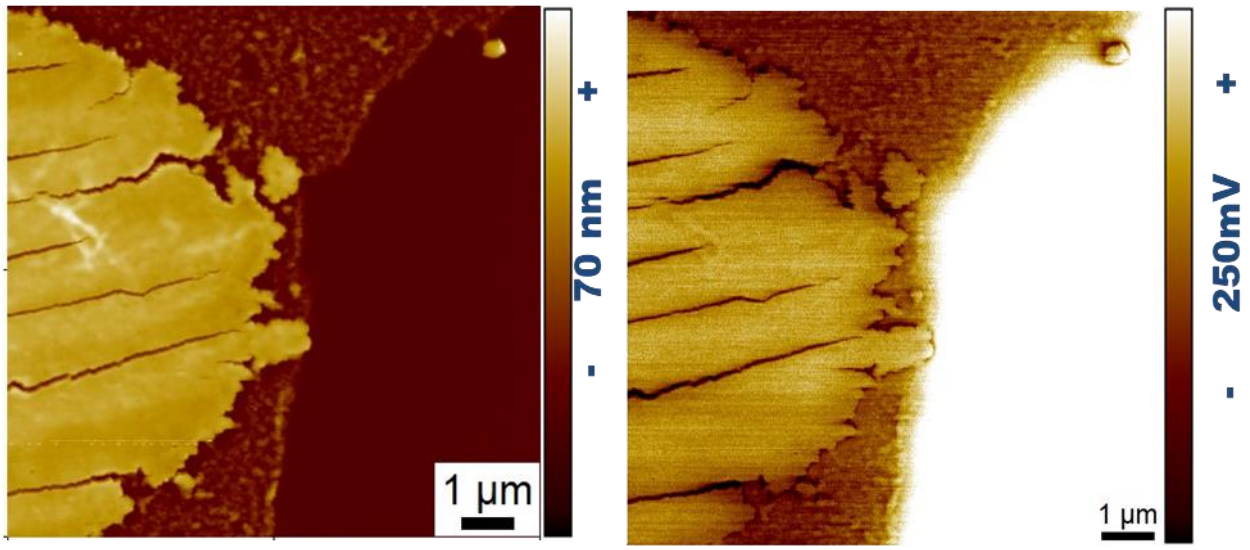


*Figure 3-7. (a) Topography of 2D PANI on Si substrate, (b) Corresponding surface potential image of 2D PANI on Si substrate.*

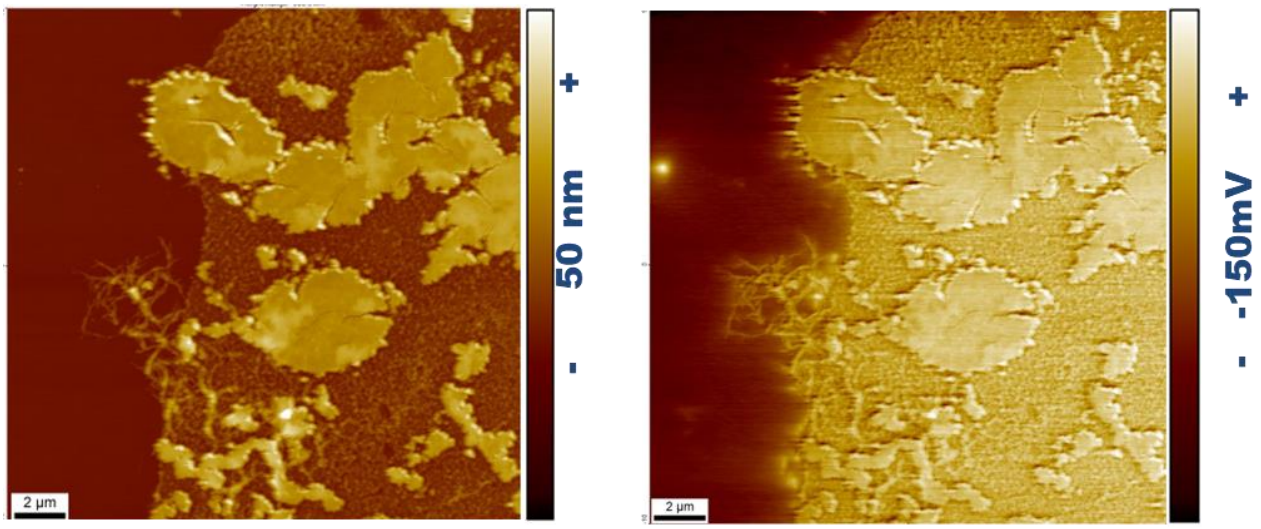


*Figure 3-8. (a) Topography of 2D PANI on Au substrate, (b) Corresponding surface potential image of 2D PANI on Au substrate.*

The resulting work function values are shown in Figure 3-9. The work function of 2D PANI is lower than the one of the substrates when it is deposited on Au, while the opposite scenario is observed when the substrate is Si. This is a consequence of the fact that the signal measured by KPFM is related to long-range forces and the measured vales are always a convolution between the actual signal from the sample and the one from the substrate, that becomes significant especially in the case of thin films. Our observation suggests that the intrinsic work function of 2D PANI likely lies in between the measured values for the two substrates. For comparison, bulk PANI work function has been reported to be in the range 4.4 - 4.8 eV [66]. Interestingly, in both cases the work function of thin PANI has always a slightly higher value than the thick islands. We ascribe this observation to the differences between the thickness of the two regions of the 2D PANI.

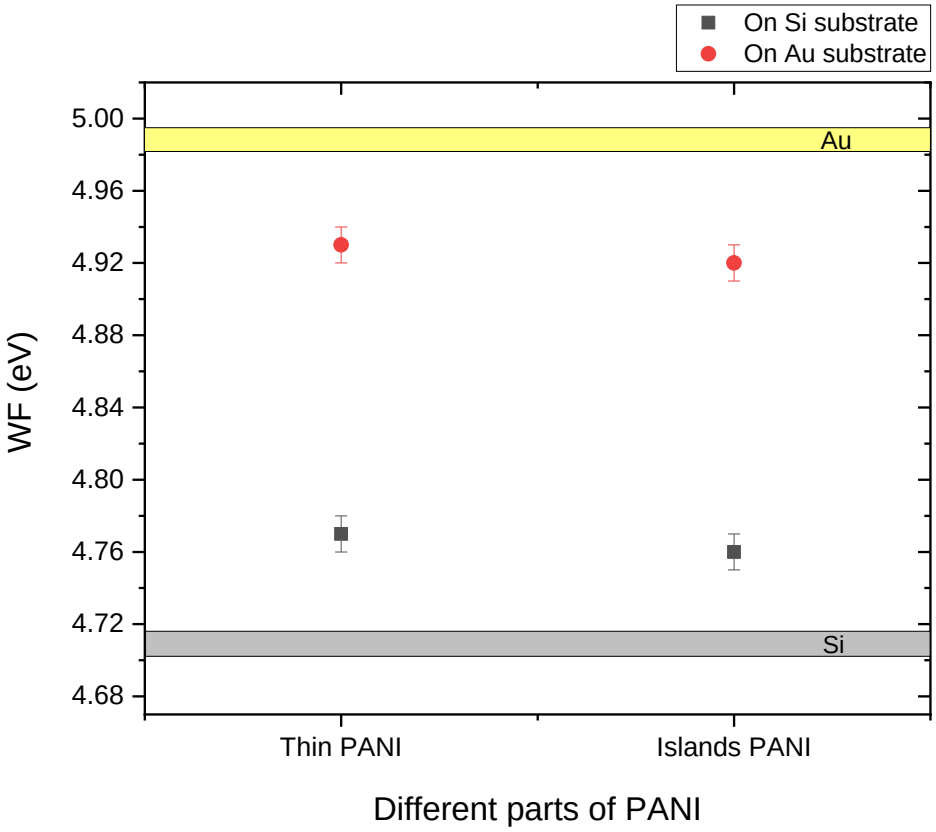


*Figure 3-9. Summary graph of each material under study and their corresponding work function value.*

Photoexcitation of PANI with light did not lead to changes of work function due to charge generation or accumulation, as demonstrated by additional KPFM measurements under illumination. (Figure A13).

### *3.4.2 Measurement of the electric conductivity of 2D PANI films at the microscale.*

The conductivity of 2D PANI was studied via conductive AFM (C-AFM) in the TUNA mode. The technique can be utilized to study electrical charges generated by the conductive tip that touches the surface of the sample and flow vertically through the material. The technique has been previously explained in Chapter 1 of the present PhD thesis.

We performed C-AFM measurements, on PANI samples on conductive Au substrates. In particular, we studied how the electrical conductivity changes for the different PANI structures (thick islands vs thin layers). Figure 3-10 shows the typical topography of one of the samples tested.

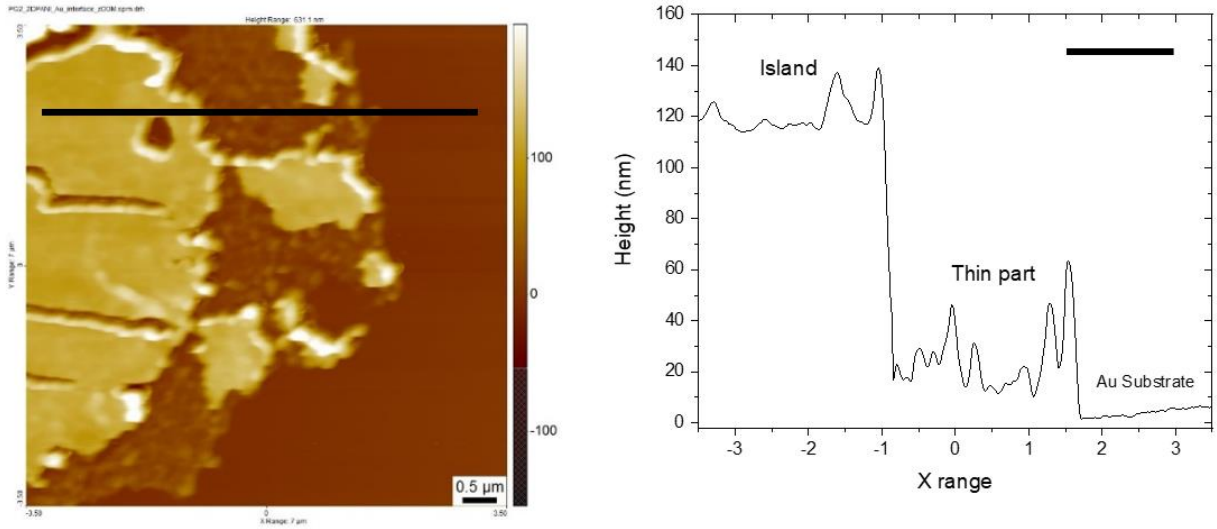


*Figure 3-10. (a) Topography of 2D PANI on Au substrate, (b) Corresponding height profile.*

Typical, a topography AFM image was taken while measuring and the corresponding current map with an applied bias of 100 mV. Figures 3-11 and A14 show examples of these measurements. It is evident from 3-11b that the 2D PANI's thin layer conducts electrical current better than the islands that form on top. This may be related to the difference in thickness of the two distinct regions. As we pass from the thin region of PANI to the thick islands formed on top, by Ohms law, we shall have a higher resistance.

Furthermore, by using C-AFM it is also possible to block the tip on a selected area and ramp tehe applied voltage to obtain I-V curves. Figure 3-12 shows an area where we performed I-V curves along a specific line of points running from the thin area of the 2D PANI to the islands and back to the thin layer. We repeated such measurements on different regions within the same sample (see figures A15-17 in appendix).

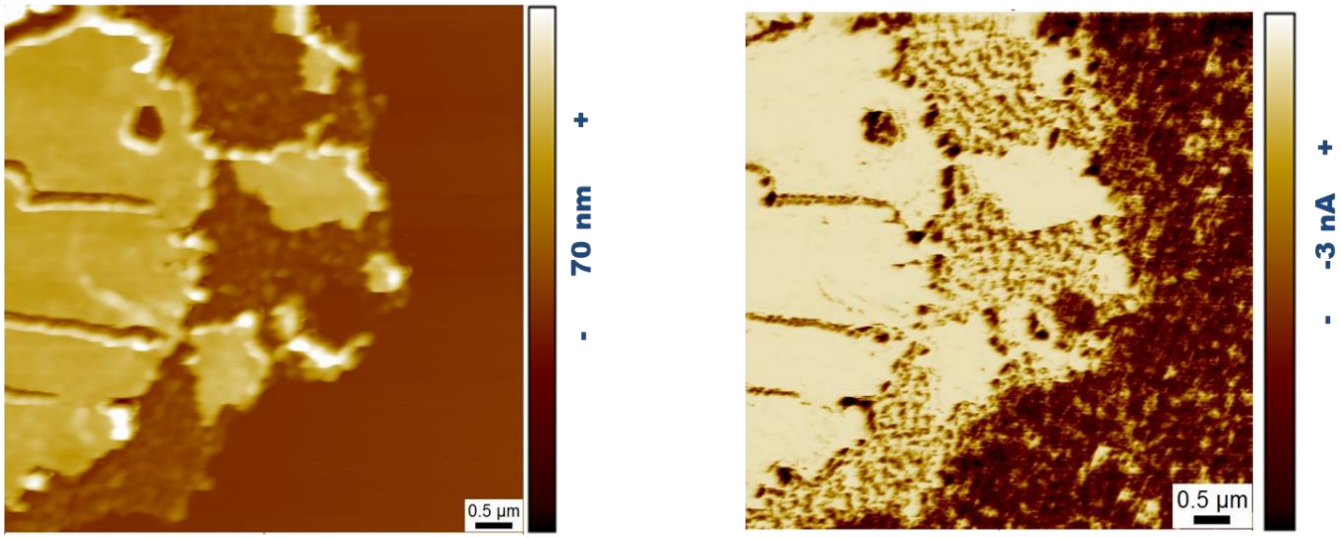


*Figure 3-11. (a) Topography of 2D PANI on Au substrate, (b) Corresponding current map of 2D PANI on Au substrate.*

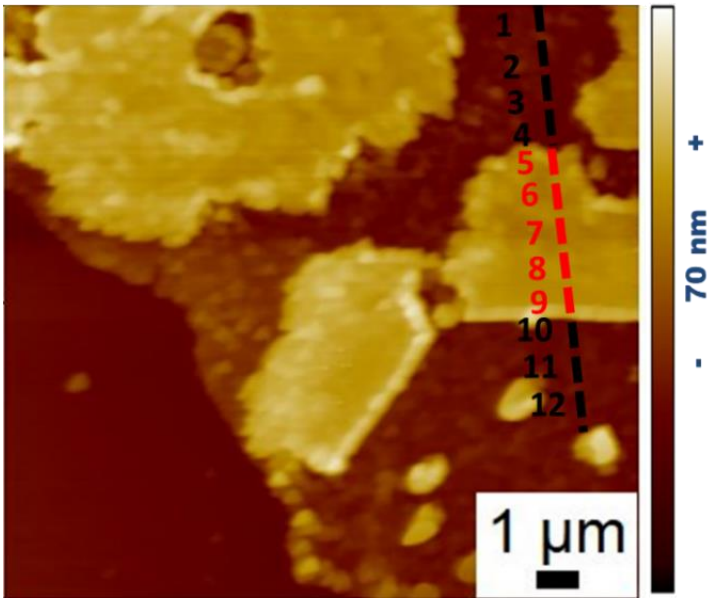


*Figure 3-12. AFM image of 2D PANI on Au substrate. Numbers are corresponding to the different points we applied voltage to extract the IV curves.*

Figure 3-13 summarizes these measurements, incorporating all the curves taken on both the thick islands and the thin layers. It is evident that the 2D PANI's thin layer conducts the electrical current significantly better than the islands. From all the measured current values, we can calculate the resistivity of the different regions of the samples. The resistivity of the thin layers is found to be $\rho=10^{-6} – 10^{-5}$ Ω while the one of the thick islands is $\rho=10^{-5} – 10^{-4}$ Ω (for reference, the value of the Au substrate is $\rho_{Au}=\sim10^{-8}$ Ω).

The observation that the less crystalline parts (thin part) of 2D PANI show a lower electrical resistance than the more crystalline islands might seem surprising. However we shall consider that in PANI, as already introduced at the beginning of this section, the charge transport is highly anisotropic, with a vertical conductivity as small as $5.0 \times 10^{-5}$ S $cm^{-1}$ that is nearly 3 orders of magnitude lower than the horizontal one. Such a low value means that, in the vertical direction (that is what is probed with conductive AFM), even perfect crystalline PANI is to be considered as an amorphous material and it is reasonable to assume that both the thick islands and the thin parts of 2D PANI have a similar intrinsic resistivity ρ. Therefore, the different electrical resistances of the thin and thick parts of q2D PANI can be simply explained by considering the second Ohm's law, that states that the resistance R of a conductor is

proportional to the product of its intrinsic resistivity times its length, i.e. R = ρ x L , where L is the conductor length. Accordingly, we observe that the thinner PANI parts show the lower resistance value.

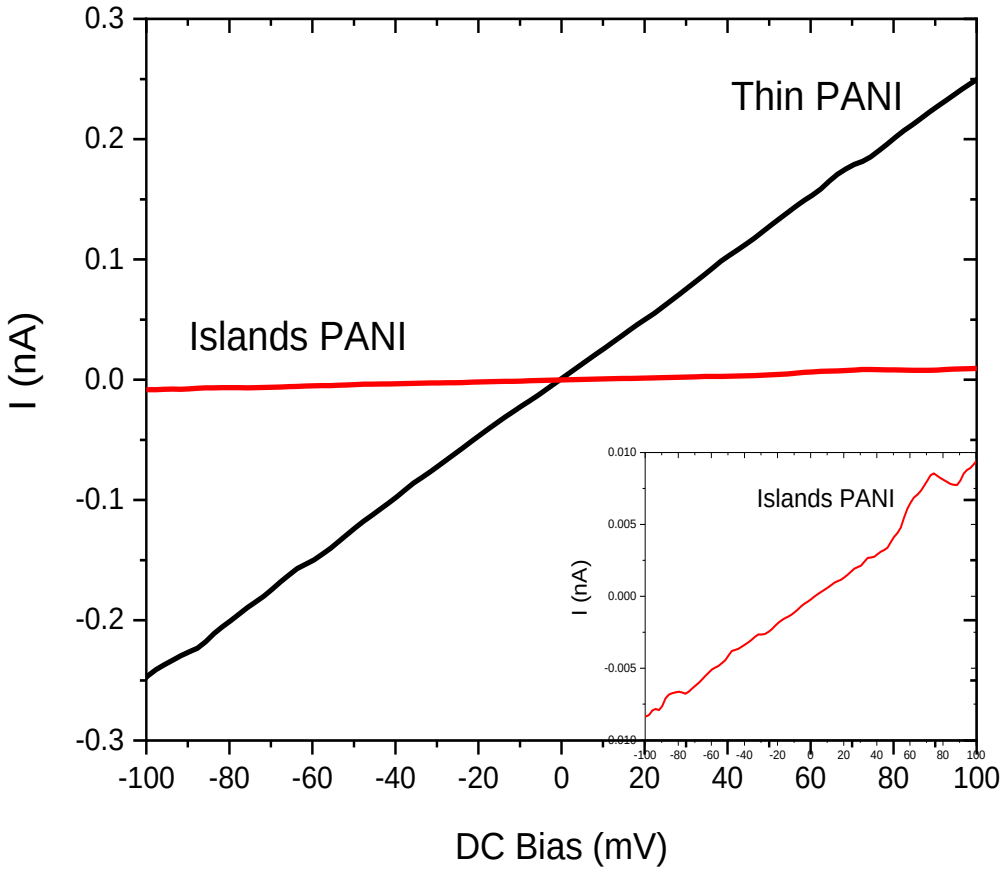


*Figure 3-13. Summary graph of all the IV curves of the corresponding points shown in Figure 3-12.*

## 3.5 Conclusions

A novel and versatile technique has been implemented to realize a two-dimensional polyaniline thin film [38]. Furthermore, we investigated the electrical properties of the 2D PANI, which appears to have two distinct regions. A semicrystalline thin layer and thicker more crystalline oval-shaped structures (islands) formed on top of the thin layer. We examined the Polyaniline that had been deposited on two distinct substrates and determined its work function value employing KPFM. Because of their differing thicknesses and structural traits, the thin layer of PANI shows a slightly higher work function than the islands in each case. Additionally, we utilized C-AFM to measure the conductivity of the two different 2D PANI regions. In fact, the conductivity of the thin layer is higher than that of the formed islands. Raman has revealed a semi-crystalline character for the thin layer in contrast to the more crystalline islands on top. The overall variation in conductivity may be connected to this difference in thickness and crystallinity. When exposed to light, the 2D PANI under investigation exhibits no changes in its electrical characteristics. We can fully explore and realize the potential of 2D PANI in electronics and other fields by using the SMAIS and other methods to realize a more uniform film.

# REFERENCES


[1] A. J. Heeger, “Semiconducting and Metallic Polymers: The Fourth Generation of Polymeric Materials (Nobel Lecture),” *Angewandte Chemie International Edition*, vol. 40, no. 14, pp. 2591–2611, Jul. 2001, doi: 10.1002/1521-3773(20010716)40:14<2591::AID-ANIE2591>3.0.CO;2-0.

[2] F. M. Kelly, L. Meunier, C. Cochrane, and V. Koncar, “Polyaniline: Application as solid state electrochromic in a flexible textile display,” *Displays*, vol. 34, no. 1, pp. 1–7, Jan. 2013, doi: 10.1016/j.displa.2012.10.001.

[3] B. H. Lee, S. H. Park, H. Back, and K. Lee, “Novel Film-Casting Method for High-Performance Flexible Polymer Electrodes,” *Adv Funct Mater*, vol. 21, no. 3, pp. 487–493, Feb. 2011, doi: 10.1002/adfm.201000589.

[4] M. S. White *et al.*, “Ultrathin, highly flexible and stretchable PLEDs,” *Nat Photonics*, vol. 7, no. 10, pp. 811–816, Oct. 2013, doi: 10.1038/nphoton.2013.188.

[5] S. Wang *et al.*, “Skin electronics from scalable fabrication of an intrinsically stretchable transistor array,” *Nature*, vol. 555, no. 7694, pp. 83–88, Mar. 2018, doi: 10.1038/nature25494.

[6] L. Pan *et al.*, “Hierarchical nanostructured conducting polymer hydrogel with high electrochemical activity,” *Proceedings of the National Academy of Sciences*, vol. 109, no. 24, pp. 9287–9292, Jun. 2012, doi: 10.1073/pnas.1202636109.

[7] S. D. Kang and G. J. Snyder, “Charge-transport model for conducting polymers,” *Nat Mater*, vol. 16, no. 2, pp. 252–257, Feb. 2017, doi: 10.1038/nmat4784.

[8] R. Noriega *et al.*, “A general relationship between disorder, aggregation and charge transport in conjugated polymers,” *Nat Mater*, vol. 12, no. 11, pp. 1038–1044, Nov. 2013, doi: 10.1038/nmat3722.

[9] H.-J. Lee *et al.*, “Close-packed polymer crystals from two-monomer-connected precursors,” *Nat Commun*, vol. 7, no. 1, p. 12803, Sep. 2016, doi: 10.1038/ncomms12803.

[10] H.-J. Lee, S.-O. Hur, M.-K. Ahn, M. Changez, and J.-S. Lee, “In situ formation of molecular-scale ordered polyaniline films by zinc coordination,” *Nanoscale*, vol. 9, no. 19, pp. 6545–6550, 2017, doi: 10.1039/C7NR01060E.

[11] A. Dodabalapur, L. Torsi, and H. E. Katz, “Organic Transistors: Two-Dimensional Transport and Improved Electrical Characteristics,” *Science (1979)*, vol. 268, no. 5208, pp. 270–271, Apr. 1995, doi: 10.1126/science.268.5208.270.

[12] H. Sirringhaus *et al.*, “Two-dimensional charge transport in self-organized, high-mobility conjugated polymers,” *Nature*, vol. 401, no. 6754, pp. 685–688, Oct. 1999, doi: 10.1038/44359.

[13] K. Kang *et al.*, “2D coherent charge transport in highly ordered conducting polymers doped by solid state diffusion,” *Nat Mater*, vol. 15, no. 8, pp. 896–902, Aug. 2016, doi: 10.1038/nmat4634.

[14] L. W. Shacklette and R. H. Baughman, “Defect Generation and Charge Transport in Polyaniline,” *Molecular Crystals and Liquid Crystals Incorporating Nonlinear Optics*, vol. 189, no. 1, pp. 193–212, Oct. 1990, doi: 10.1080/00268949008037232.

[15] W. P. Su and A. J. Epstein, “Optical and Magnetic Signatures of Localized Excitations in Pernigraniline: Role of Neutral Solitons,” *Phys Rev Lett*, vol. 70, no. 21, pp. 3359–3359, May 1993, doi: 10.1103/PhysRevLett.70.3359.4.

[16] K. Lee, S. Cho, S. Heum Park, A. J. Heeger, C.-W. Lee, and S.-H. Lee, “Metallic transport in polyaniline,” *Nature*, vol. 441, no. 7089, pp. 65–68, May 2006, doi: 10.1038/nature04705.

[17] T. Zhang *et al.*, “Engineering crystalline quasi-two-dimensional polyaniline thin film with enhanced electrical and chemiresistive sensing performances,” *Nat Commun*, vol. 10, no. 1, Dec. 2019, doi: 10.1038/s41467-019-11921-3.

[18] D. Verma and V. Dutta, “Novel microstructure in spin coated polyaniline thin films,” *Journal of Physics: Condensed Matter*, vol. 19, no. 18, p. 186212, May 2007, doi: 10.1088/0953-8984/19/18/186212.

[19] O. P. Dimitriev, O. N. Kopylov, and A. Tracz, “Mechanisms of polyaniline film formation via solution casting: Intra-chain contraction versus inter-chain association,” *Eur Polym J*, vol. 66, pp. 119–128, May 2015, doi: 10.1016/j.eurpolymj.2015.02.011.

[20] A. Modlińska and D. Bauman, “The Langmuir-Blodgett Technique as a Tool for Homeotropic Alignment of Fluorinated Liquid Crystals Mixed with Arachidic Acid,” *Int J Mol Sci*, vol. 12, no. 8, pp. 4923–4945, Aug. 2011, doi: 10.3390/ijms12084923.

[21] N. Nuraje, K. Su, N. Yang, and H. Matsui, “Liquid/Liquid Interfacial Polymerization To Grow Single Crystalline Nanoneedles of Various Conducting Polymers,” *ACS Nano*, vol. 2, no. 3, pp. 502–506, Mar. 2008, doi: 10.1021/nn7001536.

[22] J. M. D’Arcy *et al.*, “Versatile solution for growing thin films of conducting polymers,” *Proceedings of the National Academy of Sciences*, vol. 107, no. 46, pp. 19673–19678, Nov. 2010, doi: 10.1073/pnas.1008595107.

[23] N. Kumari Jangid Asst, “Recent advancement in synthesis and properties of Polyaniline,” 2019, doi: 10.15680/IJIRSET.2019.0804019.

[24] K. Namsheer and C. S. Rout, “Conducting polymers: a comprehensive review on recent advances in synthesis, properties and applications,” *RSC Advances*, vol. 11, no. 10. Royal Society of Chemistry, pp. 5659–5697, Feb. 03, 2021. doi: 10.1039/d0ra07800j.

[25] T. A. Skotheim and J. Reynolds, Eds., *Handbook of Conducting Polymers, 2 Volume Set*. CRC Press, 2007. doi: 10.1201/b12346.

[26] T.-H. Le, Y. Kim, and H. Yoon, “Electrical and Electrochemical Properties of Conducting Polymers,” *Polymers (Basel)*, vol. 9, no. 12, p. 150, Apr. 2017, doi: 10.3390/polym9040150.

[27] M. Wan, “Some Issues Related to Polyaniline Micro-/Nanostructures,” *Macromol Rapid Commun*, vol. 30, no. 12, pp. 963–975, Jun. 2009, doi: 10.1002/marc.200800817.

[28] *Conducting Polymers with Micro or Nanometer Structure*. Berlin, Heidelberg: Springer Berlin Heidelberg, 2008. doi: 10.1007/978-3-540-69323-9.

[29] W.-S. Huang, B. D. Humphrey, and A. G. MacDiarmid, “Polyaniline, a novel conducting polymer. Morphology and chemistry of its oxidation and reduction in aqueous electrolytes,” *Journal of the Chemical Society, Faraday Transactions 1: Physical Chemistry in Condensed Phases*, vol. 82, no. 8, p. 2385, 1986, doi: 10.1039/f19868202385.

[30] “https://www.nobelprize.org/prizes/chemistry/2000/summary/”. (Accessed 20 October 2023)

[31] W.-S. Huang, B. D. Humphrey, and A. G. Macdiarmid, “Polyaniline, a Novel Conducting Polymer Morphology and Chemistry of its Oxidation and Reduction in Aqueous Electrolytes,” 1986.

[32] J.-C. Chiang and A. G. Macdiarmid, “‘POLYANILINE’: PROTONIC ACID DOPING OF THE EMERALDINE FORM TO THE METALLIC REGIME,” 1986.

[33] T. Hagiwara, M. Yamaura, and K. Iwata, “Structural analysis of deprotonated polyaniline by solid-state 13C N.M.R.,” *Synth Met*, vol. 26, no. 2, pp. 195–201, Oct. 1988, doi: 10.1016/0379-6779(88)90346-3.

[34] A. G. Macdiarmid, J. C. Chiang, A. F. Richter, and A. J. Epstein, “POLYANILINE: A NEW CONCEPT IN CONDUCTING POLYMERS,” 1987.

[35] M. Wan, “Some issues related to polyaniline micro-/nanostructures,” *Macromol Rapid Commun*, vol. 30, no. 12, pp. 963–975, Jun. 2009, doi: 10.1002/marc.200800817.

[36] S. Liu *et al.*, “Two-Dimensional Mesoscale-Ordered Conducting Polymers,” *Angewandte Chemie*, vol. 128, no. 40, pp. 12704–12709, Sep. 2016, doi: 10.1002/ange.201606988.

[37] S. Liu *et al.*, “Patterning two-dimensional free-standing surfaces with mesoporous conducting polymers,” *Nat Commun*, vol. 6, Nov. 2015, doi: 10.1038/ncomms9817.

[38] H. Tian *et al.*, “Growth of 2D Mesoporous Polyaniline with Controlled Pore Structures on Ultrathin MoS2 Nanosheets by Block Copolymer Self-Assembly in Solution,” *ACS Appl Mater Interfaces*, vol. 9, no. 50, pp. 43975–43982, Dec. 2017, doi: 10.1021/acsami.7b13666.

[39] M. Wan *et al.*, “High dielectric response of 2D-polyaniline nanoflake based epoxy nanocomposites,” *RSC Adv*, vol. 5, no. 60, pp. 48421–48425, 2015, doi: 10.1039/c5ra05660h.

[40] Y. Wang, X. Chu, Z. Zhu, D. Xiong, H. Zhang, and W. Yang, “Dynamically evolving 2D supramolecular polyaniline nanosheets for long-stability flexible supercapacitors,” *Chemical Engineering Journal*, vol. 423, Nov. 2021, doi: 10.1016/j.cej.2021.130203.

[41] H. Li, J. Wang, Q. Chu, Z. Wang, F. Zhang, and S. Wang, “Theoretical and experimental specific capacitance of polyaniline in sulfuric acid,” *J Power Sources*, vol. 190, no. 2, pp. 578–586, May 2009, doi: 10.1016/j.jpowsour.2009.01.052.

[42] X. Zheng, L. Yao, Y. Qiu, S. Wang, and K. Zhang, “Core-Sheath Porous Polyaniline Nanorods/Graphene Fiber-Shaped Supercapacitors with High Specific Capacitance and Rate Capability,” *ACS Appl Energy Mater*, vol. 2, no. 6, pp. 4335–4344, Jun. 2019, doi: 10.1021/acsaem.9b00558.

[43] X. Chu *et al.*, “An ultrathin robust polymer membrane for wearable solid-state electrochemical energy storage,” *Nano Energy*, vol. 76, Oct. 2020, doi: 10.1016/j.nanoen.2020.105179.

[44] B. Yao *et al.*, “Paper-based solid-state supercapacitors with pencil-drawing graphite/polyaniline networks hybrid electrodes,” *Nano Energy*, vol. 2, no. 6, pp. 1071–1078, Nov. 2013, doi: 10.1016/j.nanoen.2013.09.002.

[45] R. Dong, T. Zhang, and X. Feng, “Interface-Assisted Synthesis of 2D Materials: Trend and Challenges,” *Chemical Reviews*, vol. 118, no. 13. American Chemical Society, pp. 6189–6325, Jul. 11, 2018. doi: 10.1021/acs.chemrev.8b00056.

[46] K. S. Novoselov *et al.*, “Electric Field Effect in Atomically Thin Carbon Films,” *Science (1979)*, vol. 306, no. 5696, pp. 666–669, Oct. 2004, doi: 10.1126/science.1102896.

[47] V. Nicolosi, M. Chhowalla, M. G. Kanatzidis, M. S. Strano, and J. N. Coleman, “Liquid Exfoliation of Layered Materials,” *Science (1979)*, vol. 340, no. 6139, Jun. 2013, doi: 10.1126/science.1226419.

[48] J. N. Coleman *et al.*, “Two-Dimensional Nanosheets Produced by Liquid Exfoliation of Layered Materials,” *Science (1979)*, vol. 331, no. 6017, pp. 568–571, Feb. 2011, doi: 10.1126/science.1194975.

[49] Y. Hernandez *et al.*, “High-yield production of graphene by liquid-phase exfoliation of graphite,” *Nat Nanotechnol*, vol. 3, no. 9, pp. 563–568, Sep. 2008, doi: 10.1038/nnano.2008.215.

[50] K. R. Paton *et al.*, “Scalable production of large quantities of defect-free few-layer graphene by shear exfoliation in liquids,” *Nat Mater*, vol. 13, no. 6, pp. 624–630, Jun. 2014, doi: 10.1038/nmat3944.

[51] P. Joensen, R. F. Frindt, and S. R. Morrison, “Single-layer MoS2,” *Mater Res Bull*, vol. 21, no. 4, pp. 457–461, Apr. 1986, doi: 10.1016/0025-5408(86)90011-5.

[52] M. B. Dines, “Lithium intercalation via -Butyllithium of the layered transition metal dichalcogenides,” *Mater Res Bull*, vol. 10, no. 4, pp. 287–291, Apr. 1975, doi: 10.1016/0025-5408(75)90115-4.

[53] R. Ma, K. Takada, K. Fukuda, N. Iyi, Y. Bando, and T. Sasaki, “Topochemical Synthesis of Monometallic ($Co^{2+}$–$Co^{3+}$) Layered Double Hydroxide and Its Exfoliation into Positively Charged $Co(OH)_2$ Nanosheets,” *Angewandte Chemie International Edition*, vol. 47, no. 1, pp. 86–89, Jan. 2008, doi: 10.1002/anie.200703941.

[54] Z. Liu *et al.*, “Synthesis, Anion Exchange, and Delamination of Co−Al Layered Double Hydroxide: Assembly of the Exfoliated Nanosheet/Polyanion Composite Films and Magneto-

Optical Studies," *J Am Chem Soc*, vol. 128, no. 14, pp. 4872–4880, Apr. 2006, doi: 10.1021/ja0584471.

[55] S. Yang *et al.*, "Ultrafast Delamination of Graphite into High-Quality Graphene Using Alternating Currents," *Angewandte Chemie International Edition*, vol. 56, no. 23, pp. 6669–6675, Jun. 2017, doi: 10.1002/anie.201702076.

[56] K. K. Kim *et al.*, "Synthesis of Monolayer Hexagonal Boron Nitride on Cu Foil Using Chemical Vapor Deposition," *Nano Lett*, vol. 12, no. 1, pp. 161–166, Jan. 2012, doi: 10.1021/nl203249a.

[57] X. Li *et al.*, "Large-Area Synthesis of High-Quality and Uniform Graphene Films on Copper Foils," *Science (1979)*, vol. 324, no. 5932, pp. 1312–1314, Jun. 2009, doi: 10.1126/science.1171245.

[58] I. Y. Choi, J. Lee, H. Ahn, J. Lee, H. C. Choi, and M. J. Park, "High-Conductivity Two-Dimensional Polyaniline Nanosheets Developed on Ice Surfaces," *Angewandte Chemie International Edition*, vol. 54, no. 36, pp. 10497–10501, Sep. 2015, doi: 10.1002/anie.201503332.

[59] Y. Wang *et al.*, "Graphene-Assisted Solution Growth of Vertically Oriented Organic Semiconducting Single Crystals," *ACS Nano*, vol. 9, no. 10, pp. 9486–9496, Oct. 2015, doi: 10.1021/acsnano.5b03465.

[60] S. Liu *et al.*, "Two-Dimensional Mesoscale-Ordered Conducting Polymers," *Angewandte Chemie International Edition*, vol. 55, no. 40, pp. 12516–12521, Sep. 2016, doi: 10.1002/anie.201606988.

[61] J. Mahmood *et al.*, "Two-dimensional polyaniline ($C_3N$) from carbonized organic single crystals in solid state," *Proceedings of the National Academy of Sciences*, vol. 113, no. 27, pp. 7414–7419, Jul. 2016, doi: 10.1073/pnas.1605318113.

[62] F. Wang *et al.*, "Nanometre-thick single-crystalline nanosheets grown at the water–air interface," *Nat Commun*, vol. 7, no. 1, p. 10444, Jan. 2016, doi: 10.1038/ncomms10444.

[63] K. Liu *et al.*, "On-water surface synthesis of crystalline, few-layer two-dimensional polymers assisted by surfactant monolayers," *Nat Chem*, vol. 11, no. 11, pp. 994–1000, Nov. 2019, doi: 10.1038/s41557-019-0327-5.

[64] M. Kim, C. Lee, and J. Jang, "Fabrication of Highly Flexible, Scalable, and High-Performance Supercapacitors Using Polyaniline/Reduced Graphene Oxide Film with Enhanced Electrical Conductivity and Crystallinity," *Adv Funct Mater*, vol. 24, no. 17, pp. 2489–2499, May 2014, doi: 10.1002/adfm.201303282.

[65] M. Kim, C. Lee, and J. Jang, "Fabrication of highly flexible, scalable, and high-performance supercapacitors using polyaniline/reduced graphene oxide film with enhanced electrical conductivity and crystallinity," *Adv Funct Mater*, vol. 24, no. 17, pp. 2489–2499, May 2014, doi: 10.1002/adfm.201303282.

[66] O. Abdulrazzaq *et al.*, "Tuning the work function of polyaniline via camphorsulfonic acid: an X-ray photoelectron spectroscopy investigation," *RSC Adv*, vol. 5, no. 1, pp. 33–40, 2015, doi: 10.1039/C4RA11832D.

# CHAPTER 4

## Morphological and electrical characteristics of layered 2D materials.

**The present chapter discusses the morphological and electrical properties of various two-dimensional layered nano-materials.**

Two-dimensional (2D) materials like Graphene have triggered a great interest first at academic, then at industrial level, because of their promising potential applications. Particularly appealing among the novel 2D materials are the carbides and nitrides of transition metals, known as MXenes and transition and post-transition metal dichalcogenides. In the following chapter, MXenes, in their pristine form as well as chemically functionalized with different organic molecules, isolated sheets of $In_2Se_3$, electrochemically functionalised $MoS_2$ films and soot molecules are studied with atomic force microscope to understand their morphology and with Kelvin probe force microscopy (KPFM) as well as conductive AFM in order to address their electrical properties.

*The materials under study presented in the following Chapter have been synthesised by our collaborators while most of the materials' characterisation was carried out in our ISOF/CNR laboratory and our group in Bologna. The MXenes solution was synthesised by our collaborators in Chalmers University in Sweden. The solution of $In_2Se_3$ sheets have been synthesized in the University of Dresden and the group of Prof. Xinliang Feng, while the $MoS_2$ electrochemically functionalised films were prepared by our collaborators at ISMN/CNR in Bologna and University of Bicocca in Milano. Last, the soot molecules were synthesized at the university of Naples and studied with SPM methods at atomic resolution a part of whick I personally performed at IBM Research in Zurich as a part of my secondment period within the Marie-Curie ITN project ULTIMATE.*

## 4.1 General Introduction

Due to their unique electronic, mechanical and optical characteristics, 2D materials have been the subject of much research over the past ten years for a wide range of applications[1], [2], [3], [4], [5], [6]. Besides their direct use as monolayers, they can also function as building blocks which can be easily assembled into a wide range of novel materials, such as composites, membranes, and layered structures[7]. The carbides and nitrides of transition metals (also referred to as MXenes) or the transition metal dichalcogenides are particularly intriguing among these novel 2D materials. This rapidly expanding family of materials exhibits a special combination of intriguing properties and potential applications. Both MXenes and transition and post-transition metal dichalcogenides have been extensively studied and used in devices and applications due to their intriguing electrical, mechanical, and thermal properties. Unconventional graphene-like materials, especially small molecules and particles derived from soot that can be classified as nanometric, highly irregular graphene-like particles, are also very interesting. Specifically, the formation of carbonaceous nanoparticles, also known as soot particles, during the incomplete combustion of hydrocarbon fuels at high temperatures is still an ongoing subject of discussion in the combustion community and has been the focus of multiple studies [8]. Particle inception, or the transition from gas-phase polycyclic aromatic hydrocarbons (PAHs) to condensed-phase clusters or early soot, is the most frequently discussed and important point of controversy [9]. In the following section, we introduce a variety of 2D materials that we investigated using SPM methods.

## 4.2 MXenes

### 4.2.1 Introduction

Transition metal carbides, carbon nitrides, and nitrides, usually known as (MXenes)[10], [11], [12], [13], [14], [15], are among the most recent additions to the 2D world. [8]–[13]In general, their formula is $M_{n+1}X_nT_x$ (n = 1-3), where M denotes an early transition metal (such as Hf, V, Sc, Ti, Zr, Nb, Ta, Cr, Mo, and so forth), X is carbon or/and nitrogen, and $T_x$ represents the surface terminations (such as OH, O, or F). Some examples of MXenes are $Ti_2CT_x$[13], $Ti_3C_2T_x$[14], and $Nb_4C_3T_x$[16]. MXenes have a $[MX]_nM$ arrangement, where n+1 layers of M

cover n layers of X. Figure 4-1 depicts the structures of $M_2X$, $M_3X_2$, and $M_4X_3M$. The first MXene to be synthesised as $Ti_3C_2T_x$, which was reported in 2011 [14]. Since then, more than 19 different MXene combinations have been synthesized (indicated in blue in the Fig. 4-1 below), with dozens more predicted to exist [17], [18], [19]. Additionally, MXenes containing multiple M elements can be found in two states: ordered phases and solid solutions. In solid solutions two distinct transition metals are seen arranged randomly in the M layers (shown in FIG. 4-1 as green). In contrast, the ordered MXenes have a 2D carbide structure with single or double layers of one transition metal (like Ti) positioned between the layers of another transition metal (like Mo) (third row in FIG. 4-1). According to density functional theory (DFT) calculations, ordered MXenes are energetically more stable than their counterparts in solid solutions for specific combinations of transition metals, and more ordered MXenes than the ones predicted have been reported[11]. In Fig. 4-1 these ordered compositions are indicated in orange. Together with carbides, there have also been reports of 2D transition metal carbonitrides ($Ti_3CN$)[13] and nitrides (that is, $Ti_4N_3$)[20] with several predictions regarding the properties of nitrides, primarily from the $M_2N$ family [21], [22], [23], [24].

The remarkable properties of MXene include its tuneable bandgap (from insulators to metal-like conductors), thermal and electric conductivities, and high Young modulus. Significantly, MXenes' hydrophilic surfaces and high metallic conductivities set them apart from most other 2D materials, including graphene. Last but not least, (i) composition (such as changing the type of transition metals "M" and "X" elements), (ii) surface functionalization (through chemical and thermal treatments), and (iii) structure/morphology alterations can all be used to modify their properties and applications performances.

Modifications of the surface functional groups, stoichiometry, or solid solution formation can be used to modify the electronic and electric properties of MXenes, which are essential for their applications. According to experimental results, MXenes pressed discs have electric conductivities that are higher than those of carbon nanotubes and reduced graphene oxide materials. These conductivities are comparable to multi-layered graphene[25]. The more functional groups and layers there are, the higher the resistivity[13]. These factors cause simulated conductivities to generally yield higher values than the ones observed experimentally[26]. Their conductivities can also be influenced by the humidity of the surrounding environment, indicating possible uses in humidity sensing materials[27]. By modifying or eliminating functional groups and intercalated molecules, surface modification via thermal and alkaline treatments can greatly improve electrical properties, with conductivity increases of up to two orders of magnitude[28], [29], [30].

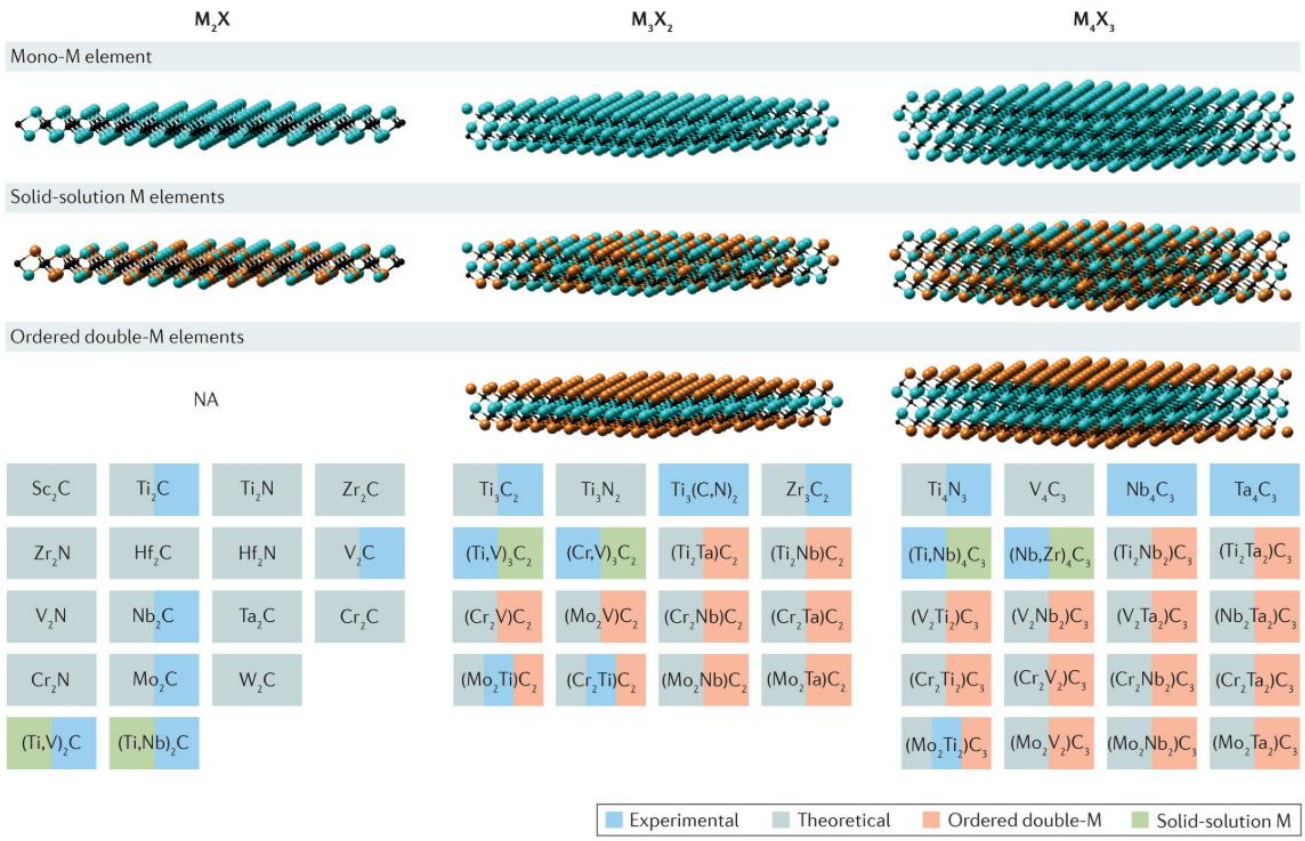


*Figure 4.1. MXenes reported in literature. Picture taken from ref.* [15]

In addition to their electrical properties, the strong M-C and M-N bonds, which underpin the mechanical properties of MXenes, have generated a great deal of interest. According to early simulations, elastic constants ($c_{11}$) were found to be at least twice as large as those found in MAX phases [31]and other 2D materials such as $MoS_2$. MXenes have higher bending stiffness than graphene, despite having $c_{11}$ values that are two to four times lower[25], [31]. This makes them viable reinforcements for composites[13]. Furthermore, compared to graphene, MXenes' interaction with polymeric matrices is improved by functional groups, especially in case of nitride MXenes. Additionally, terminations impact $c_{11}$ values and critical deformations, outperforming other promising materials in the field such as graphene and rendering them appropriate for flexible electronics[26], [32].

MXenes, as opposed to MAX phases, provide the opportunity for magnetization, which has led to in-depth research on their magnetic characteristics [33], [34], [35], [36], [37]. Magnetic moments are predicted for many pristine compounds, such as $Ti_4C_3$[37], $Ti_3CN$[38], $Fe_2C$[39], $Cr_2C$[40], $Ti_3N_2$[26], [41]. Functionalization groups, however, have the ability to change the

magnetic behaviour. For instance, $Ti_3CNT_x$ and $Ti_4C_3T_x$ lose their magnetic properties when specific functional groups are added[35], [37], but $Cr_2CT_x$ and $Cr_2NT_x$ maintain their ferromagnetic properties at room temperature also when OH and F groups are present[42], [43]. It is expected that $Mn_2NT_x$, regardless of the surface terminations, is ferromagnetic[44]. It is significant to note that due to difficulties in controlling surface chemistry and the restricted synthesis of MXene compounds, particularly pristine ones, these magnetic properties are currently only computational predictions and have not been observed experimentally [26].

Moreover, MXenes exhibit interesting thermal and optical properties. More specifically, simulation studies indicate that MXenes have higher thermal conductivities and lower thermal expansion coefficients than phosphorene and $MoS_2$ monolayers[45], [46]. Anisotropic thermal properties in the armchair and zigzag directions are exhibited by MXenes, which enable customization by manipulating the flake length[47]. The fact that $Ti_3C_2T_x$ is the only MXene compound whose thermal conductivity has been experimentally assessed highlights the necessity of evaluating other compounds. The correlation between thermal conductivity and particle size highlights the significance of managing and refining the synthesis morphology of MXenes[26].

MXenes are also promising candidates for flexible transparent electrode applications because they can possess both metallic conductivity and optical transparency in the visible spectrum[48], [49]. Their strong UV reflectivity points to potential uses as coating materials for anti-ultraviolet radiation[50]. The optical properties are influenced by functional groups, specifically those with fluorinated and hydroxyl terminations, which decrease absorption and reflectivity in the visible range and increase reflectivity in the UV region.

The versatility of MXenes is appealing to a wide range of applications. Their chemical stability, possibility of ion intercalation, and adjustable bang gaps can be exploited in catalysis and energy storage applications, such as fuel cells, hydrogen storage, and lithium-ion batteries (LIBs); moreover, the high Young modulus, good electrical conductivity, and possibility to tune the surface chemistry are particularly suited for composites [15], [25]. Promising outcomes have been obtained in a wide range of fields, including biomedical [51], [52], environmental [53], [54], flexible/wearable electronics devices [55], [56], [57], and opto-spintronics [58], [59], [60].

In a few cases, MXenes demonstrated performance comparable to or superior to that of any other material used today, such as for energy storage systems [61], [62], [63], surface-

enhanced Raman scattering substrates [64], and electromagnetic interference shielding in aerospace and electronic components [65], [66].

Here, we have analyzed the moprhology of MXenes individual sheets sunthesized by our collaboratos at the University of Chalmers. Moreover, our aim is to determine the electrical characteristics and more specifically the possibility to tune relevant parameters such as the work function through a molecular funcionalization. To this end, the work function of pristine MXenes and functionalized MXenese (FMXenes) are investigated employing ing Kelvin probe force microscopy.

### 4.2.2 Preparation of MXenes

Firstly, a MXenes solution was created by selectively etching specific atomic layers from layered precursors such as MAX phases, a standard procedure for preparing MXenes as shown in the Figure 4-2 below [15]. In addition to the pristine solution of MXenes two different solutions of functionalized MXenes were prepared. One was non-covalently functionalized with ((vinylbenzyl)trimethylammonium chloride) (VTA) molecules while the other one was covalently functionalized with Sodium 2-mercaptoethanesulfonate (MPS) molecules as shown in Figure 4-3. The preparation of MXenes solutions has been performed at Chalmers University.


*Figure 4-2. Schematic of the procedure for the preparation of MXenes ink. Figure taken from ref.* [15]

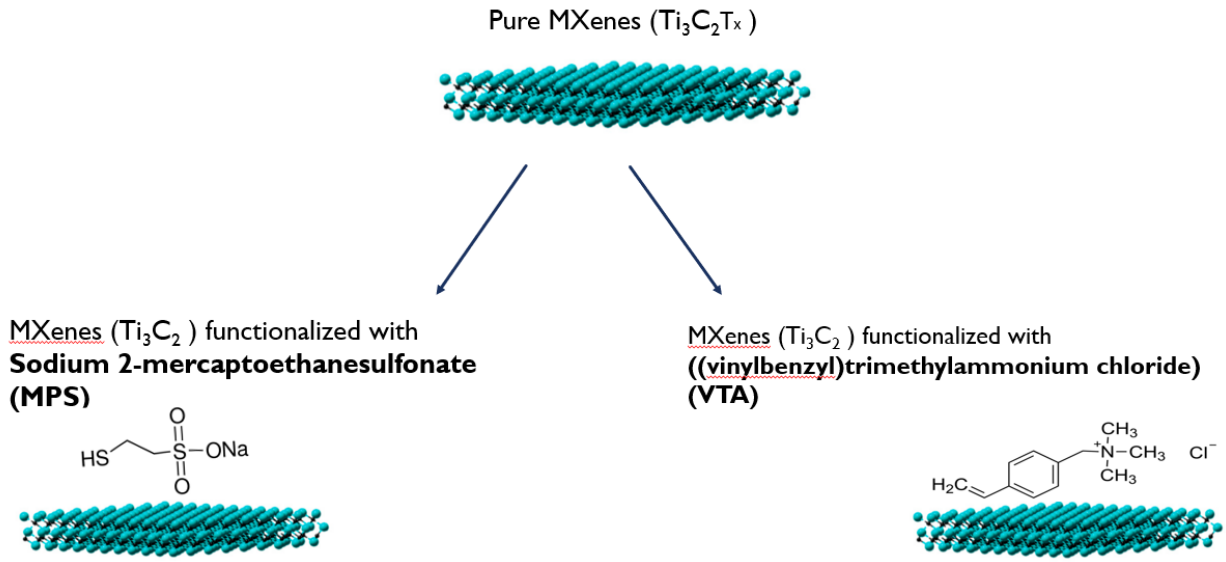


*Figure 4-3. Schematic of the different MXenes ink prepared.*

The MXene flakes were suspended in EtOH and DMSO. In order to explore the materials' chemical, morphological, and electrical properties, we deposited isolated sheets of MXenes and thin films of MXenes flakes using the spin coating method, which is a universal solution-based deposition technique.

The simplicity of the spin coating technique has made it one of the most well-known and widely used methods to form thin films on a substrate, particularly in the fields of polymer chemistry and organic electronics research and development. The mechanism operates using the conflict between centrifugal and viscous forces within a suspension of particles or polymers, which is compelled to rotate at thousands of turns per minute. Four sequential steps make up a typical spin-coating process, as shown in Figure 4-4: suspension deposition, spin-up, spin-off and evaporation[67]. The first step involves drop-casting a certain amount of suspension onto the selected substrate while it is at a resting state. There should be more liquid present than what the intended coating calls for. The substrate is centered on the rotor stage's axis of rotation and vacuum tightened to it. Care should be taken to adjust the vacuum pressure and the substrate's planarity with regard to the rotation plane. Deviance from planarity results in asymmetric forces during spinning, which negatively affects the film's uniformity. The substrate is forced to spin at a constant radial acceleration during spin-off. The liquid moves radially outward due to the centrifugal force that is created. When the substrate reaches the desired angular speed and (angular) acceleration is zero, the spin-off

phase begins. The suspension forms a homogeneous layer that becomes thinner when the surplus liquid around the edge of the substrate is removed by sweeping. The non-volatile components of the suspension, such as the particles, molecules, polymer chains, etc., aggregate and deposit on the substrate during this phase. Increased suspension viscosity and, in fact, a slowdown in both the spin-off process and the remaining liquid flow accompany the thinning of the liquid film. More material accumulates if the film's homogeneity is disrupted, which occurs at the substrate's edges. Spin-off eventually comes to an end, and evaporation takes over as the primary thinning mechanism. The substrate stops rotating as soon as the thinning is finished, and the coating is deposited. The process can be modelled most easily by assuming that the fluid solution is Newtonian, meaning that the shear stress resulting from the fluid flow is linear in the shear velocity. Key parameters influencing thickness t and surface morphology of the deposited film are solution concentration $C$, solution viscosity $\eta$, angular velocity $\omega$, as well as substrate characteristics, solvent physicochemical properties (boiling point, volatility), and solute diffusivity[68]. The film thickness $t$ increases with increasing $C$ and increasing $\eta$, but it decreases with increasing $\omega$ for a flat substrate and sufficiently high velocity ($\omega$~103 rpm). However, a small change in concentration can significantly alter the rheology of water-based suspensions[69]. Concerning the impact of solvent properties on film thickness, the more volatile the solvent, the thicker the resulting film will be for a given initial viscosity. Solvent-solute molecular interactions, as opposed to solute-solute and solvent-solvent ones, should be preferred in an efficient solvent for good film uniformity.

It is also possible to carry out pre- and post-treatment. Although they technically do not belong in the spin-coating deposition process, they might be essential to getting desired outcomes. Spin-coated polymer film thermal curing is a typical post-treatment example. Prior to the deposition, we thoroughly clean the substrates following a standard procedure. We immerse the substrates in an acetone sonication bath for 15 minutes at 60$^{o}$ C followed by another sonication bath in isopropanol again for 15 minutes at 60$^{o}$ C. Finally, we carefully dry the substrates with liquid Nitrogen. After the cleaning process we treat the substrates with air plasma. This treatment enhances the substrate's hydrophilicity and enhances the compatibility of the solution with the substrate. Improved solute-substrate interfacial interactions usually have a favourable impact on the outcome of the deposition process.

In the current work, we employed the spin-coating method to deposit Mxene flakes on the desired flat substrate, such as monocrystalline doped silicon (Si) and thermal-growth $SiO_2$ on Si.

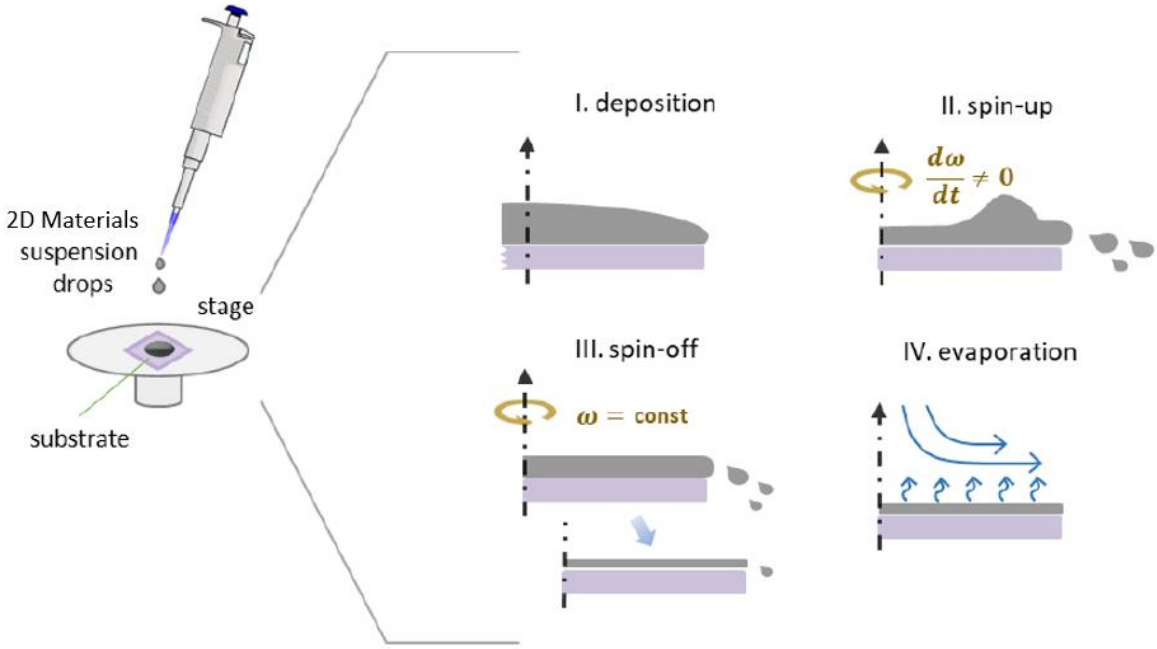


*Figure 4-4. Spin-coating deposition process. Every stage of the procedure is depicted independently. The deposited material suspension is shown in dark grey on top of a substrate (like $SiO_2$) in lavender colour.*

For every deposition, we used a Laurell Tech. Corp. WS-650Mz spin-coater. It has various supports installed in order to securely hold substrates of varying thicknesses and sizes. We used an angular velocity of 2k rpm and an angular acceleration of 0.5 rpm/min. These settings were carefully adjusted in accordance with the properties of the materials under study and the kind of equipment used in the laboratory. Although a spinning time of about one minute might be sufficient to achieve a good coating of the surface, 1.5 minutes was selected to allow the solvent to completely evaporate.

On a cleaned and plasma treated silicon substrate, MXenes suspension at a concentration of 2.5 g/L yields nearly three homogeneous layers. Instead, isolated Mxenes flakes could be deposited at higher dilutions (<0.3g/L) so that their morphology could be examined under a microscope.

### 4.2.3 Results and discussion

**Atomic force microscopy**

We employed AFM in order to define the thickness of the MXenes sheets prior to any functionalization and as well as the two functionalised type of MXenes (FMXenes). The topography of the pristine MXenes deposited on a flat Si substrate is shown in Figure 4-5 below. The sheets have a flat surface with low roughness. The AFM image's corresponding histogram shows that the thinnest pristine Mxene sheet found is 1.9nm. From the histogram analysis, we can derive important details about the thickness of the various Mxene layers (single layer, double, etc.). By collecting similar histograms from a very large number of isolated sheets measured in diverse captured AFM images, we have realized the graph in figure 4-6. The thickness of the different number of layers lays on a straight line, from the slope of which we can calculate the interlayer distance, that is found to be ~1.6 nm. Another important piece of information that can be extracted from this graph is the intercept, which corresponds to an extra 0.4 nm-thick layer of absorbed water or solvent.

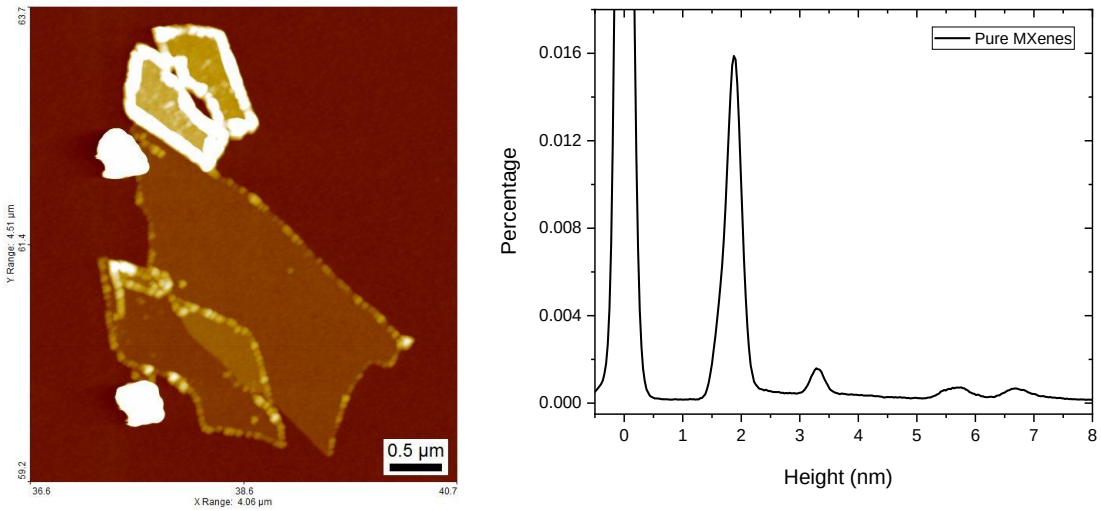


*Figure 4-5. (a) AFM image of Pristine MXenes on Si substrate, (b) Corresponding histogram of the isolated MXenes sheets shown on the left AFM image.*

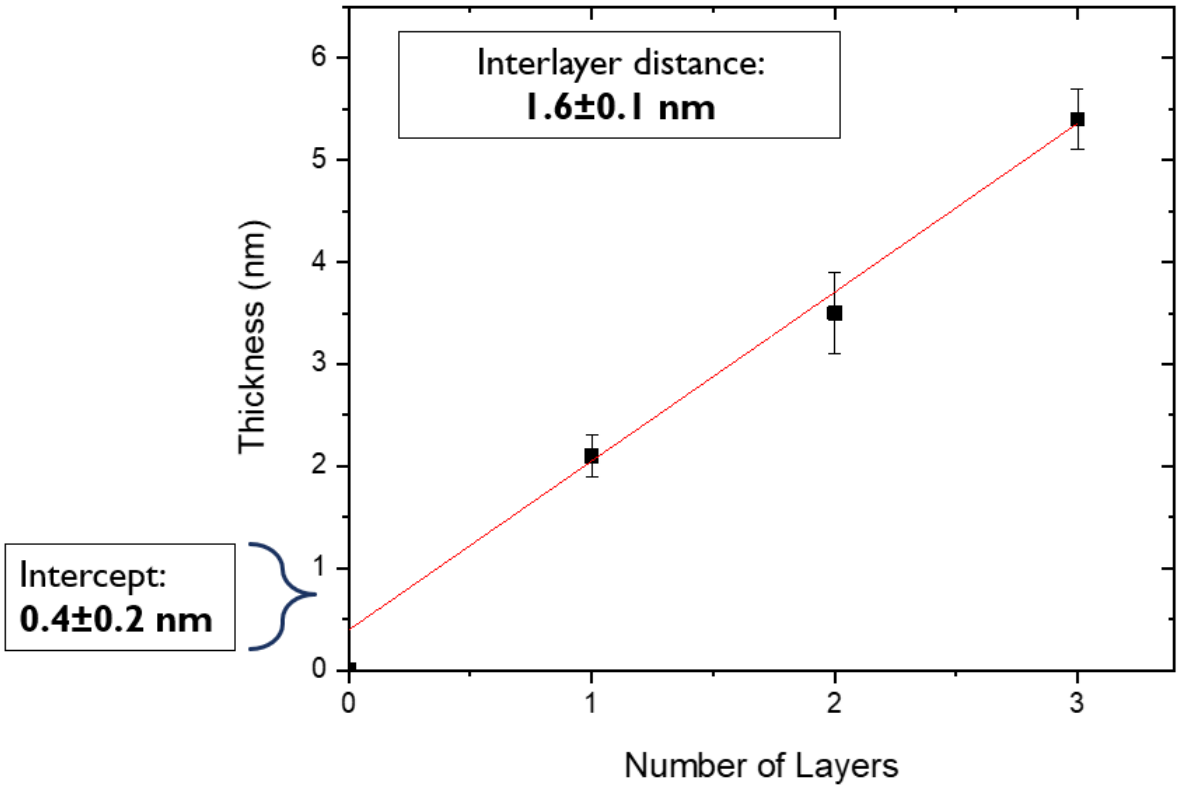


*Figure 4-6. Diagram showing the thickness of pristine isolated MXenes sheets in respect to the number of layers.*

Furthermore, we investigated the two different types of functionalized MXenes to assess their morphological properties with respect to the pristine ones. AFM topography images of functionalized MXene sheets are presented in Figure 4-7. Also in this case, the sheets seem to have a low level of roughness and a comparatively flat surface. Additionally, we determined the interlayer distance between multiple sheets that were deposited on a Si substrate for a large number of AFM images. The calculated interlayer distance for the VTA functionalization is 1.5 nm, whereas the interlayer distance for the functionalized MXenes sheets containing MPS molecules is found to be similar to that of the pristine MXenes. The interlayer distance between the pristine and functionalized sheets is summarized in the table in Figure 4-8. As is evident in every instance, a 0.4 nm extra sublayer is identified. This sublayer is thought to be caused by solvent or water molecules that have become trapped between the first layer of MXenes and the surface (substrate). We anticipate that, for future technologies and

applications on devices, it will be important to understand in detail the origin of this absorbed layer and how to eliminate it.

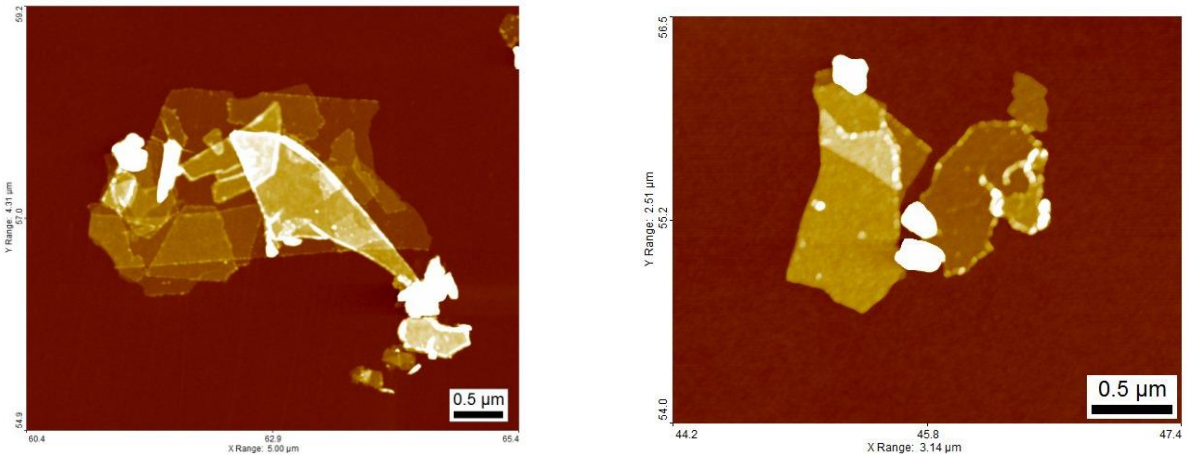


*Figure 4-7. AFM images of functionalized MXenes (a) with MPS molecules, and (b) with VTA molecules.*

| Materials | Interlayer distance(nm) | Absorbed molecules "sublayer" |
|---|---|---|
| Pure MXenes | 1.6±0.1 | 0.4±0.2 |
| FMxenes (MPS) | 1.6±0.1 | 0.4±0.1 |
| FMxenes (VTA) | 1.5±0.1 | 0.4±0.1 |

*Figure 4-8. Summary table of the different MXenes under study values of interlayer distance and sublayers measured for each material.*

**Kelvin probe force microscopy**

To determine the work function of MXenes and FMXenes and investigate the possibility of tuning MXenes' work function after functionalization, we employed Kelvin probe force microscopy. The topography of the functionalized and pristine MXenes sheets, along with the corresponding surface potential images, is displayed in Figure 4-9. As previously stated in Chapter 1 of this thesis, we measure the surface potential difference between the material and the substrate to determine the work function of a material using KPFM. The surface potential of the three types of MXenes under investigation is only slightly higher than the one of the Si substrate (Fig. 4-9 and diagram of Figure 4-10).

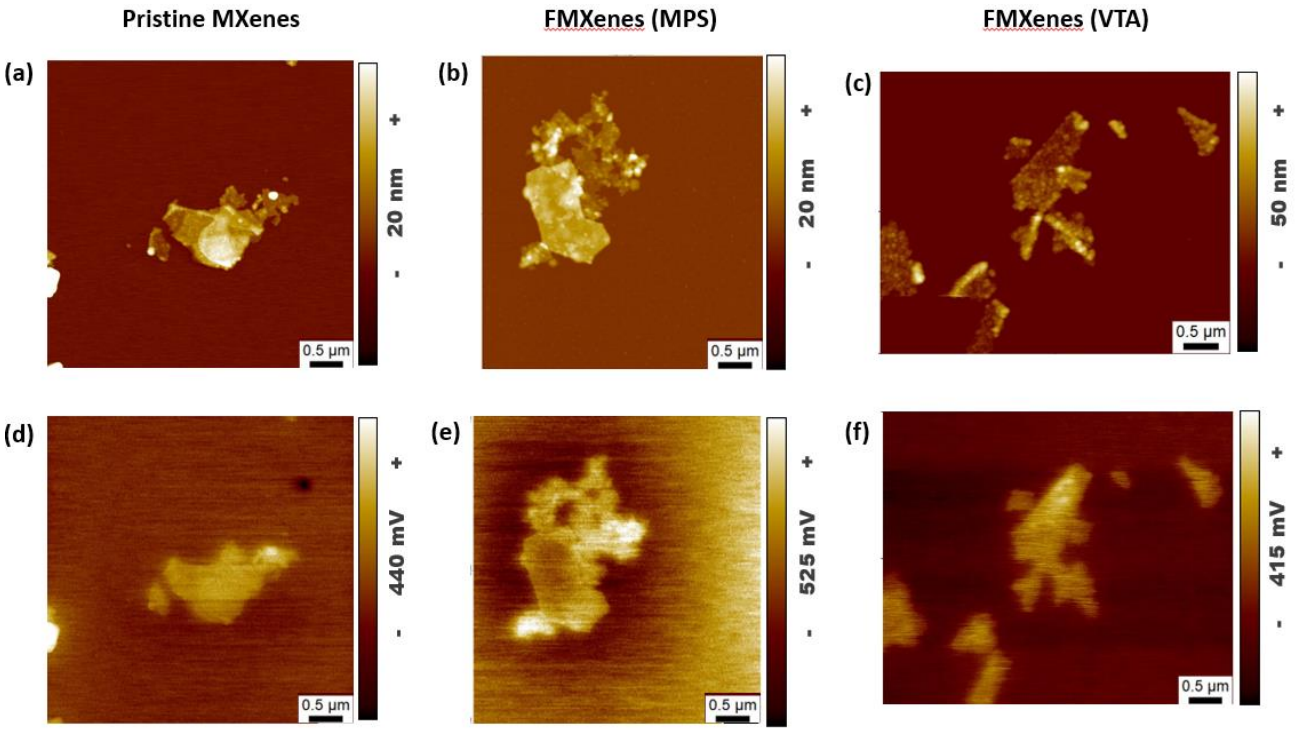


*Figure 4-9. AFM images of (a) pristine MXenes, functionalized with (b) MPS molecules, and (c) with VTA molecules MXenes sheets and their corresponding surface potential images of (d) pristine MXenes, functionalized with (e) MPS molecules, and (f) with VTA molecules MXenes sheets, all deposited on Si substrate.*

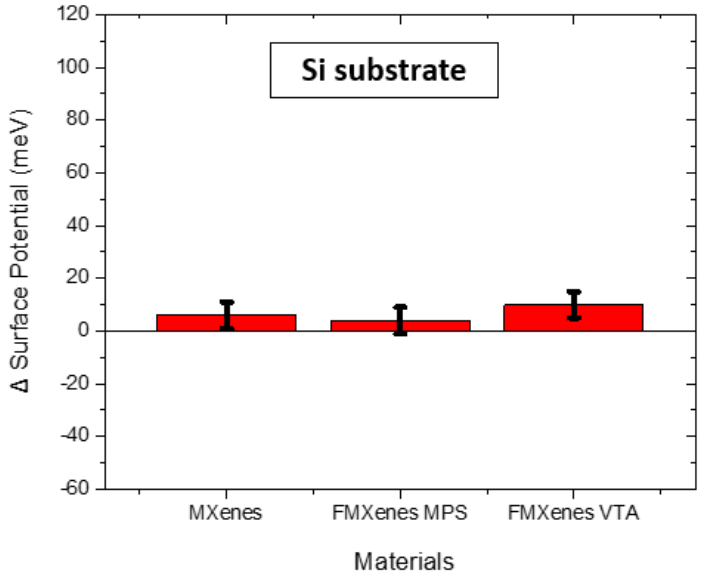


*Figure 4-10. Diagram of the work function values of all three types of MXenes deposited on Si substrate.*

All the MXenes under study were also deposited on HOPG substrate. All three types of sheets' topography and surface potential values are displayed in Figure 4-11. We notice some significant differences in the surface potential images. The functionalized sheets with MPS molecules exhibit a relatively lower surface potential value than HOPG, but it is fairly evident that both the pristine MXenes and the functionalized ones with VTA molecules have a higher surface potential than HOPG. The differences in surface potential and, by extension, work function between the three types of MXenes provide insight into how to tune the electrical properties of MXenes. Interestingly, both the type of functionalization and the substrate used appear to induce changes in the work function, allowing for a wide range of applications in electronics and beyond.

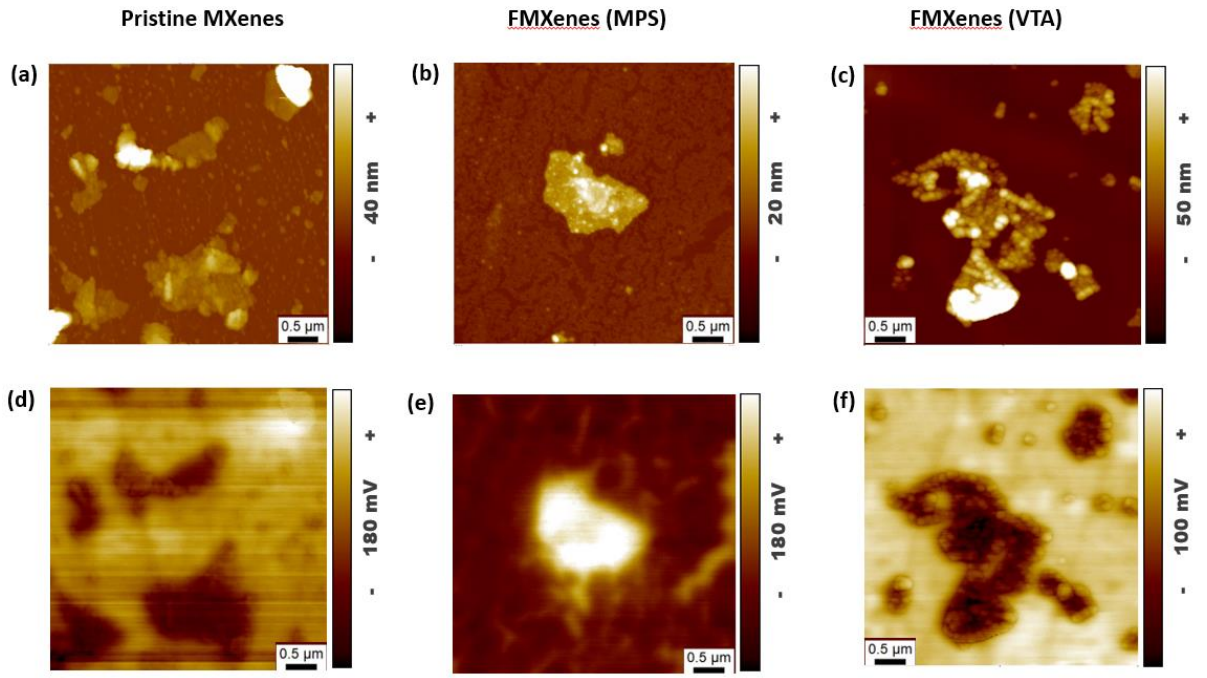


*Figure 4-11 AFM images of (a) pristine MXenes, functionalized with (b) MPS molecules, and (c) with VTA molecules MXenes sheets and their corresponding surface potential images of (d) pristine MXenes, functionalized with (e) MPS molecules, and (f) with VTA molecules MXenes sheets, all deposited on HOPG substrate.*

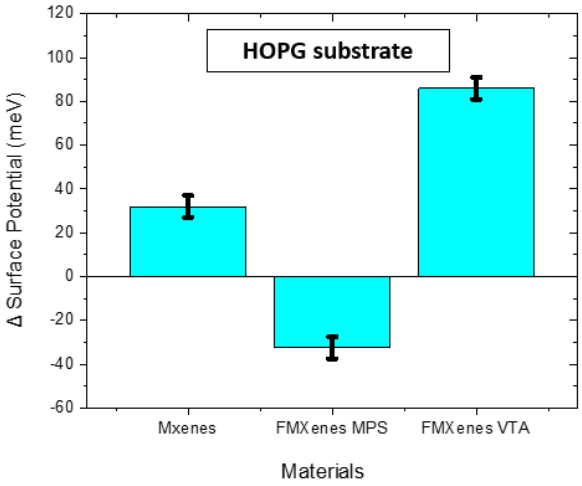


*Figure 4-12 Diagram of the work function values of all three types of MXenes deposited on HOPG substrate.*

### 4.2.4 Conclusions

The morphological characteristics of pristine MXenes isolated sheets and functionalized MXenes sheets were investigated in detail via AFM. More specifically, apart from the exact thickness of the materials under study, we were also able to identify an additional sublayer that forms between the substrate and the first layer of deposited MXenes, a significant result for the implementation of MXenes future applications and devices. Last, we also studied in detail the electronic characteristics of these materials.

## 4.3 $In_2Se_3$

### 4.3.1 Introduction

$In_2S_3$ is a prototypical non-layered n-type semiconductor and has a defect spinel structure featuring ordered vacancies in the IIIA sub-lattice (vac) in either cubic or tetragonal form (Figure 4-13) [70], [71]. With its five uncommon phases (δ, κ, α', β', and γ') and three common phases (α,β, and γ) (Figure 4-14), $In_2Se_3$ can access a wide range of physical properties[72]. While the γ phase has a defective wurtzite structure, the α, α', β, δ, and κ phases have layered structures. Additionally, according to stacking sequences, the β phase has trigonal (1T), 2H, and 3R structures, and the α phase has hexagonal (2H) and rhombohedral (3R) stacked forms[72]. Additionally, β-$In_2Se_3$ demonstrates exceptional photoresponsivity, good mobility, and unique ferroelectricity[73] In comparison to gapless graphene and other transition metal dichalcogenides, the electronic properties of $In_2Se_3$ exhibit notable advantages[74], [75], [76], [77]. The bandgap of semiconducting $In_2Se_3$ varies with thickness, ranging from 1.3 eV in bulk crystal to 2.8 eV in a monolayer [78], [79]. $In_2Se_3$ exhibits high sensitivity, broad response (from ultraviolet (325 nm) to short-wavelength infrared (1800 nm)), and high absorption coefficient when utilized as an optical material[80]. In contrast to other direct-bandgap 2D materials that are sensitive to air, like black phosphorus (BP), intact $In_2Se_3$ flakes exhibit exceptional stability in air. Recently, photodetectors based on single $In_2Se_3$ nanosheets have demonstrated fast, reversible, stable photo response characteristics along with high

photosensitivity ($10^5$ A W−1). On/off ratio and high mobility transistors have already been achieved[81]. Because of this, 2D $In_2Se_3$ materials have huge potential for technological applications in electronics. These include enhanced transistor mobility, as well as the ability to integrate light emitters and photodetectors into a single material system (same die), all of which are feasible on almost any substrate, including transparent and flexible substrates[82].

The outstanding traits of $In_2Se_3$ surpass those of numerous other two-dimensional materials (like graphene, BP, and $MoS_2$), thereby offering a solid foundation for large-area photodetectors[83]. However, a barrier to their practical implementation is the scalable production of large crystal domain, defect-free $In_2Se_3$ flakes[77].

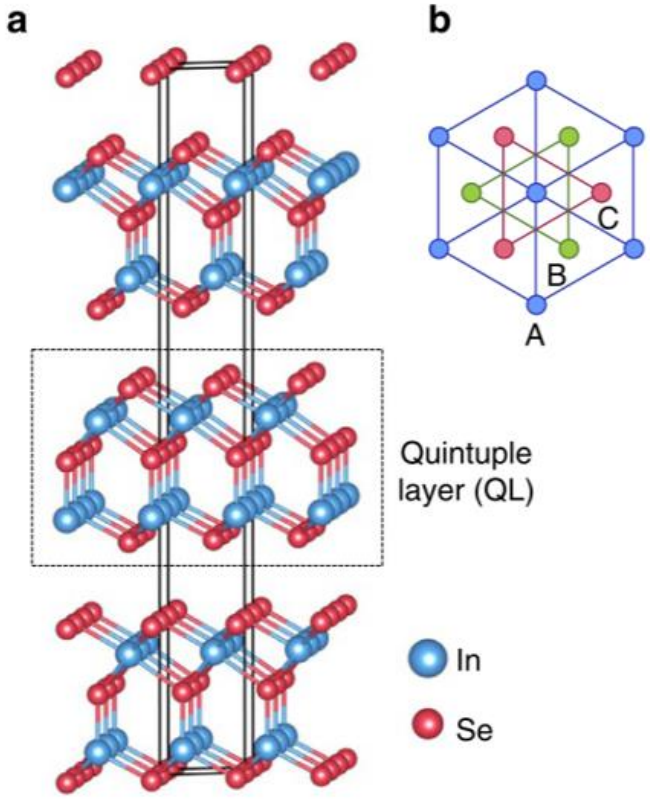


*Figure 4-13. $In_2Se_3$ layered structures. (a) Three-dimensional crystal structure of layered $In_2Se_3$, where the black dashed square represents a quintuple layer (QL) and the In and Se atoms are shown in blue and red, respectively. (b) The system's top view when viewed vertically. Only one elemental species is present in each atomic layer of a QL, and the atoms are arranged in one of the three triangular lattices (A, B, or C) as shown. Picture taken from ref.* [84]

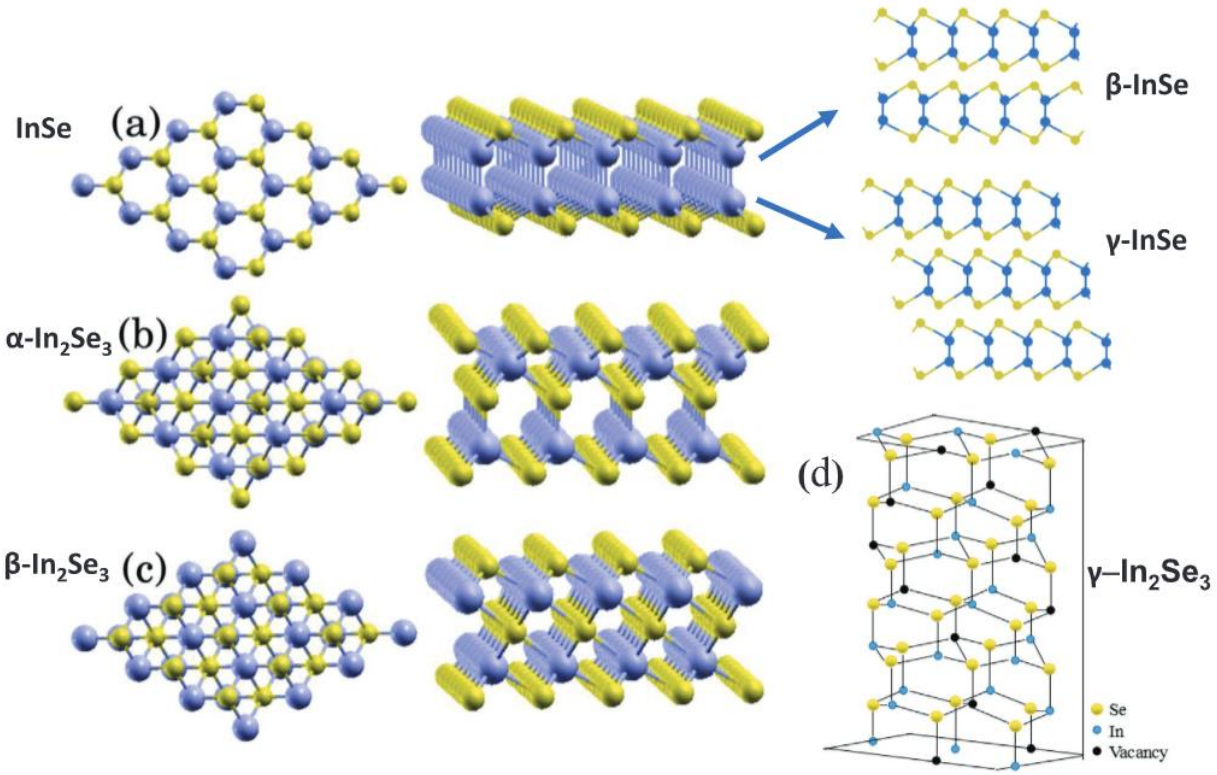


*Figure 4-14. Illustration of top and side views of a single layer of a) InSe (derived with β and γ phases), b) $In_2Se_3$ (α phase), c) $In_2Se_3$ (β phase), and d) structures of γ-$In_2Se_3$. Image taken from ref.* [85]

### 4.3.2 Preparation of $In_2Se_3$

The starting solution was prepared by our collaborators via electrochemical exfoliation to produce an $In_2Se_3$ solution[77], [86]. Next, the $In_2Se_3$ sheets/flakes were dispersed in Dimethylformamide (DMF) at a concentration of 2 mg/mL. The sheets were then spin-coated onto Si and $SiO_2$ substrates, following the procedure already outlined before in this Chapter.

To obtain also isolated sheets, we employed solutions at a lower concentration. Due to the fact that the $In_2Se_3$ sheets were dispersed in DMF, we performed an additional procedure after deposition on the substrates to remove the solvent. When using SPM characterization techniques, DMF and other solvents may have an impact on the characterization and investigation of a material's properties. To remove DMF from our flakes, we immersed the spin coated substrates in an $H_2O$ sonication bath for an hour at 60$^oC$, followed by an acetone sonication bath for another 30 minutes at 60$^oC$. After this procedure, we observed that DMF is removed from the surface of the $In_2Se_3$ sheets almost completely.

### 4.3.3 Results and Discussion

**Atomic force microscopy**

In order to study the morphological properties of isolated $In_2Se_3$ sheets we deposited them on Si substrate via spin coating. The presence of residual solvent traces is a common problem that microscopists encounter when studying nanomaterials deposited on surfaces from solution. This presence may have an impact on height, surface roughness, and—more importantly—measurements of the deposited materials' mechanical or electrical characteristics. Isolated $In_2Se_3$ sheets placed on a flat Si substrate are shown in Figure 4-15 both before and after solvent residue—in this case, DMF—is eliminated by sonication in water for 30 minutes at 75 $^o$ C followed by sonication in isopropanol for 1h at 100$^oC$ The tiny white spots that are appearing all over the image, as shown in 4-15a, can be attributed to DMF clusters. The sheets are still intact and solvent-free after using the solvent removal procedure (Figure 4-15b). This is a critical step for performing accurate SPM measurements. In our study, the deposited isolated sheets typically show a thickness of 2.3$\pm$02 m, which indicate that they are primarily bilayers and a flat surface with low roughness.

**(a)** **(b)**

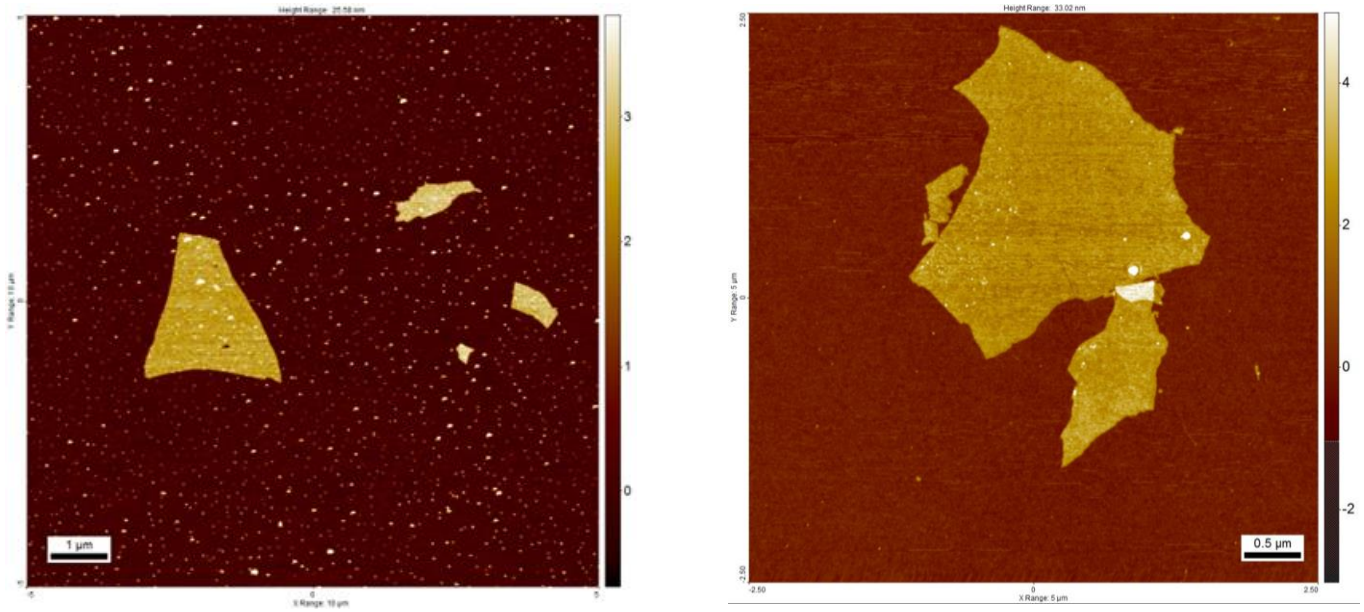


*Figure 4-15. AFM images of isolated $In_2Se_3$ sheets (a)prior to solvent (DMF) removal and (b) after the solvent removal.*

One of the most intriguing possibilities offered by two-dimensional materials is their capacity to form heterostructures by combining them with other two-dimensional materials [87], [88]. Here, we use the spin coating technique to deposit individual sheets of GO and $In_2Se_3$ on a Si substrate. Figure 4-16 shows an AFM image of both materials deposited on the same substrate, as well as their respective height profiles.

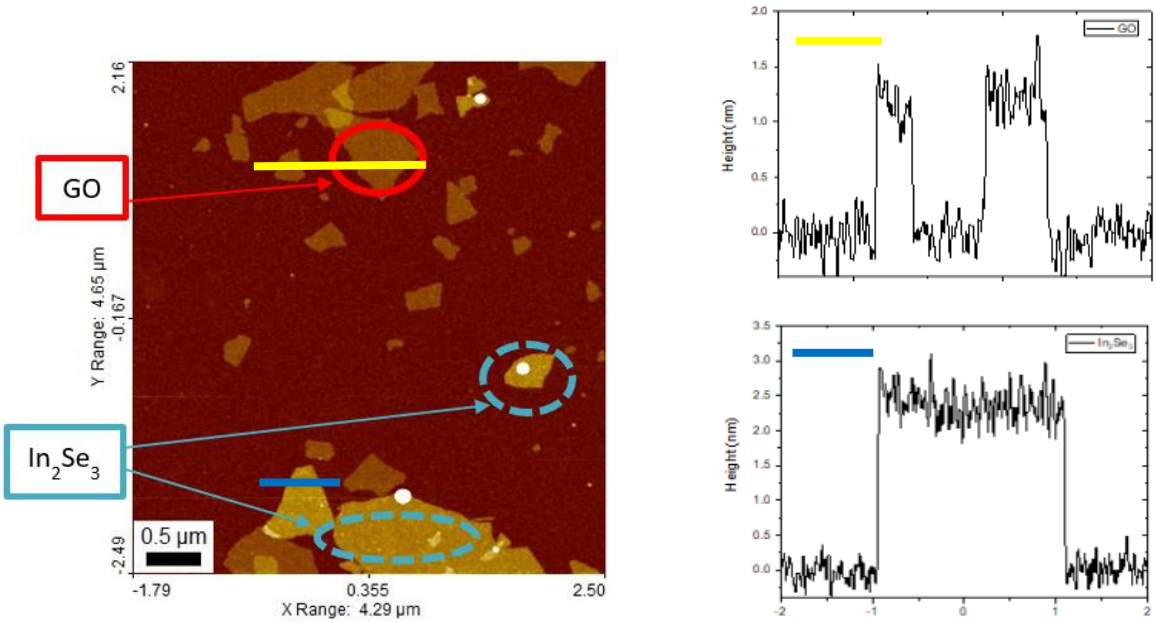


*Figure 4-16. AFM image of $In_2Se_3$ and GO sheets with their corresponding height profiles.*

**Kelvin probe force microscopy**

Aside from the intriguing morphological properties that combining 2D materials may yield, the interactions among them and their electrical properties are particularly interesting. In this case, we measure the surface potential values of the combined GO and $In_2Se_3$ isolated sheets. The sheets display different surface potential values with respect to the substrate (Si), as illustrated in figure 4-17 below. While GO shows a higher value, $In_2Se_3$ sheets have a surface potential value that is comparable to the substrate's. In general, the combination of semiconducting and insulating nanosheets such as the ones described here is of interest for the production of layered nano-devices.

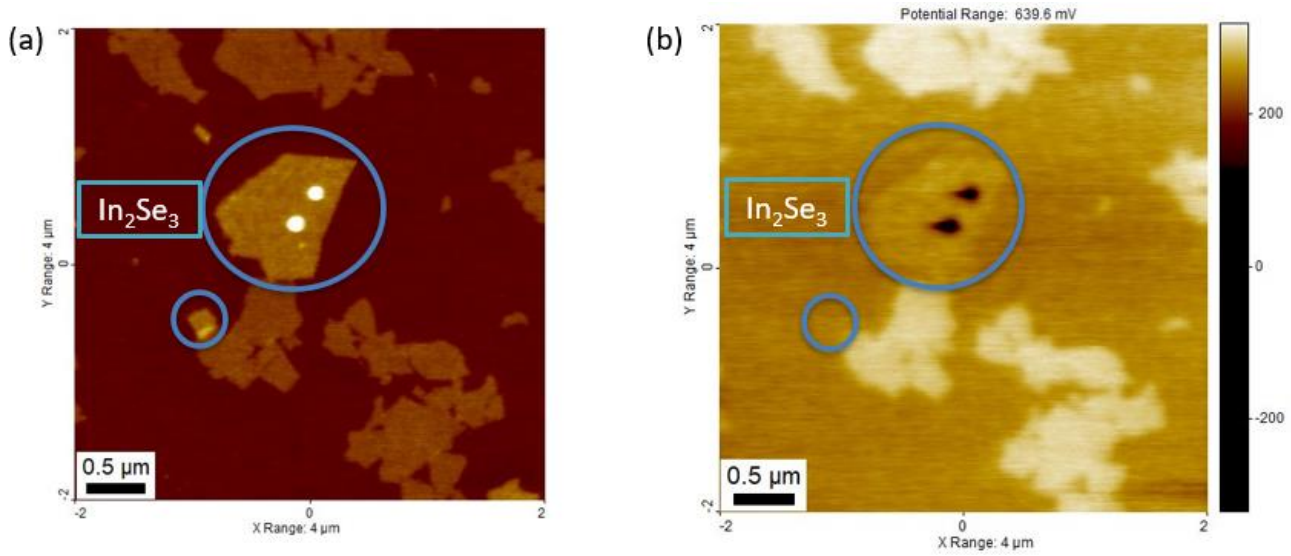


*Figure 4-17. (a) AFM image of $In_2Se_3$ and GO sheets and, (b) corresponding surface potential of the sheets.*

### 4.3.4. Conclusions

Here, we studied the thickness of isolated $In_2Se_3$ sheets produced by electrochemical exfoliation and deposited on flat Si substrate via spin-coating. Moreover, by combining these isolated $In_2Se_3$ sheets with single layer GO isolated sheets we were able to construct a new heterostructure. Last, we verified their substantial variations in work function when deposited on a flat Si substrate by using KPFM.

## 4.4 Electrochemically functionalised $MoS_2$ films

### 4.4.1. Introduction

$MoS_2$ is one of the most researched layered transition metal-dichalcogenides (TMDCs) because it is widely found in nature as molybdenite. The semiconductor monolayer $MoS_2$ has a direct bandgap of 1.8 eV [89]. This remarkable feature of $MoS_2$ will help to significantly offset the main weakness of graphene, that is its lack of bandgap, paving the way for the use of 2D materials in next-generation optoelectronic and switching devices. The following areas are where $MoS_2$ has made the most progresses thus far: energy conversion, storage, and hydrogen evolution reaction (HER) [90], [91], [92]. $MoS_2$ with an odd number of layers can also generate oscillating piezoelectric voltage and current outputs, suggesting that it may find use in stretchable electronics and nanodevice powering [93].

Mo (+4) and S (-2) are arranged to a sandwich structure in the single layer of $MoS_2$ films by covalent bonds in a sequence of S-Mo-S [94], [95], while relatively weak van der Waals forces interact between the sandwich layers (Fig. 4.2a). Each layer is typically around 0.65 nm thick. Monolayer $MoS_2$ with octahedral crystal symmetry configuration (referred to as 1T) is found to be metallic (Fig. 4.2b) [96], whereas that with trigonal prismatic polytype (2H) is found to be semiconducting. With a Young's modulus of 0.33 ± 0.07 TPa, $MoS_2$ exhibits mechanical flexibility very similar to graphene [97].

One of the main reasons $MoS_2$ is used so widely in optoelectronics is its tunable bandgap. $MoS_2$ multilayers (bulk) features an indirect-band gap semiconductor; conversely, monolayer $MoS_2$ has a direct band gap of ~2eV, and exhibits a significant absorption coefficient between 400 and 500 nm, which clearly decreases above 500 nm[98]. A range of applications are facilitated by direct bandgaps, which allow for adjustable photoresponsivity, targeted detectivity, and response time. Because of their high refractive index, $MoS_2$ monolayers and multilayers are appropriate for coating applications. The direct bandgap of monolayer $MoS_2$ can also be exploited for photoluminescence (PL). PL can be affected by a number of variables, including structure, doping, and band gap. Although transition metal dichalcogenides (TMDs) generally have low PL quantum yields (QY), it has been reported that $MoS_2$'s QY can be raised to 95% by chemical treatment with an organic superacid. Together with an observed carrier lifetime of almost 10.8 ns, this improvement in quantum yield raises the possibility of high-performance laser and solar cell applications[98], [99], [100], [101].

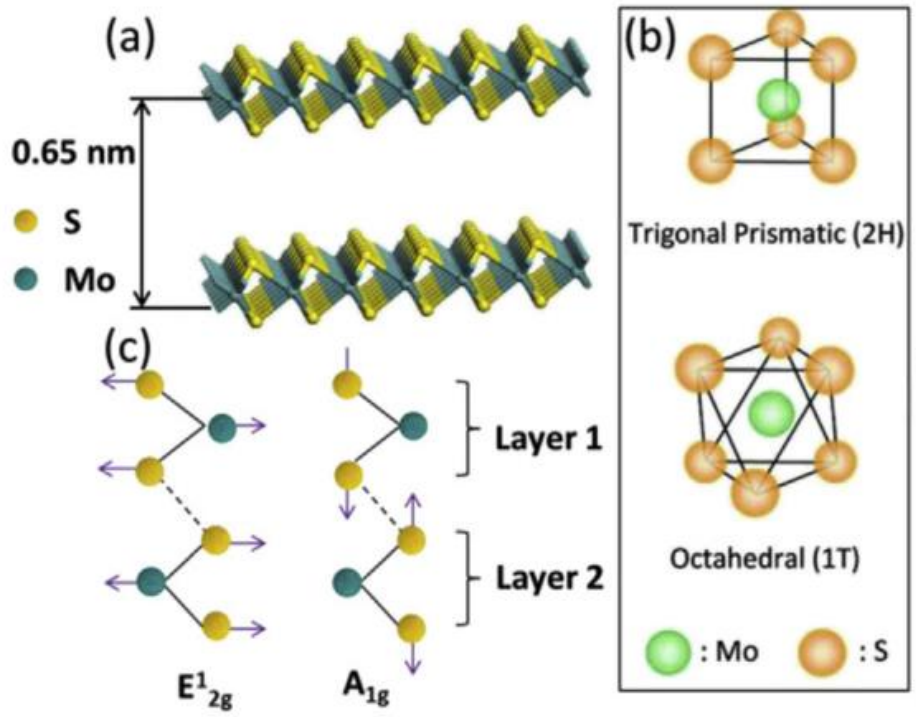


*Figure 4-18. Sigle layer structure of $MoS_2$. Figure taken from reference* [95]

With a Young's modulus of 0.33 ± 0.07 TPa, monolayer $MoS_2$ has good elasticity similar to graphene oxide and high strength comparable to graphene. It not only can withstand huge deformations, but its electrical properties can be altered by mechanical strain, turning it from a semiconductor to a metal. Indeed, elevated strain levels have the potential to cause structural distortion and convert $MoS_2$ into a metallic state[102], [103].

The semiconductor behaviour of $MoS_2$ is altered by doping with different elements, including chromium, copper, scandium (Sc), nickel, zinc, and titanium (Ti). For example, doping monolayer $MoS_2$ with chromium, copper, or scandium results in an n-type semiconductor; doping it with nickel or zinc results in a p-type semiconductor. Depending on the doping concentration, $MoS_2$ doped with titanium at different levels can exhibit p-type, n-type, or even ferromagnetic half-metal behaviour with potential applications in the field of spintronics. However, no change in the electronic properties was observed when

substitutional doping with Ti at three concentrations (2.04%, 3.57%, and 7.69%) was carried out[104], [105], [106].

$MoS_2$'s large band gap (1.8 eV) could allow potentially to downwsize electronic devices. Unlike graphene, $MoS_2$ exhibits a large production yield and cost-effectiveness due to its simple fabrication, high mobility with high-κ dielectric materials, and lack of surface dangling bonds[99]. Because of its covalent and Van der Waals bonds, it is especially well suited for thin-film transistors and gas sensing applications. $MoS_2$, which performs better and has less contact resistance, solves problems with metal-semiconductor interfaces that arise in silicon devices. As it might offers superior on/off switching characteristics and high efficiency, it has potential applications for aggressive transistors downscaling down to a predicted 1 nm gate lowest limit. $MoS_2$ might help to mitigate the nanoscale drawbacks of Silicon transistors, including high resistance, capacitance, and tunnelling issues. Field-effect transistors with reduced contact resistance and enhanced gate control can be made exploiting the synthesis and device fabrication possibilities of $MoS_2$[99], [107].

$MoS_2$ has uses in biosensing, optical sensors, and bio-applications such as DNA, cancer, and coronavirus detection, in addition to electronics. Research indicates that it may be useful in treating Alzheimer's and cancer, and it is proven to be biocompatible when injected into a human body. Among its many uses there is also the possibility to use it as a lubricant, a component of hydrogen evolution reactions, and an appropriate material for battery electrodes. All things considered, $MoS_2$'s distinct qualities make it a material that holds great promise for a range of electronic, sensing, microwave, and terahertz applications[108], [109], [110], [111].

### 4.4.2 Preparation of Electrochemically functionalised $MoS_2$ films

D.C. pulsed magnetron sputtering was used to create large-area $MoS_2$ films on silicon substrates. More specifically, the silicon surface was sputtered with a thin layer of Mo, and then exposed to sulphur vapours at high temperatures to induce sulfurization. Physical vapor deposition (PVD) allows to grow uniform $MoS_2$ films on a wafer scale, minimizing waste and providing thickness control without the need for chemical processes[112], [113]. Then the $MoS_2$ films were functionalized via electrochemical nanolithography (ECL). In ECL, a metalized

stamp is gently pressed up against the substrate in an environment with a high relative humidity (RH> 95%). In these specific circumstances, capillary forces induce the formation of a water meniscus between the stamp protrusions and the surface, resulting in the formation of a two-electrode nano-electrochemical cell[114]. An applied positive voltage causes oxidation on the substrate, whereas an applied negative voltage causes the sample surface to be electrochemically reduced. Crucially, only the areas beneath the stamp protrusions are subject to the electrochemical reaction[114]. The formation of patterned structures is the outcome of this exact control, and the size of these structures is precisely determined by the dimensions and form of the stamp features. In this work, we chose a parallel-line stamp because of its simple geometry and allow us to clearly illustrate the concepts of our research.

ECL has a disruptive effect on $MoS_2$ when it is applied in oxidative conditions because it breaks down the $MoS_2$ into $MoO_3$, which can then be removed by a subsequent lift-off process in water. This process creates a topographic pattern while preserving the untreated zone. ECL has a less severe effect when used in electrochemically reductive conditions; it merely causes a localized increase in surface roughness. The substrate maintains $MoS_2$'s chemical stability and mean structure in these circumstances.

### 4.4.3 Results and Discussion

**Kelvin Probe Force Microscopy**

The topography and corresponding surface potential images of a printed $MoS_2$ sample are shown in Figure 4-19 below. Although the surface roughness is slightly different in Fig. 4-19a's morphology, Fig. 4-19b's surface potential image clearly shows a net contrast in the printed zones, accurately replicating the stamp's features and registering an increase of about - 15 mV. This increase, in our experimental configuration, is indicative of a reduction in work function, meaning the Fermi energy EF is shifted towards the vacuum. This is probably due to the introduction of electronic midgap empty states by sulphur vacancies (Vs) in the vicinity of the conduction band edge.

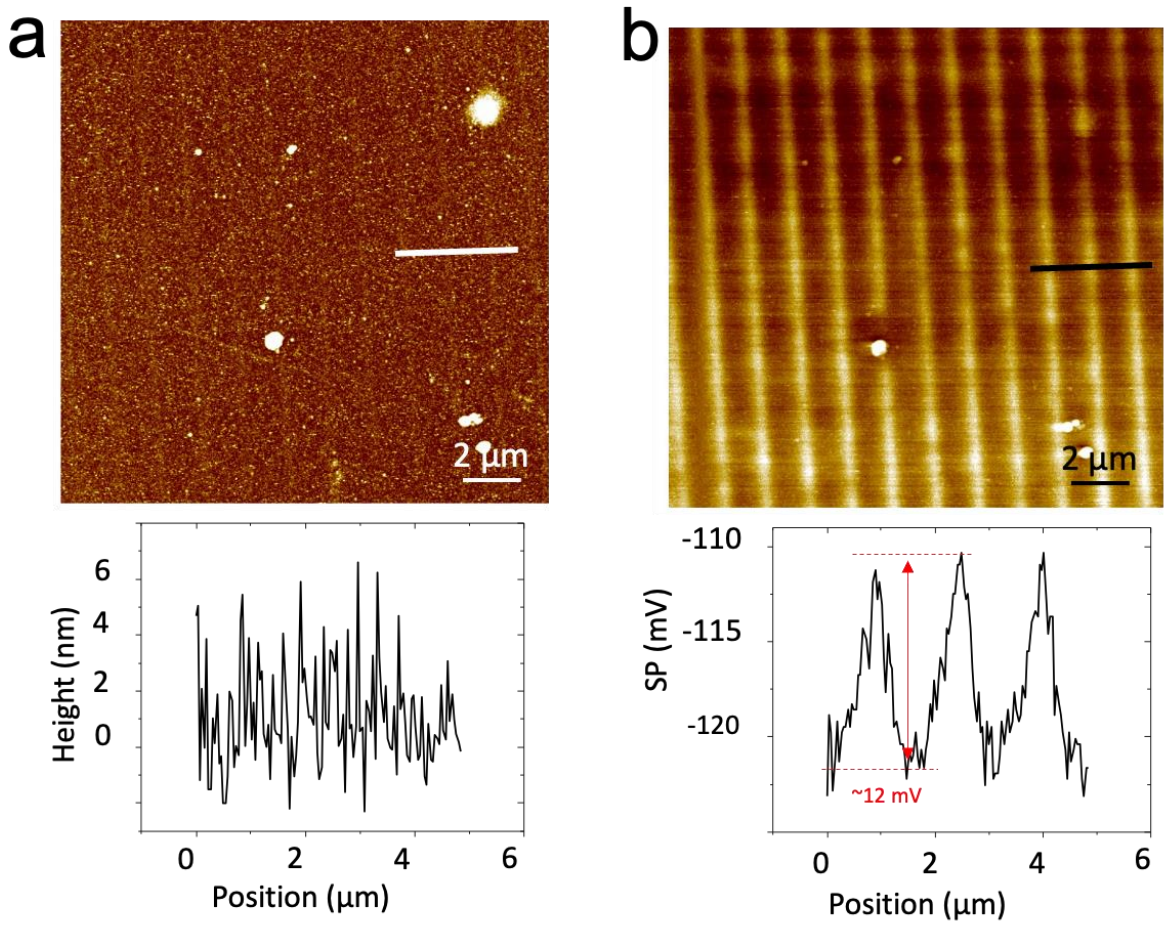


*Figure 4-19 (a) Topography, and (b) corresponding surface potential of the printed zones in PVD $MoS_2$ thin film. Below the images their corresponding height profile can be seen.*

Noteworthy, when a defect such as a dust particle is present in the $MoS_2$ film (Figure 4-20), the functionalization is not successful in the adjacent area, probably because the particle acts as a spacer, hindering effective contact between the stamp and the substrate.

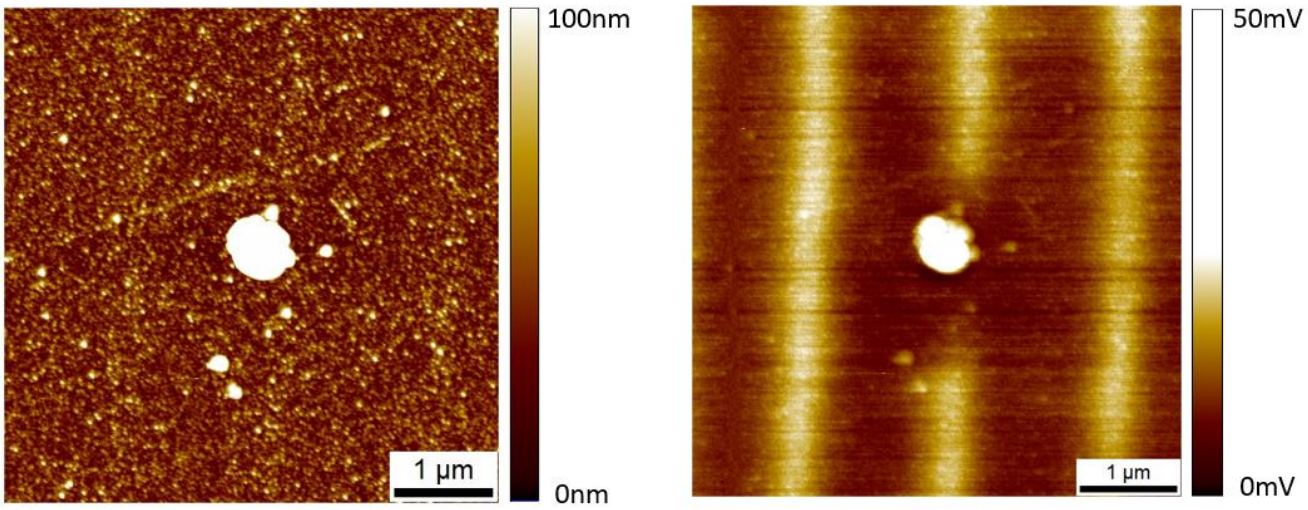


*Figure 4-20 (a) AFM image of the $MoS_2$ film and (b) corresponding surface potential. The large white spot is a defect.*

**Conductive AFM and adhesion force microscopy**

Utilizing conductive atomic force microscopy (cAFM) in the PFTUNA configuration—a particular AFM, module, developed by Bruker [https://www.bruker.com/en/products-and-solutions/microscopes/materials-afm/afm-modes/pf-tuna.html] that permits simultaneous probing of morphology, adhesion between the AFM tip and surfaces, and electrical conductivity—we further characterized the surface properties of the printed structures.

Notably, we found notable differences in adhesion and current between the pristine and electrochemically treated (EC) zones (Figure 4-21). The printed stripes, in particular, showed adhesion values that were four to five times higher than those in pristine areas. Furthermore, the PFTUNA map showed a more than 30% increase in electrical conductivity within the same zones. Even though our measurement qualitatively concurs with earlier specific studies that demonstrate that sulphur vacancies (Vs) significantly improves contact resistance [115], the simultaneous increase in adhesion force in the zones treated with ECL suggests that the improvements in electrical properties observed by conductive AFM could be the result of a combination of this two effects: the presence of midgap states and the adhesion-induced increase in tip-sample interaction time, both of which reduce (local) contact resistance.

Notably, in the areas between the printed stripes, there was no change in electrical conductivity or adhesion force relative to pristine $MoS_2$.

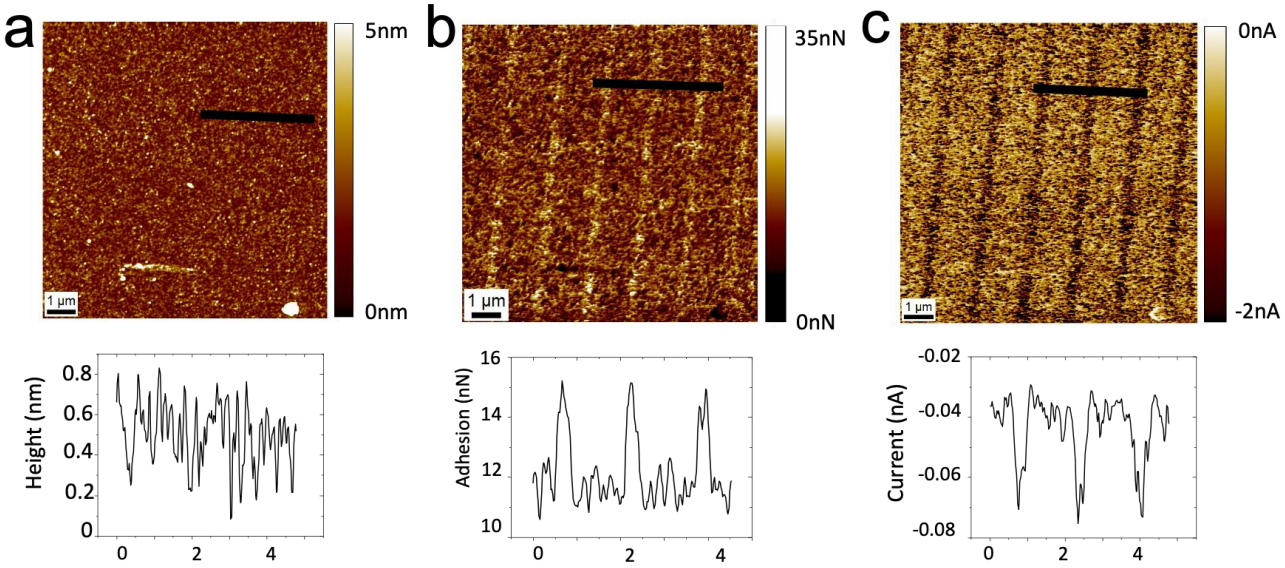


*Figure 4-21. (a) Topography, (b) adhesion and (c) corresponding current map measured by C-AFM of $MoS_2$ patterned film. Vs rich stripes exhibit a significant reduction of electrical conductivity c.a. 30% concerning pristine zones.*

### 4.4.4 Conclusions

Here, we studied electrochemically functionalized $MoS_2$ thin films via conductive AFM and KPFM methods. The topography of the film appeared to be uniform but the difference in the surface potential value has been a valuable tool to visualize and study the functionalization due to the presence of S vacancies. Variations in adhesion and current were found to be connected to the functionalization, providing new opportunities for applications in electronics.

## 4.5 Soot molecules

### 4.5.1 Introduction

A side project of this research concerned the characterization of unconventional graphene-like materials, in particular small molecules and particles derived from soot, which can be categorized as nanometric, highly irregular graphene-like particles. The motivation of this activity is that the process through which carbonaceous nanoparticles, or soot particles, are created during the high-temperature incomplete combustion of hydrocarbon fuels is still a topic of intense discussion in the combustion community and is the subject of numerous studies[8]. The most frequently discussed and crucial point of disagreement is particle inception, which is the change from gas-phase polycyclic aromatic hydrocarbons (PAHs) to condensed-phase clusters or early soot[9]. In order to effectively reduce carbon particle emissions from combustion systems, it is imperative to unravel the physics and chemistry underlying this process. Concerns about soot particle emissions into the atmosphere are significant for the environment, human health, and climate change[116], [117]. However, other motivations for understanding the formation of carbonaceous nanoparticles under pyrolytic and combustion conditions include material science applications such as the production of carbon blacks or the recent surge in interest in environmentally friendly methane pyrolysis methods such as "turquoise" hydrogen production, which produce hydrogen with low or even negative carbon emissions[118], [119]. Also, the production of novel materials by flame synthesis[120] is an appealing technological approach for creating graphene, fullerenes, and other carbon nanostructures, as well as fluorescent carbon nanoparticles with adjustable optical and electrical characteristics [108]. Finally, also the astrophysics community is very interested in PAHs and carbon nanoparticles because they are related to fuel-rich combustion and can be thought of as a cheap, accessible model for extra-terrestrial carbonaceous molecules and grains[121], [122].

Because of the aforementioned factors, the development of PAHs, condensed-phase carbonaceous species, and soot nanoparticles has been thoroughly studied over the past few decades and is still an active area of research[123], [124], [125]. Significant progress has been made in the past few years, both experimentally [126], [127], [128] and computationally, especially when it comes to the formation mechanisms and the chemical characterization of early soot particles[129], [130]. The discovery of resonantly stabilized aromatic π-radicals (RSRs) as important intermediaries in the nucleation and growth of soot particles is one of the

major advancements that has garnered a lot of attention lately. Current research indicates that covalently bound complexes may form in addition to fast molecular clustering reaction pathways involving radical-chain reactions of RSRs[128]. Fully or partially embedded five-membered ring structures may form[131] during the mass/molecular growth process. In the soot community, the chemical growth of aromatic compounds has long been sought as a substitute or supplement to the purely physical coalescence caused by van der Waals/dispersion forces[8], [124], [132]. A comprehensive analysis of the significance and ramifications of the physical and chemical pathways, as well as their combinations, has been conducted by Frenklach[124], D'Anna[132], Wang[123], and others. More recently, Martin et al. [133], [134], have reviewed these routes in detail.

### 4.5.2. Preparation of Soot molecules

Initially, incipient soot nanoparticles were extracted from a lightly sooting laminar premixed flame of ethylene and air. The operating parameters were the same as those employed in prior studies[8], [135], [136], [137], including earlier AFM studies[138], [139]. The flame was stabilized on a water-cooled McKenna burner, with a cold gas velocity of 9.8 cm/s and an equivalency ratio of 2.01. Using a high-dilution horizontal tubular probe placed at a burner-to-probe separation distance of Z= 7 mm—the smallest distance that could be probed without disturbing the flame front—incipient soot, suspended in burned combustion gases, was extracted from the flame center line. The combustion products were quickly mixed with $N_2$ through a 200µm-diameter orifice on the bottom of the dilution probe, resulting in a 1:3000 dilution ratio. Using a fast insertion method and accounting for heat loss adjustments, an R-type thermocouple (Pt/Pt-13%Rh) with a spherical junction and a diameter of 300µm was used to measure the flame temperature[8].

We analysed the morphology of the soot molecules by atomic resolution low temperature, ultra-high vacuum (UHV) AFM and STM, performed at the IBM laboratory at Zurich. This activity was realized during one of my secondments as a part of my PhD program. I personally spent two weeks in the laboratory and took and analysed parts of the experimental results I will present in the following.

To achieve atomic resolution with the AFM, it is necessary to operate in the short-range regime of forces, where chemical interactions make significant contributions [140]. As Giessibl, points out, it is desirable to work with a cantilever of high stiffness with oscillation amplitudes on the order of 1 Å in this force regime. the low-temperature STM/AFM we used is based on a qPlus sensor design and operates in ultrahigh vacuum at 5 K. Stable operation is possible at oscillation amplitudes as small as 0.2 Å thanks to the high stiffness of the tuning fork (spring constant $k_0 = 1.8 \times 10^3$N/m, resonance frequency $f_0$ = 23,165 Hz, and quality factor $Q = 5\times10^4$). A metal tip was mounted on the tuning fork's free prong, and a separate tip wire (insulated from the tuning fork electrodes) was used to measure the tunneling current [140]. The sample was subjected to the bias voltage V. We employed a PtIr-wire with a diameter of 25 µm as the tip, which was sharpened both in situ by making indentations into the bare Cu surface and ex situ by focused ion beam milling. With a sample bias voltage V, all STM images were measured in constant-current mode. At V = 0 V, constant-height mode AFM images were obtained. The substrate utilized in this experiment was a Cu(111) single crystal that had two monolayer (ML) thick NaCl(100) islands partially covering it; these islands are referred to as NaCl(2 ML)/Cu(111). Additionally, in order to increase the resolution in the AFM mode, a CO molecule was purposefully picked up with the tip from NaCl for these measurements. More details of the measurements can be found in ref. [8], [140]

In order to prepare the sample for the low temperature scanning probe apparatus, a special treatment transfer is required. By gently pressing a quartz filter coated in soot onto a small Si wafer, soot was transferred onto it. The wafer was then placed in front of the cold sample (T≈10 K) in the UHV system, and Joule heating was used to flash-anneal it from room temperature to roughly 900 K in a matter of seconds[8]. It has been demonstrated that rapid heating can facilitate the process of sublimation over decomposition[141] for molecules with masses up to roughly 1000 Da.

### 4.5.3 Results and Discussion

In order to clarify the molecular structures of soot particles and explore their implications for the growth process of incipient soot particles, this work presents AFM measurements in conjunction with orbital density imaging, scanning tunneling microscopy (STM), and atom manipulation[8].

Most of the compounds in the Z = 7 mm condition could be resolved by AFM, which was

advantageous for the study's statistical significance. Because open-shell π-radical systems have been shown to be important in the process of soot formation in recent investigations,[142], [143], [144], [145], [146] we improved our analysis by using orbital density imaging with scanning tunneling microscopy (STM). In order to achieve this, we focused our research on the species deposited on bilayer NaCl islands. By electronically separating the molecules from the metallic surface, this insulating layer stops the molecules from hybridizing with the surface. When using STM to image the molecules' frontier orbital densities, this decoupling is advantageous [147]. The significance of electronic characterization through STM is twofold: firstly, it validates and enhances the structural assignments derived from AFM through comparison with computed frontier orbital densities and spin densities[148]. Additionally, STM orbital images shed light on the open-/closed-shell nature of adsorbates as well as their spin ground state.

To simulate the hydrogen dissociation processes occurring in the flame, atom manipulation was used[8], [149], [150]. The atom manipulation experiments allow us to study the products formed by such dehydrogenations and provide information about likely flame reaction pathways, i.e., atomic sites from which hydrogen atoms are likely to dissociate. The key discoveries from our analysis of the Z = 7 mm soot sample's molecules are as follows: 1) structures with partially and fully embedded five- and seven-membered rings suggest hydrogen abstraction acetylene addition (HACA) and cross-linking pathways occurring in tandem; 2) various classes of open-shell π-radicals were discovered; and 3) catacondensed (polycyclic aromatic hydrocarbons (PAHs) that have two or more adjacent rings that share only one carbon atom) and pentalinked (planar crosslinked species containing a double bond between two pentagonal rings) molecules suggest cross-linking of small aromatics. We can learn more about the growth of particles in the flame by analysing the species that we have found. These insights are useful for enhancing combustion processes and generating carbon materials in addition to hydrogen production because they show how PAHs grow and how soot originates.

AFM data of the molecules obtained from the flame at a Z = 7 mm burner-to-probe separation distance are displayed in Figure 4-22. The assigned and provisionally assigned molecular structures are displayed in Figure 4-23 below. In addition to the AFM images displayed in Figure 4-22, constant-height AFM images have been acquired for the assignments at varying tip-heights. Additionally, maps of the frontier orbital densities calculated by DFT have been compared to constant-current STM images obtained at various sample voltages, corresponding to ion resonances [8]. When compared to the Z = 8 mm sample that was previously studied by AFM [8] the majority, or roughly 80%, of the analyzed compounds could be resolved at the atomic scale for the Z = 7 mm condition which is advantageous for the

study's statistical significance. For the Z = 8 mm sample, approximately half of the molecules could not be analyzed at atomic resolution due to some three-dimensional character. The more planar morphology of the molecules is most likely the cause of this difference between samples prepared at Z = 7 mm and 8 mm. While the Z = 8 mm sample shows more particles grown by coagulation, the Z = 7 mm sample primarily contains only nucleated, not coagulated particles [8]. It is reasonable to assume that the Z = 8 mm sample is more "graphitized" than the Z = 7 mm sample due to the evidence of linking particle coagulation and carbonization/aging[151], [152].

The H/C plots for molecules from the Z = 7 mm and Z = 8 mm samples that were resolved by AFM are shown in Figure 4-24. In the Z = 8 mm samples [153], [154], the composition of most aromatic molecules is in the range of 20–40 carbon atoms (250–500 Da), and their typical H/C ratio is 0.4–0.5. This supports previous computational and experimental studies that found that the majority of the PAHs in incipient soot are moderately sized, roughly coronene to circumpyrene in size [155], [156].

The aromatic molecules are mostly found in the H-rich area of the graph (top right), although they are also distributed in close proximity to the maximally pericondensed line (black line in Figure 3). This is especially noticeable when the molecules' mass increases, and for those with more than 35 carbon atoms, H/C almost reaches an asymptote, typically falling between 0.4 and 0.5 (a pericondensed aromatic molecule with 50 C atoms has a H/C of 0.35). Some molecules do, however, occasionally also lie below the maximally pericondensed line[8].

### 4.5.4 Conclusions

Concluding, in this work, individual structures with open-shell π-radicals have been presented and the different π-electrons' localization degrees have been analysed. Weak localization is provided by delocalized π-radicals at the edge of pericondensed aromatics, which may also contribute to some multicenter bonds that stabilize the soot particles. Through atom manipulation, partially localized π-radicals on zigzag edges were discovered and produced.

Ultimately, it is observed that π-radicals formed on pentagonal and methylene-type edges were strongly localized. Moreover, these sites offer chances for multiple reactive sites per molecule, as in π-diradicals, which can react quickly via the PARLH initiation mechanism[8].

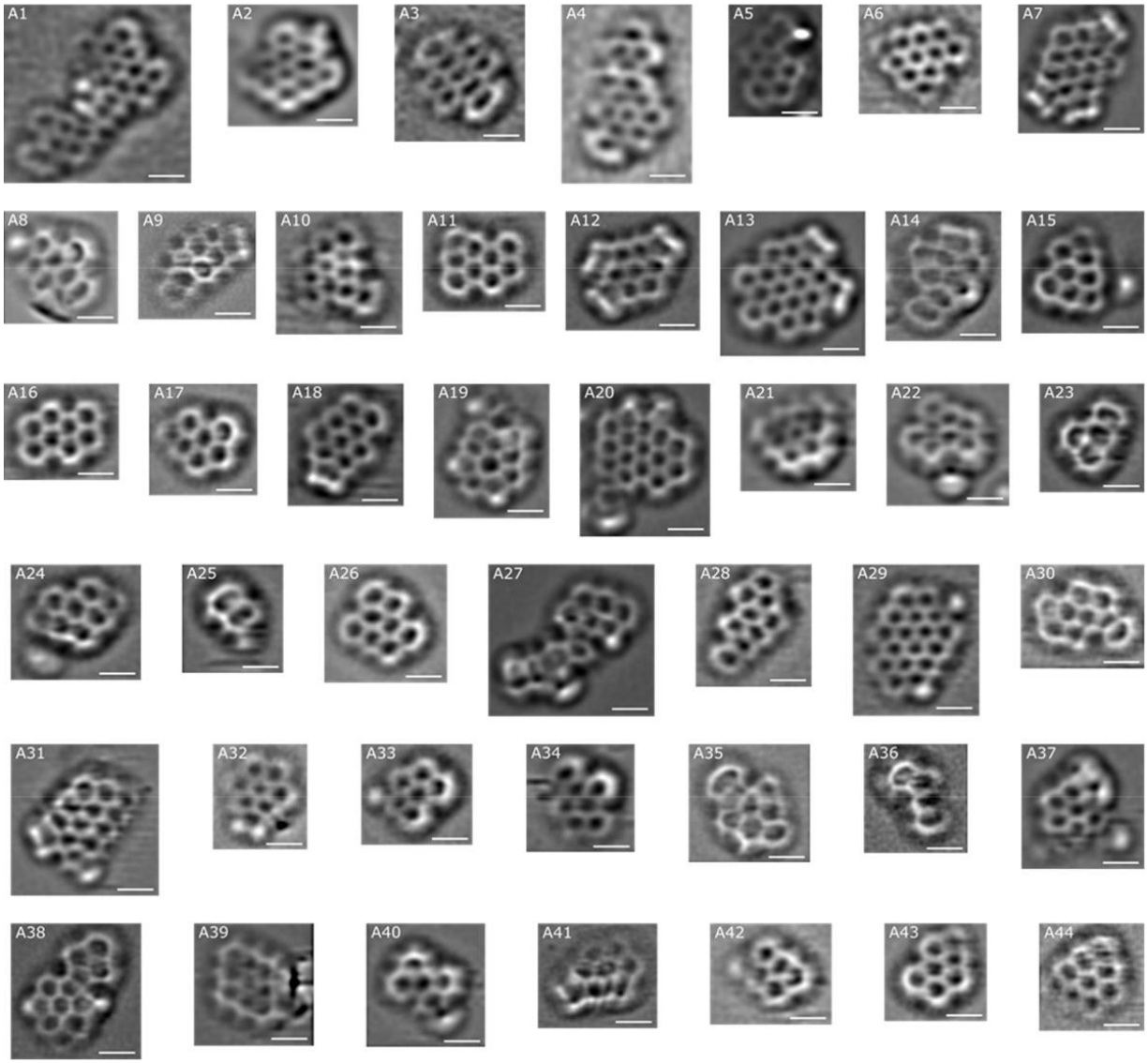


*Figure 4-22. Laplace-filtered constant-height CO-tip AFM images of Z = 7 mm soot molecules. All molecules were measured on a NaCl bilayer on Cu(111). The assignment of structures A1 through A31has been done with high confidence. The assignment of Structures A32-A44 is provisional. Every scale bar is equivalent to 5 Å. For further information, see* [8]

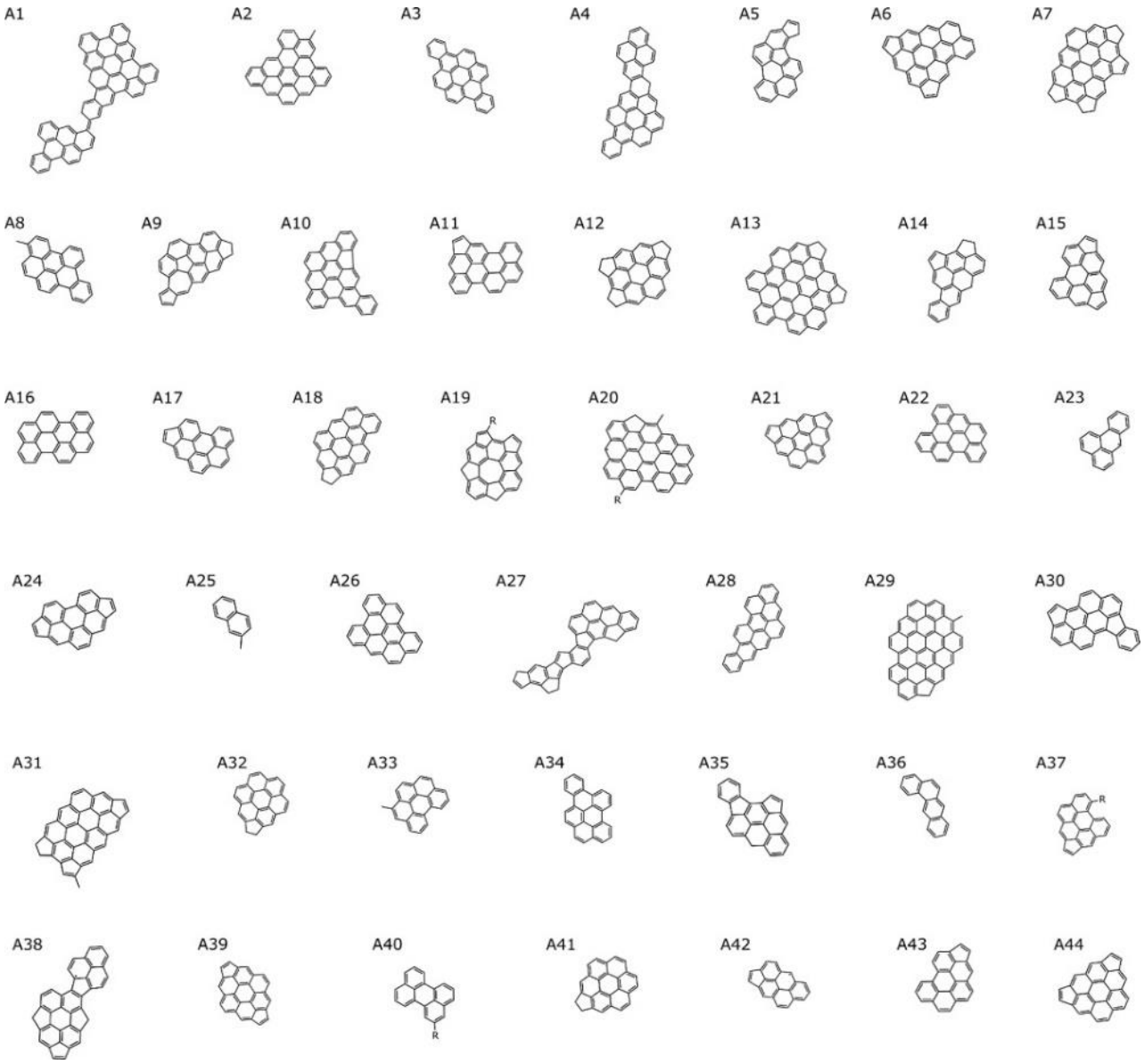


*Figure 4-23. Structures A1 through A31 of the molecules for which AFM data are displayed in Figure 4-22 have been assigned, and structures A32 through A44 have been provisionally assigned. Picture taken from* [8]

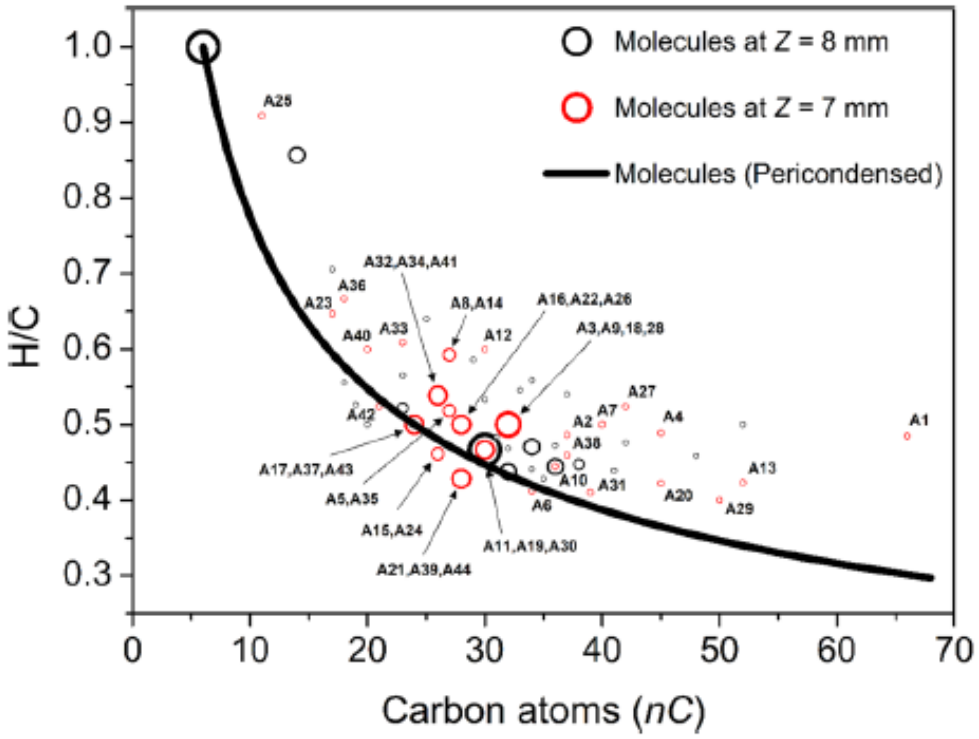


*Figure 4-24. H/C ratio in relation to nC, the number of aromatic carbon atoms. H are side chains that are unknown (-R). The black circles represent the molecules for the Z = 8 mm sample (from Commodo et al.* [153]*); the red circles represent the molecules of the Z = 7 mm sample (this work); the line corresponds to the calculated trend for maximally pericondensed PAHs,48 i.e., H/C = (nC/6)−0.5. The sizes of the symbols represent the corresponding abundances in the sampled molecular pool.*

## 4.6 General Conclusions

To define their morphological and electrical characteristics and ensure their use in future technologies, various 2D materials have been studied using conductive AFM, kelvin probe force microscopy, and atomic force microscopy.

The thickness of pristine MXenes isolated sheets and functionalized MXenes sheets were investigated via AFM and found to be comparable to the one already reported in the literature. Through statistical studies, we were able to identify an additional sublayer that forms between the substrate and the first layer of deposited MXenes, information that has to be taken into account and further investigated when such sheets are implemented in applications. Furthermore, we have demonstrated that by a careful choice of surface functionalization and type of substrate, it is possible to tune the electronic characteristics of MXenes flakes.

In addition, we investigated the morphological properties of isolated $In_2Se_3$ sheets produced by electrochemical exfoliation. Furthermore, we were able to construct a new heterostructure by combining these isolated sheets with single layer GO isolated sheets. We were able to verify their substantial variations in work function when deposited on a flat Si substrate by using KPFM.

Electrochemically functionalized $MoS_2$ thin films were studied using both conductive AFM and KPFM methods. Even though the topography of the film appears to be uniform the difference in the surface potential value is a valuable tool to visualize and study the functionalization due to the presence of S vacancies. Variations in adhesion and current are found to be connected to the functionalization, providing new opportunities for electronic applications.

Last, using atomic-resolution STM and AFM with CO functionalized tips, we were able to resolve individual molecules of early soot at the Z = 7 mm condition. Our results provide specific structures of soot-formed molecules, including evidence for cross-linking, fully embedded five- and seven-membered rings, and an explanation for the formation of moderately-sized aromatics. We believe these findings are significant in the context of particle formation and growth.

# REFERENCES


[1] A. Cepellotti, G. Fugallo, L. Paulatto, M. Lazzeri, F. Mauri, and N. Marzari, "Phonon hydrodynamics in two-dimensional materials," *Nat Commun*, vol. 6, no. 1, p. 6400, Mar. 2015, doi: 10.1038/ncomms7400.

[2] D. Akinwande, N. Petrone, and J. Hone, "Two-dimensional flexible nanoelectronics," *Nat Commun*, vol. 5, no. 1, p. 5678, Dec. 2014, doi: 10.1038/ncomms6678.

[3] F. H. L. Koppens, T. Mueller, Ph. Avouris, A. C. Ferrari, M. S. Vitiello, and M. Polini, "Photodetectors based on graphene, other two-dimensional materials and hybrid systems," *Nat Nanotechnol*, vol. 9, no. 10, pp. 780–793, Oct. 2014, doi: 10.1038/nnano.2014.215.

[4] F. Xia, H. Wang, D. Xiao, M. Dubey, and A. Ramasubramaniam, "Two-dimensional material nanophotonics," *Nat Photonics*, vol. 8, no. 12, pp. 899–907, Dec. 2014, doi: 10.1038/nphoton.2014.271.

[5] J. N. Coleman *et al.*, "Two-dimensional nanosheets produced by liquid exfoliation of layered materials," *Science (1979)*, vol. 331, no. 6017, pp. 568–571, Feb. 2011, doi: 10.1126/science.1194975.

[6] G. Fiori *et al.*, "Electronics based on two-dimensional materials," *Nat Nanotechnol*, vol. 9, no. 10, pp. 768–779, Oct. 2014, doi: 10.1038/nnano.2014.207.

[7] A. K. Geim and I. V. Grigorieva, "Van der Waals heterostructures," *Nature*, vol. 499, no. 7459, pp. 419–425, Jul. 2013, doi: 10.1038/nature12385.

[8] L. A. Lieske *et al.*, "Portraits of Soot Molecules Reveal Pathways to Large Aromatics, Five-/Seven-Membered Rings, and Inception through π-Radical Localization," *ACS Nano*, vol. 17, no. 14, pp. 13563–13574, Jul. 2023, doi: 10.1021/acsnano.3c02194.

[9] H. A. Michelsen *et al.*, "A Review of Terminology Used to Describe Soot Formation and Evolution under Combustion and Pyrolytic Conditions," *ACS Nano*, vol. 14, no. 10, pp. 12470–12490, Oct. 2020, doi: 10.1021/acsnano.0c06226.

[10] Y. Gogotsi, "Transition metal carbides go 2D," *Nat Mater*, vol. 14, no. 11, pp. 1079–1080, Nov. 2015, doi: 10.1038/nmat4386.

[11] B. Anasori *et al.*, "Two-Dimensional, Ordered, Double Transition Metals Carbides (MXenes)," *ACS Nano*, vol. 9, no. 10, pp. 9507–9516, Oct. 2015, doi: 10.1021/acsnano.5b03591.

[12] M. Naguib *et al.*, "New Two-Dimensional Niobium and Vanadium Carbides as Promising Materials for Li-Ion Batteries," *J Am Chem Soc*, vol. 135, no. 43, pp. 15966–15969, Oct. 2013, doi: 10.1021/ja405735d.

[13] M. Naguib *et al.*, "Two-Dimensional Transition Metal Carbides," *ACS Nano*, vol. 6, no. 2, pp. 1322–1331, Feb. 2012, doi: 10.1021/nn204153h.

[14] M. Naguib *et al.*, "Two-Dimensional Nanocrystals Produced by Exfoliation of $Ti_3AlC_2$," *Advanced Materials*, vol. 23, no. 37, pp. 4248–4253, Oct. 2011, doi: 10.1002/adma.201102306.

[15] B. Anasori, M. R. Lukatskaya, and Y. Gogotsi, "2D metal carbides and nitrides (MXenes) for energy storage," *Nature Reviews Materials*, vol. 2, no. 2. Nature Publishing Group, Jan. 17, 2017. doi: 10.1038/natrevmats.2016.98.

[16] M. Ghidiu *et al.*, "Synthesis and characterization of two-dimensional $Nb_4C_3$ (MXene)," *Chem. Commun.*, vol. 50, no. 67, pp. 9517–9520, 2014, doi: 10.1039/C4CC03366C.

[17] M. Khazaei, M. Arai, T. Sasaki, M. Estili, and Y. Sakka, "Two-dimensional molybdenum carbides: potential thermoelectric materials of the MXene family," *Phys. Chem. Chem. Phys.*, vol. 16, no. 17, pp. 7841–7849, 2014, doi: 10.1039/C4CP00467A.

[18] M. Kurtoglu, M. Naguib, Y. Gogotsi, and M. W. Barsoum, "First principles study of two-dimensional early transition metal carbides," *MRS Commun*, vol. 2, no. 4, pp. 133–137, Dec. 2012, doi: 10.1557/mrc.2012.25.

[19] M. Khazaei *et al.*, "Novel Electronic and Magnetic Properties of Two-Dimensional Transition Metal Carbides and Nitrides," *Adv Funct Mater*, vol. 23, no. 17, pp. 2185–2192, May 2013, doi: 10.1002/adfm.201202502.

[20] P. Urbankowski *et al.*, "Synthesis of two-dimensional titanium nitride $Ti_4N_3$ (MXene)," *Nanoscale*, vol. 8, no. 22, pp. 11385–11391, 2016, doi: 10.1039/C6NR02253G.

[21] M. Khazaei *et al.*, "Nearly free electron states in MXenes," *Phys Rev B*, vol. 93, no. 20, p. 205125, May 2016, doi: 10.1103/PhysRevB.93.205125.

[22] Y. Xie and P. R. C. Kent, "Hybrid density functional study of structural and electronic properties of functionalized Ti N) monolayers," *Phys Rev B*, vol. 87, no. 23, p. 235441, Jun. 2013, doi: 10.1103/PhysRevB.87.235441.

[23] A. L. Ivanovskii and A. N. Enyashin, "Graphene-like transition-metal nanocarbides and nanonitrides," *Russian Chemical Reviews*, vol. 82, no. 8, pp. 735–746, Aug. 2013, doi: 10.1070/RC2013v082n08ABEH004398.

[24] M. Khazaei *et al.*, "Novel Electronic and Magnetic Properties of Two-Dimensional Transition Metal Carbides and Nitrides," *Adv Funct Mater*, vol. 23, no. 17, pp. 2185–2192, May 2013, doi: 10.1002/adfm.201202502.

[25] M. Naguib, V. N. Mochalin, M. W. Barsoum, and Y. Gogotsi, "25th anniversary article: MXenes: A new family of two-dimensional materials," *Advanced Materials*, vol. 26, no. 7, pp. 992–1005, Feb. 2014, doi: 10.1002/adma.201304138.

[26] R. M. Ronchi, J. T. Arantes, and S. F. Santos, "Synthesis, structure, properties and applications of MXenes: Current status and perspectives," *Ceramics International*, vol. 45, no. 15. Elsevier Ltd, pp. 18167–18188, Oct. 15, 2019. doi: 10.1016/j.ceramint.2019.06.114.

[27] M. Ghidiu, S. Kota, V. Drozd, and M. W. Barsoum, “Pressure-induced shear and interlayer expansion in $Ti_3C_2$ MXene in the presence of water,” *Sci Adv*, vol. 4, no. 1, Jan. 2018, doi: 10.1126/sciadv.aao6850.

[28] J. L. Hart, K. Hantanasirisakul, A. C. Lang, B. Anasori, Y. Gogotsi, and M. L. Taheri, “Direct Correlation of MXene Surface Chemistry and Electronic Properties,” *Microscopy and Microanalysis*, vol. 24, no. S1, pp. 1606–1607, Aug. 2018, doi: 10.1017/S1431927618008516.

[29] H. Kim, B. Anasori, Y. Gogotsi, and H. N. Alshareef, “Thermoelectric Properties of Two-Dimensional Molybdenum-Based MXenes,” *Chemistry of Materials*, vol. 29, no. 15, pp. 6472–6479, Aug. 2017, doi: 10.1021/acs.chemmater.7b02056.

[30] J. Halim *et al.*, “Synthesis and Characterization of 2D Molybdenum Carbide (MXene),” *Adv Funct Mater*, vol. 26, no. 18, pp. 3118–3127, May 2016, doi: 10.1002/adfm.201505328.

[31] M. Kurtoglu, M. Naguib, Y. Gogotsi, and M. W. Barsoum, “First principles study of two-dimensional early transition metal carbides,” *MRS Commun*, vol. 2, no. 4, pp. 133–137, Dec. 2012, doi: 10.1557/mrc.2012.25.

[32] V. N. Borysiuk, V. N. Mochalin, and Y. Gogotsi, “Bending rigidity of two-dimensional titanium carbide (MXene) nanoribbons: A molecular dynamics study,” *Comput Mater Sci*, vol. 143, pp. 418–424, Feb. 2018, doi: 10.1016/j.commatsci.2017.11.028.

[33] M. Khazaei, A. Ranjbar, M. Arai, T. Sasaki, and S. Yunoki, “Electronic properties and applications of MXenes: a theoretical review,” *J Mater Chem C Mater*, vol. 5, no. 10, pp. 2488–2503, 2017, doi: 10.1039/C7TC00140A.

[34] Y. Xie and P. R. C. Kent, “Hybrid density functional study of structural and electronic properties of functionalized Ti N) monolayers,” *Phys Rev B*, vol. 87, no. 23, p. 235441, Jun. 2013, doi: 10.1103/PhysRevB.87.235441.

[35] Q. Tang, Z. Zhou, and P. Shen, “Are MXenes Promising Anode Materials for Li Ion Batteries? Computational Studies on Electronic Properties and Li Storage Capability of $Ti_3C_2$ and $Ti_3C_2X_2$ (X = F, OH) Monolayer,” *J Am Chem Soc*, vol. 134, no. 40, pp. 16909–16916, Oct. 2012, doi: 10.1021/ja308463r.

[36] I. R. Shein and A. L. Ivanovskii, “Graphene-like titanium carbides and nitrides Tin+1Cn, Tin+1Nn (n=1, 2, and 3) from de-intercalated MAX phases: First-principles probing of their structural, electronic properties and relative stability,” *Comput Mater Sci*, vol. 65, pp. 104–114, Dec. 2012, doi: 10.1016/j.commatsci.2012.07.011.

[37] P. Urbankowski *et al.*, “Synthesis of two-dimensional titanium nitride $Ti_4N_3$ (MXene),” *Nanoscale*, vol. 8, no. 22, pp. 11385–11391, 2016, doi: 10.1039/C6NR02253G.

[38] F. Wu *et al.*, “Theoretical understanding of magnetic and electronic structures of Ti3C2 monolayer and its derivatives,” *Solid State Commun*, vol. 222, pp. 9–13, Nov. 2015, doi: 10.1016/j.ssc.2015.08.023.

[39] Y. Yue, “Fe 2 C monolayer: An intrinsic ferromagnetic MXene,” *J Magn Magn Mater*, vol. 434, pp. 164–168, Jul. 2017, doi: 10.1016/j.jmmm.2017.03.058.

[40] X. Zou, G. Li, Q. Wang, D. Tang, B. Wu, and X. Wang, “Energy storage properties of selectively functionalized Cr-group MXenes,” *Comput Mater Sci*, vol. 150, pp. 236–243, Jul. 2018, doi: 10.1016/j.commatsci.2018.04.014.

[41] I. R. Shein and A. L. Ivanovskii, “Graphene-like titanium carbides and nitrides Tin+1Cn, Tin+1Nn (n=1, 2, and 3) from de-intercalated MAX phases: First-principles probing of their structural, electronic properties and relative stability,” *Comput Mater Sci*, vol. 65, pp. 104–114, Dec. 2012, doi: 10.1016/j.commatsci.2012.07.011.

[42] A. L. Ivanovskii and A. N. Enyashin, “Graphene-like transition-metal nanocarbides and nanonitrides,” *Russian Chemical Reviews*, vol. 82, no. 8, pp. 735–746, Aug. 2013, doi: 10.1070/RC2013v082n08ABEH004398.

[43] M. Khazaei *et al.*, “Novel Electronic and Magnetic Properties of Two-Dimensional Transition Metal Carbides and Nitrides,” *Adv Funct Mater*, vol. 23, no. 17, pp. 2185–2192, May 2013, doi: 10.1002/adfm.201202502.

[44] H. Kumar, N. C. Frey, L. Dong, B. Anasori, Y. Gogotsi, and V. B. Shenoy, “Tunable Magnetism and Transport Properties in Nitride MXenes,” *ACS Nano*, vol. 11, no. 8, pp. 7648–7655, Aug. 2017, doi: 10.1021/acsnano.7b02578.

[45] X.-H. Zha *et al.*, “Promising electron mobility and high thermal conductivity in $Sc_2CT_2$ (T = F, OH) MXenes,” *Nanoscale*, vol. 8, no. 11, pp. 6110–6117, 2016, doi: 10.1039/C5NR08639F.

[46] K. Luo *et al.*, “First-principles study on the electrical and thermal properties of the semiconducting $Sc_3(CN)F_2$ MXene,” *RSC Adv*, vol. 8, no. 40, pp. 22452–22459, 2018, doi: 10.1039/C8RA03424A.

[47] X.-H. Zha *et al.*, “Promising electron mobility and high thermal conductivity in $Sc_2CT_2$ (T = F, OH) MXenes,” *Nanoscale*, vol. 8, no. 11, pp. 6110–6117, 2016, doi: 10.1039/C5NR08639F.

[48] K. Hantanasirisakul *et al.*, “Fabrication of $Ti_3C_2T_x$ MXene Transparent Thin Films with Tunable Optoelectronic Properties,” *Adv Electron Mater*, vol. 2, no. 6, Jun. 2016, doi: 10.1002/aelm.201600050.

[49] C. (John) Zhang *et al.*, “Transparent, Flexible, and Conductive 2D Titanium Carbide (MXene) Films with High Volumetric Capacitance,” *Advanced Materials*, vol. 29, no. 36, Sep. 2017, doi: 10.1002/adma.201702678.

[50] G. R. Berdiyorov, “Optical properties of functionalized Ti3C2T2 (T = F, O, OH) MXene: First-principles calculations,” *AIP Adv*, vol. 6, no. 5, May 2016, doi: 10.1063/1.4948799.

[51] C. Xing *et al.*, “Two-Dimensional MXene ($Ti_3C_2$)-Integrated Cellulose Hydrogels: Toward Smart Three-Dimensional Network Nanoplatforms Exhibiting Light-Induced Swelling and Bimodal Photothermal/Chemotherapy Anticancer Activity,” *ACS Appl Mater Interfaces*, vol. 10, no. 33, pp. 27631–27643, Aug. 2018, doi: 10.1021/acsami.8b08314.

[52] X. Yu, X. Cai, H. Cui, S.-W. Lee, X.-F. Yu, and B. Liu, “Fluorine-free preparation of titanium carbide MXene quantum dots with high near-infrared photothermal performances for cancer therapy,” *Nanoscale*, vol. 9, no. 45, pp. 17859–17864, 2017, doi: 10.1039/C7NR05997C.

[53] X. Guo, X. Zhang, S. Zhao, Q. Huang, and J. Xue, “High adsorption capacity of heavy metals on two-dimensional MXenes: an ab initio study with molecular dynamics simulation,” *Physical Chemistry Chemical Physics*, vol. 18, no. 1, pp. 228–233, 2016, doi: 10.1039/C5CP06078H.

[54] L. M. Azofra, N. Li, D. R. MacFarlane, and C. Sun, “Promising prospects for 2D $d^2$–$d^4$ $M_3C_2$ transition metal carbides (MXenes) in $N_2$ capture and conversion into ammonia,” *Energy Environ Sci*, vol. 9, no. 8, pp. 2545–2549, 2016, doi: 10.1039/C6EE01800A.

[55] Y. Dong *et al.*, “Metallic MXenes: A new family of materials for flexible triboelectric nanogenerators,” *Nano Energy*, vol. 44, pp. 103–110, Feb. 2018, doi: 10.1016/j.nanoen.2017.11.044.

[56] T. Hu, J. Yang, and X. Wang, “Carbon vacancies in $Ti_2CT_2$ MXenes: defects or a new opportunity?,” *Physical Chemistry Chemical Physics*, vol. 19, no. 47, pp. 31773–31780, 2017, doi: 10.1039/C7CP06593K.

[57] A. Sarycheva, A. Polemi, Y. Liu, K. Dandekar, B. Anasori, and Y. Gogotsi, “2D titanium carbide (MXene) for wireless communication,” *Sci Adv*, vol. 4, no. 9, Sep. 2018, doi: 10.1126/sciadv.aau0920.

[58] Y. Yue, “Fe 2 C monolayer: An intrinsic ferromagnetic MXene,” *J Magn Magn Mater*, vol. 434, pp. 164–168, Jul. 2017, doi: 10.1016/j.jmmm.2017.03.058.

[59] G. Gao, G. Ding, J. Li, K. Yao, M. Wu, and M. Qian, “Monolayer MXenes: promising half-metals and spin gapless semiconductors,” *Nanoscale*, vol. 8, no. 16, pp. 8986–8994, 2016, doi: 10.1039/C6NR01333C.

[60] M. Mariano *et al.*, “Solution-processed titanium carbide MXene films examined as highly transparent conductors,” *Nanoscale*, vol. 8, no. 36, pp. 16371–16378, 2016, doi: 10.1039/C6NR03682A.

[61] M. Naguib *et al.*, “New Two-Dimensional Niobium and Vanadium Carbides as Promising Materials for Li-Ion Batteries,” *J Am Chem Soc*, vol. 135, no. 43, pp. 15966–15969, Oct. 2013, doi: 10.1021/ja405735d.

[62] Q. Hu *et al.*, “MXene: A New Family of Promising Hydrogen Storage Medium,” *J Phys Chem A*, vol. 117, no. 51, pp. 14253–14260, Dec. 2013, doi: 10.1021/jp409585v.

[63] M. Ghidiu, M. R. Lukatskaya, M.-Q. Zhao, Y. Gogotsi, and M. W. Barsoum, “Conductive two-dimensional titanium carbide ‘clay’ with high volumetric capacitance,” *Nature*, vol. 516, no. 7529, pp. 78–81, Dec. 2014, doi: 10.1038/nature13970.

[64] B. Soundiraraju and B. K. George, “Two-Dimensional Titanium Nitride ($Ti_2N$) MXene: Synthesis, Characterization, and Potential Application as Surface-Enhanced Raman Scattering Substrate,” *ACS Nano*, vol. 11, no. 9, pp. 8892–8900, Sep. 2017, doi: 10.1021/acsnano.7b03129.

[65] X. Liu, J. Wu, J. He, and L. Zhang, “Electromagnetic interference shielding effectiveness of titanium carbide sheets,” *Mater Lett*, vol. 205, pp. 261–263, Oct. 2017, doi: 10.1016/j.matlet.2017.06.101.

[66] F. Shahzad *et al.*, “Electromagnetic interference shielding with 2D transition metal carbides (MXenes),” *Science (1979)*, vol. 353, no. 6304, pp. 1137–1140, Sep. 2016, doi: 10.1126/science.aag2421.

[67] L. E. Scriven, “Physics and Applications of DIP Coating and Spin Coating,” *MRS Proceedings*, vol. 121, p. 717, Feb. 1988, doi: 10.1557/PROC-121-717.

[68] S. Fakirov, Ed., *Nano-size Polymers*. Cham: Springer International Publishing, 2016. doi: 10.1007/978-3-319-39715-3.

[69] S. Naficy *et al.*, “Graphene oxide dispersions: tuning rheology to enable fabrication,” *Mater. Horiz.*, vol. 1, no. 3, pp. 326–331, 2014, doi: 10.1039/C3MH00144J.

[70] R. Jayakrishnan, T. T. John, C. S. Kartha, K. P. Vijayakumar, T. Abe, and Y. Kashiwaba, “Defect analysis of sprayed β-$In_2S_3$ thin films using photoluminescence studies,” *Semicond Sci Technol*, vol. 20, no. 12, pp. 1162–1167, Dec. 2005, doi: 10.1088/0268-1242/20/12/003.

[71] J. Lu *et al.*, “Epitaxial growth of large-scale In2S3 nanoflakes and the construction of a high performance In2S3/Si photodetector,” *J Mater Chem C Mater*, vol. 7, no. 39, pp. 12104–12113, 2019, doi: 10.1039/c9tc03795k.

[72] J. Li, H. Li, X. Niu, and Z. Wang, “Low-Dimensional In2Se3Compounds: From Material Preparations to Device Applications,” *ACS Nano*, vol. 15, no. 12. American Chemical Society, pp. 18683–18707, Dec. 28, 2021. doi: 10.1021/acsnano.1c03836.

[73] M. S. Claro, J. Grzonka, N. Nicoara, P. J. Ferreira, and S. Sadewasser, “Wafer-scale fabrication of fast two-dimensional β-In 2 Se 3 photodetectors.”

[74] K. Kim, J.-Y. Choi, T. Kim, S.-H. Cho, and H.-J. Chung, “A role for graphene in silicon-based semiconductor devices,” *Nature*, vol. 479, no. 7373, pp. 338–344, Nov. 2011, doi: 10.1038/nature10680.

[75] N. Youngblood, C. Chen, S. J. Koester, and M. Li, “Waveguide-integrated black phosphorus photodetector with high responsivity and low dark current,” *Nat Photonics*, vol. 9, no. 4, pp. 247–252, Apr. 2015, doi: 10.1038/nphoton.2015.23.

[76] A. H. Woomer, T. W. Farnsworth, J. Hu, R. A. Wells, C. L. Donley, and S. C. Warren, “Phosphorene: Synthesis, Scale-Up, and Quantitative Optical Spectroscopy,” *ACS Nano*, vol. 9, no. 9, pp. 8869–8884, Sep. 2015, doi: 10.1021/acsnano.5b02599.

[77] H. Shi *et al.*, “Ultrafast Electrochemical Synthesis of Defect-Free In2Se3 Flakes for Large-Area Optoelectronics,” *Advanced Materials*, vol. 32, no. 8, Feb. 2020, doi: 10.1002/adma.201907244.

[78] Z. Q. Zheng, J. D. Yao, and G. W. Yang, “Growth of centimeter-scale high-quality $In_2Se_3$ films for transparent, flexible and high performance photodetectors,” *J Mater Chem C Mater*, vol. 4, no. 34, pp. 8094–8103, 2016, doi: 10.1039/C6TC02296K.

[79] W. Ding *et al.*, “Prediction of intrinsic two-dimensional ferroelectrics in In2Se3 and other III2-VI3 van der Waals materials,” *Nat Commun*, vol. 8, no. 1, p. 14956, Apr. 2017, doi: 10.1038/ncomms14956.

[80] J. O. Island, S. I. Blanter, M. Buscema, H. S. J. van der Zant, and A. Castellanos-Gomez, “Gate Controlled Photocurrent Generation Mechanisms in High-Gain $In_2Se_3$ Phototransistors,” *Nano Lett*, vol. 15, no. 12, pp. 7853–7858, Dec. 2015, doi: 10.1021/acs.nanolett.5b02523.

[81] D. A. Bandurin *et al.*, “High electron mobility, quantum Hall effect and anomalous optical response in atomically thin InSe,” *Nat Nanotechnol*, vol. 12, no. 3, pp. 223–227, Mar. 2017, doi: 10.1038/nnano.2016.242.

[82] Y. Zhou *et al.*, “Epitaxy and Photoresponse of Two-Dimensional GaSe Crystals on Flexible Transparent Mica Sheets,” *ACS Nano*, vol. 8, no. 2, pp. 1485–1490, Feb. 2014, doi: 10.1021/nn405529r.

[83] S. Witomska, T. Leydecker, A. Ciesielski, and P. Samorì, “Production and Patterning of Liquid Phase–Exfoliated 2D Sheets for Applications in Optoelectronics,” *Adv Funct Mater*, vol. 29, no. 22, May 2019, doi: 10.1002/adfm.201901126.

[84] W. Ding *et al.*, “Prediction of intrinsic two-dimensional ferroelectrics in In 2 Se 3 and other III 2 -VI 3 van der Waals materials,” *Nat Commun*, vol. 8, Apr. 2017, doi: 10.1038/ncomms14956.

[85] Z. Lu *et al.*, “2D Materials Based on Main Group Element Compounds: Phases, Synthesis, Characterization, and Applications,” *Advanced Functional Materials*, vol. 30, no. 40. Wiley-VCH Verlag, Oct. 01, 2020. doi: 10.1002/adfm.202001127.

[86] C. Polyzoidis *et al.*, “Piezo-Phototronic In2Se3 Nanosheets as a Material Platform for Printable Electronics toward Multifunctional Sensing Applications,” *Adv Mater Technol*, vol. 8, no. 17, Sep. 2023, doi: 10.1002/admt.202300203.

[87] K. S. Novoselov, A. Mishchenko, A. Carvalho, and A. H. Castro Neto, “2D materials and van der Waals heterostructures,” *Science (1979)*, vol. 353, no. 6298, Jul. 2016, doi: 10.1126/science.aac9439.

[88] P. V. Pham *et al.*, “2D Heterostructures for Ubiquitous Electronics and Optoelectronics: Principles, Opportunities, and Challenges,” *Chem Rev*, vol. 122, no. 6, pp. 6514–6613, Mar. 2022, doi: 10.1021/acs.chemrev.1c00735.

[89] R. Ganatra and Q. Zhang, “Few-Layer $MoS_2$ : A Promising Layered Semiconductor,” *ACS Nano*, vol. 8, no. 5, pp. 4074–4099, May 2014, doi: 10.1021/nn405938z.

[90] Y. Li, H. Wang, L. Xie, Y. Liang, G. Hong, and H. Dai, "MoS $_2$ Nanoparticles Grown on Graphene: An Advanced Catalyst for the Hydrogen Evolution Reaction," *J Am Chem Soc*, vol. 133, no. 19, pp. 7296–7299, May 2011, doi: 10.1021/ja201269b.

[91] S. Ding, D. Zhang, J. S. Chen, and X. W. (David) Lou, "Facile synthesis of hierarchical MoS $_2$ microspheres composed of few-layered nanosheets and their lithium storage properties," *Nanoscale*, vol. 4, no. 1, pp. 95–98, 2012, doi: 10.1039/C1NR11552A.

[92] S. Wi *et al.*, "Enhancement of Photovoltaic Response in Multilayer MoS $_2$ Induced by Plasma Doping," *ACS Nano*, vol. 8, no. 5, pp. 5270–5281, May 2014, doi: 10.1021/nn5013429.

[93] W. Wu *et al.*, "Piezoelectricity of single-atomic-layer MoS2 for energy conversion and piezotronics," *Nature*, vol. 514, no. 7523, pp. 470–474, Oct. 2014, doi: 10.1038/nature13792.

[94] D. Jariwala, V. K. Sangwan, L. J. Lauhon, T. J. Marks, and M. C. Hersam, "Emerging Device Applications for Semiconducting Two-Dimensional Transition Metal Dichalcogenides," *ACS Nano*, vol. 8, no. 2, pp. 1102–1120, Feb. 2014, doi: 10.1021/nn500064s.

[95] X. Li and H. Zhu, "Two-dimensional MoS2: Properties, preparation, and applications," *Journal of Materiomics*, vol. 1, no. 1, pp. 33–44, Mar. 2015, doi: 10.1016/j.jmat.2015.03.003.

[96] G. Eda, H. Yamaguchi, D. Voiry, T. Fujita, M. Chen, and M. Chhowalla, "Photoluminescence from Chemically Exfoliated MoS $_2$," *Nano Lett*, vol. 11, no. 12, pp. 5111–5116, Dec. 2011, doi: 10.1021/nl201874w.

[97] G. Eda, H. Yamaguchi, D. Voiry, T. Fujita, M. Chen, and M. Chhowalla, "Photoluminescence from Chemically Exfoliated MoS $_2$," *Nano Lett*, vol. 11, no. 12, pp. 5111–5116, Dec. 2011, doi: 10.1021/nl201874w.

[98] M. Amani *et al.*, "Near-unity photoluminescence quantum yield in MoS2," *Science (1979)*, vol. 350, no. 6264, pp. 1065–1068, Nov. 2015, doi: 10.1126/science.aad2114.

[99] O. Samy, S. Zeng, M. D. Birowosuto, and A. El Moutaouakil, "A Review on MoS2 Properties, Synthesis, Sensing Applications and Challenges," *Crystals (Basel)*, vol. 11, no. 4, p. 355, Mar. 2021, doi: 10.3390/cryst11040355.

[100] Y. Cheng *et al.*, "Tuning Photoluminescence Performance of Monolayer MoS $_2$ via H $_2$ O $_2$ Aqueous Solution," *Chinese Physics Letters*, vol. 32, no. 11, p. 117801, Nov. 2015, doi: 10.1088/0256-307X/32/11/117801.

[101] M. S. Ullah, A. H. Bin Yousuf, A. D. Es-Sakhi, and M. H. Chowdhury, "Analysis of optical and electronic properties of MoS2 for optoelectronics and FET applications," 2018, p. 020001. doi: 10.1063/1.5034320.

[102] M. Ghorbani-Asl, N. Zibouche, M. Wahiduzzaman, A. F. Oliveira, A. Kuc, and T. Heine, "Electromechanics in MoS2 and WS2: nanotubes vs. monolayers," *Sci Rep*, vol. 3, no. 1, p. 2961, Oct. 2013, doi: 10.1038/srep02961.

[103] M. Ghorbani-Asl, N. Zibouche, M. Wahiduzzaman, A. F. Oliveira, A. Kuc, and T. Heine, “Electromechanics in MoS2 and WS2: nanotubes vs. monolayers,” *Sci Rep*, vol. 3, no. 1, p. 2961, Oct. 2013, doi: 10.1038/srep02961.

[104] Y.-C. Tsai and Y. Li, “Impact of Doping Concentration on Electronic Properties of Transition Metal-Doped Monolayer Molybdenum Disulfide,” *IEEE Trans Electron Devices*, vol. 65, no. 2, pp. 733–738, Feb. 2018, doi: 10.1109/TED.2017.2782667.

[105] E. S. Kadantsev and P. Hawrylak, “Electronic structure of a single MoS2 monolayer,” *Solid State Commun*, vol. 152, no. 10, pp. 909–913, May 2012, doi: 10.1016/j.ssc.2012.02.005.

[106] P. Johari and V. B. Shenoy, “Tuning the Electronic Properties of Semiconducting Transition Metal Dichalcogenides by Applying Mechanical Strains,” *ACS Nano*, vol. 6, no. 6, pp. 5449–5456, Jun. 2012, doi: 10.1021/nn301320r.

[107] H. Iwai, K. Kakushima, and H. Wong, “CHALLENGES FOR FUTURE SEMICONDUCTOR MANUFACTURING,” *International Journal of High Speed Electronics and Systems*, vol. 16, no. 01, pp. 43–81, Mar. 2006, doi: 10.1142/S0129156406003539.

[108] L. Liu, Z. Liu, P. Huang, Z. Wu, and S. Jiang, “Protein-induced ultrathin molybdenum disulfide (MoS $_2$ ) flakes for a water-based lubricating system,” *RSC Adv*, vol. 6, no. 114, pp. 113315–113321, 2016, doi: 10.1039/C6RA23786J.

[109] R. F. Hossain, I. G. Deaguero, T. Boland, and A. B. Kaul, “Biocompatible, large-format, inkjet printed heterostructure MoS2-graphene photodetectors on conformable substrates,” *NPJ 2D Mater Appl*, vol. 1, no. 1, p. 28, Sep. 2017, doi: 10.1038/s41699-017-0034-2.

[110] Z. Sobanska, L. Zapor, M. Szparaga, and M. Stepnik, “Biological effects of molybdenum compounds in nanosized forms under <i>in vitro</i> and <i>in vivo</i> conditions,” *Int J Occup Med Environ Health*, vol. 33, no. 1, pp. 1–19, Jan. 2020, doi: 10.13075/ijomeh.1896.01411.

[111] X. Weng and S. Neethirajan, “Immunosensor Based on Antibody-Functionalized MoS $_2$ for Rapid Detection of Avian Coronavirus on Cotton Thread,” *IEEE Sens J*, vol. 18, no. 11, pp. 4358–4363, Jun. 2018, doi: 10.1109/JSEN.2018.2829084.

[112] J. Chai *et al.*, “MoS2/Polymer Heterostructures Enabling Stable Resistive Switching and Multistate Randomness,” *Advanced Materials*, vol. 32, no. 42, Oct. 2020, doi: 10.1002/adma.202002704.

[113] R. Ono *et al.*, “Elucidation of PVD MoS2film formation process and its structure focusing on sub-monolayer region,” *Jpn J Appl Phys*, vol. 61, no. SC, May 2022, doi: 10.35848/1347-4065/ac3fc9.

[114] C. Albonetti *et al.*, “Parallel-local anodic oxidation of silicon surfaces by soft stamps,” *Nanotechnology*, vol. 19, no. 43, p. 435303, Oct. 2008, doi: 10.1088/0957-4484/19/43/435303.

[115] X. Zheng *et al.*, “Spatial defects nanoengineering for bipolar conductivity in MoS2,” *Nat Commun*, vol. 11, no. 1, p. 3463, Jul. 2020, doi: 10.1038/s41467-020-17241-1.

[116] T. C. Bond *et al.*, “Bounding the role of black carbon in the climate system: A scientific assessment,” *Journal of Geophysical Research: Atmospheres*, vol. 118, no. 11, pp. 5380–5552, Jun. 2013, doi: 10.1002/jgrd.50171.

[117] C. I. Davidson, R. F. Phalen, and P. A. Solomon, “Airborne Particulate Matter and Human Health: A Review,” *Aerosol Science and Technology*, vol. 39, no. 8, pp. 737–749, Aug. 2005, doi: 10.1080/02786820500191348.

[118] M. Hermesmann and T. E. Müller, “Green, Turquoise, Blue, or Grey? Environmentally friendly Hydrogen Production in Transforming Energy Systems,” *Prog Energy Combust Sci*, vol. 90, p. 100996, May 2022, doi: 10.1016/j.pecs.2022.100996.

[119] G. A. Kelesidis, E. Goudeli, and S. E. Pratsinis, “Flame synthesis of functional nanostructured materials and devices: Surface growth and aggregation,” *Proceedings of the Combustion Institute*, vol. 36, no. 1, pp. 29–50, 2017, doi: 10.1016/j.proci.2016.08.078.

[120] C. Liu *et al.*, “Flame-formed carbon nanoparticles exhibit quantum dot behaviors,” *Proceedings of the National Academy of Sciences*, vol. 116, no. 26, pp. 12692–12697, Jun. 2019, doi: 10.1073/pnas.1900205116.

[121] R. I. Kaiser and N. Hansen, “An Aromatic Universe–A Physical Chemistry Perspective,” *J Phys Chem A*, vol. 125, no. 18, pp. 3826–3840, May 2021, doi: 10.1021/acs.jpca.1c00606.

[122] L. J. Allamandola, G. G. M. Tielens, and J. R. Barker, “Interstellar polycyclic aromatic hydrocarbons - The infrared emission bands, the excitation/emission mechanism, and the astrophysical implications,” *Astrophys J Suppl Ser*, vol. 71, p. 733, Dec. 1989, doi: 10.1086/191396.

[123] H. Wang, “Formation of nascent soot and other condensed-phase materials in flames,” *Proceedings of the Combustion Institute*, vol. 33, no. 1, pp. 41–67, 2011, doi: 10.1016/j.proci.2010.09.009.

[124] M. Frenklach, “Reaction mechanism of soot formation in flames,” *Physical Chemistry Chemical Physics*, vol. 4, no. 11, pp. 2028–2037, May 2002, doi: 10.1039/b110045a.

[125] H. Richter and J. B. Howard, “Formation of polycyclic aromatic hydrocarbons and their growth to soot—a review of chemical reaction pathways,” *Prog Energy Combust Sci*, vol. 26, no. 4–6, pp. 565–608, Aug. 2000, doi: 10.1016/S0360-1285(00)00009-5.

[126] M. Commodo *et al.*, “On the early stages of soot formation: Molecular structure elucidation by high-resolution atomic force microscopy,” *Combust Flame*, vol. 205, pp. 154–164, Jul. 2019, doi: 10.1016/j.combustflame.2019.03.042.

[127] F. Schulz *et al.*, “Insights into incipient soot formation by atomic force microscopy,” *Proceedings of the Combustion Institute*, vol. 37, no. 1, pp. 885–892, 2019, doi: 10.1016/j.proci.2018.06.100.

[128] K. O. Johansson, M. P. Head-Gordon, P. E. Schrader, K. R. Wilson, and H. A. Michelsen, “Resonance-stabilized hydrocarbon-radical chain reactions may explain soot inception and

growth," *Science (1979)*, vol. 361, no. 6406, pp. 997–1000, Sep. 2018, doi: 10.1126/science.aat3417.

[129] J. W. Martin *et al.*, "Reactivity of Polycyclic Aromatic Hydrocarbon Soot Precursors: Implications of Localized π-Radicals on Rim-Based Pentagonal Rings," *The Journal of Physical Chemistry C*, vol. 123, no. 43, pp. 26673–26682, Oct. 2019, doi: 10.1021/acs.jpcc.9b07558.

[130] F. S. Gentile *et al.*, "Soot inception: A DFT study of σ and π dimerization of resonantly stabilized aromatic radicals," *Fuel*, vol. 279, p. 118491, Nov. 2020, doi: 10.1016/j.fuel.2020.118491.

[131] J. B. Howard, J. T. McKinnon, Y. Makarovsky, A. L. Lafleur, and M. E. Johnson, "Fullerenes C60 and C70 in flames," *Nature*, vol. 352, no. 6331, pp. 139–141, Jul. 1991, doi: 10.1038/352139a0.

[132] A. D'Anna, "Combustion-formed nanoparticles," *Proceedings of the Combustion Institute*, vol. 32, no. 1, pp. 593–613, 2009, doi: 10.1016/j.proci.2008.09.005.

[133] J. W. Martin *et al.*, "π-Diradical Aromatic Soot Precursors in Flames," *J Am Chem Soc*, vol. 143, no. 31, pp. 12212–12219, Aug. 2021, doi: 10.1021/jacs.1c05030.

[134] J. W. Martin, M. Salamanca, and M. Kraft, "Soot inception: Carbonaceous nanoparticle formation in flames," *Prog Energy Combust Sci*, vol. 88, p. 100956, Jan. 2022, doi: 10.1016/j.pecs.2021.100956.

[135] A. N. Morozov, A. M. Mebel, and M. Frenklach, "Acceleration of a Chemical Reaction due to Nonequilibrium Collisional Dynamics: Dimerization of Polyaromatics," *Journal of Physical Chemistry Letters*, vol. 13, no. 49, pp. 11528–11535, Dec. 2022, doi: 10.1021/acs.jpclett.2c03066.

[136] H. Sabbah *et al.*, "Molecular content of nascent soot: Family characterization using two-step laser desorption laser ionization mass spectrometry," in *Proceedings of the Combustion Institute*, Elsevier Ltd, 2021, pp. 1241–1248. doi: 10.1016/j.proci.2020.09.022.

[137] M. Commodo, G. De Falco, A. Bruno, C. Borriello, P. Minutolo, and A. D'Anna, "Physicochemical evolution of nascent soot particles in a laminar premixed flame: From nucleation to early growth," *Combust Flame*, vol. 162, no. 10, pp. 3854–3863, Apr. 2015, doi: 10.1016/j.combustflame.2015.07.022.

[138] M. Commodo *et al.*, "On the early stages of soot formation: Molecular structure elucidation by high-resolution atomic force microscopy," *Combust Flame*, vol. 205, pp. 154–164, Jul. 2019, doi: 10.1016/j.combustflame.2019.03.042.

[139] F. Schulz *et al.*, "Insights into incipient soot formation by atomic force microscopy," *Proceedings of the Combustion Institute*, vol. 37, no. 1, pp. 885–892, 2019, doi: 10.1016/j.proci.2018.06.100.

[140] L. Gross, F. Mohn, N. Moll, P. Liljeroth, and G. Meyer, "The Chemical Structure of a Molecule Resolved by Atomic Force Microscopy," *Science (1979)*, vol. 325, no. 5944, pp. 1110–1114, Aug. 2009, doi: 10.1126/science.1176210.

[141] G. Rapenne *et al.*, “Launching and landing single molecular wheelbarrows on a Cu(1 0 0) surface,” *Chem Phys Lett*, vol. 431, no. 1–3, pp. 219–222, Nov. 2006, doi: 10.1016/j.cplett.2006.09.080.

[142] J. W. Martin *et al.*, “π-Diradical Aromatic Soot Precursors in Flames,” *J Am Chem Soc*, vol. 143, no. 31, pp. 12212–12219, Aug. 2021, doi: 10.1021/jacs.1c05030.

[143] L. Pascazio, J. W. Martin, A. Menon, D. Hou, X. You, and M. Kraft, “Aromatic penta-linked hydrocarbons in soot nanoparticle formation,” *Proceedings of the Combustion Institute*, vol. 38, no. 1, pp. 1525–1532, 2021, doi: 10.1016/j.proci.2020.09.029.

[144] A. Menon *et al.*, “Reactive localized π-radicals on rim-based pentagonal rings: Properties and concentration in flames,” *Proceedings of the Combustion Institute*, vol. 38, no. 1, pp. 565–573, 2021, doi: 10.1016/j.proci.2020.07.042.

[145] F. S. Gentile *et al.*, “Soot inception: A DFT study of σ and π dimerization of resonantly stabilized aromatic radicals,” *Fuel*, vol. 279, p. 118491, Nov. 2020, doi: 10.1016/j.fuel.2020.118491.

[146] J. W. Martin *et al.*, “Reactivity of Polycyclic Aromatic Hydrocarbon Soot Precursors: Implications of Localized π-Radicals on Rim-Based Pentagonal Rings,” *The Journal of Physical Chemistry C*, vol. 123, no. 43, pp. 26673–26682, Oct. 2019, doi: 10.1021/acs.jpcc.9b07558.

[147] J. Repp, G. Meyer, S. M. Stojković, A. Gourdon, and C. Joachim, “Molecules on Insulating Films: Scanning-Tunneling Microscopy Imaging of Individual Molecular Orbitals,” *Phys Rev Lett*, vol. 94, no. 2, p. 026803, Jan. 2005, doi: 10.1103/PhysRevLett.94.026803.

[148] B. Schuler, G. Meyer, D. Peña, O. C. Mullins, and L. Gross, “Unraveling the Molecular Structures of Asphaltenes by Atomic Force Microscopy,” *J Am Chem Soc*, vol. 137, no. 31, pp. 9870–9876, Aug. 2015, doi: 10.1021/jacs.5b04056.

[149] A. D’Anna, “Combustion-formed nanoparticles,” *Proceedings of the Combustion Institute*, vol. 32, no. 1, pp. 593–613, 2009, doi: 10.1016/j.proci.2008.09.005.

[150] H. Wang, “Formation of nascent soot and other condensed-phase materials in flames,” *Proceedings of the Combustion Institute*, vol. 33, no. 1, pp. 41–67, 2011, doi: 10.1016/j.proci.2010.09.009.

[151] J. W. Martin *et al.*, “Flexoelectricity and the Formation of Carbon Nanoparticles in Flames,” *The Journal of Physical Chemistry C*, vol. 122, no. 38, pp. 22210–22215, Sep. 2018, doi: 10.1021/acs.jpcc.8b08264.

[152] G. Basile, A. Rolando, A. D’Alessio, A. D’Anna, and P. Minutolo, “Coagulation and carbonization processes in slightly sooting premixed flames,” *Proceedings of the Combustion Institute*, vol. 29, no. 2, pp. 2391–2397, Jan. 2002, doi: 10.1016/S1540-7489(02)80291-7.

[153] M. Commodo *et al.*, “On the early stages of soot formation: Molecular structure elucidation by high-resolution atomic force microscopy,” *Combust Flame*, vol. 205, pp. 154–164, Jul. 2019, doi: 10.1016/j.combustflame.2019.03.042.

[154] F. Schulz *et al.*, “Insights into incipient soot formation by atomic force microscopy,” *Proceedings of the Combustion Institute*, vol. 37, no. 1, pp. 885–892, 2019, doi: 10.1016/j.proci.2018.06.100.

[155] E. M. Adkins and J. H. Miller, “Extinction measurements for optical band gap determination of soot in a series of nitrogen-diluted ethylene/air non-premixed flames,” *Physical Chemistry Chemical Physics*, vol. 17, no. 4, pp. 2686–2695, 2015, doi: 10.1039/C4CP04452E.

[156] R. S. Jacobson, A. R. Korte, A. Vertes, and J. H. Miller, “The Molecular Composition of Soot,” *Angewandte Chemie International Edition*, vol. 59, no. 11, pp. 4484–4490, Mar. 2020, doi: 10.1002/anie.201914115.

# CHAPTER 5

# Self-assembly of molecular materials using Temperature-enhanced solvent vapour annealing (TESVA)

**The present chapter describes the realisation of a new experimental setup to manipulate and self-assemble molecules on a substrate.**

One of the main objectives of material science is the assembly of controlled nano-structures with low-cost, up-scalable methods in order to produce functional systems towards numerous applications. In this chapter, we present the setup and assembly of a home-made device to perform temperature enhanced solvent vapor annealing for the growth and manipulation of various molecules when deposited on a substrate. The self-assembly and/or growth happens in a chamber with controlled atmosphere. Tiny amounts of solvent molecules are condensed on the surface, enhancing in this way the mobility of molecules present on the surface, and fostering their self-assembly. This is achieved by changing the temperature difference between the surface of the substrate and a solvent reservoir. Tuning the temperature difference, substrate, or solvent we can realise new nano-structures, which cannot be obtained by conventional deposition methods. The newly organised networks are then characterised by SPM. Our work suggests the exciting possibility of allowing any system to rearrange in an innovative but controlled way on a different surface when the right solvent and temperature difference is realized.

## 5.1 Introduction

Solution processing of (macro)molecules is a straightforward and adaptable technique that enables molecules to self-assemble into functional architecture with tunable physico-chemical properties and structure, opening up possibilities for their technological application in micro- and nanoelectronics [1], [2], [3], [4], [5].

In particular, highly ordered structures can be obtained by “supramolecular” chemistry, i.e. the branch of chemistry exploiting “weak” reversible interaction forces such as van der Waals,

electrostatic interaction, hydrogen bonding etc. The weak, reversible nature of such interactions, as compared to the irreversible ones such, as example, covalent chemistry, allow to create ordered structures on long range, where molecules can attach or detach at a given position until finding the most favourable, low energy supramolecular order. Supramolecular assemblying (0.1–1 nm) is primarily determined by the chemical structure of the molecule and substrate, and therefore by the interaction between intra- and intermolecular interactions as well as molecule–substrate interactions.[6] However, hydrodynamic forces also play a significant role in the larger-scale self-assembly (from 1 nm to several mm), which is primarily dependent on the processing methodologies used [4]. Thus, it should theoretically be possible to modulate the self-assembly from the nanometer up to the several-micrometer scale by regulating the interaction between the forces discussed here.

In the field of supramolecular chemistry, the most conventional technique to deposit molecules on a substrate is using spin-coating. The technique has been described in detail in Chapter 4 of the current thesis.

In this way, a rapid and highly homogenous solvent evaporation is achieved, which can result in the creation of nanoscale assemblies like fibrils or crystals [5].

A slower technique is drop-casting. In this approach, a drop of solution is deposited on the substrate, and left there to evaporate. Solvent evaporation increases the local concentration of solute molecules which begin to interact more with each other and with the substrate, leading eventually to ordered nanostructures.

By using drop-casting, on the other hand, larger crystals or macroscopic structures can grow because of the much slower solvent evaporation process [7], [8]. Using these solution-processing techniques results in a film with a degree of order and eventually crystallinity that is usually lower than that produced by vacuum processing, which involves the thermal evaporation/sublimation of the molecules. This is because physical processes like, as example, dewetting or drop pinning during evaporation create inhomogeneities on the surface, as example the well-known “coffee stain” effect [5].

In this context, solvent vapor annealing (SVA), which includes exposing the deposited samples to a solvent vapor-rich environment, has become more common in recent years. Figure 5-1 below shows an example of the standard instrument configuration used to perform SVA. During SVA, a thin layer of solvent forms on the substrates, which in the right conditions can feature nanometric thickness; molecules already present on the substrate can diffuse in this quasi 2-dimensional layer, which allows the molecules to rearrange into structures characterized by a higher degree of order as compared to the starting samples significantly improving, as example, the performance of electronic devices. Some examples of these

rearranged molecules and nanometric structures can be seen in Figure 5-2 and 5-3.

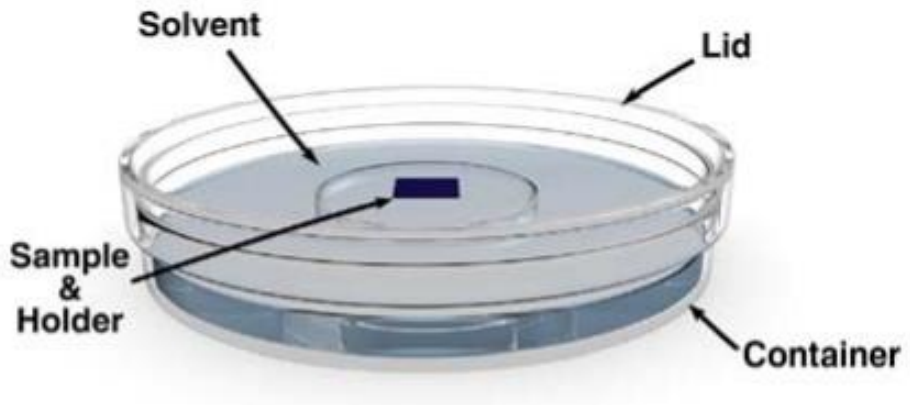


*Figure 5-1. Illustration of a solvent vapour annealing instrumentation, figure taken from* [9].

The standard solvent vapour annealing process consists of four key steps [10].

1) Initially, target molecules are dissolved in solution, typically using a good solvent for such molecules. This solvent can even be different from the one where final self-assembly will be achieved.

This solution is then deposited on the target substrate using above-mentioned standard deposition techniques such as spin coating, dip coating, or others. At difference with standard deposition, in this step we do not want to achieve ordered structures; at the contrary, the higher the disorder and the system energy the better, because such disordered molecules will be easier to rearrange during SVA. A few of these essential factors have been addressed in Chapter 4 for the deposition of MXenes and other 2D materials on substrates mainly via spin-coating.

2) The prepared thin film is inserted in a sealed chamber, where a reservoir of a solvent is present. Solvent evaporates within the chamber saturating the atmosphere and condensing on the sample (Figure 5-1). Since the solvent used has an impact on the annealing process, selection is essential. Different copolymer blocks, for instance, can selectively swell or become

plasticized by the solvent vapor[10].

3) Upon interaction with the solvent molecules, the material structure can change and rearrange at the nanometric scale. For example, block polymers treated with SVA can undergo a swelling of the polymer film that increases the mobility of the polymer chains [10]. Consequently, this makes it easier for the block copolymer morphology to be reorganized. The solvent vapor lowers the polymer's glass transition temperature, facilitating an easier rearrangement [10].

4) Eventually, the solvent vapor is allowed to evaporate, leaving behind the reorganized structure.

The impact of SVA on the final structure is then examined by characterizing the thin film's morphology using a variety of techniques, including spectroscopy, microscopy, and scattering methods. The efficiency of SVA depends upon multiple factors, such as solvent selection, duration of exposure, and the particular characteristics of the system under study.

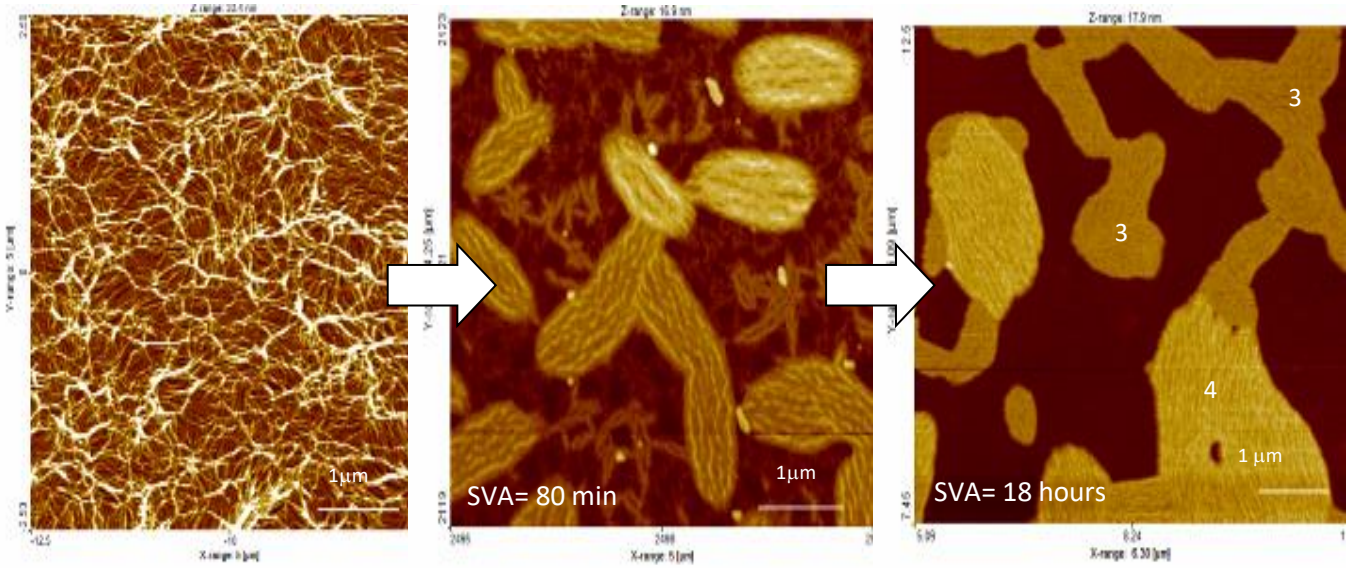


*Figure 5-2. AFM images of Macromolecules deposited on Si/SiOx a) Original morphology after spin-coating. b) After 80 min of SVA. c) After 18 h of SVA, figure taken from ref.* [5]

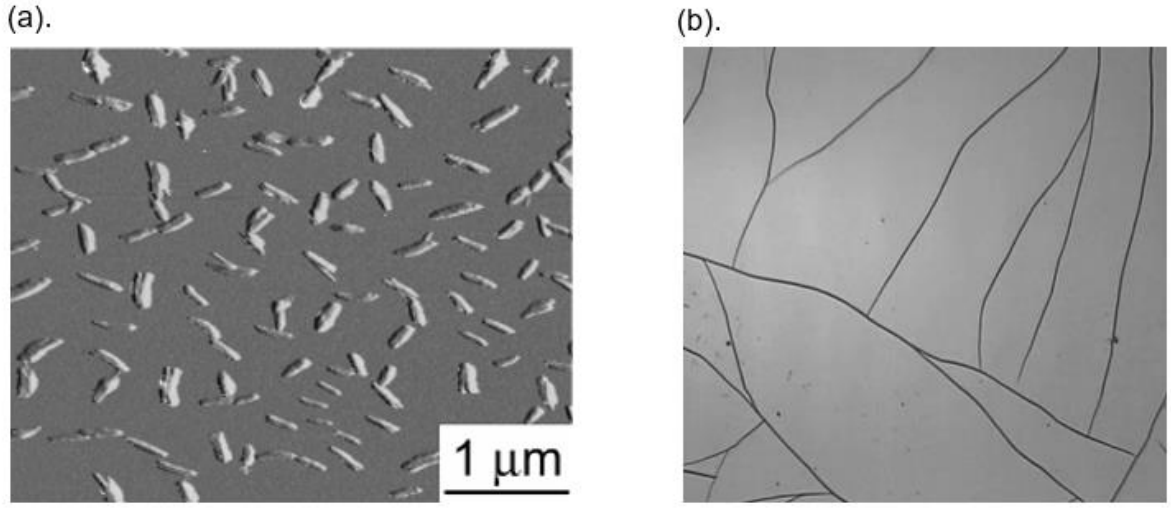


*Figure 5-3. (a) AFM image of PDI nanostructures obtained by spin-coating a $SiO_x$ substrate, (b) Optical microscope image during SVA in THF of PDI spin-cast on $SiO_x$ showing self-assembly length scales spanning over three orders of magnitude, figure taken from ref.* [11]

SVA is often used to improve the quality of some materials but provides no control on the amount of solvent interacting with the target molecules. A more powerful and versatile option of this technique is temperature-enhanced solvent vapour annealing (TESVA), where the temperature of the sample and of a solvent reservoir can be controlled, in this way enhancing or blocking the effects of SVA [5]. By controlling temperature, TESVA allow to condense a thin solvent layer on the substrate, to promote molecular migration in the deposited material. This is typically achieved using few °C of temperature difference, in contrast to thermal annealing, which increases the mobility of molecules at a surface by raising the substrate temperature to significant levels. Therefore, when the substrate is cooled in relation to the reservoir (DT < 0 C), TESVA can yield rearrangement on large scale, with the molecules self-assembling in new macroscopic structures that can even become visible by bare eye.

Figure 5-4 schematically illustrates the TESVA instrumentation used. The TESVA process begins with the traditional spin coating, in which a solution containing the molecules we want to rearrange is first deposited on a flat surface, typically a $Si/SiO_x$ substrate. After that, the sample is placed inside a sealed annealing chamber that is filled with a volatile solvent's vapours. The primary parameter, the difference ($\Delta T$) between the substrate temperature $T_{sub}$ and the liquid solvent reservoir temperature $T_{solv}$, is precisely controlled using a Peltier module within a

range of +10/-10 °C. Only a few nanometers thick layer of liquid is adsorbed on the surface in the case of positive or null Δ*T*. The condensed layer's thickness (d) is determined by van der Waals and gravitational energies using the following formula:

$\Pi(d) = \rho g\,(d + H)$

where Π(d) is the so-called ‘‘disjoining pressure’’, ρ is the liquid density, g the gravitational constant, and H the height of the sample above solvent reservoir.

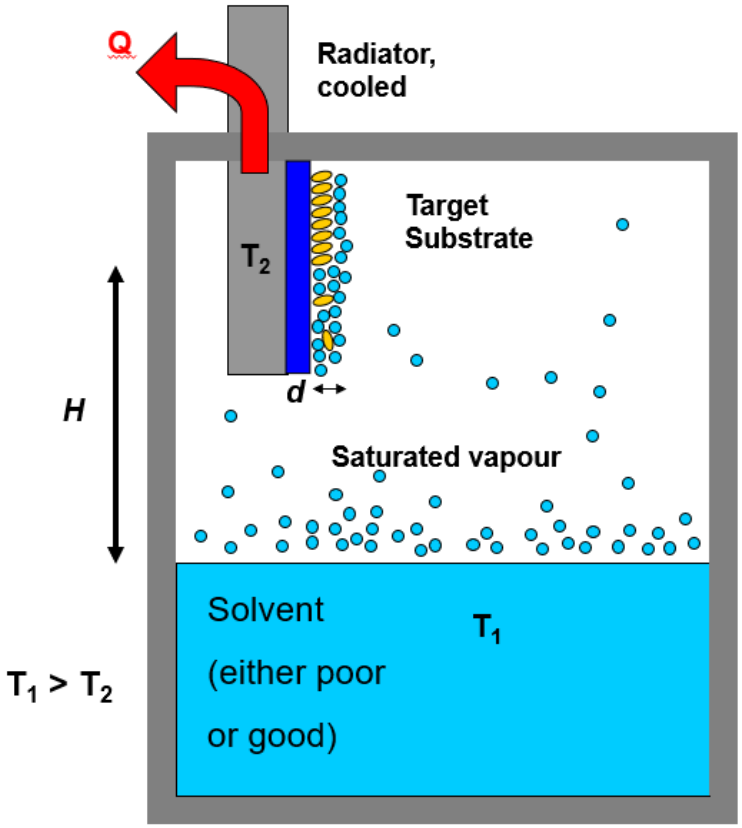


*Figure 5-4. Schematic illustration of the temperature-enhanced solvent vapour annealing (TESVA) process and instrumentation.*

This ultrathin wetting film has been measured experimentally for various liquids [12]. The height difference (H) contribution will begin to make up for a negative ΔT, thickening the wetting film in the process. Within a narrow range of ΔT, the wetting layer will only be slightly thicker and grow with time [13].Macroscopic solvent amounts (as droplets) will condense on

the surface when $\Delta T$ falls below a critical value due to the oversaturation of solvent vapor in the atmosphere.

In the case of solutions, the precise value of d can be challenging to estimate due to the substrate's and the liquid's characteristics, particularly when the solute molecules exhibit self-assembly and liquid crystalline properties, as well as when there are surface irregularities like nanocrystals surface steps or random roughness [14]. Generally speaking, d can be smaller than 30 nm when H is macroscopic (~1 cm). See References [5], [15] for a more thorough discussion.

Since both solvent and solute molecules are confined in a very thin but laterally extended layer and their numbers per unit area are comparable due to the nanometric thickness of the film, the term "solution" cannot be used in this context. Van der Waals interactions are the most common type of interaction between the substrate, solute, and solvent.

Ultimately, if $\Delta T \ll 0$, the deposited molecules resolubilize as a macroscopic layer of solvent absorbs on the sample surface. It is important to note that the temperature effect in TESVA differs significantly from traditional thermal annealing. While a higher temperature is required for thermal annealing to produce greater mobility, a lower temperature is required for TESVA in order to increase the amount of solvent on the surface, solubilize the molecules, and lower the crystallization barrier. Therefore, unlike vacuum evaporation, TESVA promotes molecular mobility at surfaces at lower temperatures rather than activating it thermally. In these circumstances, the growth of macroscopic structures can be aided by a nanometric layer of liquid.

There are many examples of successful growth of macroscopic structures via TESVA in literature. For instance, a one-step in situ process for producing controlled molecular-scale ordered polyaniline (PANI) films using Zn ions and TESVA was reported (Figure 5-5) [16]. High-voltage electron microscopy verified that the resulting PANI film grew as a face-centered cubic structure of, which was crosslinked by coordination with Zn ions. The PANI films' conductivity was significantly increased, and a new class of molecular ordering was created by the in-situ coordination crosslinking, indicating the films' potential application in a range of electrical and energy-related devices.

In a different work, the self-assembly of functionalized polycyclic aromatic hydrocarbon molecules on solid surfaces via Temperature-enhanced Solvent Vapor Annealing (TESVA) has been reported[5]. New C3 symmetric hexa-peri-hexabenzocoronene with alternating hydrophilic and hydrophobic side chains was the subject of the study. By improving the molecules' long-range mobility, TESVA allowed the molecules to diffuse for hundreds of micrometres on a $Si/SiO_x$ surface. This produced large, well-ordered crystals with an edge-on

columnar arrangement, which differs from structures obtained with conventional solution-processing methods. TESVA facilitated macroscopic self-healing in the adsorbed film by offering more control over hydrodynamic forces during self-assembly through its temperature modulation [5]. Atomic force microscopy and optical microscopy were eventually used to track the surface reorganization in real time.

TESVA is a practical approach that enables ordered structures on surfaces to self-assemble in a regulated, adaptable, and economical manner.

Large-scale reactors full of saturated vapors in which the temperature can be controlled are now already present in the majority of chemical production plants, making them easily convertible for TESVA treatments.

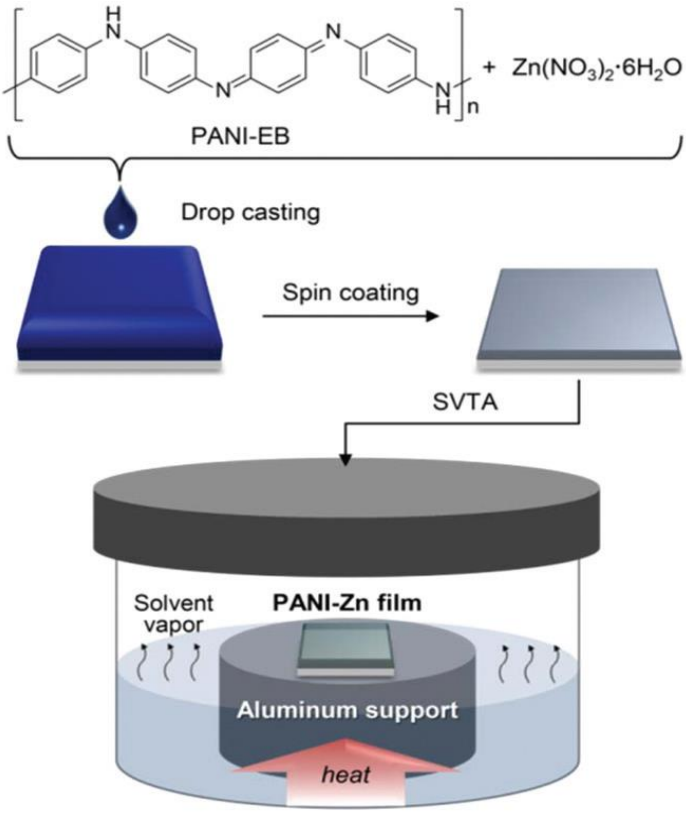


*Figure 5-5. Schematic illustration of a standard temperature-enhanced solvent vapour annealing (TESVA) experiment, figure taken from ref.* [16]

**Assembly of the experimental setup**

As previously stated, an advancement in the development of the SVA technique is the development of the temperature-enhanced solvent vapour annealing, or TESVA. Even though TESVA has already been into use and has had many significant results a realisation of a more automated instrumentation for performing solvent vapour annealing in a controlled way is in need.

Here we present a home-built platform to perform temperature enhanced solvent vapor annealing device was realised in our laboratory (Fig. 5-6) for the growth and manipulation of various molecules when deposited on a substrate. The self-assembly and/or growth happens in a chamber by controlling the temperature difference between the solvent used and the surface of the substrate where our initial system has been deposited. By changing the temperature difference, substrate, or solvent we can realise new nanostructures, which cannot be obtained by conventional deposition methods.

The TESVA apparatus was developed as a collaboration between our group at ISOF/CNR in Bologna and A.P.E Research within our Marie-Curie ITN project ULTIMATE. The device was perceived and installed in our lab in Bologna with the help of PhD student Anton Naumenko and researcher Dr. Derek Jones.

Figure 5-6 depicts our completed TESVA system. The system consists of a chamber into which we place our samples and the solvent we intend to use in the experiment. The chamber is set on a hot plate which gradually warms the chamber and causes the solvent within it to evaporate in a controlled manner. There is an external cooling system using a liquid nitrogen-filled container, tubes connecting it to the sample holder within the chamber so that the liquid nitrogen can flow through it, and a valve controlling the nitrogen flow. The apparatus has three thermocouples connected to it. One thermocouple is attached to the hot plate and the other to the basis inside the chamber, to calculate any heat losses from the hot plate to the interior part of the chamber where the solvent is placed. The 3$^{rd}$ thermocouple is attached to the sample holder to control the temperature difference between the sample and the solvent, a crucial parameter influencing the sample's thickness as mentioned before in the current Chapter.

Each thermocouple is connected to a digital thermometer that records up to eight distinct temperatures for a limitless period of time. The data can be readily exported from the

thermometer using a USB port. More recently a camera system has been set up to record and capture images and videos of the sample undergoing TESVA in real time. Although the camera's focussing mode needs still to be improved, we were able to take pictures of the samples' surfaces inside the chamber.

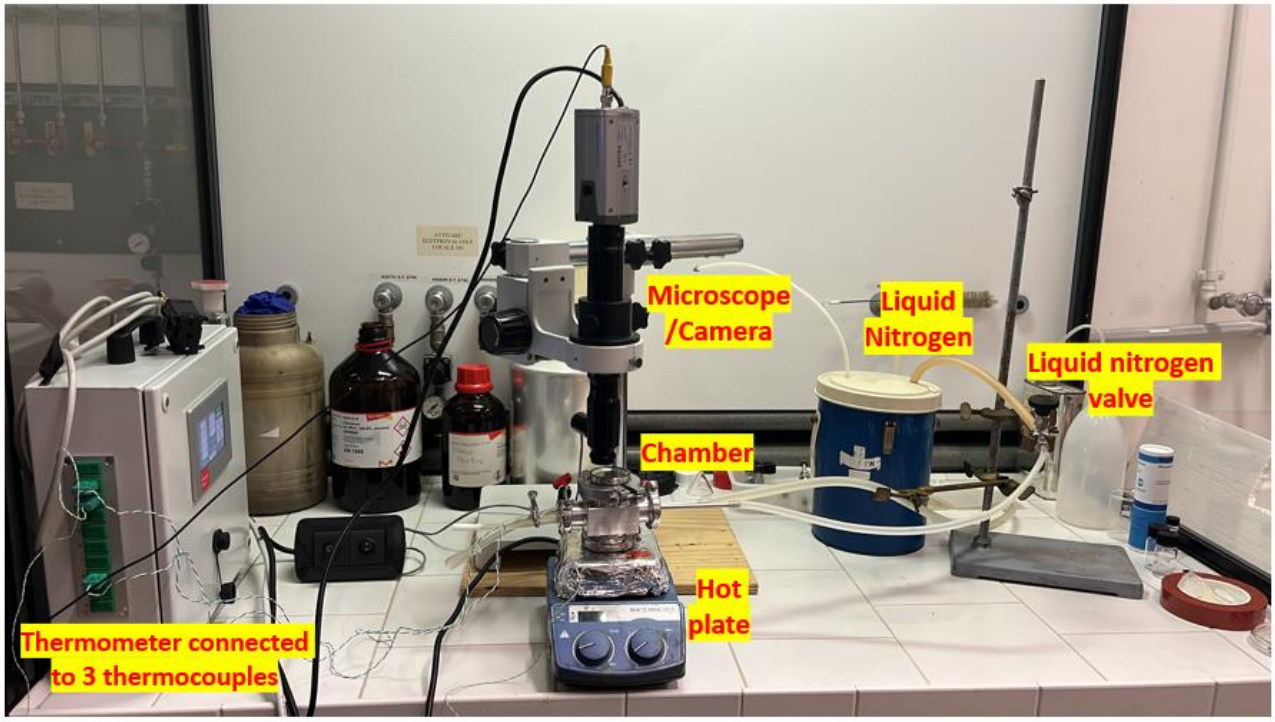


*Figure 5-6 TESVA system with all parts assigned.*

A close-up of the main chamber and the sample holder inside is shown in Figure 5-7 below. Both top and bottom of the chamber are sealed. The upper lid can be easily removed to introduce the solvent and the sample. The solvent is deposited with a pipette on the bottom of the chamber, while the sample is deposited on the nitrogen-cooled sample holder. The sample holder allows for multiple samples to be placed simultaneously, providing us with the chance to deposit different systems and expose them to the same solvent vapors in order to monitor changes between them and reduce waiting times for the experiment.

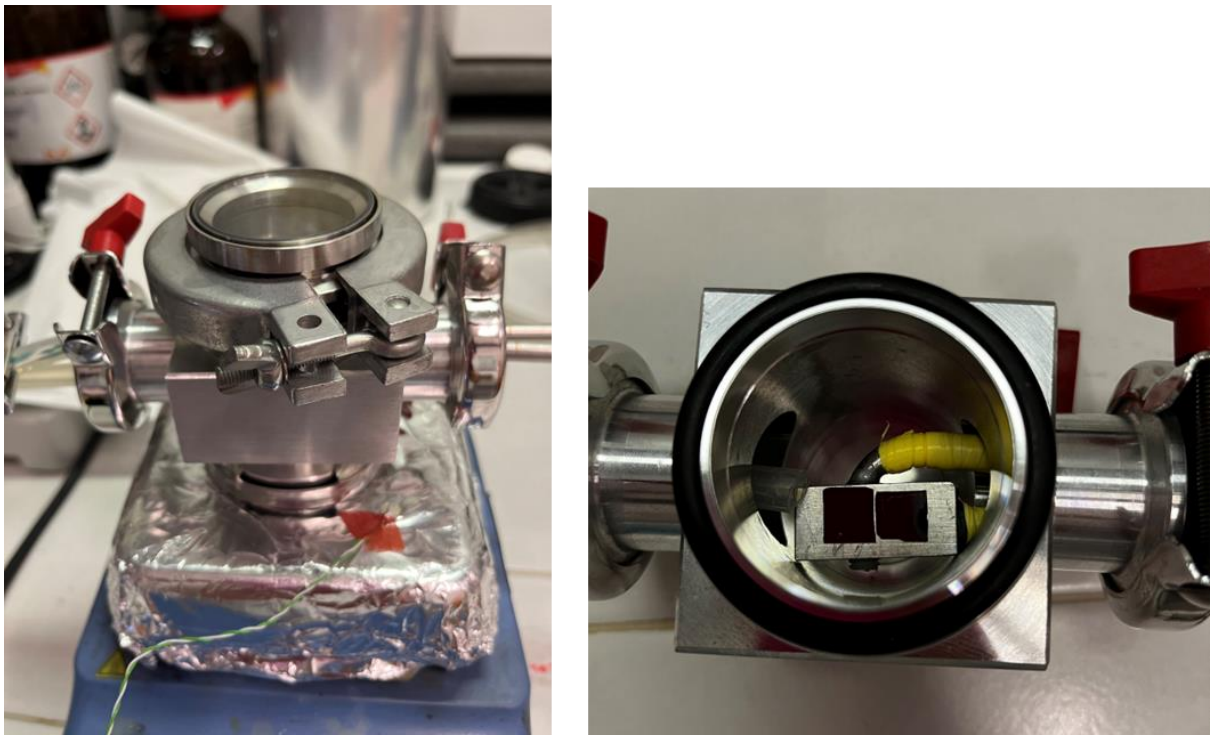

*Figure 5-7. Left: A close up of the TESVA chamber, right: Example of how multiple samples can be inserted and placed inside the chamber in order to perform a TESVA experiment.*

**Self-organised Porphyrins**

As a test material for TESVA, we chose porphyrins, which are promising photoelectronic materials for different applications such as sensors, electronics, photosensitized solar cells, and organic light-emitting devices. Porphyrins are stable organic chromophores that absorb visible light well and/or luminesce with a high level of efficiency. Because of their exceptional photochemical and photophysical qualities as well as their distinct aromatic structure, porphyrins and their metallo-derivatives can be employed in these kinds of devices [17], [18]. The environment and the intermolecular configuration of the chromophores have a significant influence on the photonic properties in addition to the molecular structure. Figure 5-8 shows various structures of key synthetic porphyrin. The rigid, planar macrocycles can accommodate auxiliary moieties like H-bonding motifs and exocyclic ligands at predetermined geometries, allowing for the synthesis of specific supramolecular systems [18]. In a broad range of temperature, pH, and other environmental factors, the core of the

porphyrins remains stable. By adding a range of exocyclic organic motifs and selecting the metal ion chelated in the center of the anionic porphyrin, one can adjust the oxidation and reduction potentials, and consequently the chemical and photonic activities. The metalated compounds' axial ligation provides an extra method of assembly. Because of their well-developed chemistry, porphyrins are the subject of most of the supramolecular chemistry of these macrocycles.

Porphyrins are naturally occurring tetrapyrrolic macrocycles [19]. Porphyrins generally have several Q-bands between 500 and 650 nm with ε 10–20 times less and very strong absorption bands around 400–430 nm (Soret band) with absorbtivities, ε, on the order of $10^5$ $M^{-1}$ $cm^{-1}$. The Gouterman four-orbital model provides an excellent explanation for the electronic spectra, which are dependent on coordinated metal ions and exocyclic modifications [18]. Strong absorptions are also exhibited by porphyrins, usually towards the red[18]. Typical free base porphyrins and some of their metalloderivatives ($Zn^{2+}$, $Mg^{2+}$, etc.) have fluorescence quantum yields between 1% and 15% and corresponding lifetimes between 1 and 15 ns. When Pd and Pt derivatives are utilized in oxygen pressure sensing, for instance, a significant portion of the molecules in the excited state intersystem cross to the triplet state, resulting in phosphorescence quantum yields in matrices that can exceed 90% [18].

Due to their potential applications and the significance of improved theoretical frameworks The development of novel multi-porphyrin architectures through self-assembly and self-organization remains an active field of research. There is a long and rich history of a single type of porphyrin self-organizing into crystalline materials through homo-coordination and nonspecific intermolecular interactions [17], [20]. Exocyclic moieties for particular intermolecular interactions that control how a porphyrin organizes itself into more robust or ordered crystalline systems have been incorporated into more recent efforts [21]. Discrete porphyrin arrays that self-assemble in lipid bilayers' liquid crystalline matrix via electrostatic interactions and served as photo-gated ion conductors are a more recent example of these arrays [22]. Subsequently, arrays assembled through particular intermolecular interactions—like those involving H-bonds [23] and metal–ion coordination—were reported [18], [24]. Linear tapes with H-bonds and coordination chemistry in lipid bilayers demonstrate photo-gated electronic conductivity. The device's function depends on its hierarchical structure, including the molecule, tape alignment, and device organization [25]. Moreover, long-chain hydrocarbons can be used to form liquid crystals, and designed intermolecular interactions can be used to form self-organized systems with various topologies. Self-assembled monolayers can be formed by covalent attachment to surfaces, and packing forces in crystalline materials can be designed. Rapid advancements have been made in

supramolecular synthetic techniques and strategies, and porphyrins' rigid framework makes them especially suitable for the construction of intricate and durable architectures. Materials in one, two, and three dimensions are now commonly available. Research is currently focused on hierarchically organized porphyrinic materials, where the local structure differs from the global organization. These porphyrin assemblies are essential components for the development of many useful photonic devices, as well as models for the study of light-harvesting antennas and photosynthetic reaction centers [26].

Porphyrin systems are an ideal candidate for self-assembling experiments with our TESVA setup for all of the aforementioned reasons.

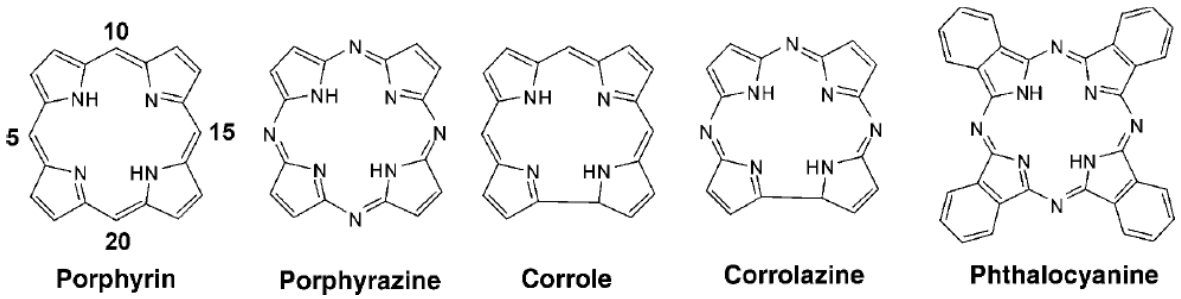


*Figure 5-8. Illustration of different types of Porphyrin structures. Figure taken from ref.* [18]

## 5.3 Results and discussion

Before the realisation and implementation of the TESVA device we experimented with various systems utilising conventional SVA. We performed these experiments using a standard SVA configuration as the one shown in Figure 5-1.

Meso-tetraaryl porphyrins (TpyP(4)) are excellent candidates to use as building blocks in the synthesis of complex structures because of their versatile physicochemical properties and straightforward synthetic routes (Figure 5-9a). As we mentioned before, these properties are interesting because they can be used to investigate novel aspects of the supramolecular

reactivity of these molecules, that are also widely employed as chromophores, in addition to their many potential applications. In order to test these compounds as candidate system for solvent vapour annealing, we tried forming porphyrin-based networks using sodium ions (5-9b) coordinated by 4-pyridyl moieties at the meso- position of the porphyrin rings (Figure 5-9a) [27]. In addition, it is anticipated that the nanostructures comprising these deposits exhibit both tuneable optical and morphological features and a long-range order.

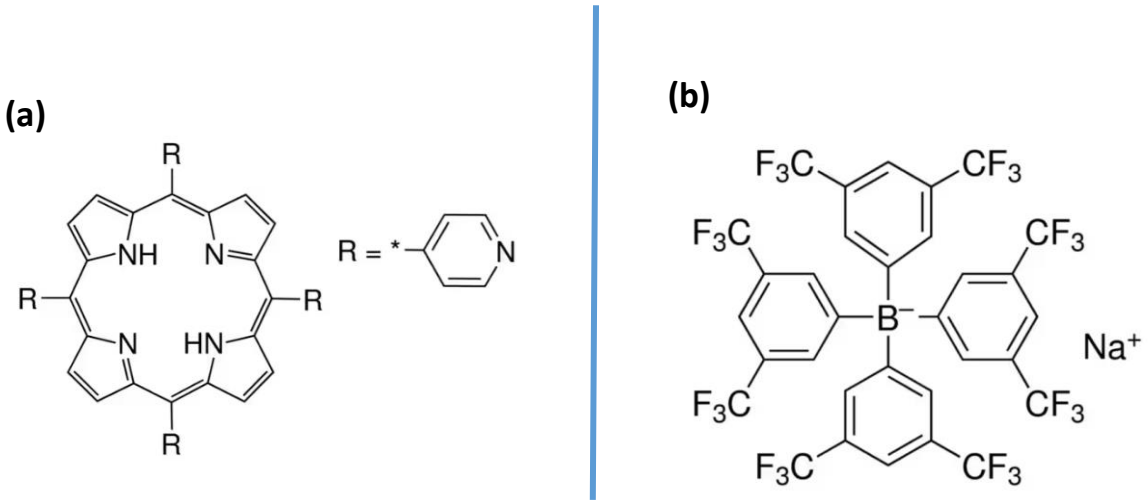


*Figure 5-9. Schematic illustration of the molecular structure of (a) Meso-tetraaryl porphyrins and (b) NaBARF salt.*

Using NaBARF (Figure 5-9b) as a counteranion in $CH_2Cl_2$ allows for easy dissolution of alkaline metal ions. Na+ cations can interact with the unprotonated N atoms at the core of these species in such a weakly polar solvent and in the presence of different tetraaryl porphyrins, forming sitting-atop complexes that resemble the behavior of hydrogen ions functioning as Lewis acids [27].

By coordinating Na+ ions by the pyridyl groups at the macrocycle periphery of different porphyrin units, an efficient multiporphyrin assembly could be achieved (Figure 5-10).

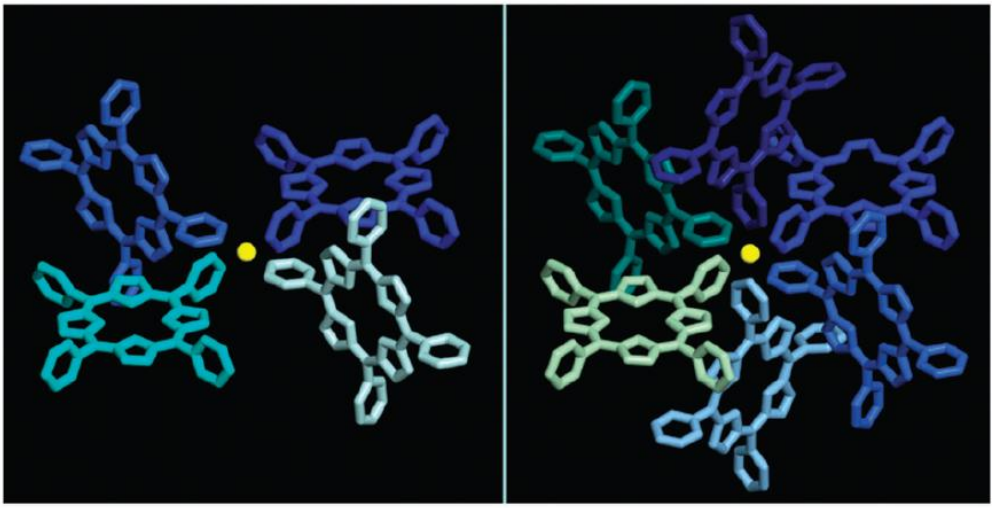

*Figure 5-10. A cartoon illustration of two high symmetry coordination geometries that the Na+ ions could display when interacting with the porphyrin macrocycles' meso-pyridyl groups. Figure taken from ref.* [27]

Initially, a tiny amount of TpyP(4) powder (ca 1 mg) was placed in a 7 mL screw cap glass vial having a PTFE liner filled with 4 mL $CH_2Cl_2$ [27]. Then, the solution was left under stirring at room temperature overnight. The successful synthesis was confirmed by the colour of the final solution (muted magenta). We diluted approximately 3-4 drops in 1-2 mL fresh $CH_2Cl_2$. The final solution should have an absorbance of 0.3 at the peak located around 510 nm. Last, to obtain the deposition of the porphyrins, we added ca. 1 mg of NaBARF (Sodium tetrakis[3,5-bis(trifluoromethyl)phenyl]borate) [27], [28]to the porphyrin solution and we mixed it rapidly. The molecular structure of NaBARF used may be found in Figure 5-9b.

A detailed explanation of the spin coating process is provided in Chapter 4. By spin coating 100 µL on the substrate, we were able to achieve nearly complete surface coverage, as shown in Figure 5-11a below. We prepared two identical samples with the same covering and substrate. One was placed outside as a reference, and the other was introduced inside a standard container for SVA performance. We conducted SVA in the presence of methanol vapours for two hours. The outcome of the SVA experiment is displayed in Figure 5-11b below; the porphyrin structures lose their defined shape, and the initial network appears to be disrupted by methanol vapors. Even though we did not observe the formation of a uniform nanofilm of porphyrins, the disruption of the network is considered a significant alteration that confirms the success of the experiment. Instead, the reference sample showed no changes.

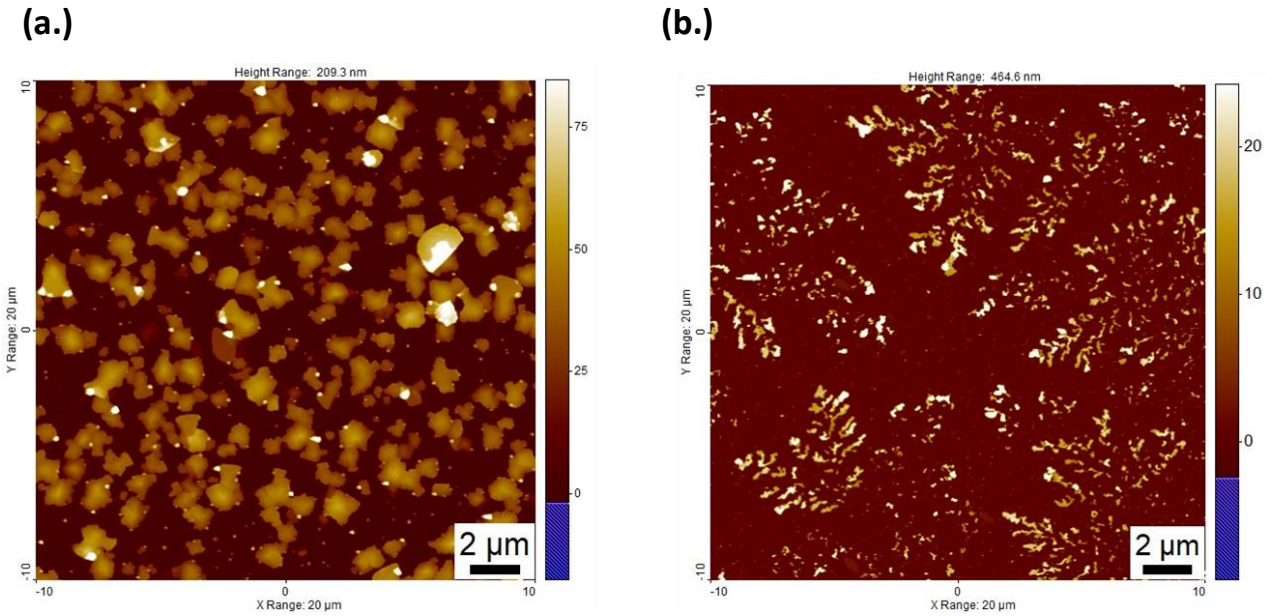


*Figure 5-11 AFM images of porphyrins (a) before SVA, and (b) after SVA in methanol.*

We used the same system to perform TESVA, with the only difference that we prepared two distinct solutions: one containing the porphyrins and another one containing the salt (NaBARF). As mentioned before, from the concentrated solution of the porphyrins we diluted approximately 2 drops in 1 mL fresh $CH_2Cl_2$ in order to prepare our porphyrins solution. Then we dissolved ca. 1 mg of NaBARF in 1 mL of $CH_2Cl_2$We spin coated 100µL of the porphyrins solution on the substrate and then we spin coated 100µL of the NaBARF solution on top. We made two identical samples in order to perform the experiments on the one and keep the other as a reference. One of the prepared samples was placed inside the chamber, and the other was retained as a reference. However, we chose to utilize a different solvent respect to the SVA experiment, which was previously mentioned, because methanol did not increase order in the porphyrin network but disrupted it. Thus, we used dichloromethane (DCM, formula $CH_2Cl_2$) a solvent more volatile (b.p.=64°C) and less polar than methanol. Upon TESVA in DCM, the initial morphology of the deposited material changed. A considerable crystal growth was visible. The crystals had different thicknesses and seemed to be fairly defined. These alterations in the deposited material's morphology following TESVA operation are a crucial sign that our TESVA device was effectively realized. There were no morphological changes in the reference sample that was stored outside.

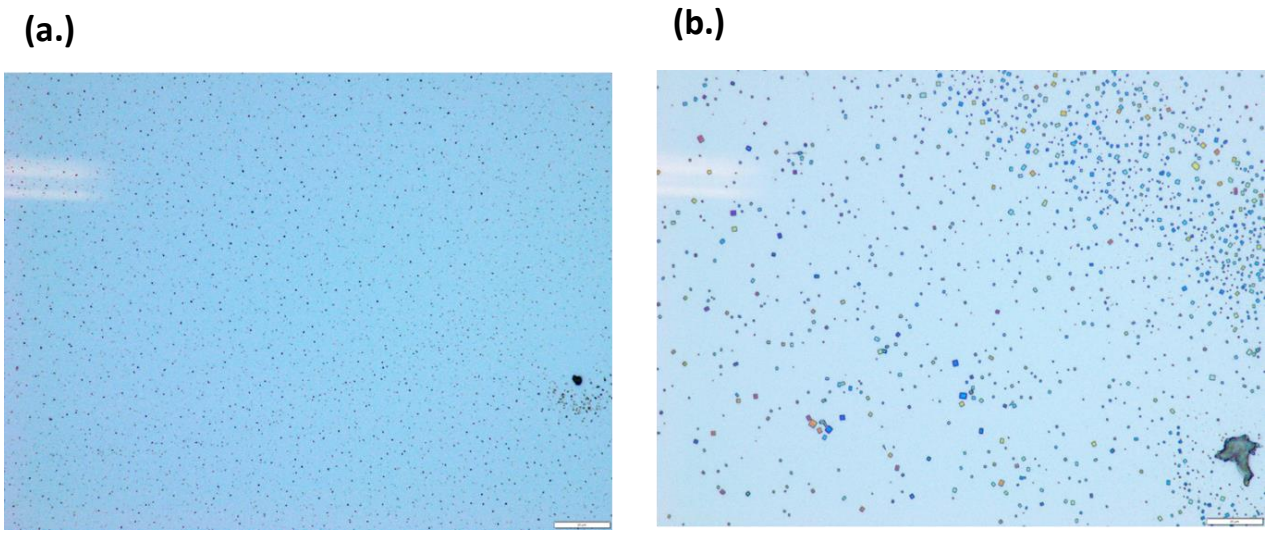


*Figure 5-12. Microscope images of porphyrins (a) before TESVA, and (b) after TESVA in $CH_2Cl_2$.*

We also tested the case of a mixed solution of the porphyrins and the salt. We repeated the steps mentioned in the first SVA experiment of this section and we ended up with a diluted solution containing the TpyP(4) and NaBARF in $CH_2Cl_2$. We again prepared via spin-coating two identical samples. Next, we inserted one of the two samples into the $CH_2Cl_2$ vapour chamber. As a reference, the other one was kept outside. We performed TESVA heating the bottom of the chamber, where the solvent reservoir was located, at 40°C for eighteen hours overnight. In this case, no active cooling of the sample was needed because, due to the good conductivity of the sample holder and to the chamber T being much higher than room temperature, we measured ≈10-degree temperature differential between the solvent and the sample surface even in the absence of liquid nitrogen.

The microscope images obtained for our system under study both before and after TESVA are displayed in Figure 5-12. It is clear that prior to TESVA, the porphyrin and NaBARF mixture was uniformly deposited over the surface, but after TESVA, the majority of the substrate surface appeared material-free and new, large crystals had formed in its place.

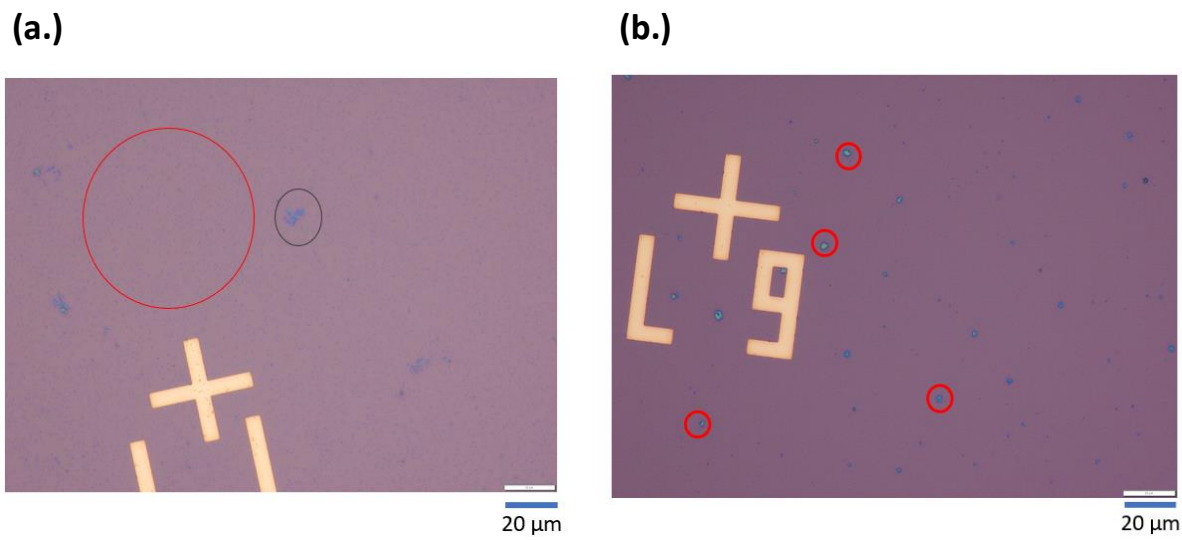


*Figure 5-13. Microscope images of porphyrins (a.) before TESVA, and (b.) after TESVA $CH_2Cl_2$.*

We used AFM both before and after the experiment to verify the changes and examine the morphological features of the materials under study. Figure 5-14 shows the AFM images captured before and after TESVA. The changes are quite noticeable, as expected from the microscope images. Initially, the material is deposited everywhere and has a morphology similar to that of Figure 5-11a. We were able to image a range of the crystals present on the surface using AFM after the completion of TESVA. Each crystal showed a similar flower-like structure as shown in the Figure 5.14b. This flower-like structure has about 100nm of height and possesses a needle-like texture. The rest of the substrate's surface appears to be entirely clean, and the crystals are fairly well-defined.

We imaged a large number of newly formed crystals for statistical purposes. A few of the topographies that correlate with the crystals are shown in Figure 5-15. Every crystal has a comparable height and shape to one another. Any differences could be attributed to different growth patterns based on when we removed the sample from the chamber. For example, if a lot of material was initially deposited in one area of the surface, this could lead to a larger crystal after TESVA was carried out.

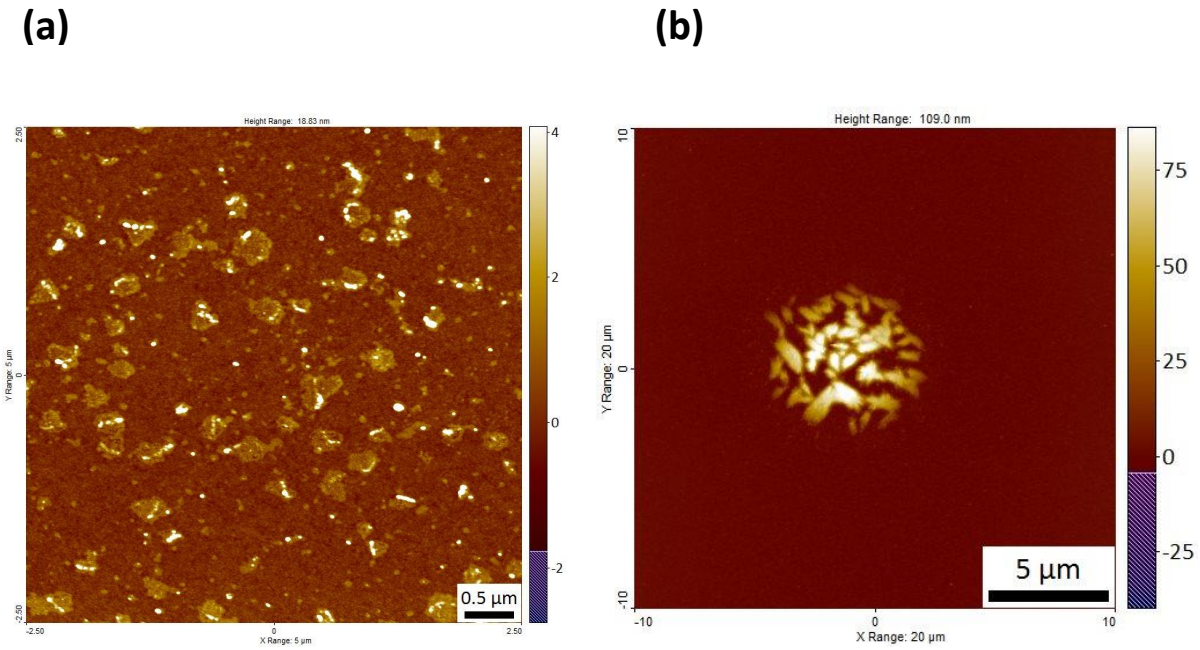


*Figure 5-14. AFM images of porphyrins (a) before TESVA, and (b) after TESVA in $CH_2Cl_2$.*

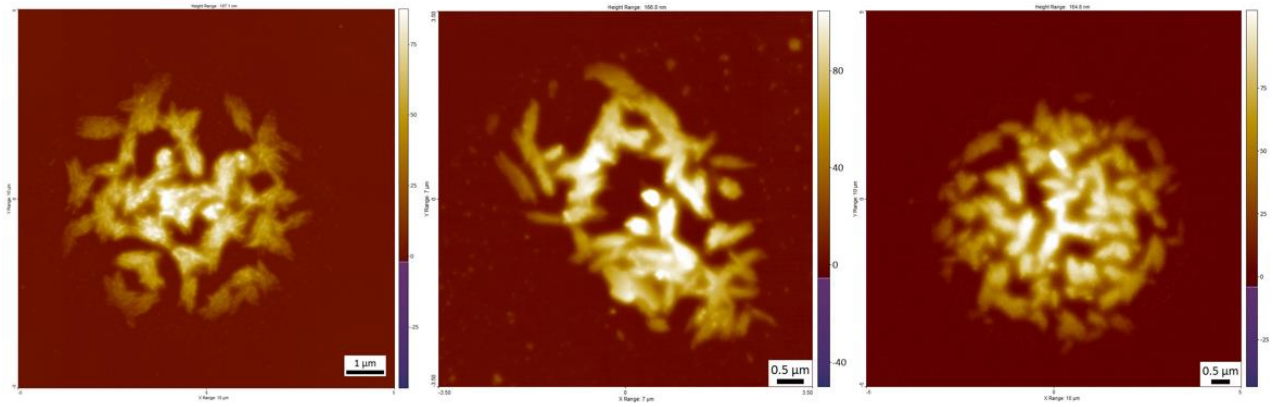


*Figure 5-15. AFM images of porphyrins after TESVA in $CH_2Cl_2$.*

## 5.4 Conclusions

In nature, hierarchical self-assembly is a ubiquitous cooperative process. Supramolecular chemistry allows the formation of nanoscale, thermodynamically stable architectures in solution by carefully utilizing various weak forces [11].

Supramolecular structures and materials are distinguished by characteristics such as reversibility, response to external stimuli, adaptability, and self-healing due to the extremely weak interactions involved. The understanding of self-assembly at surfaces is still very limited, despite the recent unravelling of the subtle mechanism governing the self-assembly of supramolecular species in solution. This is because the formation of ordered, self-assembled nanostructures at surfaces is more complex, requiring additional control over interfacial interactions [11].

Understanding functional architectures with pre-programmed structure and properties is crucial for achieving full control over their growth across multiple length scales. These architectures have potential applications in (opto)electronics, magnetism, catalysis, and medicine as active building blocks.

In this chapter we pointed out the importance of solvent vapour annealing, a technique that allows for network reorganisation and manipulation of diverse functional architectures.

Meso-tetraaryl porphyrins are ideal candidates for use as building blocks in the synthesis of complex structures due to their versatile physicochemical properties and simple synthetic pathways. In light of this, we decided to test these materials as potential systems for solvent vapour annealing and to monitor any potential modifications. Indeed, changes in the morphology of the porphyrins after the implementation of SVA were observed.

The development of temperature-enhanced solvent vapour annealing, or TESVA, is a step forward in the development of SVA. Even though TESVA has been used and produced many noteworthy results, more automated instrumentation is still required to carry out solvent vapour annealing in a controlled manner.

In that context, we developed a novel tool for temperature-enhanced solvent vapor annealing that allows for the growth and manipulation of different molecules when they are deposited on a substrate. By maintaining a specific temperature difference between the substrate's surface and the solvent used we could control the self-assembly and/or growth take place in a chamber where our initial system has been deposited. Conventional deposition methods cannot yield new nano-structures that can be realized by varying the substrate, solvent, or temperature difference. SPM techniques are then used to characterize the newly organized networks.

Utilizing TESVA, we successfully synthesized porphyrin crystals with distinct morphological features that are significantly larger and more homogeneous than the ones obtained with spontaneous self-assembly.

We infer that, in general, using TESVA any system could be able to reorganize itself in a novel but controlled manner on a target surface, given a suitable solvent and temperature differential.

# REFERENCES


[1] F. Cacialli *et al.*, "Cyclodextrin-threaded conjugated polyrotaxanes as insulated molecular wires with reduced interstrand interactions," *Nat Mater*, vol. 1, no. 3, pp. 160–164, Nov. 2002, doi: 10.1038/nmat750.

[2] K. Müllen and J. P. Rabe, "Nanographenes as Active Components of Single-Molecule Electronics and How a Scanning Tunneling Microscope Puts Them To Work," *Acc Chem Res*, vol. 41, no. 4, pp. 511–520, Apr. 2008, doi: 10.1021/ar7001446.

[3] R. H. Friend *et al.*, "Electroluminescence in conjugated polymers," *Nature*, vol. 397, no. 6715, pp. 121–128, Jan. 1999, doi: 10.1038/16393.

[4] V. Palermo and P. Samorì, "Molecular Self-Assembly across Multiple Length Scales," *Angewandte Chemie International Edition*, vol. 46, no. 24, pp. 4428–4432, Jun. 2007, doi: 10.1002/anie.200700416.

[5] E. Treossi, A. Liscio, X. Feng, V. Palermo, K. Müllen, and P. Samorì, "Temperature-enhanced solvent vapor annealing of a C3 symmetric hexa-peri-hexabenzocoronene: Controlling the self-assembly from nano- to macroscale," *Small*, vol. 5, no. 1, pp. 112–119, Jan. 2009, doi: 10.1002/smll.200801002.

[6] J. P. Rabe and S. Buchholz, "Commensurability and Mobility in Two-Dimensional Molecular Patterns on Graphite," *Science (1979)*, vol. 253, no. 5018, pp. 424–427, Jul. 1991, doi: 10.1126/science.253.5018.424.

[7] F. J. M. Hoeben, P. Jonkheijm, E. W. Meijer, and A. P. H. J. Schenning, "About Supramolecular Assemblies of π-Conjugated Systems," *Chem Rev*, vol. 105, no. 4, pp. 1491–1546, Apr. 2005, doi: 10.1021/cr030070z.

[8] M. Mas-Torrent *et al.*, "Correlation between Crystal Structure and Mobility in Organic Field-Effect Transistors Based on Single Crystals of Tetrathiafulvalene Derivatives," *J Am Chem Soc*, vol. 126, no. 27, pp. 8546–8553, Jul. 2004, doi: 10.1021/ja048342i.

[9] S. Böhme, J. Arias-Zapata, J. Garnier, C. Girardot, A. Legrain, and M. Zelsmann, "Annealing treatments of cylindrical siloxane-based block copolymers optimized for nanomanufacturing," *Micro and Nano Engineering*, vol. 1, pp. 56–62, Nov. 2018, doi: 10.1016/j.mne.2018.10.005.

[10] C. Sinturel, M. Vayer, M. Morris, and M. A. Hillmyer, "Solvent vapor annealing of block polymer thin films," *Macromolecules*, vol. 46, no. 14. pp. 5399–5415, Jul. 23, 2013. doi: 10.1021/ma400735a.

[11] G. De Luca *et al.*, "Nucleation-governed reversible self-assembly of an organic semiconductor at surfaces: Long-range mass transport forming giant functional fibers," *Adv Funct Mater*, vol. 17, no. 18, pp. 3791–3798, Dec. 2007, doi: 10.1002/adfm.200700549.

[12] A. K. Doerr *et al.*, "Observation of Capillary Waves on Liquid Thin Films from Mesoscopic to Atomic Length Scales," *Phys Rev Lett*, vol. 83, no. 17, pp. 3470–3473, Oct. 1999, doi: 10.1103/PhysRevLett.83.3470.

[13] M. Strzelczyk, P. Miiller-Buschbaum, M. Tolan, and W. Press, "Growing wetting films: An x-ray study."

[14] I. M. Tidswell, T. A. Rabedeau, P. S. Pershan, and S. D. Kosowsky, “Complete wetting of a rough surface: An x-ray study,” *Phys Rev Lett*, vol. 66, no. 16, pp. 2108–2111, Apr. 1991, doi: 10.1103/PhysRevLett.66.2108.

[15] P. G. de Gennes, “Wetting: statics and dynamics,” *Rev Mod Phys*, vol. 57, no. 3, pp. 827–863, Jul. 1985, doi: 10.1103/RevModPhys.57.827.

[16] H.-J. Lee, S.-O. Hur, M.-K. Ahn, M. Changez, and J.-S. Lee, “In situ formation of molecular-scale ordered polyaniline films by zinc coordination,” *Nanoscale*, vol. 9, no. 19, pp. 6545–6550, 2017, doi: 10.1039/C7NR01060E.

[17] K. M. Kadish *et al.*, “The Porphyrin Handbook Editors.”

[18] C. M. Drain, A. Varotto, and I. Radivojevic, “Self-organized porphyrinic materials,” *Chem Rev*, vol. 109, no. 5, pp. 1630–1658, May 2009, doi: 10.1021/cr8002483.

[19] D. C. Mauzerall, “Evolution of Porphyrins,” *Clin Dermatol*, vol. 16, no. 2, pp. 195–201, Mar. 1998, doi: 10.1016/S0738-081X(97)00200-9.

[20] M. P. Byrn, C. J. Curtis, S. I. Khan, P. A. Sawin, R. Tsurumi, and C. E. Strouse, “Tetraarylporphyrin sponges. Composition, structural systematics, and applications of a large class of programmable lattice clathrates,” *J Am Chem Soc*, vol. 112, no. 5, pp. 1865–1874, Feb. 1990, doi: 10.1021/ja00161a034.

[21] I. Goldberg, “Crystal engineering of porphyrin framework solids,” *Chemical Communications*, no. 10, p. 1243, 2005, doi: 10.1039/b416425c.

[22] C. M. Drain and D. C. Mauzerall, “Photogating of ionic currents across lipid bilayers Hydrophobic ion conductance by an ion chain mechanism.”

[23] C. M. Drain, K. C. Russell, and J. M. Lehn, “Self-assembly of a multi-porphyrin supramolecular macrocycle by hydrogen bond molecular recognition,” *Chemical Communications*, no. 3, pp. 337–338, 1996, doi: 10.1039/cc9960000337.

[24] C. M. Drain *et al.*, “Designing supramolecular porphyrin arrays that self-organize into nanoscale optical and magnetic materials,” *Proceedings of the National Academy of Sciences*, vol. 99, no. suppl_2, pp. 6498–6502, Apr. 2002, doi: 10.1073/pnas.012521899.

[25] C. M. Drain, “Self-organization of self-assembled photonic materials into functional devices: Photo-switched conductors,” *Proceedings of the National Academy of Sciences*, vol. 99, no. 8, pp. 5178–5182, Apr. 2002, doi: 10.1073/pnas.062635099.

[26] M. R. Wasielewski, “Energy, Charge, and Spin Transport in Molecules and Self-Assembled Nanostructures Inspired by Photosynthesis,” *J Org Chem*, vol. 71, no. 14, pp. 5051–5066, Jul. 2006, doi: 10.1021/jo060225d.

[27] M. Trapani *et al.*, “Metal-mediated self-assembly of tetrapyridyl porphyrins by Na+ ions,” *Chemical Communications*, vol. 48, no. 42, pp. 5136–5138, Apr. 2012, doi: 10.1039/c2cc31140b.

[28] G. De Luca, A. Romeo, L. M. Scolaro, G. Ricciardi, and A. Rosa, “Sitting-atop metallo-porphyrin complexes: Experimental and theoretical investigations on such elusive species,” *Inorg Chem*, vol. 48, no. 17, pp. 8493–8507, Sep. 2009, doi: 10.1021/ic9012153.

# CONCLUSIONS AND OUTLOOK

**The present chapter discusses the overall conclusions of the current doctoral thesis and provides an outlook for future steps.**

The increased focus on 2DMs, primarily due to graphene, has created new opportunities in several fields, including electronics, energy storage, and conversion technologies to name only a few of them. Although graphene continues to be a primary focus, several other two-dimensional materials are being investigated, such as metal chalcogenides, boron nitride, MXenes, and two-dimensional polymers.

The main goal of the current doctoral thesis was to improve synthesis and employ advanced characterization techniques at the nanoscale in order to improve the synthesis and fabrication of newly synthesized 2D materials, so that they have the necessary quality and performances to be more easily integrated into real-world applications, and to gain a thorough understanding of their fundamental properties. The work also featured a particular emphasis on the self-assembly of organic molecules on surfaces and their potential interactions with other two-dimensional materials.

This doctoral thesis was inserted in the framework of a Marie Curie training network called ULTIMATE (https://ultimate.u-strasbg.fr/index.php). The project was coordinated by prof. Samorì at the university of Strasbourg and featured some of the most recognized European groups working in the field of basic and applied research on 2D materials. In the context of the whole project, the tasks of our research unit, over more than the last three years, were specifically to create effective processing techniques for the self-assembly of certain building blocks into two-dimensional structures and to support the other research nodes more dedicated to the synthesis through our characterization capabilities. Advanced characterization methods with nanometer-size resolution for structural analysis and electrical characterization were performed using Atomic Force Microscopy (AFM), Kelvin Probe Force Microscopy (KPFM), and Conductive AFM. Furthermore, X-ray photoelectron spectroscopy was employed to characterize their chemical composition.

In chapter 2, we investigated the electrical properties of coordination polymer films made using shear coating, a novel method which could be in principle easily extended also of many other systems, thanks to its versatility. By changing the node (metal component) of the CP network under investigation, and by tuning the duration of polymer formation process and the number of coatings, we demonstrated the possibility of tuning their work function. The work function was impacted by changes in the reaction time and number of coatings, but overall, Cu-based CPs showed a higher work function value than Zn-based CPs in every case. Additionally, Zn-based CPs were found to be non-conductive in contrast to Cu-based CPs. The resistivity of Cu CPs can also be tuned by changing the number of coatings or reaction time. Zn CPs can withstand higher temperatures than Cu CPs, according to our studies on thermal stability. Cu CPs changing after heat treatment can be used to tune the film's work function, as they were found to increase after thermal treatment. We can fully realize the potential of these CPs in electronics and other fields by exploring them further and utilizing additional metal elements, substrates, and coatings.

In chapter 3 we characterized two-dimensional polyaniline thin films produced by a novel technique, called SMAIS by our collaborators at the Technical University of Dresden (TUD) in Germany. We further delved into the 2D PANI's electrical characteristics, which exhibited two distinct regions. On top of a semicrystalline thin layer formed thicker, more crystalline oval-shaped structures (islands). We examined the polyaniline that had been deposited on two different substrates and used KPFM to determine its work function. In every instance, the thin layer of PANI exhibited a marginally higher work function than the islands due to their varying thicknesses. Furthermore, we measured the conductivity of the two distinct 2D PANI regions using C-AFM. The thin layer's conductivity was found to be higher than the one of the islands. These results are again connected to the difference in thickness of the two regions. . The 2D PANI under investigation showed no changes in electrical characteristics when exposed to light. With the help of the SMAIS and other techniques, we may produce a more uniform film and fully explore and realize the potential of 2D PANI in electronics and other fields.

In chapter 4 our focus was on the investigation of the morphological and electrical traits of various 2D materials via conductive AFM, kelvin probe force microscopy, and atomic force microscopy.

Using AFM, we precisely estimated the thickness of both functionalized and pristine $Ti_3C_2T_x$ MXenes isolated sheets produced by our collaborators at Chalmers university, Sweden, finding a value which was comparable to that previously reported in the literature. We discovered an extra sublayer that exists between the substrate and the first layer of deposited MXenes through statistical analyses; this constitutes a piece of information that needs to be

considered and further researched before such sheets are used in applications. Furthermore, employing KPFM, we have demonstrated that by a careful choice of surface functionalization and type of substrate, it is possible to tune the electrical properties of MXenes flakes.

Moreover, we examined the morphological characteristics of isolated $In_2Se_3$ sheets generated through electrochemical exfoliation by our partners at TUD. Additionally, by merging them with single layer GO isolated sheets, we were able to create a new heterostructure. Using KPFM, we were able to confirm their significant differences in work function when deposited on a flat Si substrate.

In the same chapter, $MoS_2$ thin films functionalized electrochemically were investigated by means of conductive AFM and KPFM techniques. Despite the film's apparent uniform topography, the variation in surface potential value is a useful tool for studying and visualizing the functionalization brought on by the presence of S vacancies. The results obtained showed that differences in adhesion and current are related to the functionalization, opening up new possibilities for electronic applications.

Last, we reported the successful imaging of individual molecules of early soot using atomic-resolution STM and AFM with CO functionalized tips, an activity that was part of my secondment plan at IBM in Zurich. The precise structures of soot-formed molecules that we observed, along with proof of cross-linking, fully embedded five- and seven-membered rings, provied an explanation for the formation of aromatics with a moderate size. These findings, we believe, bear significance for the formation and growth of particles that have a major impact on human health and the environment.

In the last chapter of the current thesis, Chapter 5, we demonstrated the utility of solvent vapour annealing as (SVA), a method that enables the manipulation of various functional architectures and network reorganization, using porphyrins as a test model. Because of their adaptable physicochemical characteristics and straightforward synthetic routes, meso-tetraaryl porphyrins are excellent choices to employ as building blocks in the synthesis of complex structuresmolecule, that have also a large use as, a model to test and develop our SVA setup, and we observed their morphological alterations following the use of SVA. Temperature-enhanced solvent vapour annealing, or TESVA, is an advancement in the field of SVA. For solvent vapour annealing to be carried out in a controlled manner, more automated instrumentation is still needed, even though TESVA has been used and has yielded many notable results.

In that regard, we developed a novel apparatus for TESVA, which enables the growth and modification of various molecules when deposited on a substrate. Novel nano-structures that

can be achieved by adjusting the substrate, solvent, or temperature difference between the solvent and the substrate's surface cannot be produced by conventional deposition techniques. Indeed, thanks to TESVA carried out with the innovative apparatus developed in our lab, we successfully synthesized porphyrin crystals with distinct morphological features that are significantly larger and more homogeneous than those obtained through spontaneous self-assembly. What our work suggests is the fascinating possibility that any system could be able to reorganize itself in a novel but controlled way on a different surface, provided that the solvent and temperature differential are suitable.

In conclusion, we were able to successfully accomplish the objectives established at the start of this PhD project. New synthetic and conventional 2D materials were created and investigated in terms of their morphological, electrical, and structural properties. Furthermore, a new set-up was developed for future innovative synthesis and manipulation of various molecular building blocks using the TESVA technique.

Our next steps will primarily involve further developing the TESVA apparatus as well as testing new suitable systems that could be implemented to achieve uniform nanostructured thin films. MOFs and two-dimensional polymers are promising candidates. Additionally, 2D material isolated flakes such as GO and MXenes can be further tested using TESVA in search of potentially interesting reorganizations on various substrates.

New types of functionalised MXenes can be studied further using KPFM to track differences in their work function and better understand the nature of these differences. Prospective candidates for exotic heterostructures that enable unique electronic characteristics that may be used in future electronic devices and beyond, include MXenes, $In_2Se_3$, and GO sheets.

Last, the structural properties of the two-dimensional polyaniline and MOFs studied in this thesis can still be optimized using other synthesis techniques or different metallic elements. In either case, these materials are promising for a variety of applications due to their unique morphological and physicochemical properties.

To summarize, during the course of this thesis, we were able to successfully synthesize and self-assemble a range of 2D materials on different substrates. Following that, these materials were carefully examined employing a wide range of characterization methods, with a focus on their electrical characteristics. Our hope is that this work will act as a guide for future studies and improved analysis of two-dimensional materials.

# APPENDIX A

Metal-organic coordination polymer multilayers produced by sequential in situ self-assembly

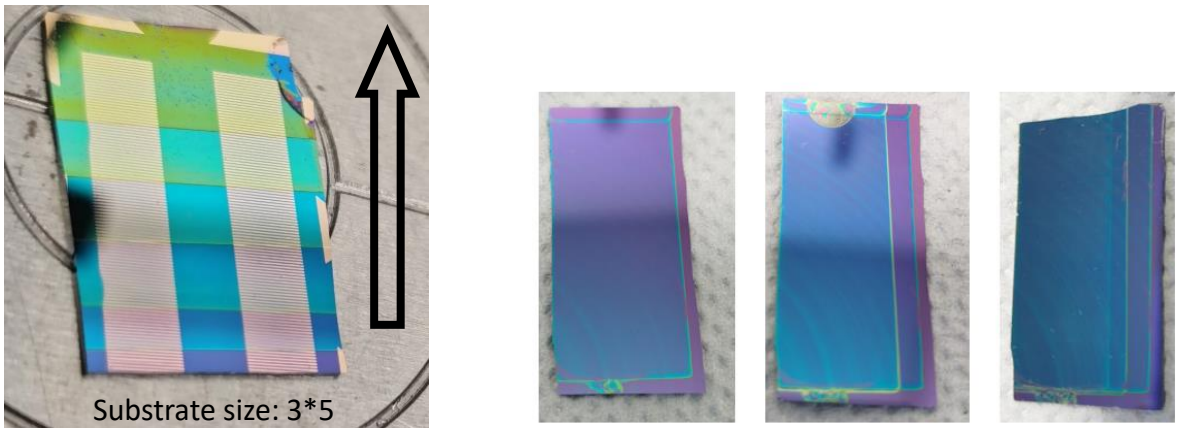


*Figure A1. Image of the multicoated and single coated samples.*

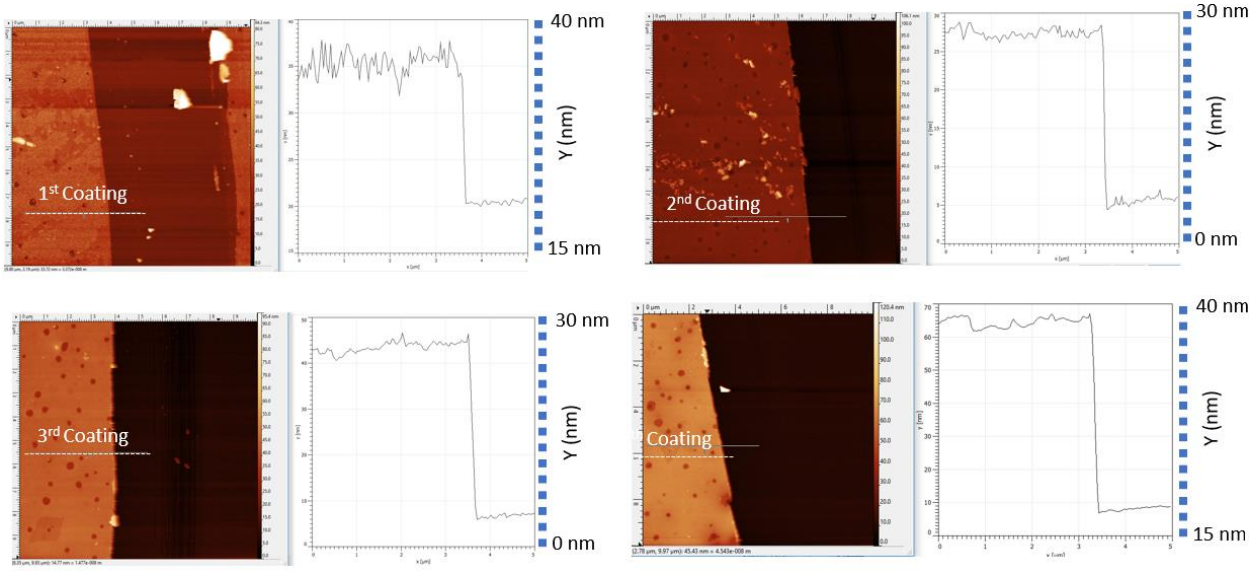


*Figure A2. AFM images showing the thickness of the various coatings.*

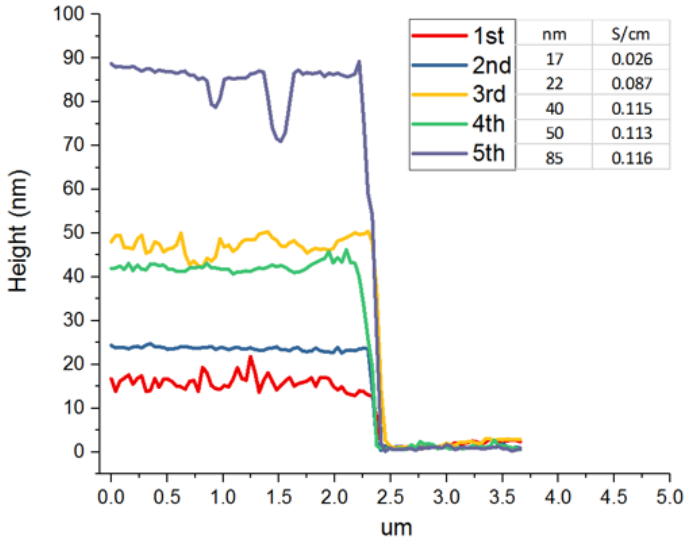


*Figure A3. Height profile graph showing the height of the various coatings.*

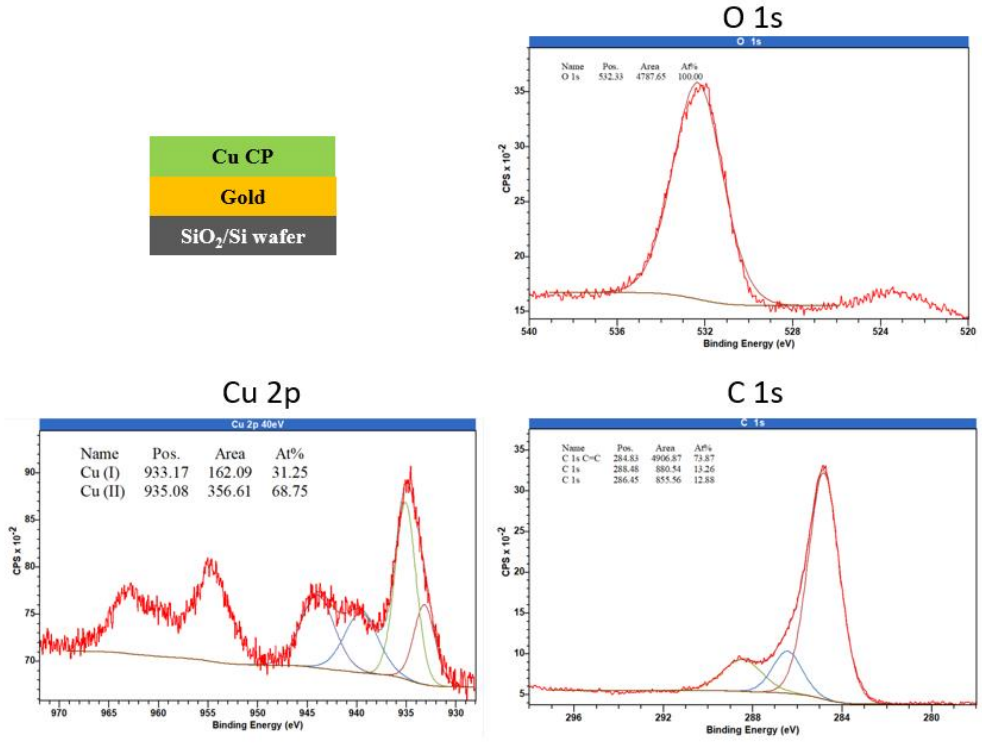


*Figure A4. High-resolution XPS spectra for Cu, C, and O in case of the Cu CP film.*

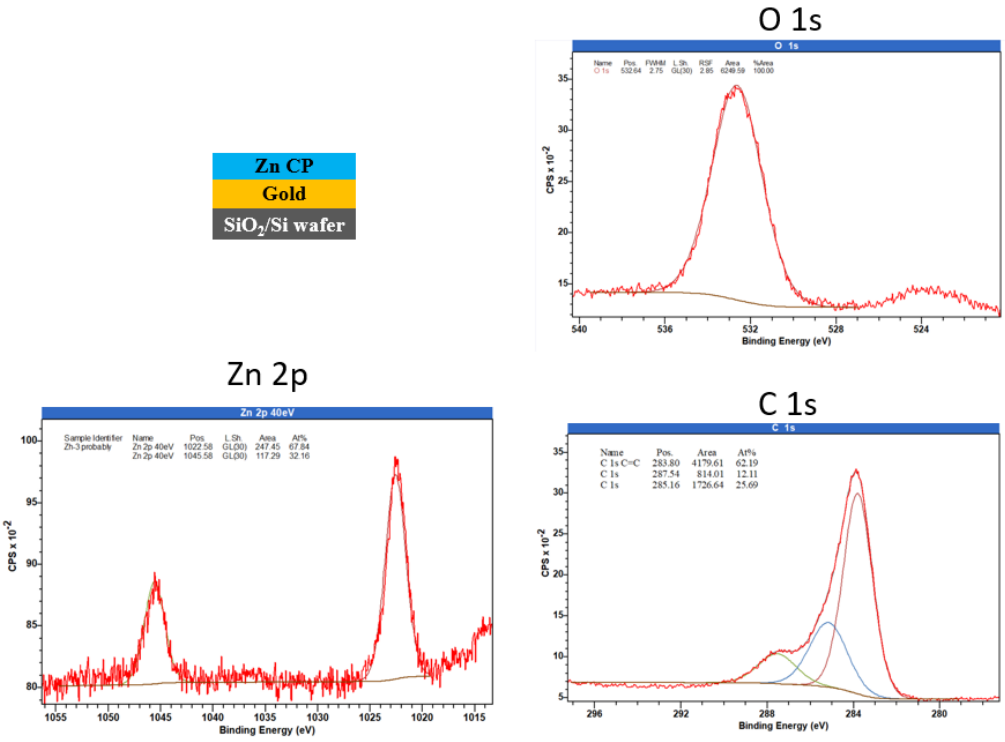


*Figure A5. High-resolution XPS spectra for Zn, C, and O in case of the Zn CP film.*

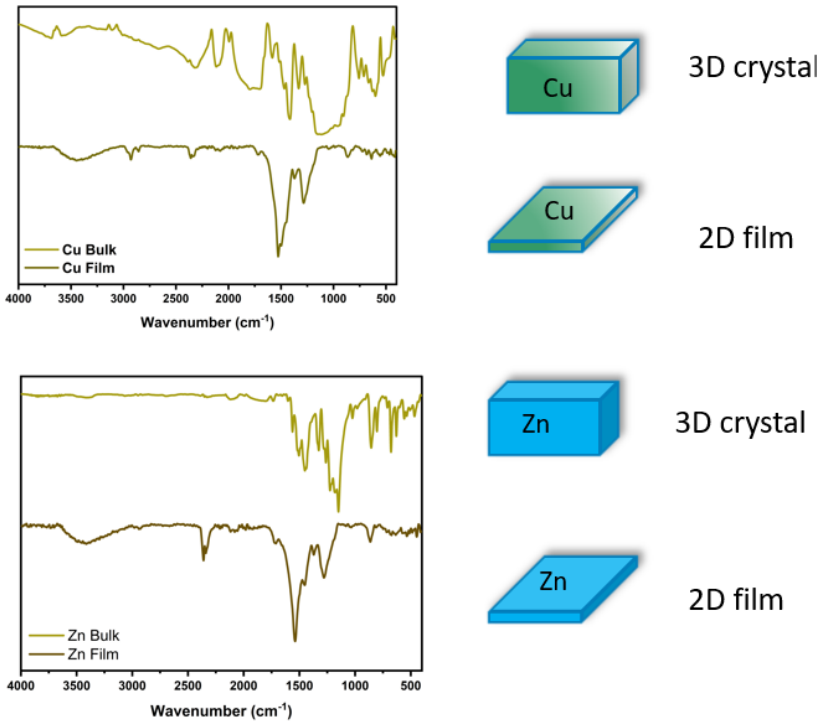


*Figure A6. Comparison of the IR spectra of both Cu and Zn CP films to the bulk crystals.*

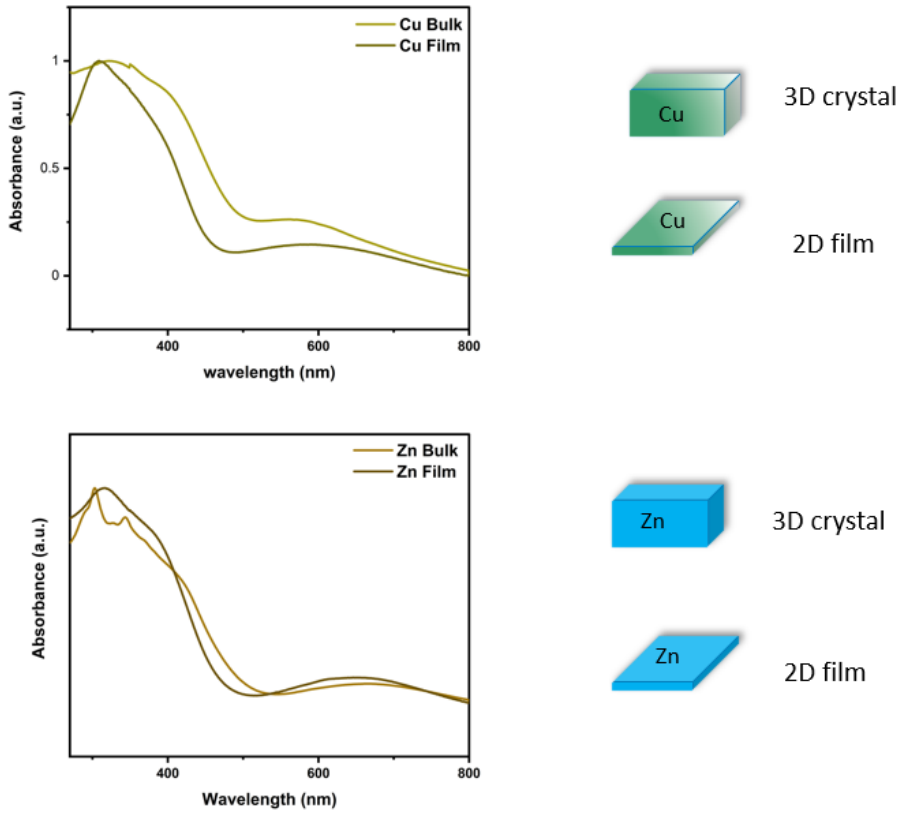


*Figure A7. Comparison of the UV-Vis spectra of both Cu and Zn CP films to the bulk crystals.*

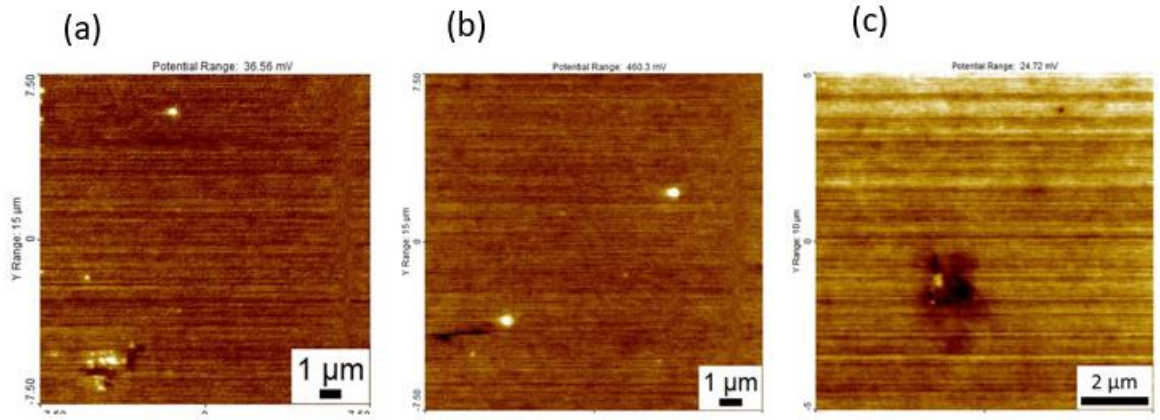


*Figure A8. Surface potential images of (a) single coated Cu-CP thin film, (b) single coated Zn-CP thin film and (c) multicoated sample.*

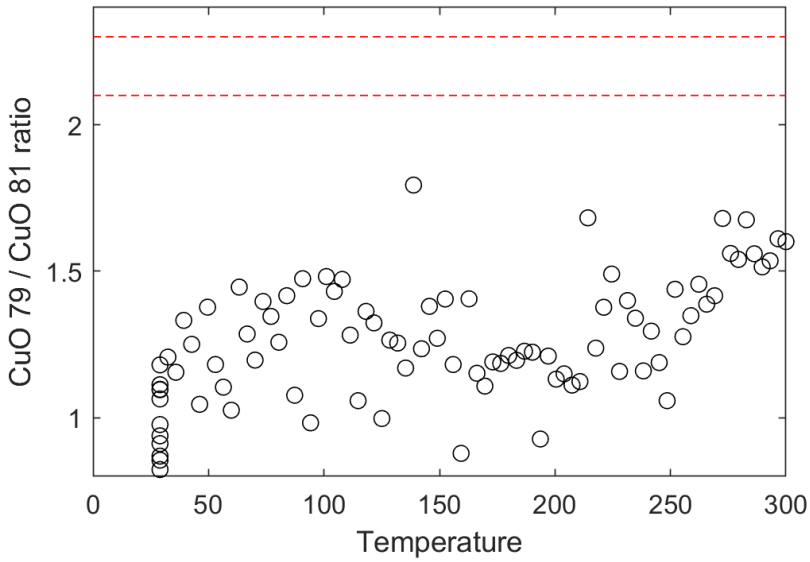


*Figure A9. CuO ratio data from the residual gas analyser-thermal stability experiment. Numbers 79 and 81 stand for specific atomic mass.*

## Morphological and electrical characterization of 2-dimensional polyaniline films self-assembled on water

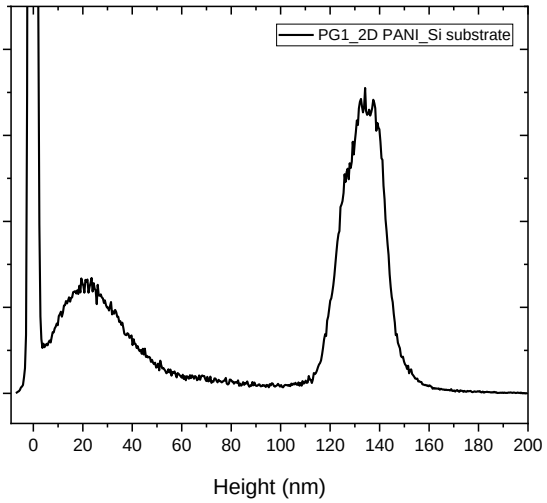


*Figure A10. Histogram of Figure 3-5.*

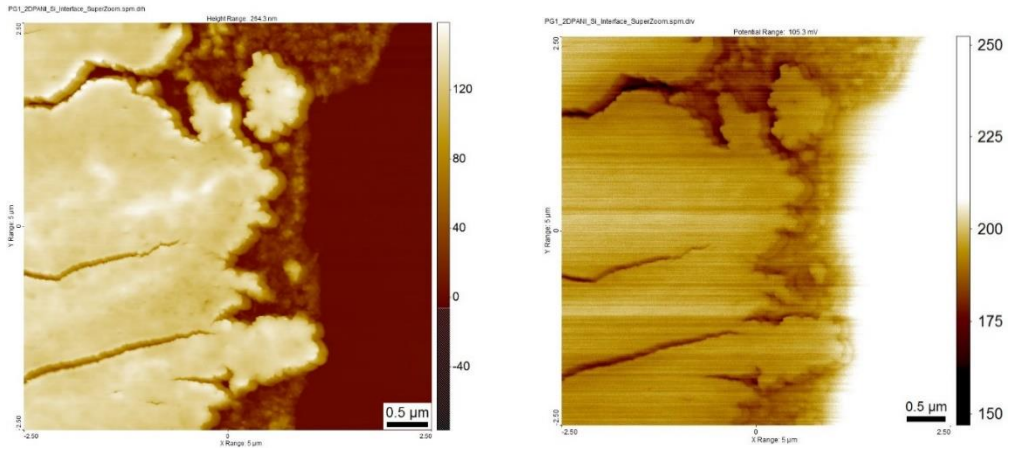


*Figure A11. (a) Topography of 2D PANI on Si substrate, (b) Corresponding surface potential image of 2D PANI on Si substrate.*

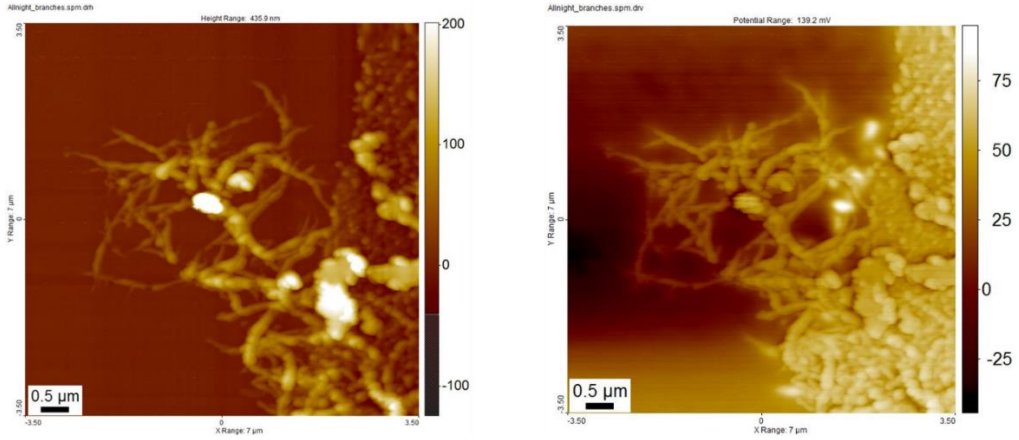


*Figure A12. (a) Topography of 2D PANI on Au substrate, (b) Corresponding surface potential image of 2D PANI on Au substrate.*

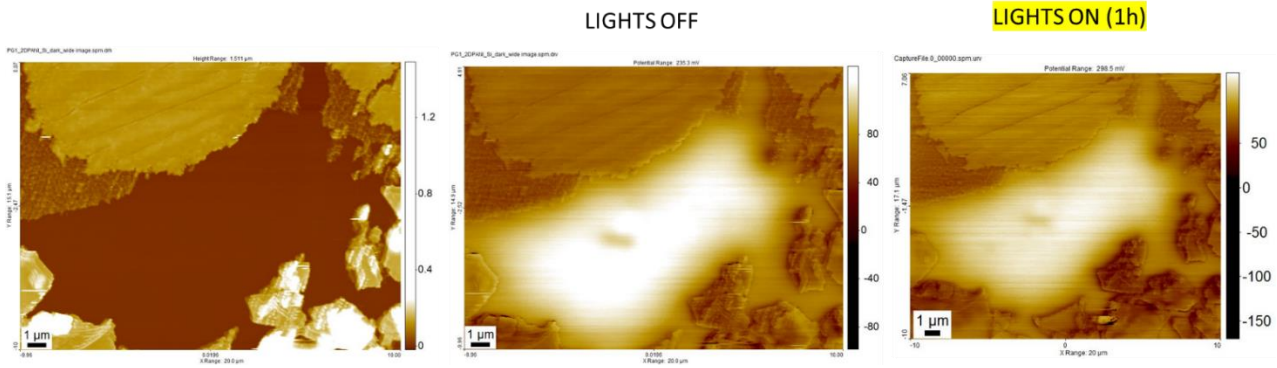


*Figure A13. From left to right: First image corresponds to the morphology of the 2D PANI, in the middle, the corresponding surface potential image when no illumination takes place, last image is the corresponding surface potential image after one hour of illumination.*

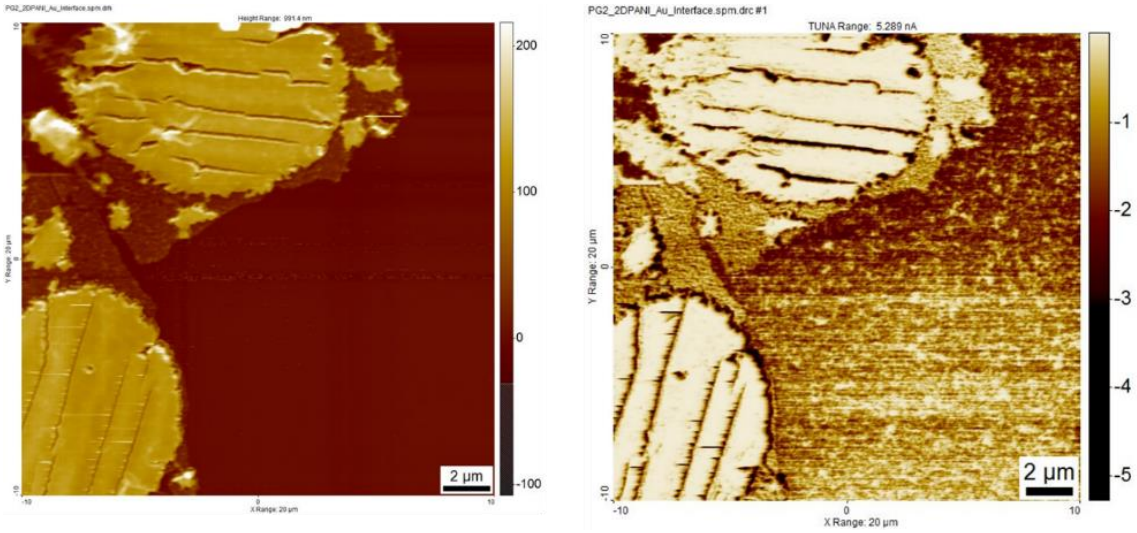


*Figure A14. (a) Topography of 2D PANI on Au substrate, (b) Corresponding current map of 2D PANI on Au substrate. Applied bias -100V.*

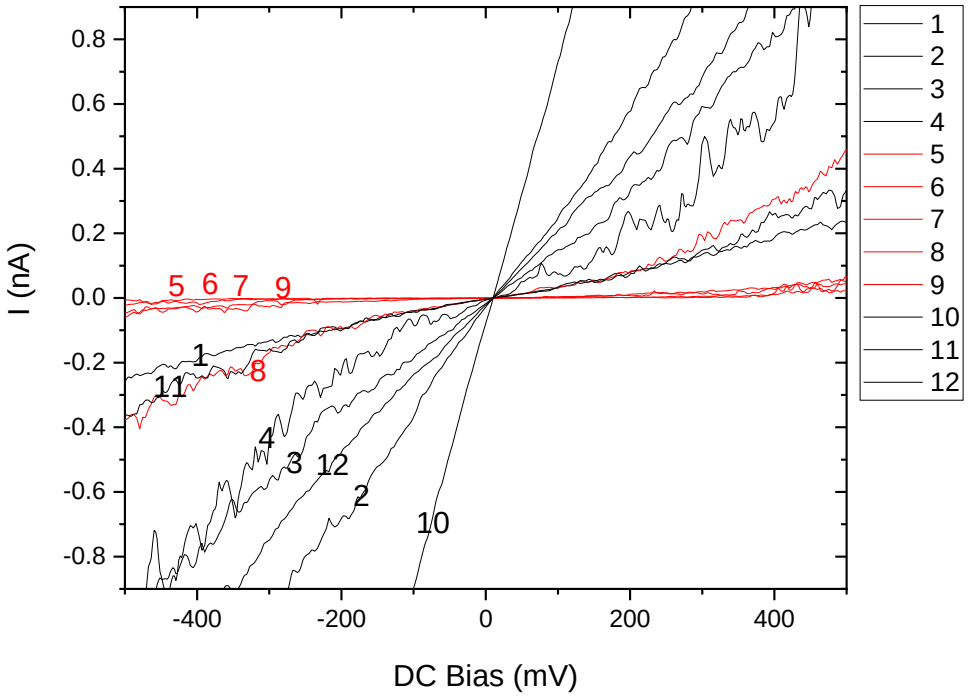


*Figure A15. Summary graph of all the IV curves of the corresponding points shown in Figure 3-10.*

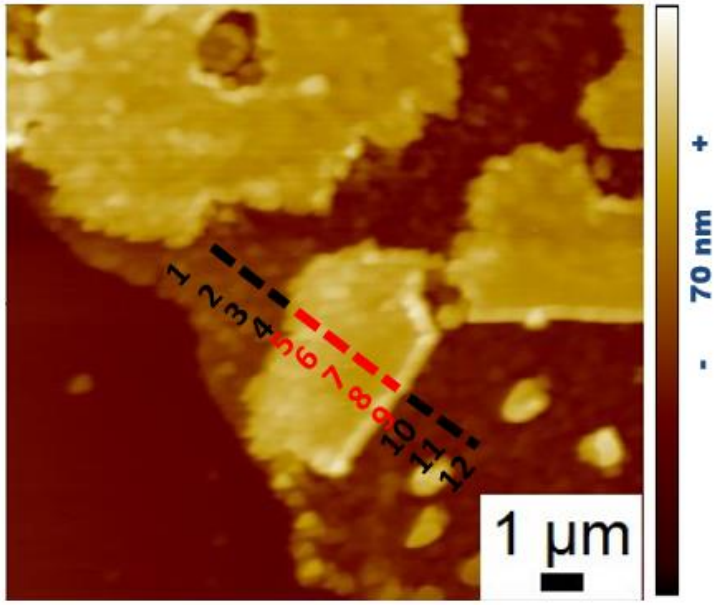


*Figure A16. AFM image of 2D PANI on Au substrate. Numbers are corresponding to the different points we applied voltage to extract the IV curves.*

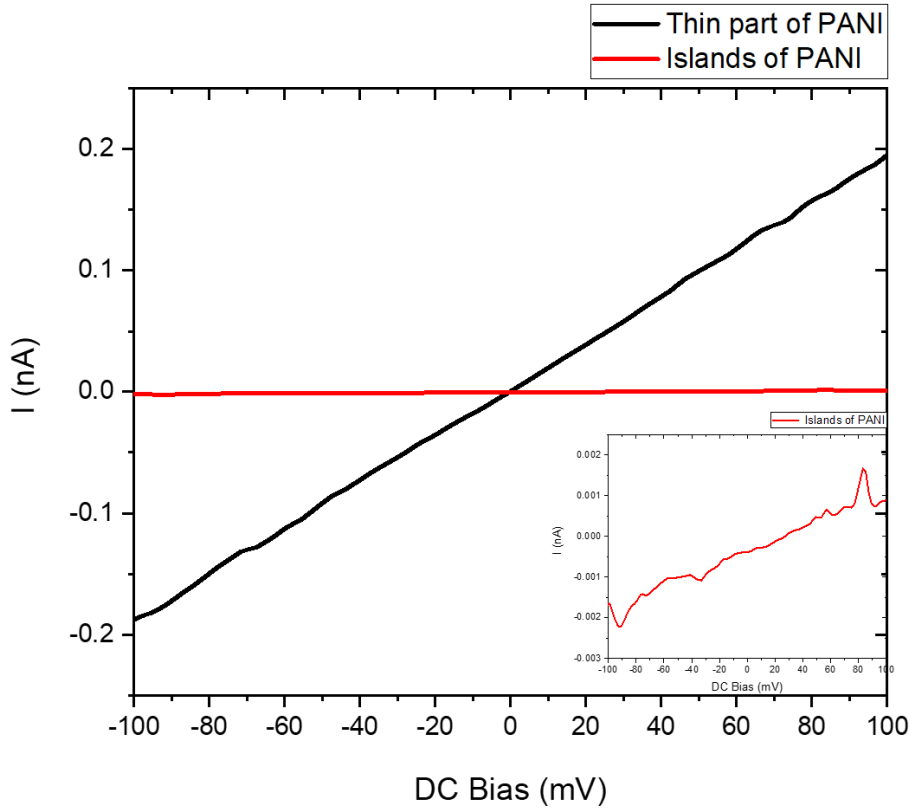


*Figure A17. Summary graph of all the IV curves of the corresponding points shown in Figure A16.*

# List of Acronyms

- **1D** One-dimensional
- **2DM** Bi-dimensional material
- **2D** Bi-dimensional
- **3D** Tri-dimensional
- **AC** Alternate current
- **AFM** Atomic Force Microscopy
- **AM** Amplitude modulation
- **C-AFM** Conductive Atomic Force Microscopy
- **CB** Conduction band
- **CPD** Contact potential difference
- **CP** Coordination polymer
- **CVD** Chemical vapor deposition
- **DMSO** Dimethylsulfoxide
- **DCM** Dichloromethane
- **DMF** N,N-Dimethylformamide
- **ES** Emeraldine salt
- **EB** Emeraldine base
- **ESCA** Electron Spectroscopy for Chemical Analysis
- **FT-IR** Fourier-transform infrared spectroscopy
- **FWHM** Full Width Half Maximum
- **HSA** Hemispherical electrostatic analyser
- **HOPG** Highly oriented pyrolytic graphite
- **ITN** Innovative training networks
- **KPFM** Kelvin Probe Force Microscopy
- **ML** Monolayer

- **MOF** Metal-organic framework
- **MPS** Sodium 2-mercaptoethanesulfonate
- **NaBARF** Sodium tetrakis[3,5-bis(trifluoromethyl)phenyl]borate
- **NMR** Nuclear magnetic resonance
- **OM** Optical Microscopy
- **OFET** Organic field effect transistors
- **OHPTP** 2,3,6,7,11,12,15,16- octahydroxyphenanthro[9,10:b]triphenylene
- **PS** Photoemission spectroscopy
- **PANI** Polyaniline
- **PSC** Polymer solar cells
- **q2D** Quasi bi-dimensional
- **RGA** Residual Gas Analyser
- **RSF** Relative Sensitivity Factor
- **SPM** Scanning probe microscopy
- **SEM** Scanning Electron Microscopy
- **SAM** Self-assembled monolayer
- **SMAIS** Surfactant monolayer assisted interfacial synthesis
- **TUNA** Tunneling Atomic Force Microscopy
- **TESVA** Temperature-enhanced solvent vapor annealing
- **TpyP(4)** Meso-tetraaryl porphyrins
- **TEM** Transmission Electron Microscopy
- **ULTIMATE** Bottom-Up generation of atomicalLy precise syntheTIc 2D MATerials for high performance in energy and Electronic applications
- **UV/vis** Ultraviolet–visible spectroscopy
- **UHV** Ultra-high vacuum
- **VTA** ((vinylbenzyl)trimethylammonium chloride)
- **VRH** Variable-Range Hopping
- **VB** Valence band
- **WF** Work function

- **XPS** X-ray Photoemission Spectroscopy
- **XRD** X-Ray Diffraction

# List of Activities during the PhD

**ORCHID ID**: 0009-0005-5359-6041

## Published work

1. "Portraits of Soot Molecules Reveal Pathways to Large Aromatics, Five-/Seven-Membered Rings, and Inception through π-Radical Localization"; Leonard-Alexander Lieske, Mario Commodo, Jacob W. Martin, Katharina Kaiser, **Vasiliki Benekou**, Patrizia Minutolo, Andrea D'Anna, and Leo Gross;
   *ACS Nano* ***2023*** *17 (14), 13563-13574,* www.pubs.acs.org/doi/10.1021/acsnano.3c02194

   I contributed to this work by performing part of the on-surface STM and AFM experiments during my secondment period within ULTIMATE Project at IBM Research and the group of Dr. Leo Gross.

## Articles in preparation:

1. "Chemical, electrical, and thermal characterization of metal-organic coordination polymer multilayers produced by sequential in situ self-assembly."
   **Vasiliki Benekou**, Zhe Zhang, Lukas Sporrer, Andrea Candini, Alessandro Kovtun, Stefan Mannsfeld, Renhao Dong, Xinliang Feng, Vincenzo Palermo

   I contributed to this work by performing the KPFM, C-AFM, and XPS experiments and writing of the manuscript.
   Part of this work was carried out during my period abroad at University of Dresden and the group of Prof. Xinliang Feng.

2. "Molecules as lubricants at the nanoscale: solvent annealing of thin organic films"
   **Vasiliki Benekou**, Andrea Candini, Vincenzo Palermo

Invited review article, ChemPlusChem, Special issue: Early Career Series Revisited
***Submitted***

**3.** "Spatially controlled distribution of sulphur atomic vacancies in $MoS_2$ thin films."
Massimiliano Cavallini, Gabriele Calabrese, Seyed A. Mirshokraee, **Vasiliki Benekou**, Giorgio Tseberlidis, Maurizio Acciarri, Alessio Mezzi, Fabiola Liscio, Andrea Candini, Alessandro Lavacchi, Giampiero Ruani, Vincenzo Palermo, Eugenio Lunedi, Carlo Santoro, Denis Gentili

I contributed to this work by performing the KPFM and C-AFM experiments on the electrochemically functionalised $MoS_2$ thin films.

**4.** "Covalent functionalization by using blue light activated radicals: on the reaction mechanisms of Arylazo Sulfones binding on Graphene.
Alessandro Mameli, Alessandro Kovtun, Derek Jones, **Vasiliki Benekou**, Vincenzo Palermo, Marco Bandini, Manuela Melucci

I contributed to this work by performing the AFM characterization on both the functionalised and pristine Graphene.

## Oral Contributions

**1.** Title presentation: *"Tuning the electrode work function by the deposition of chemically functionalized MXenes-an SPM study"* (15 min)

Conference: " Chem2DMat 2021" From 31 August to 3 September 2021, online.

**2.** Title presentation: *"Tuning the electrical properties of Metal Organic Frameworks thin films"* (15 min)

Conference: "Graphene Week 2022", $5^{th}$–$9^{th}$ September 2022, Munich, Germany.
Won Student grant for participation.

**3.** Title presentation: "*Chemical, electrical, and thermal characterization of metal-organic coordination polymer multilayers produced by sequential in situ self-assembly*" (15 min)

Conference: "Chem2DMat 2023", 15th -18th May 2023, Bologna, Italy.

## Courses, Schools and other

**1.** Graphene for Research, Innovation, Collaboration (September 2020) Online
**2.** Course on Atomic Force Microscopy: applications to nanomechanics, Dr. Alberto Rota (Unimore) October 2021
**3.** Seminar "Tunable Frictional Response of Induced Strained Graphene", Andrea Mescola, Instituto Nanoscienze CNR (4/11/21) Online
**4.** Seminar "Optically pumped lasing nanostructures as novel illumination sources", Francesca Mattino (24/06/21) Online
**5.** Lectures on the physics of graphene and 2D materials-University of Aachen (Dr. Stampfer) Online
**6.** School on Self-Assembly on Surfaces and 2D Reactivity (Organized by ULTIMATE/September 2020) Online
**7.** Workshop on "Exploitation of Results and IPR", (Organized by ULTIMATE/April 2021) Online
**8.** Seminar "Combining Enhanced Sampling simulations and Deep Learning for the study of Intrinsically Disordered Proteins", Daniele Montepietra (03/11/22) Online
**9.** Seminar "Quantum anharmonic effects and nonlinear electron-phonon coupling: beyond the standard approaches from first principles", Raffaello Bianco (13/09/22) Online
**10.** Seminar "Invariance principles of transport coefficients and their application to superionic conductors", Federico Grasselli (08/07/22) Online
**11.** 2nd School on Optoelectronic and Energy applications of 2D Materials (Organized by ULTIMATE (UNISTRA)/January 2022) Online
**12.** 3rd workshop on Business and Management skills, (Organized by ULTIMATE(APE)/May 2022), Trieste, Italy

**13.** Seminar “Nano-tools for the nervous system, from regenerative scaffolds to nanoparticles”, Ilaria Tonazzini (Istituto Nanoscienze-CNR and Scuola Normale Superiore), (18/05/23) Online

**14.** Seminar “Superconducting spintronic tunnel diode”, Maria Spies (Istituto Nanoscienze-CNR and Scuola Normale Superiore), (20/04/23) Online

**15.** 22 Weekly scientific seminars (ISOF-CNR)

**16.** 4th workshop on Outreach, (Organized by ULTIMATE(IIT)/November 2023) Genova, Italy

**17.** 5th workshop on Entrepreneurship and Career Planning (Organized by ULTIMATE(IBM)/May 2023) Zurich, Switzerland

**18.** AFM teaching activities for students and participation in schools’ lab tours at CNR-ISOF for the project RM@Schools

**19.** PhD representative of the ESRs (Early-stage researchers) within the Marie-Curie ITN project ULTIMATE

## Period abroad (secondments)

**1.** Secondment period at IBM Research (2 weeks), Dr. Leo Gross group, “Study of samples on the early stages of soot formation via high-resolution atomic force microscopy”, November 2021, Zurich, Switzerland
(The results obtained during this secondment are included in the published article: www.pubs.acs.org/doi/10.1021/acsnano.3c02194)

**2.** Secondment at University of Strasbourg (2 weeks), ISIS Institute, group of Prof. Paolo Samori, “Characterization of exfoliated 2D materials”, July 2022, Strasbourg, France

**3.** Secondment period at University of Dresden (6 weeks), group of Prof. Xinliang Feng, “Preparation of coordination polymer thin films by shear coating technique and characterisation by C-AFM and Raman spectroscopy”, October 2022, January 2023, July 2023, Dresden, Germany
(The results obtained during this secondment are included in the article in preparation: “Chemical, electrical, and thermal characterization of metal-organic coordination polymer multilayers produced by sequential in situ self-assembly.”)

# Acknowledgements

This dissertation thesis is completed under the guidance of Dr. Vincenzo Palermo. I would like to express my deepest gratitude to my advisor for his invaluable help and patient guidance. Dr. Vincenzo Palermo provided me with many opportunities to grow, challenge myself and become a better scientist. I deeply thank you.

I want to also thank my Co-supervisor Dr. Andrea Candini who was always eager to help, discuss, schedule experiments, and realise results together. All of that is appreciated.

Sincere gratitude is extended to the PhD school Coordinator, Prof. Marco Affronte and my co-supervisor, Prof. Andrea Alessandrini, for their availability and support during this doctoral thesis.

I would like to express my gratitude to each and every one of our partners for their contributions. I am grateful to Prof. Xinliang Feng for having me join his research team during my 1.5-month secondment period at the University of Dresden. Sincere gratitude is extended to Dr. Renhao Dong for all of the productive conversations and collaboration. I would also like to thank specially the PhD students Lukas Sporrer for preparing the monomer for the formation of the coordination polymer, and Zhe Zhang for realizing the coordination polymer thin films. Mr. Peng Zhang and Dr. Ali Shaygan Nia are also thanked for providing us with 2D PANI samples and the $In_2Se_3$ solution, respectively. A big thank you to all of the group in Dresden for their assistance and welcoming atmosphere.

For his preparation of the MXenes solution, I would like to thank Prof. Jinhua Sun of Chalmers University in Sweden. Furthermore, I'd like to extend my gratitude to Dr. Massimiliano Cavallini for all of our fruitful discussions about electrochemically functionalized Mos2 thin films, as well as M. Acciarri's group at Bicocca University in Milano, who prepared the MoS2 samples under study.

I would like to thank Dr. Leo Gross for welcoming me to IBM Research in Zurich, where I spent part of my secondment period and learned a great deal about the exciting field of atomic resolution imaging. Thank you, Leonard Lieske, and the group at IBM for your assistance and hospitality. Sincere gratitude is extended to everyone who helped with our published work on soot molecules.

Furthermore, I would like to thank Prof. Paolo Samori and his entire team at ISIS at the University of Strasbourg for helping me and working so well together during my secondment period.

I'd like to thank PhD student Anton Naumenko for his contribution to the development of the TESVA setup, as well as Dr. Derek Jones for his ongoing assistance and support throughout this project. I am especially grateful to Prof. Giovanna de Luca for her help with the synthesis of the porphyrins and her willingness to assist and instruct me in advanced chemistry.

I am particularly grateful to Dr. Alessandro Kovtun for sharing his knowledge in many scientific fields, and for teaching me how to perform characterization via XPS independently.

For their cooperation and for always making me feel welcome, I would like to thank all of the present and past members of my group at ISOF.

Last but not least, I'd like to thank my friends and family for their continuous love and support.

This dissertation would not have been possible without funding from the H2020-MSCA-ITN ULTIMATE (grant number 813036).